From Nanohardness to Strength Properties of Cohesive-Frictional Materials – Application to Shale Materials

by

Francois P. GANNEAU

Ingénieur de l'Ecole Polytechnique (2002)

Submitted to the Department of Civil And Environmental Engineering
in partial fulfillment of the requirements for the degree of

Master of Science in Civil And Environmental Engineering

at the

MASSACHUSETTS INSTITUTE OF TECHNOLOGY

September 2004

Signature of Author .....
Department of Civil And Environmental Engineering
13 August 2004

Certified by .....
Franz-Josef Ulm
Associate Professor of Civil and Environmental Engineering
Thesis Supervisor

Accepted by .....
Heidi Nepf
Chairman, Departmental Committee on Graduate Students

From Nanohardness to Strength Properties of Cohesive-Frictional Materials – Application to Shale Materials

by

Francois P. GANNEAU

Submitted to the Department of Civil And Environmental Engineering
on 13 August 2004, in partial fulfillment of the
requirements for the degree of
Master of Science in Civil And Environmental Engineering

Abstract

Advanced experimental and theoretical micromechanics such as nanoindentation makes it possible today to break down highly heterogeneous materials to the scale where physical chemistry meets (continuum) mechanics, to extract intrinsic material properties that do not change from one material to another, and to upscale the intrinsic material behavior from the sub-microscale to the macroscale.

While well established for elastic properties, the extraction of strength properties of cohesive-frictional materials from nanoindentation tests has not been investigated in the same depth. The focus of this thesis is to investigate in depth the link between nanohardness of cohesive-frictional materials and strength properties. To address our objectives, we develop a rational methodology based on limit analysis theorems and implement this methodology in a finite element based computational environment.

By applying this technique to indentation analysis, we show that it is possible to extract the cohesion and the friction angle from two conical indentation tests having different apex angles. The methodology is validated on a model cohesive-frictional material, bulk metallic glass, and a first application to a highly heterogeneous natural composite material, shale materials, is shown. The results are important in particular for the Oil and Gas industry, for which the reduced strength properties (cohesion and friction angle) are critical for the success of drilling operations.

Thesis Supervisor: Franz-Josef Ulm
Title: Associate Professor of Civil and Environmental Engineering

Contents

List of Tables

List of Figures

Acknowledgement

I want to express my deep gratitude to Franz-Josef ULM for the enthusiasm, interest and especially the availability with which he followed my work, as well as for the financial support which he provided over the summer and fall term of 2004. Jean Salençon shared his knowledge and gave me fruitful advice, I am very grateful for this. I would also like to thank the other members of the research group from whom I learned a lot during my time at MIT: Emilio Silva, Hesson Park and especially Georgios Constantinides for the helpful discussions and his experimental expertise. A special thanks goes to Sandra Tenorio, Forest Flager and Chris Bobko who helpfully proofread my writing. Last I want to thank the Presidential Fellowships Fy 2003 as well as The Schoettler Scholarship Fund for financial support during my two first terms at MIT.

Part I

General Presentation

Chapter 1

Introduction

1.1 Industrial Context

The Oil and Gas industry sustains financial losses due to wellbore failure of over $1 billion each year. Yet, such an estimate may well be a conservative one as many critical issues related to production stability are still neither well understood nor adequately evaluated. The analysis of wellbore stability requires assessment of the rock strength and its potential risk of failure, resulting in wellbore collapse, unwanted hydraulic fracturing, wellbore breakouts, sand production, and perforation collapse. Some potential risks related to wellbore stability are sketched in Figure 1-1.

Shales make up the majority of the geologic section in sedimentary basins, which is where most oil and gas exploration and production occurs. An understanding of shales is thus essential for petroleum-related earth sciences (e.g. geologic modeling, seismic interpretation) and drilling engineering (e.g. wellbore stability, pore pressure prediction). It is well known that shale materials in oil and gas drilling applications are the major source of wellbore drilling instability, due to the highly heterogeneous and anisotropic composition of shale materials, with possible heterogeneities that manifest themselves at multiple scales: from the scale of the platy minerals of clays in the sub-micrometer range, to the scale of silt-size (quartz) grains in the micrometer range, to the scale of the deposition layers of shales in the sub-mm to cm range.

The reduced strength properties, namely the cohesion c and the friction angle φ, of shales and other surrounding rocks play a critical role in the stability. Equations for calculating the

necessary drilling fluid density in order to ensure hole stability use both c and φ [23]. If either is off (usually more sensitive to c than to φ), then the calculated fluid density will be off as well. If the density is too low then the hole can become unstable during drilling, resulting in increased costs and sometimes loss of the hole section (requiring redrilling). If the density is too high, then unintentional creation of a hydraulic fracture may result. Knowledge of c (but usually not φ) is needed also for predicting whether or not one needs sand control[1] in the reservoir section of the well in order to prevent sand production. In addition, in reservoirs subject to large amounts of pore pressure reduction (depletion) during their lifetime, the effective stress state can sometimes approach the yield or failure condition of the rock (as defined by c and φ). It is important to be able to predict and possibly avoid this risk of failure.

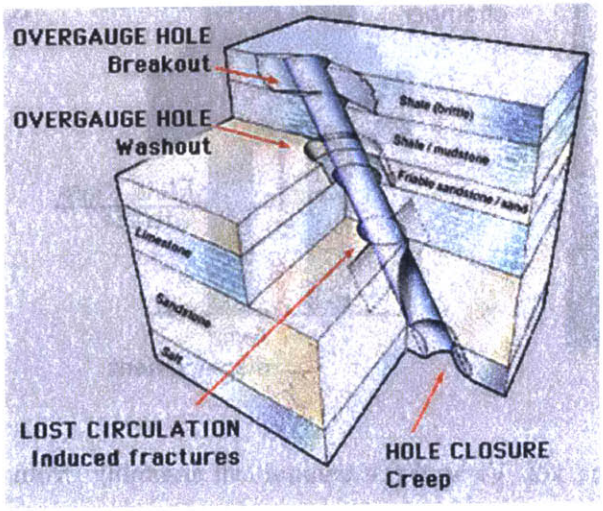

Figure 1-1: Borehole and surrounding rock.

In order to appropriately choose the drilling fluid chemistry and density (i.e. bore hole stability analysis, etc.), drilling through shale rock type materials still requires expensive macroscopic material sampling for macroscopic material characterization of the mechanical, or more precisely poromechanical behavior. Strength properties are usually estimated using triaxial test meth-

[1] Sand control is a physical means of excluding sand particles from entering the well along with the produced fluids or gas.

ods. Figure 1-2 displays a triaxial equipment. To construct the strength domain, deviatoric loading is applied at increasing confining pressure. By plotting measured effective compressive

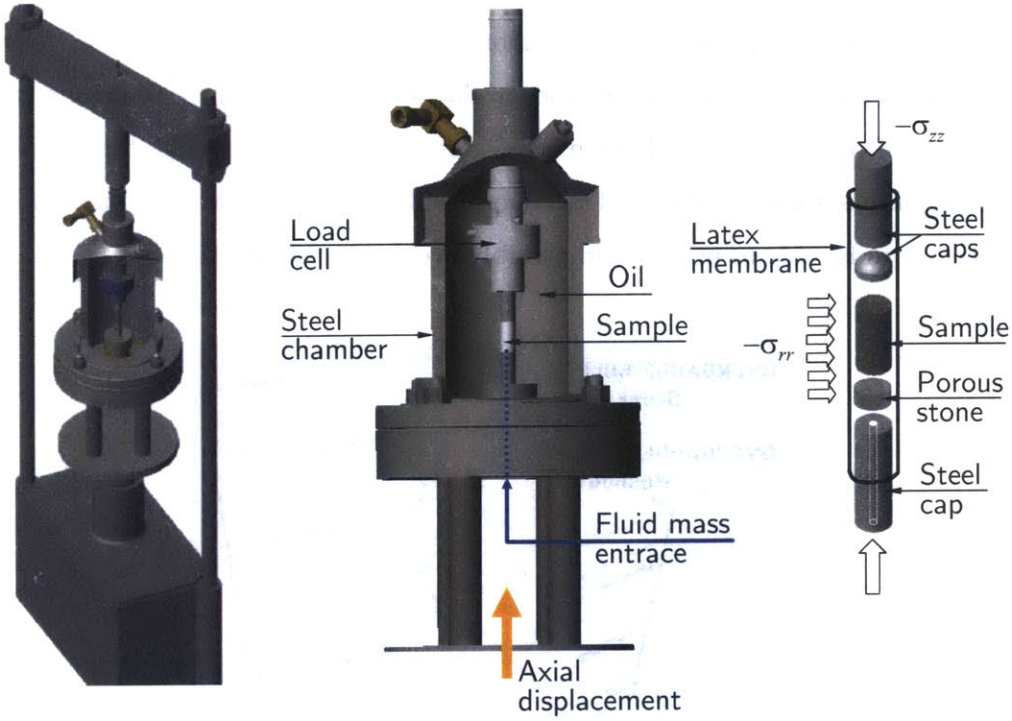

Figure 1-2: View of the triaxial cell assembly (from [36]).

strengths as a function of the effective confining stress (see e.g. [24]), the friction angle φ and the unconfined compressive strength C_0 is extracted (Fig. 1-3). For a Mohr-Coulomb material, C_0 is linked to the cohesion c by:

$$C_0(1 - \sin(\varphi)) = 2c\cos(\varphi) \tag{1.1}$$

1.2 Research Motivation and Objectives

Advanced experimental and theoretical micromechanics such as nanoindentation (see Chapter 2 for a review of the state-of-the-art technique) makes it possible today to break down highly

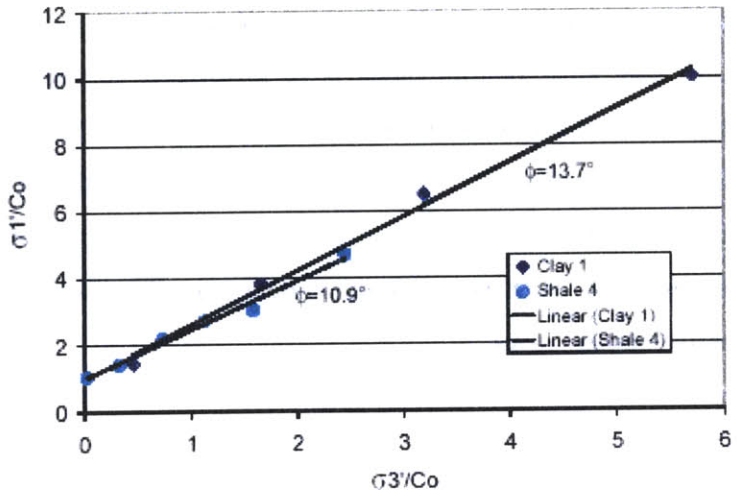

Figure 1-3: Triaxial strength domain of shale materials (from [24]).

heterogeneous materials to the scale where physical chemistry meets continuum mechanics, that is where the intrinsic properties do not change from one material to another. Once this scale of invariant material properties is identified, it is possible to upscale the intrinsic material behavior from the sub-microscale to the macroscale. This approach has been successfully implemented by Constantinides and Ulm [18] for cementitious materials to extract the intrinsic elastic properties of the high density and low density C-S-H[2] phases; and by Hellmich and Ulm [33] for all minerals tissues (bones). A similar approach is currently under development for shale materials. The work presented here contributes to this effort.

Our purpose is to identify intrinsic strength properties through nanohardness measurements obtained by nanoindentation techniques (see Fig. 1-4 for a schematic of the test). For metals, which do not exhibit any frictional behavior, the link between hardness[3] and uniaxial yield strength is well established by now [10] [82]. For ceramics, hardness is commonly used to characterize resistance to deformation, densification and fracture [70].

We will argue, however in this study that hardness H is not a material property, as it varies with the indenter geometry. It is an experimental parameter, namely the mean contact

[2]C-S-H: Calcium Silica Hydrates, main binding phase in all Portland cement-based systems.

[3]Hardness H is usually defined as the average pressure below the indenter, i.e. $H = P/A_{true}$, where P and A_{true} are respectively the driving force and the "true" projected contact area below the nanoindenter.

pressure below the indenter, from which "true" physical properties can be inferred [92]. With regards to cohesive and frictional materials, hardness H is at least a function of c and φ; i.e. $H = H(c, \varphi, ...)$. The focus of this thesis is to investigate in depth the link between nanohardness of cohesive-frictional materials and strength properties. In contrast to metals or ceramics, we deal with a two parameter problem that requires two different relations between hardness and strength properties. Cohesion and friction angle need to be extracted from two different indentation tests (i.e. with two different indenters). Whether and how this can be achieved is the objective of this thesis.

1.3 Chosen Approach

To address our objectives, we develop a rational methodology based on limit analysis theorems and implement this methodology in a finite element based computational environment.

Limit analyses is a powerful method for analyzing indentation problems: the lower and upper bound theorems provide rigorous bounds on the exact collapse load. However, the conventional analytical techniques used to solve limit theorems (e.g. methods of characteristics) are very difficult to apply for complex geometries (such as cones) and loading conditions. Furthermore, crude upper and lower bound loads may not adequately predict the collapse load. It is indeed often difficult to construct statically admissible stress fields which give a lower bound close to the true collapse load. Regarding the upper bound, an accurate estimation is very difficult to obtain in cases where the material dilates at failure.

Therefore, a more robust numerical approach for computing lower and upper bound is highly desirable. More precisely, it is the purpose of this work to derive, through lower and upper bound approach, an accurate estimate of the dimensionless parameter $\frac{P}{cA} = \frac{H}{c}$ as a function of φ:

$$\frac{P}{cA} = \frac{H}{c} = \mathcal{F}(\varphi) \tag{1.2}$$

for different indenter shapes, where c is the cohesion, φ the friction angle of the material, P the driving force and $A = \pi R^2$ the projected contact area (Fig. 1-4).

Once this hardness-cohesion-friction angle relation is established, we will develop and validate a method to extract meaningful strength properties from nano and microhardness mea-

surements.

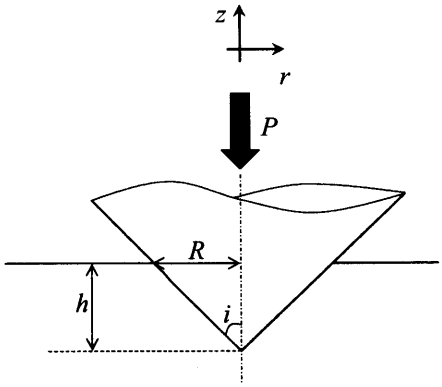

Figure 1-4: Conical indentation test schematic. (P is the driving force, h the penetration depth, R the radius and i the semi-apex angle).

1.4 Thesis Outline

This report is divided into three major parts. The first part deals with the presentation of the topic and comprises two Chapters. Following this introduction, Chapter 2 discusses the existing knowledge about the extraction of material properties from nanoindentation tests.

The second part focuses on the computational implementation of the Limit Analysis theorems in axisymmetric conditions. Chapter 3 describes the lower bound implementation; that is the discretization of statically and plastically admissible stress fields. Chapter 4 discusses the application of the method for different indenters and boundary conditions. We explore the possibilities of the method for perfectly rough cones and frictionless indenters, and move on to spherical indentation. Chapter 5 presents the implementation of the upper bound theorem, based on the discretization of kinematically and plastically admissible velocity fields. Useful upper bounds for conical and spherical indenters are derived in Chapter 6. In addition the upper bound approach is verified and we address the same type of problems as in Chapter 4.

Part III of this thesis focuses on the validation and application of the derived solutions. Chapter 7 concentrates on the validation of the derived hardness-cohesion-friction angle relation

through application of the method to a model material: metallic glass. Chapter 8 deals with the application to shales and aims at extracting the cohesion of these materials from nano and micro-hardness tests. Finally Chapter 9 summarizes the main findings of this study, and gives suggestions for future research.

In the Appendix, technical proofs and additional information are provided.

1.5 Research Significance

Providing the means of assessing the intrinsic strength properties of highly heterogeneous materials, such as shales and other frictional materials, is a significant contribution to the existing knowledge of nanoindentation analysis. This shall make it possible to estimate critical properties for the wellbore drilling stability through very simple and fairly cheap nanoindentation tests, on very small material samples.

In addition, at a completely different scale, the indentation solutions can also be applied to the circular foundation problem, and especially to the problem of driving a pile (or any body of revolution) into a cohesive-frictional soil. Both problems received much attention during the past 20 to 30 years. Those stability problems are indeed of great interest for off shore rigs and other marine foundations (e.g. [65] [32]). The methodology developed in this thesis may as well be useful for these applications at the macroscale.

Chapter 2

Instrumented Indentation

It has long been hypothesized that the localized contact response measured by an instrumented indentation experiment can serve to characterize the mechanical properties of materials as quantitatively as conventional testing techniques such as uniaxial compression and tension. This Chapter gives a brief overview of the current knowledge on nanoindentation analysis. From this discussion, the gap in the knowledge about the link between hardness and strength properties of cohesive-frictional materials is identified.

2.1 Introduction

The instrumented indentation test provides a continuous record of the variation of the penetration depth, h, as a function of imposed indentation load, P, into the indented specimen surface. Figure 2-1 illustrates the operating principle of the nanoindentation test apparatus. Advances in hardware and software control currently enable maximum penetration depths on the nanometer scale, such that nanoscale instrumented indentation provides a convenient, non-destructive means to evaluate the basic mechanical response of small material volumes of a bulk, thin film, or composite materials. Commercially available indenters accommodate various indenter geometries, including sharp pyramidal, conical or spherical probes, so that elastic and plastic mechanical properties can be estimated at any scale within the limits defined by the indenter dimensions and maximum penetration depth. Thus, instrumented indentation is a versatile tool for material characterization, particularly at scales where classical mechanical

tests based on volume-averaged stresses are inadequate.

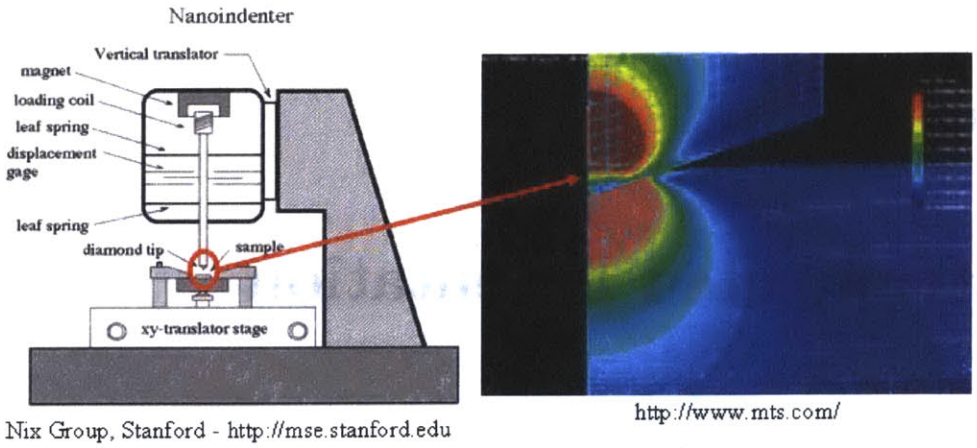

Figure 2-1: Nanoindentation setup and stress field below the indenter tip.

2.2 Historical Background

Contact Mechanics may be said to have started in 1882 with the publication by Heinrich Hertz of his classic paper *On the contact of elastic solids* [35]. Members of the audience were quick to perceive the importance of Hertz's theory, and persuaded him to publish a second paper in a technical journal. However, developments in the theory did not appear in the literature until the beginning of the 20th century (from [47]).

The engineering application of indentation methods to assess material properties can be traced back to the work of the Swedish engineer Brinell. Pushing a small ball of hardened steel or tungsten carbide against the surface of the specimen, Brinell empirically correlated the shape of the permanent impression (indentation) with the strength of metal alloys. The first accessible work of this pioneering approach of the Swedish engineer can be found in a 1900 International congress in Paris [10]. The merits of Brinell's proposal were quickly appreciated by contemporaries: Meyer (1908), O'Neill (1944) and Tabor (1951) [82] suggested empirical relations to transform indentation data into meaningful mechanical properties.

The indentation test provides a $P-h$ curve, and the extraction of material properties requires an inverse analysis of these data. The theoretical foundation of elastic indentation is set by Boussinesq's problem and the Hertz contact problem: Boussinesq's stress and displacement solution of an elastic half-space loaded by a rigid, axisymmetric indenter [9], which was subsequently extended for conical and cylindrical indenter geometry, provides a linear $P-h$ relation. Hertz's elastic contact solution [35] of two spherical surfaces with different radii and elastic constants provides a means of evaluating the contact area of indentation, and forms the basis of much experimental and theoretical work in indentation analysis based on contact mechanics. Subsequently, Sneddon [78] derived general relationships among load, displacement and contact area for any indenter describable as a solid of revolution.

Incorporating plasticity phenomena in the indentation analysis is a much more complex problem. The nonlinear nature of the constitutive relations, as well as the increased number of material properties required to describe material behavior, complicate the derivation of analytical solutions. As a result, much of our knowledge of the importance of plasticity in indenter contact problems has been derived through experimentation, and more recently through finite element simulations. Various researchers have proposed semi-analytical procedures by which the experimental $P-h$ response can be used to derive elasto-plastic properties; such as the elastic modulus E, the strain hardening exponent n and the initial yield stress σ_0 (at zero offset strain) for a Von Mises type material [21], [69], [31], [96], [19], [16]. Experimental data has demonstrated that analysis of indentation data via elastic solutions provides reasonable estimates of the elastic modulus and hardness of the indented material, provided that the contact area is measured or calculated accurately.

2.3 Indentation Analysis of Elastic and Elasto-Plastic Properties

A typical indentation test is composed of a loading and an unloading response (Fig. 2-2). The slope of the unloading curve can be used as a measure of the elastic properties of the material. The behavior of the material during unloading is assumed to be purely elastic, in which case elastic punch theory can be employed to determine the elastic properties. For a linear elastic

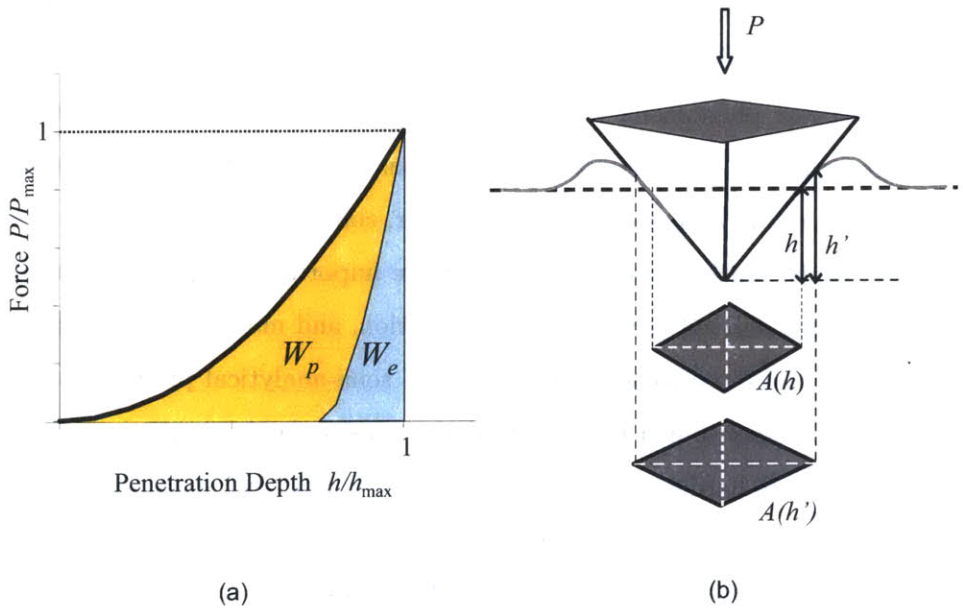

Figure 2-2: Principle of indentation test: (a) $P-h$ curve. (b) Indenter with pile-up phenomenon and projected contact area.

material, use of the elastic solution for a flat cylindrical punch relating the applied force, P, with the indentation depth, h, yields the following expression for the initial unloading response dP/dh:

$$\frac{dP}{dh} = c^* A^{1/2} E^* \tag{2.1}$$

where $c^* = 2/\sqrt{\pi}$, A is the contact area, and E^* the indentation modulus. For an isotropic material, E^* is related to the elastic constants of the indented material and indenter E, ν and E_{in}, ν_{in} by:

$$\frac{1}{E^*} = \frac{1-\nu^2}{E} + \frac{1-\nu_{in}^2}{E_{in}} \tag{2.2}$$

Eq. (2.1) is based on the elastic solution of the flat-ended cylindrical punch, but holds for any punch that can be described by a smooth solid of revolution (spherical, conical, elliptical etc.) [69]. Berkovich and Vickers indenters (three- and four-sided pyramidal cones, respectively), which are more commonly applied in instrumented indentation techniques, cannot be described as bodies of revolution. However, it has been found experimentally and by means of finite element simulations that the deviation from relation (2.1) of pyramidal and other geometrical shapes during unloading is negligible [50], [69] [19]. The constant $c^* = 1.142$ for the Vickers pyramid indenter (square cross section), and $c^* = 1.167$ for the Berkovich indenter (triangular cross section) differ little from $c^* = 2/\sqrt{\pi} = 1.128\,4$ of the flat cylindrical indenter. In other words, relation (2.1) can be used without large error, even when the indenter is not a true body of revolution; that is it can be considered as a general characteristic of elastic indentation mechanics.

The key to an accurate estimation of the elasto-plastic properties is an accurate identification of the true maximum contact area $A_{\max}$ at maximum indentation load $P_{\max}$ (see Fig. 2-2). For a flat indenter, A coincides with the circular cylinder cross-section. Historically, A represents the projected contact area. The determination of the true contact area requires consideration of pile-up or sink-in phenomena that occur during loading as a consequence of plastic deformation. These phenomena have received some attention in recent years [80], [79], [29], and led to the development of unique correlations between penetration depth h and true contact area A for commercially available sharp indenters [31], [19]. This method circumvents the need for contact

area measurement through visual observations while, at the same time, taking into account material pile-up and sink-in at the indentation perimeter. These developments provide a means of determining the indentation modulus directly from the $P-h$ response obtained during the complete loading/unloading cycle:

$$E^* = d^* \frac{H}{1 - W_p/W_t} \tag{2.3}$$

where $d^* = 5$ for the Vickers pyramid indenter and $d^* = 4.678$ for the Berkovich indenter; $H = P/A\,(h)$ is the average pressure under the indenter; $W_t = \int_0^h P(s)ds$ is the total work done by the indenter in deforming the material; and W_p is the plastic work. These quantities are extracted from the $P-h$ curve, as sketched in Figure 2-2.

In practical applications, E^* is determined with the help of (2.1) or (2.3) for the maximum load $P_{\max}$ and penetration depth $h_{\max}$, that are associated with a specific material scale under consideration. As a rough estimate, the effective material length scale of the bulk material under investigation in an indentation test operated to penetration depth $h_{\max}$ is $L \simeq 4 \times h_{\max}$ (see Fig. 2-2 (b)). The stiffness is computed by fitting the unloading curve to a power law as suggested by Oliver and Pharr [69] (see also [68] for a more recent review of unloading curves):

$$P = a(h - h_f)^m \tag{2.4}$$

where h_f is the residual depth, and a and m are fitted parameters. For a conical indenter, h' (i.e. the true penetration depth or "contact height", see Fig. 2-2) can be determined by the following formula [69]:

$$h' = h_{\max} - \varepsilon \frac{P_{\max}}{S} \tag{2.5}$$

where ε is a geometric parameter (0.72 for a conical indenter) and $S = \frac{dP}{dh}$ is the unloading slope[1]. This formula implies that $h' < h$, meaning that the material sinks-in under the indenter. However, for workhardening metals, pile-up may occur, implying $h' > h$. For such materials, E^* is overestimated. Loubet et al. [55] and Hochstetter et al. [37] have proposed a different method

[1]The accuracy of the determination of the slope S remains a question of debate.

to estimate the contact height, which takes into account pile-up or sink-in of the material:

$$h' = \alpha(h_{\max} - \frac{P_{\max}}{S}) \tag{2.6}$$

with $\alpha = 1.2$ for a Berkovich indenter.

More recently (2003), dual indentation reverse analysis algorithms have been proposed [16] [12], which improve the accuracy of the property estimation. The methods are based on incorporating a second result from an indenter with a different apex angle. A flow chart of the dual indentation reverse algorithm from [16] is presented in Figure 2-3. This algorithm resolves the uniqueness of the problem within the range of the study in the aforementioned paper; that is for a Von Mises type material.

In the case of thin films on substrate, the indentation is no longer geometrically self-similar (for deep indentation in the order of the film thickness), thus allowing for determination of mechanical properties other than hardness and stiffness. Huber et al. [41] developed a method to extract reduced modulus as well as nonlinear hardening behavior of both the film and the substrate. The approach is based on dimensionless quantities evaluated at different penetration depths and the use of artificial neural network for solving the (complicated) inverse problem.

Bucaille et al. [11] modeled the viscoplastic behavior of a thin coating of polymer and obtained the true strain-stress curve by fitting the experimental $P - h$ curve with numerical simulation. The results are in good agreement with previously known values.

2.4 Indentation Analysis of Hardness Measurements, Link With Strength Properties

Within the context of continuum analysis, sharp pyramidal or conical indenters lead to geometrically similar indentation states. That is, for a given indenter shape or included tip angle, the average pressure below the indenter, P/A, is independent of the indentation load P or the true contact area A, where $A \propto h^2$ (e.g. [31]). Indeed, the loading response is governed by Kick's Law:

$$P = Ch^2 \tag{2.7}$$

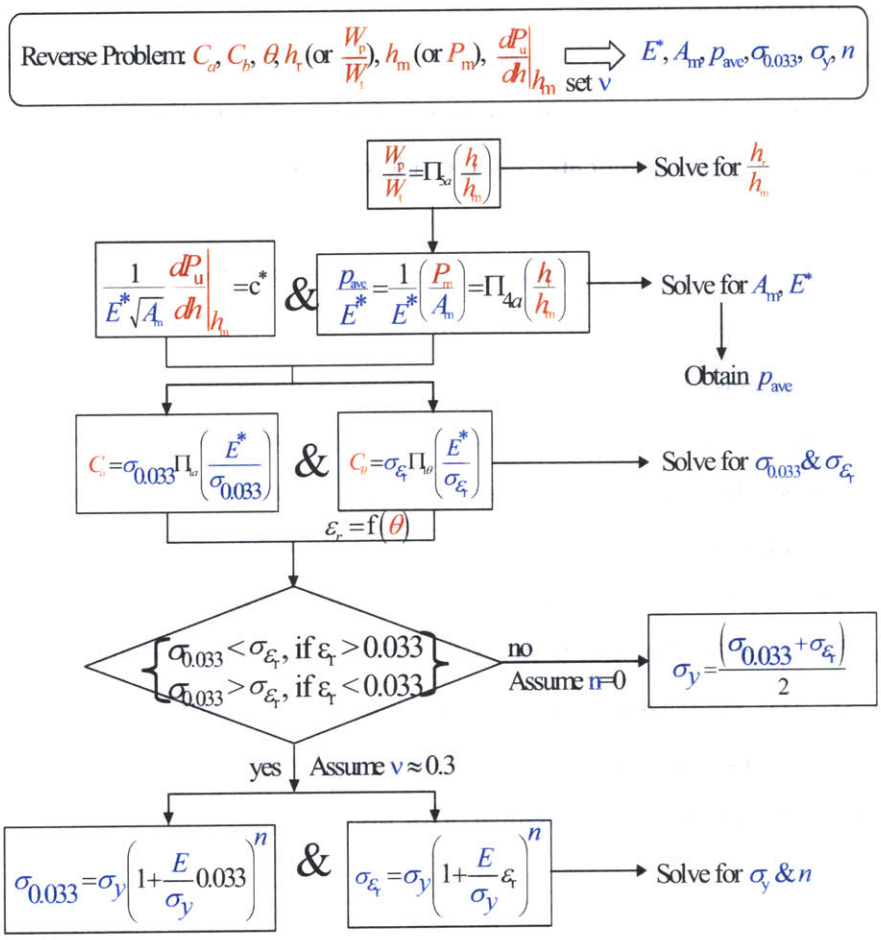

Figure 2-3: Flow chart of the dual indenter reverse algorithm (from [16]). C_a and C_b are the indentation stiffnesses, θ the indenter apex-angle, h_r the residual depth (cf. h_f in Eq. (2.4)), h_m the maximum penetration depth, $\frac{dP_u}{dh}\big|_{h_m}$ the initial unloading slope. E^* is the indentation modulus, A_m the true projected contact area (with pile-up or sink-in effect taken into account), p_{ave} the average contact pressure (hardness), $\sigma_{0.033}$ the "representative stress", σ_y the initial yield stress (at zero offset strain) and n the strain hardening exponent.

where C is the loading curvature. This loading curvature is proportional to the historic definition of hardness H. Theoretically, H can be determined at any point along the $P-h$ curve provided the true contact area (that is $A_{true} = A(h')$ in Fig. 2-2) is accounted for, i.e. $H = P/A_{true}$ for any h' (e.g. [31]) when pile-up and sink-in effects are properly dealt with. In the same way as for the elastic stiffness, the hardness $H = P_{\max}/A_{\max}$ is determined for the maximum load $P_{\max}$ and penetration depth $h_{\max}$ associated with a specific material scale under investigation. In conventional (sharp) micro-hardness tests, the area of contact $A_{\max}$ is determined by measuring the diagonal lengths of the indentation after load removal. This estimate of the contact area is based on the assumption that the elastic recovery during unloading is negligible, so that there is little change in geometry. This assumption is sound for certain very soft metals, but has not been verified for pressure sensitive-frictional materials.

The assumption of negligible elastic recovery during unloading is equivalent to the assumption that the elastic energy stored in the material system during loading to $P_{\max}$ is negligible compared to the plastic work; i.e. $1 - W_p/W_t \ll 1$; where $W_t = \int_0^h P(s)ds$ is the total work done by the indenter in deforming the material; and W_p is the plastic work (see Fig. 2-2). This may justify yield design approaches for the determination of the link between hardness (as previously defined, that is for the maximum load $P_{\max}$ and penetration depth $h_{\max}$) and strength properties of the material, as yield design assumes that the material system at plastic collapse has exhausted its capacity to store externally supplied work (here $dW_t = P(h)\,dh$) into recoverable (i.e. elastic) energy[2]. At plastic collapse, the externally supplied work rate is entirely dissipated into the form of heat (e.g. [87]). For non-frictional isotropic materials which do not exhibit any appreciable strain hardening, application of yield design delivers a ratio of hardness-to-uniaxial yield strength of roughly $H/\sigma_0 \simeq 2.7-3$, which holds for a wide range of metals [10] [82]. For polymers this ratio turns out to be on the order of 1.5, and 2 for glasses [70]. This unique relation between H and σ_0 does not hold for frictional materials, for which hardness H is a function of more than one material parameter, cohesion c and friction angle φ; $H = H(c, \varphi)$, so that the hardness-to-uniaxial strength ratio is a function of (at least) the

[2] We shall discuss in Chapter 7 the relation between hardness and plastic work when the elastic energy stored is not negligible compared to the plastic work.

friction angle:

$$\frac{H}{\sigma_0} = \mathcal{F}(\varphi) \tag{2.8}$$

The effect of the friction angle on the H/σ_0 ratio is well known for cementitious materials, for which reported values have been found to be on the order of $H/\sigma_0 = 30 - 60$ [45], that is one order of magnitude larger than typical values for metals.

Finally, it is useful to note that application of yield design theory implies under certain conditions a $P \propto h^2$ relation. Indeed, a straightforward dimensional analysis of the physical quantities of the indentation test yields[3]:

$$\frac{H}{c} = \frac{P}{cA(h')} = \mathcal{F}\left(\varphi, \frac{R}{h'}, i\right) \; ; \; A(h') = \pi \left[h' tan(i)\right]^2 \tag{2.10}$$

where R is the indenter tip radius (the indenter is usually not perfect and a has a rounded tip), i the indenter semi-apex angle and $A(h')$ the "true" projected contact area. It is important to point out that h' represents the real penetration depth, i.e. taking into account pile-up or sink-in effect. It has been shown by experiments [15] and computations [29] for some metals that the effects of the tip radius-to-penetration depth ratio R/h' is negligible so that the above relation reduces to:

$$\frac{P}{cA(h')} = \frac{H}{c} = \mathcal{F}(\varphi, i) \tag{2.11}$$

On the other hand, if fracture processes in the material affect the overall indentation response, the additional consideration of the fracture toughness K_{Ic} in the set of independent quantities (2.10) yields:

$$\frac{P}{K_{Ic}(h)^{1.5}} = \mathcal{G}\left(\varphi, \mathcal{I} = \frac{h}{(K_{Ic}/\sigma_0)^2}, \frac{R}{h}, i\right) \tag{2.12}$$

where $\mathcal{I}$ is Irwin's number which compares the structural dimension of the indentation test, i.e. here the penetration depth h, to the size of the fracture process zone $l_{ch} = (K_{Ic}/\sigma_0)^2$. For $\mathcal{I} \ll 1$, the penetration depth h is much smaller than the fracture process zone, so that

[3] For cohesive-frictional materials the cohesion c is linked to the uniaxial yield strength σ_0 by the following relation:

$$\sigma_0 = \frac{2c\cos(\varphi)}{1 - \sin(\varphi)} \tag{2.9}$$

the overall response is governed by a ductile yield process, for which a recombination of the invariants in relation (2.12) delivers the $P \propto h^2$ relation (2.7). On the contrary, if $\mathcal{I} \gg 1$ the overall indentation response is governed by a brittle fracture process, characterized by a $P \propto h^{1.5}$ response. Concerning nanoindentation tests on cementitious composites, Trtik et al. [83] found large cracks in cementitious composites below the indenter by focused ion beam investigation. In the nanoindentation tests on cementitious materials reported in [18], it was found that the power exponent varies between 1.5 and 2, indicating that some fracture processes (and related size effects) cannot be completely excluded in the analysis of hardness measurements by nanoindentation.

Recent experiments and theoretical developments have shown size effects at the sub-micron level for some materials (see below). More precisely, the micro and nanohardness have a $h^{-\frac{1}{2}}$ dependency (or $H^2 \propto 1/h$) suggesting the existence of a material length scale below which continuum plasticity theory is not valid anymore. Gao et al. [28] [44] explained these size effects by a mechanism-based strain gradient plasticity (MSG) theory that aims at bridging conventional mechanics theory and quantum-atomistic simulations. Gao et al. [40] argue that the classical continuum theory of plasticity cannot describe the collective behavior of dislocation and show very good agreement between the MSG theory and the experiments for polycrystal and single crystal Cu (linear dependency of the square of the hardness with respect to the inverse of the penetration depth).

2.5 Spherical Indentation

Spherical indentation has received much attention during the past two decades and is of particular interest compared to sharp indenters because of the non singular nature of the stress field generated at the indentation tip, and the attendant suppression of the damage and plasticity at the indented surface. The indenter surface being indeed much smoother, the beginning of the indentation curve is governed by Hertzian elastic response so that the spherical indentation technique is more suitable to extract the Young's modulus than the sharp indentation [2]. However, spherical indentation tests at the nanoscale are much more difficult to carry out since the bulk of the material activated is much larger than for sharp indentation, so that spherical

indentation appears to be rather more appropriate for microscale properties than for nanoscale properties. Alcala et al. [2] showed that the elastic modulus can be determined in a more reliable manner with spherical indentation for plasma sprayed coatings.

A great deal of research has been devoted to extract elastic properties of graded substrates[4]. Giannakopoulos et al. [81] [30] developed a general framework for the analysis and interpretation of spherical indentation on those materials. Comparing uniaxial tension and spherical indentation results, Herbert et al. [34] showed that Hertz's elastic model is suitable for spherical indentation in the limit of small displacements; allowing one to determine the elastic modulus accurately, as well as the yield strength. More recently, the extraction of yield strength and plastic hardening properties from spherical indentation has been investigated. As the penetration depth increases, a shift from a purely elastic response to an elasto-plastic response was found, that culminates in a fully plastic response. Spherical indentation allows one to follow this transition and thus enables plastic properties to be extracted. Very recently (April 2003) Ma et al. [59] developed a methodology for evaluating the yield strength and hardening behavior of metallic materials. The approach is based on the idea that spherical indentation is not self similar with depth, thus providing much more information than a conical test. Ma et al. derived dimensionless functions relating spherical indentation response to plastic flow properties.

Concerning our problem, the pure yield (i.e. in the fully plastic domain) of a cohesive-frictional material, the appropriate dimensionless relation reads:

$$\frac{H}{c} = \frac{P}{cA(h')} = \mathcal{F}\left(\varphi, \frac{R}{h'}\right) \tag{2.13}$$

where R is the spherical indenter radius.

In summary, it is readily understood from the different dimensionless relations (2.11) and (2.13) that the hardness is not a material property, in contrast to cohesion c and friction angle φ. This motivates to seek for relations that link the hardness to meaningful strength properties.

[4] A graded substrate is a layered solid, thus having elastic properties varying with depth.

2.6 Stability Problems in Geomechanics

At a completely different scale, the indentation problem is very similar to the circular foundation problem, and more particularly to the problem of driving a pile (or any body of revolution) into a cohesive-frictional soil. These problems received much attention during the past 20-30 years. Houslby [38], and Houlsby and Wroth [39], investigated strength measurements by a cone penetration test, and derived lower bounds for the hardness of a cohesive-frictional material [39] (however, the stress field solution lack the "extension elements"[5]), leading to a relationship between cone resistance and undrained strength. Cassidy and Houlsby [14] obtained lower bounds for the bearing capacity factor of cones on sand (but the proposed solution also lacks the "extension elements"). Cox et al. [1] derived a benchmark solution for smooth flat punch problem; and Salençon and Matar [60] derived heuristic solutions for the bearing capacity of a circular shallow foundation on a cohesive-frictional soil (with a vertical cohesion gradient), making it easier to design such foundations. These solutions are respectively based on the slip-line theory and the method of characteristics and will be considered in Chapter 6 for verification purposes.

Quite recently, a great amount of research was devoted to correlate hardness to unconfined compressive strength for different type of rocks [93], [94], [48], [51]. The hardness is measured with a Schmidt hammer[6] or a Shore Scleroscope[7], and by means of empirical statistical relations, the compressive strength and Young's modulus are extracted.

2.7 Concluding Remarks

This Chapter presented a non-exhaustive review of the existing information in the open literature on both elastic and plastic properties assessed through state-of-the-art nanoindentation techniques. The extraction of elastic properties from indentation results has received a great

[5] The shortcoming of not having these extension elements is discussed in Section 3.2.3.

[6] The Schmidt hammer was originally developed for measuring the strength of hardened concrete (Schmidt, 1951), but it can also be correlated with rock compressive strength according to Miller (1965). The device consists of a spring-loaded steel mass that is automatically released against a plunger when the hammer is pressed against the rock surface [94].

[7] The Shore Scleroscope hardness was first designed for use on metals, but the ISRM (International Society for Rock Mechanics) details a method for Shore hardness testing of rocks. The device measures the relative rebound of a diamond-tipped hammer that drops freely from a fixed height onto the surface of a specimen [93].

	Metals	Ceramics	Cohesive-frictional materials
Elastic properties	[69] and [16]	[70]	[69]
Plastic properties	[16]	[70]	N/A

Table 2.1: Review of the current methodologies allowing extraction of material properties.

deal of attention, and can be achieved today with good accuracy. On the other hand determination of elasto-plastic properties has been restricted primarily to non-frictional materials of the Von Mises type. Table 2.1 summarizes the existing and missing methodologies about material property assessment from nanoindentation.

From the discussion of the existing knowledge it appears that the link between nanohardness and strength properties for cohesive-frictional materials has not been investigated to the same depth as for metals or ceramics. It will be the focus of this study to elaborate such a methodology for cohesive-frictional materials. In particular, we will address the question whether and how it is possible to extract the cohesion and the friction angle from nanohardness measurements.

Part II

Computational Limit Analysis of Indentation Tests

Chapter 3

Formulation of Lower Bound Limit Analysis Using Finite Elements and Linear Programming: Axisymmetric Case

The second part of this thesis deals with the computational mechanics formulation and implementation of the limit theorems of yield design applied to indentation tests on cohesive-frictional materials. This and the next Chapter are devoted to the lower bound. The numerical approach developed is based on the formulation of Sloan [75] ,[76] and Assadi and Sloan [4], which is adapted in this Chapter for axisymmetric problems suitable to treat the indentation test. The method relies on the use of finite elements to discretize the continuum, the linearization of the Mohr-Coulomb yield criterion, and an optimization algorithm for solving linear programming problems. The lower bound analysis is indeed formulated as a linear programming problem whose objective function is the external load (to be maximized) subjected to the constraints of a statically admissible stress field. The constraints include equilibrium equations, linearized yield criterion, and stress boundary conditions. The optimal stress field is obtained by means of the optimization algorithm, and since the solution stress field satisfies all of the requirements of the lower bound theorem, the associated external load provides a strict lower bound solution.

3.1 Theoretical Background

3.1.1 Lower Bound Limit Theorem

The underlying idea of yield design is that the plastic collapse load is entirely dissipated into heat form through plastic sliding in the material bulk and along surfaces of discontinuity.

Mathematically, this is expressed by

$$\mathbf{Q}^{\lim} \cdot \mathbf{q} = \int_{\Omega} \boldsymbol{\sigma} : \mathbf{d} \; d\Omega \; + \; \int_{\Gamma} \mathbf{T}. \; [[\mathbf{V}]] \; d\Gamma \tag{3.1}$$

where $\mathbf{Q}^{\lim}$ is the collapse load vector, $\mathbf{q}$ the associated velocity vector, $\boldsymbol{\sigma}$ the statically admissible stress tensor, $\mathbf{d}$ the plastic strain rate tensor, $\mathbf{T} = \boldsymbol{\sigma} \, . \, \mathbf{n}$ the stress vector which is continuous over any surface of discontinuity Γ oriented by the unit normal $\mathbf{n}$, and $[[\mathbf{V}]]$ the velocity jump vector over the surfaces of discontinuity.

Limit theorems provide estimates of the actual dissipation capacity at plastic failure, as expressed by (3.1). More precisely, the lower bound theorem approaches the actual dissipation capacity through stress fields, which are:

- statically admissible, i.e. in equilibrium both internally and externally with the applied loads,
- plastically admissible, i.e. compatible with the strength domain of the material expressed by the yield criterion.

Among all possible stress fields $\boldsymbol{\sigma}(\mathbf{x})$, the lower bound theorem explores the ones which are statically compatible with prescribed body forces $\rho\mathbf{f}$ and surface forces $\mathbf{T}^d$, and which, at the same time, are compatible with the strength domain $D_k(\mathbf{x})$ of the constitutive material at any point $\mathbf{x}$ of the structure Ω; that is:

$$\text{in } \Omega : \rho\mathbf{f} = \operatorname{div} \boldsymbol{\sigma}'(\mathbf{x}); \text{ on } \partial\Omega_{\mathbf{T}^d} : \mathbf{T}^d = \boldsymbol{\sigma}'(\mathbf{x}) \cdot \mathbf{n}(\mathbf{x}) \tag{3.2}$$

$$\text{along } \Gamma; \; [[\mathbf{T}']] = \mathbf{0} \tag{3.3}$$

$$\forall \mathbf{x}; \quad \boldsymbol{\sigma}'(\mathbf{x}) \in D_k(\mathbf{x}) \leftrightarrow f(\mathbf{x}; \boldsymbol{\sigma}'(\mathbf{x})) \leq 0 \tag{3.4}$$

where $\partial\Omega_{\mathbf{T}^d}$ is the boundary of Ω, where surface forces are prescribed. $f(\mathbf{x};\boldsymbol{\sigma}'(\mathbf{x}))$ denotes the scalar loading function that defines the local strength domain D_k of the material composing the structure.

Then it can be shown, through application of the principle of maximum plastic work (see [87] Chapter 9 for a more detailed presentation), that stress fields satisfying (3.2), (3.3) and (3.4) provide a lower bound to the dissipation capacity (3.1) of the material system:

$$\int_{\Omega} \boldsymbol{\sigma}' : \mathbf{d}\ d\Omega\ +\ \int_{\Gamma} \mathbf{T}'_{\bullet}\ [[\mathbf{V}]]\ d\Omega = \mathbf{Q}' \cdot \mathbf{q} \leq \mathbf{Q}^{\lim} \cdot \mathbf{q} \tag{3.5}$$

The results can be summarized in form of the Lower Limit Theorem:

Theorem 1 *Any stress field $\boldsymbol{\sigma}'(\mathbf{x})$ which is statically admissible with the loading $\mathbf{Q}'$ and which is everywhere below or at yield, $\boldsymbol{\sigma}'(\mathbf{x}) \in D_k(\mathbf{x})$, delivers a lower bound $\mathbf{Q}' \cdot \mathbf{q}$ to the actual dissipation rate $\mathbf{Q}^{\lim} \cdot \mathbf{q}$ of the ultimate limit load $\mathbf{Q}^{\lim}$ along the velocity field $\mathbf{q}$:*

$$\mathbf{Q}' \cdot \mathbf{q} \leq \mathbf{Q}^{\lim} \cdot \mathbf{q} = \int_{\Omega} \max_{\substack{\boldsymbol{\sigma}'(\mathbf{x})\ SA \\ \boldsymbol{\sigma}'(\mathbf{x}) \in D_k(\mathbf{x})}} \left[\boldsymbol{\sigma}'(\mathbf{x}) : \mathbf{d}(\mathbf{x})\right] d\Omega + \int_{\Gamma} \max_{\substack{\mathbf{T}'(\mathbf{x})\ SA \\ \boldsymbol{\sigma}'(\mathbf{x}) \in D_k(\mathbf{x})}} \left[\mathbf{T}'_{\bullet}\ [[\mathbf{V}]]\right] d\Gamma \tag{3.6}$$

The lower bound theorem defines a formidable optimization problem: to maximize $\mathbf{Q}'$ through the choice of appropriate stress fields so to approximate the actual limit load $\mathbf{Q}^{\lim}$. This theorem forms the background of the linear programming problem developed below.

3.1.2 A "Rough" Lower Bound Estimate of Hardness

To motivate the forthcoming developments, consider the indenter as a rigid cylinder of radius r_0, situated on the surface of a horizontal half-space composed of a homogeneous material following the Mohr-Coulomb criterion, as sketched in Figure 3-1. A vertical force P is exerted on the cylinder in the direction of the cylinder axis (Oz), until it penetrates into the half-space. The stress field is assumed to be of the form:

$$\text{in } \Omega_1\ (z\ >\ 0\ ,\ r \leq r_0) : \boldsymbol{\sigma}'^{(1)} = q\left[\mathbf{e}_r \otimes \mathbf{e}_r + \mathbf{e}_\theta \otimes \mathbf{e}_\theta\right] - H\mathbf{e}_z \otimes \mathbf{e}_z \tag{3.7}$$

$$\text{in } \Omega_2\ (z\ >\ 0\ ,\ r > r_0) : \boldsymbol{\sigma}'^{(2)} = q'\left[\mathbf{e}_r \otimes \mathbf{e}_r + \mathbf{e}_\theta \otimes \mathbf{e}_\theta\right] \tag{3.8}$$

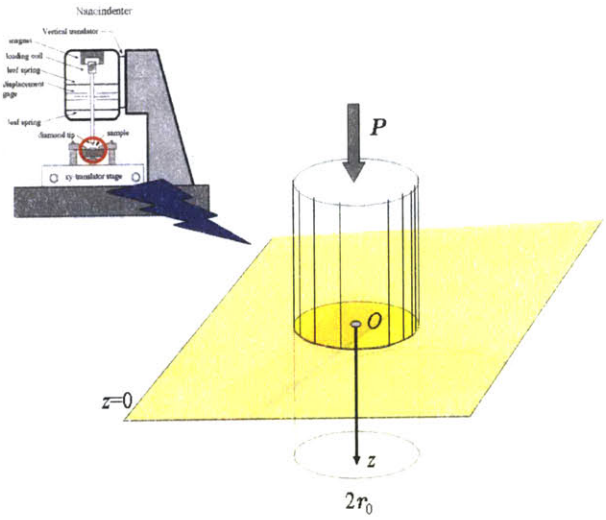

Figure 3-1: Flat punch nanoindenatation setup.

This stress field is statically admissible ($\operatorname{div} \boldsymbol{\sigma}' = 0$ is satisfied) provided that the stress continuity between Ω_1 and Ω_2 (i.e. at $r = r_0$) is ensured:

$$[[\mathbf{T}']] = \mathbf{0} \Leftrightarrow \sigma_{rr}^{(1)} = \sigma_{rr}^{(2)} = q' \tag{3.9}$$

The Mohr-Coulomb yield criterion reads:

$$F = \sigma_I(1 + \sin(\varphi)) - \sigma_{III}(1 - \sin(\varphi)) - 2c\cos(\varphi) \leqslant 0 \tag{3.10}$$

where $\sigma_I \geq \sigma_{II} \geq \sigma_{III}$ are the principal stresses, c is the cohesion and φ the friction angle. Using (3.7) to (3.9) in the Mohr-Coulomb criterion (3.10) delivers:

- In Ω_1:

$$q'(1 + \sin\varphi) + H(1 - \sin\varphi) - 2c\cos\varphi \leq 0 \tag{3.11}$$

- In Ω_2:

$$-q'(1 - \sin\varphi) - 2c\cos\varphi \leq 0 \tag{3.12}$$

Finally use of (3.12) in (3.11) yields a lower bound H' of the real hardness $H^{\lim}$ of the material:

$$H^{\lim} \geqslant H' = \max H = \frac{4c\cos\varphi}{(1-\sin\varphi)^2} \tag{3.13}$$

Figure 3-2 displays the optimized stress field in the Mohr stress plane. It can be seen that σ_{zz} is a minimum, that is H' is a maximum for this chosen stress field (3.7) (3.8).

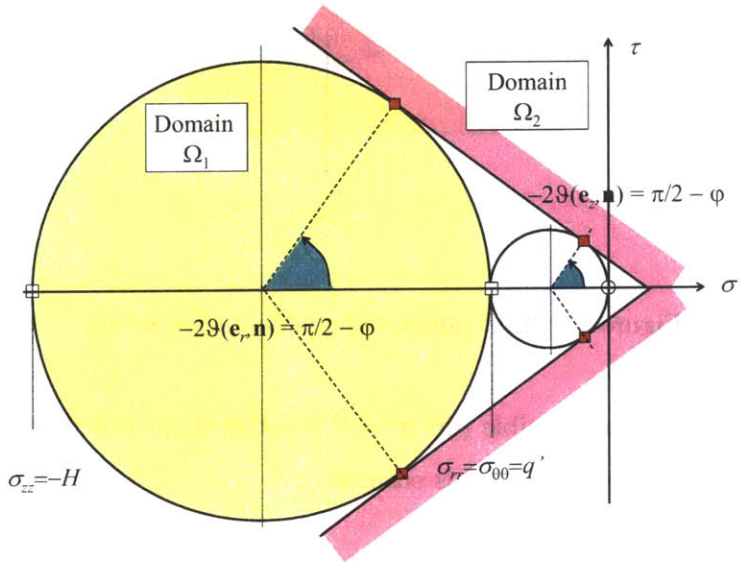

Figure 3-2: Optimized stress field in the Mohr-stress plane.

3.1.3 Limits and Shortcomings

The lower bound solution (3.13) is of the form (2.11), for which:

$$\frac{H^{\lim}}{c} \geqslant \frac{H'}{c} \geqslant \mathcal{F}'(\varphi)\ ;\ \mathcal{F}'(\varphi) = \frac{4\cos\varphi}{(1-\sin\varphi)^2} \tag{3.14}$$

But it is a lower bound which as we shall see is far from the reality. This can readily be grasped from a comparison of the derived stress field with a more realistic stress field below an indenter as showed in Figure 2-1. This highlights that it is often difficult to construct statically admissible stress fields which give a lower bound close to the true collapse load. Moreover, there is no rational method for refining statically admissible stress fields in order to improve

the accuracy of the lower bound calculation. Finally, many published solutions that are referred to as "lower bounds" do not satisfy the complete requirements (3.2) to (3.4) of the lower bound theorem (in fact the proposed solutions are often only valid in a certain domain and not in the entire domain Ω). This motivates the forthcoming developments of a robust numerical approach for computing the lower bound.

3.2 Lower Bound Theorem Discretization

3.2.1 Historical Background

The numerical lower bound formulation was first proposed in 1970 by Lysmer [58] for plane strain problems. The approach uses the concept of finite element discretization and linear programming; the material is discretized into 3-noded triangular elements with stresses as nodal variables. The stresses are assumed to vary linearly within the elements, while stress discontinuities are permitted to occur at the interface between adjacent triangles. The statically admissible stress field is defined by the constraints of equilibrium equations, stress boundary conditions, and the yield criterion. Each non-linear yield criterion is approximated by a set of linear constraints on the stresses, which lie inside the original yield surface, thus ensuring that the solutions are strict lower bounds. This leads to an expression of the collapse load subjected to a set of linear constraints on the nodals stresses. The lower bound is then obtained by maximizing the collapse load.

Since 1970 the method has been improved by Pastor [66], Pastor and Turgeman [67] and Sloan and Kleeman [77] for plane stress and plane strain problems. More recently efficient optimizing algorithms have been developed ([62] and [61]), that greatly reduce the computation time. We will adopt this strategy in what follows, and will adapt it for the axisymmetric case.

We should also mention that Sloan and Abbo are currently (November 2003) developing a 3-D software for the lower and upper bound based on non-linear programming and a smooth hyperbolic approximation of the Mohr-Coulomb yield criterion, originally formulated by Sloan and Lyamin [56] [57].

3.2.2 Finite Elements Discretization

In the (r, z) plane the material is discretized in 3-noded triangular elements; these elements are rotated around the z axis to discretize the entire material space (Fig. 3-3). Given this axisymmetric configuration, the problem (loading and geometry) is θ-invariant. Each node of these elements is associated with four unknown stresses: $\{\sigma_{rr}, \sigma_{zz}, \sigma_{rz}, \sigma_{\theta\theta}\}$ in the cylindrical coordinate system. The stress components are assumed to vary linearly within each element according to[1]:

$$\sigma_{ij}(r, z) = \sum_{k=1}^{3} N_k(r, z)\sigma_{ij}^k \tag{3.15}$$

where σ_{ij}^k $(k = 1, 2, 3)$ are the nodal stresses and N_k are linear shape functions given by

$$N_1(r, z) = [(r_2 z_3 - r_3 z_2) + z_{23} r + r_{32} z] / 2A \tag{3.16}$$

$$N_2(r, z) = [(r_3 z_1 - r_1 z_3) + z_{31} r + r_{13} z] / 2A \tag{3.17}$$

$$N_3(r, z) = [(r_1 z_2 - r_2 z_1) + z_{12} r + r_{21} z] / 2A \tag{3.18}$$

where

$$e_{kl} = e_k - e_l \ ; \ e = (r, z) \tag{3.19}$$

and

$$2A = |r_{13} z_{23} - r_{32} z_{31}| \text{ is twice the triangle area} \tag{3.20}$$

Since the problem is θ-invariant, the stress field only depends on r and z.

Statically admissible stress discontinuities are a priori permitted along shared edges between adjacent elements; that is the stress vector continuity (relation (3.3)) is enforced as a constraint condition, while out of plane stress quantities, e.g. $\sigma_{\theta\theta}$, may exhibit a jump over such interfaces. These stress discontinuities are modeled as each node is unique to a particular element. Therefore, it is possible that multiple nodes share the same set of coordinates. Figure 3-4 illustrates a finite element mesh configuration for these conditions.

[1] For purpose of clarity in the implementation presentation, the prime will be omitted on the stresses, but keep in mind that the stresses are associated with the lower bound theorem (3.6).

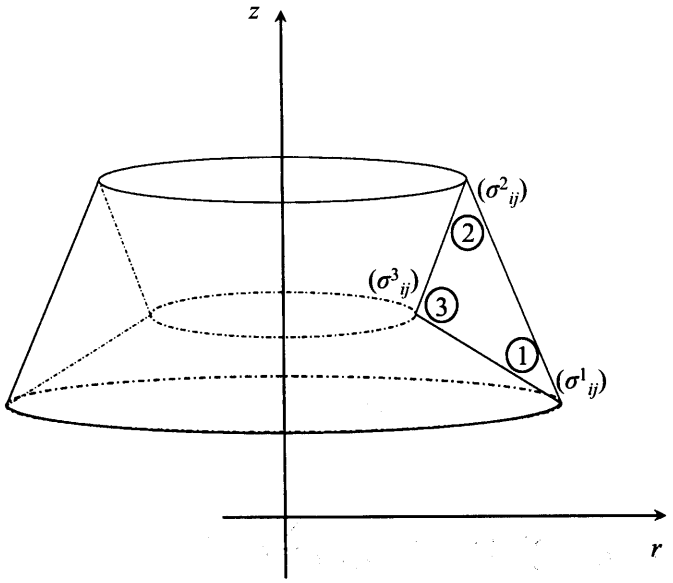

Figure 3-3: 3-noded triangular element.

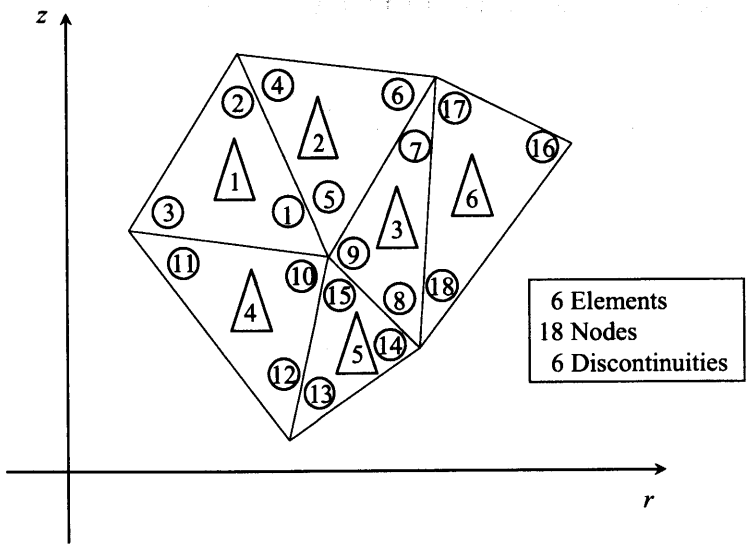

Figure 3-4: Typical mesh configuration for the lower bound.

3.2.3 Element Equilibrium

The lower bound theorem states that stresses within the element must satisfy the static equilibrium equations (3.2). In the absence of body forces[2], the momentum balance equations for the θ-invariant problem read in cylindrical coordinates:

$$\frac{\partial \sigma_{rr}}{\partial r} + \frac{\partial \sigma_{rz}}{\partial z} + \frac{\sigma_{rr} - \sigma_{\theta\theta}}{r} = 0 \tag{3.21}$$

$$\frac{\partial \sigma_{zr}}{\partial r} + \frac{\partial \sigma_{zz}}{\partial z} + \frac{\sigma_{zr}}{r} = 0 \tag{3.22}$$

Differentiating (3.15) and substituting the result into (3.21) and (3.22) yields the equilibrium constraints on the nodal stresses:

$$\sum_{k=1}^{3} \frac{\partial N_k(r,z)}{\partial r}\sigma_{rr}^k + \sum_{k=1}^{3} \frac{\partial N_k(r,z)}{\partial z}\sigma_{rz}^k + \frac{\sum_{k=1}^{3} N_k(r,z)(\sigma_{rr}^k - \sigma_{\theta\theta}^k)}{r} = 0 \tag{3.23}$$

$$\sum_{k=1}^{3} \frac{\partial N_k(r,z)}{\partial r}\sigma_{zr}^k + \sum_{k=1}^{3} \frac{\partial N_k(r,z)}{\partial z}\sigma_{zz}^k + \frac{\sum_{k=1}^{3} N_k(r,z)(\sigma_{zr}^k)}{r} = 0 \tag{3.24}$$

Since $N_k(r,z)$ is a linear function of r and z, the two first terms in (3.23) and (3.24) only depend on the nodal stresses. Consequently, the last term must be independent of r and z. This last term can be rewritten as:

$$\frac{\sum_{k=1}^{3} N_k(r,z)(\alpha^k)}{r} \tag{3.25}$$

with

$$\alpha^k = \sigma_{rr}^k - \sigma_{\theta\theta}^k \text{ for (3.23)} \tag{3.26}$$

$$\alpha^k = \sigma_{zr}^k \text{ for (3.24)} \tag{3.27}$$

Expanding (3.25) yields:

$$\frac{\sum_{k=1}^{3} N_k(r,z)(\alpha^k)}{r} = \frac{ar + bz + c}{r} = a + b\frac{z}{r} + c\frac{1}{r} \tag{3.28}$$

[2]The focus of this study are nanoindentation tests for which it is reasonable to neglect body forces.

where a, b and c are functions of only the nodal coordinates. For this expression to be independent of r and z, it is readily seen from (3.28) that b and c need to be zero, that is:

$$b = \sum_{k=1}^{3} \frac{\partial N_k(r,z)}{\partial z} \alpha^k = 0 \text{ and } c = \sum_{k=1}^{3} N_k(0,0) \times \alpha^k = 0 \tag{3.29}$$

since b and c can be expressed as the partial derivative of α with respect to r and z respectively.

The equilibrium equations for the nodal stresses combined with the above constraint conditions therefore read:

$$2\sum_{k=1}^{3} \frac{\partial N_k(r,z)}{\partial r} \sigma_{rr}^k + \sum_{k=1}^{3} \frac{\partial N_k(r,z)}{\partial z} \sigma_{rz}^k - \sum_{k=1}^{3} \frac{\partial N_k(r,z)}{\partial r} \sigma_{\theta\theta}^k = 0 \tag{3.30}$$

$$\sum_{k=1}^{3} \frac{\partial N_k(r,z)}{\partial z} (\sigma_{rr}^k - \sigma_{\theta\theta}^k) = 0 \tag{3.31}$$

$$\sum_{k=1}^{3} N_k(0,0) \times (\sigma_{rr}^k - \sigma_{\theta\theta}^k) = 0 \tag{3.32}$$

$$2\sum_{k=1}^{3} \frac{\partial N_k(r,z)}{\partial r} \sigma_{zr}^k + \sum_{k=1}^{3} \frac{\partial N_k(r,z)}{\partial z} \sigma_{zz}^k = 0 \tag{3.33}$$

$$\sum_{k=1}^{3} \frac{\partial N_k(r,z)}{\partial z} \sigma_{zr}^k = 0 \tag{3.34}$$

$$\sum_{k=1}^{3} N_k(0,0) \times \sigma_{zr}^k = 0 \tag{3.35}$$

which may be simplified as:

$$\sum_{k=1}^{3} \frac{\partial N_k(r,z)}{\partial r}(2\sigma_{rr}^k - \sigma_{\theta\theta}^k) = 0 \tag{3.36}$$

$$\sum_{k=1}^{3} \frac{\partial N_k(r,z)}{\partial z}(\sigma_{rr}^k - \sigma_{\theta\theta}^k) = 0 \tag{3.37}$$

$$\sum_{k=1}^{3} N_k(0,0) \times (\sigma_{rr}^k - \sigma_{\theta\theta}^k) = 0 \tag{3.38}$$

$$2\sum_{k=1}^{3} \frac{\partial N_k(r,z)}{\partial r}\sigma_{zr}^k + \sum_{k=1}^{3} \frac{\partial N_k(r,z)}{\partial z}\sigma_{zz}^k = 0 \tag{3.39}$$

$$\sum_{k=1}^{3} \frac{\partial N_k(r,z)}{\partial z}\sigma_{zr}^k = 0 \tag{3.40}$$

$$\sum_{k=1}^{3} N_k(0,0) \times \sigma_{zr}^k = 0 \tag{3.41}$$

The previous equations can be recast in the compact matrix form:

$$[A_1]\,[X] = [B_1] \tag{3.42}$$

where:

$$[A_1] = \begin{bmatrix} 2z_{23}/2A & 0 & 0 & -z_{23}/2A & 2z_{31}/2A & 0 \\ r_{32}/2A & 0 & 0 & -r_{32}/2A & r_{13}/2A & 0 \\ r_2z_3 - r_3z_2 & 0 & 0 & -(r_2z_3 - r_3z_2) & r_3z_1 - r_1z_3 & 0 \\ 0 & r_{32}/2A & 2z_{23}/2A & 0 & 0 & r_{13}/2A \\ 0 & 0 & r_{32}/2A & 0 & 0 & 0 \\ 0 & 0 & r_2z_3 - r_3z_2 & 0 & 0 & 0 \end{bmatrix}$$

$$\begin{bmatrix} 0 & -z_{31}/2A & 2z_{12}/2A & 0 & 0 & -z_{12}/2A \\ 0 & -r_{13}/2A & r_{21}/2A & 0 & 0 & -r_{21}/2A \\ 0 & -(r_3z_1 - r_1z_3) & r_1z_2 - r_2z_1 & 0 & 0 & -(r_1z_2 - r_2z_1) \\ 2z_{31}/2A & 0 & 0 & r_{21}/2A & 2z_{12}/2A & 0 \\ r_{13}/2A & 0 & 0 & 0 & r_{21}/2A & 0 \\ r_3z_1 - r_1z_3 & 0 & 0 & 0 & r_1z_2 - r_2z_1 & 0 \end{bmatrix} \tag{3.43}$$

$$[X]^T = \begin{bmatrix} \sigma^1_{rr} & \sigma^1_{zz} & \sigma^1_{zr} & \sigma^1_{\theta\theta} & \sigma^2_{rr} & \sigma^2_{zz} & \sigma^2_{zr} & \sigma^2_{\theta\theta} & \sigma^3_{rr} & \sigma^3_{zz} & \sigma^3_{zr} & \sigma^3_{\theta\theta} \end{bmatrix} \tag{3.44}$$

$$[B_1]^T = \begin{bmatrix} 0 & 0 & 0 & 0 & 0 & 0 & 0 \end{bmatrix} \tag{3.45}$$

3.2.4 Equilibrium Along Stress Discontinuities

A stress discontinuity is statically admissible if the shear and normal stresses acting on the discontinuity plane are continuous, that is relation (3.3). The only stress components that may exhibit a jump are out of plane stresses. The normal and shear stresses acting on a plane inclined at an angle α to the r axis are given by:

$$\sigma_n = \sin^2(\alpha)\sigma_{rr} + \cos^2(\alpha)\sigma_{zz} - \sin(2\alpha)\sigma_{rz} \tag{3.46}$$

$$\tau = \frac{1}{2}\sin(2\alpha)(\sigma_{zz} - \sigma_{rr}) + \cos(2\alpha)\sigma_{rz} \tag{3.47}$$

A typical stress discontinuity between adjacent elements is shown in Figure 3-5. It is defined by the nodal pairs (1,2) and (3,4), where the nodes in each pair share the same coordinates. Since the stresses in our model are assumed to vary linearly, the equilibrium condition is met by enforcing all pairs of nodes on opposite sides of the discontinuity to have equal shear and normal stresses. The discontinuity constraints then read:

$$[A_2]\,[X] = 0 \tag{3.48}$$

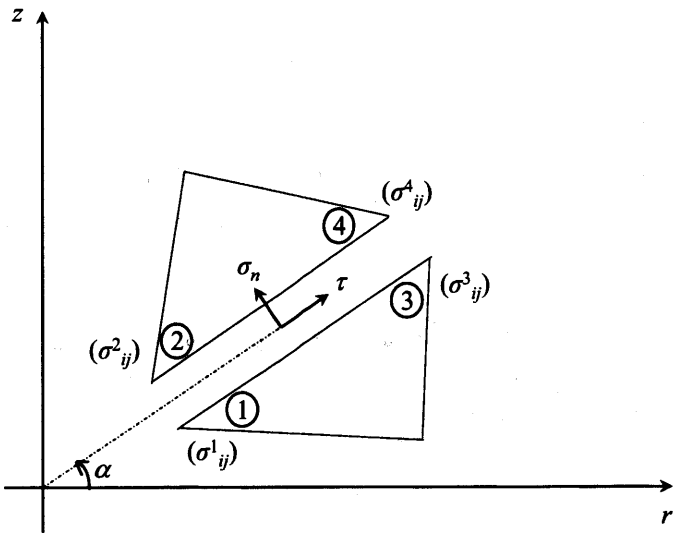

Figure 3-5: Stress discontinuity.

where

$$[A_2] = \begin{bmatrix} [T] & -[T] & 0 & 0 \\ 0 & 0 & [T] & -[T] \end{bmatrix} \tag{3.49}$$

$$[T] = \begin{bmatrix} \sin^2(\alpha) & \cos^2(\alpha) & -\sin(2\alpha) & 0 \\ -\frac{1}{2}\sin(2\alpha) & \frac{1}{2}\sin(2\alpha) & \cos(2\alpha) & 0 \end{bmatrix} \tag{3.50}$$

$$[X]^T = [\sigma^1_{rr}, \sigma^1_{zz}, \sigma^1_{zr}, \sigma^1_{\theta\theta}, ..., \sigma^4_{rr}, \sigma^4_{zz}, \sigma^4_{zr}, \sigma^4_{\theta\theta}] \tag{3.51}$$

3.2.5 Constraints From Stress Boundary Conditions

Enforcing prescribed boundary conditions, i.e. relation $(3.2)_2$, reduces to imposing additional equality constraints on the nodal stresses. If the normal and shear stresses at a boundary plane (i.e. a segment in the (r, z) frame rotated around the z axis since the problem is θ-invariant) are specified to be (q_1, t_1) and (q_2, t_2) as shown in Figure 3-6, then it is sufficient to impose the

following conditions:

$$\sigma_{n1} = q_1 \qquad \sigma_{n1} = q_1 \tag{3.52}$$

$$\tau_1 = t_1 \qquad \tau_2 = t_2 \tag{3.53}$$

since the stresses are only permitted to vary linearly along an element edge. Substituting the

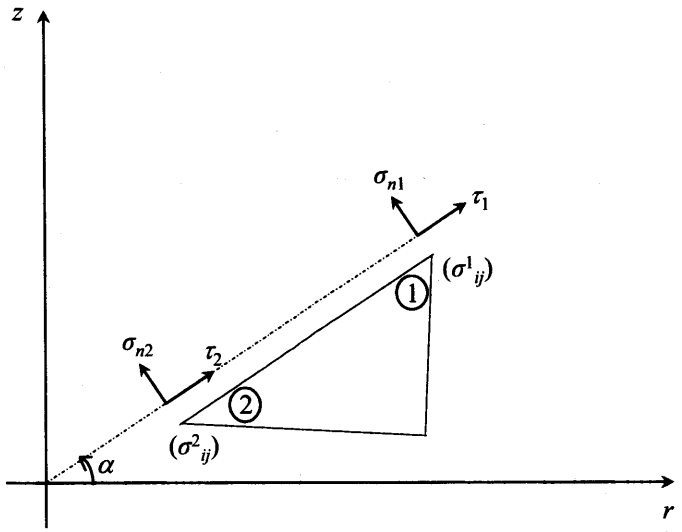

Figure 3-6: Stress boundary conditions.

stress transformation equations (3.46) and (3.47) into (3.52) and (3.53) leads to four equalities of the form:

$$[A_3][X] = [B_3] \tag{3.54}$$

where

$$[A_3] = \begin{bmatrix} [T] & 0 \\ 0 & [T] \end{bmatrix} \tag{3.55}$$

$$[B_3]^T = [q_1, t_1, q_2, t_2] \tag{3.56}$$

$$[X]^T = [\sigma^1_{rr}, \sigma^1_{zz}, \sigma^1_{zr}, \sigma^1_{\theta\theta}, \sigma^2_{rr}, \sigma^2_{zz}, \sigma^2_{zr}, \sigma^2_{\theta\theta}] \tag{3.57}$$

$[T]$ is given in (3.50).

3.2.6 Constraints From Yield Criterion

The second pillar of the lower bound theorem is the compatibility of the stress field with the strength domain of the material expressed by a yield function, i.e. relation (3.4). A key feature of the computational implementation of the lower bound theorem is the linearization of the yield criterion. This is necessary to avoid nonlinear constraints on the unknown nodal stresses. The Mohr-Coulomb criterion (3.10) can be rewritten in the form (e.g. [72]):

$$F = Sup_{(i,j\in\{1,2,3\})}(\sigma_i(1+\sin(\varphi)) - \sigma_j(1-\sin(\varphi)) - 2c\cos(\varphi)) \leqslant 0 \tag{3.58}$$

where σ_i and σ_j are principal stresses. While the three principal stresses can be determined from the four nodal stresses, the order is not known. The principal stresses are indeed:

$$\sigma_{\theta\theta}\ ;\ \sigma_+ = \frac{\sigma_{rr}+\sigma_{zz}}{2} + \frac{1}{2}Rad\ ;\ \sigma_- = \frac{\sigma_{rr}+\sigma_{zz}}{2} - \frac{1}{2}Rad \tag{3.59}$$

where

$$Rad = \sqrt{(\sigma_{rr}-\sigma_{zz})^2 + 4(\sigma_{rz})^2} \tag{3.60}$$

Given that $\sigma_+ \geqslant \sigma_-$, (3.58) can be expanded in the form:

$$(3.58) \Leftrightarrow \left\{ \begin{array}{l} \sigma_+(1+\sin(\varphi)) - \sigma_-(1-\sin(\varphi)) - 2c\cos(\varphi) \leqslant 0 \\ \sigma_+(1+\sin(\varphi)) - \sigma_{\theta\theta}(1-\sin(\varphi)) - 2c\cos(\varphi) \leqslant 0 \\ \sigma_{\theta\theta}(1+\sin(\varphi)) - \sigma_-(1-\sin(\varphi)) - 2c\cos(\varphi) \leqslant 0 \end{array} \right\} \tag{3.61}$$

for which:

$$Rad \leqslant R_i \quad (i = 1,2,3) \tag{3.62}$$

where

$$R_1 = 2c\cos(\varphi) - (\sigma_{rr} + \sigma_{zz})\sin(\varphi) \tag{3.63}$$

$$R_2 = \frac{2}{1+\sin(\varphi)}(2c\cos(\varphi) + \sigma_{\theta\theta}(1-\sin(\varphi)) - (\sigma_{rr} + \sigma_{zz}) \tag{3.64}$$

$$R_3 = \frac{2}{1-\sin(\varphi)}(2c\cos(\varphi) - \sigma_{\theta\theta}(1+\sin(\varphi)) + (\sigma_{rr} + \sigma_{zz}) \tag{3.65}$$

Relations (3.61) and (3.62) allow us to recast the Mohr-Coulomb yield criterion in the compact form:

$$\left\{ \begin{array}{c} X^2 + Y^2 \leqslant R_i^2 \\ R_i \geqslant 0 \end{array} \right\} \tag{3.66}$$

where

$$X = \sigma_{rr} - \sigma_{zz} \text{ and } Y = 2\sigma_{rz} \tag{3.67}$$

In the (X, Y) plane, the inequalities (3.66) represent three circles of radius R_i.

To define a rigorous lower bound, the stresses at each point in the studied domain must lie inside the Mohr-Coulomb circles, so that $F \leqslant 0$. Since this type of constraint is quadratic in the stresses, it is convenient to replace the Mohr-Coulomb circle by an inscribed polygon with p sides of equal length. In this way, the yield criterion is expressed as a series of linear inequalities. The coordinates for the k^{th} and $k^{th}+1$ points (see Fig. 3-7 which shows a six-sided approximation) are given by:

$$X_k = R\cos(\pi(2k-1)/p) \; ; \; Y_k = R\sin(\pi(2k-1)/p) \tag{3.68}$$

$$X_{k+1} = R\cos(\pi(2k+1)/p) \; ; \; Y_{k+1} = R\sin(\pi(2k+1)/p) \tag{3.69}$$

A stress state with coordinates X and Y must lie inside or on the yield surface. Given the convexity of the linearized yield criterion, this is satisfied if:

$$(X_{k+1} - X)(Y_k - Y) - (X_k - X)(Y_{k+1} - Y) \leqslant 0 \; ; \; k = 1, 2..., p \tag{3.70}$$

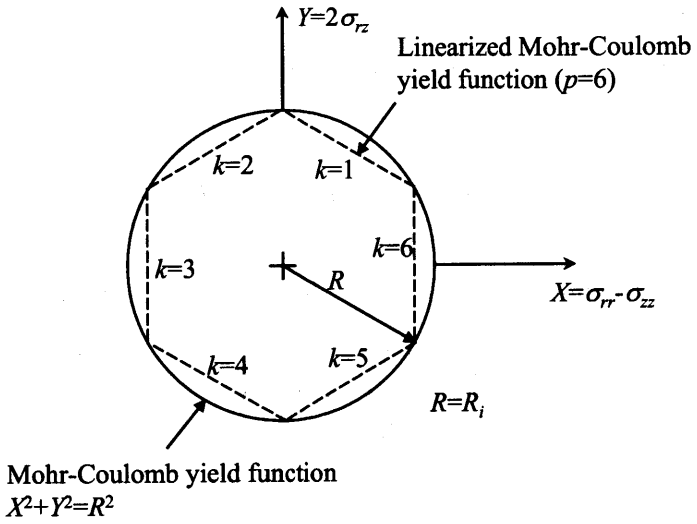

Figure 3-7: Internal linearisation of the Mohr-Coulomb yield criterion.

Substituting (3.68) and (3.69) into (3.70) generates a set of inequality constraints:

$$F_k = A_k\sigma_{rr} + B_k\sigma_{zz} + C_k\sigma_{rz} + D_k\sigma_{\theta\theta} - E \leqslant 0 \ ; \ k = 1, 2..., p \tag{3.71}$$

where F_k denotes the k^{th} side of the linearized Mohr-Coulomb yield criterion:

for $i = 1$

$$A_k = \cos(2\pi k/p) + \sin(\varphi)\cos(\pi/p) \tag{3.72}$$

$$B_k = \sin(\varphi)\cos(\pi/p) - \cos(2\pi k/p) \tag{3.73}$$

$$C_k = 2\sin(k\pi/p) \tag{3.74}$$

$$D_k = 0 \tag{3.75}$$

$$E = 2c\cos(\varphi)\cos(\pi/p) \tag{3.76}$$

for $i = 2$

$$A_k = (1+\sin(\varphi))(\sin(2\pi/p)+\sin((2k+1)\pi/p)-\sin((2k-1)\pi/p)) \quad (3.77)$$

$$B_k = (1+\sin(\varphi))(\sin(2\pi/p)+\sin((2k-1)\pi/p)-\sin((2k+1)\pi/p)) \quad (3.78)$$

$$C_k = (1+\sin(\varphi))(2\cos((2k-1)\pi/p)-2\cos((2k+1)\pi/p)) \quad (3.79)$$

$$D_k = (-1+\sin(\varphi))(2\sin(2\pi/p)) \quad (3.80)$$

$$E = 4c\cos(\varphi)\sin(2\pi/p) \quad (3.81)$$

and for $i = 3$

$$A_k = (-1+\sin(\varphi))(\sin(2\pi/p)+\sin((2k-1)\pi/p)-\sin((2k+1)\pi/p)) \quad (3.82)$$

$$B_k = (-1+\sin(\varphi))(\sin(2\pi/p)+\sin((2k+1)\pi/p)-\sin((2k-1)\pi/p)) \quad (3.83)$$

$$C_k = (-1+\sin(\varphi))(2\cos((2k+1)\pi/p)-2\cos((2k-1)\pi/p)) \quad (3.84)$$

$$D_k = (1+\sin(\varphi))(2\sin(2\pi/p)) \quad (3.85)$$

$$E = 4c\cos(\varphi)\sin(2\pi/p) \quad (3.86)$$

To completely factor F_k we note that $\sum_{n=1}^{3} N_n(r,z) = 1$ so that we can write E as:

$$\sum_{n=1}^{3} N_n(r,z)E_n \quad (3.87)$$

with $E_n = E$. Finally substituting (3.15) and (3.87) in (3.71) yields:

$$F_k = \sum_{n=1}^{3} N_n(r,z)(A_k\sigma_{rr}^n + B_k\sigma_{zz}^n + C_k\sigma_{rz}^n + D_k\sigma_{\theta\theta}^n - E_n) \leqslant 0 \ ; \ k = 1,2...,p \quad (3.88)$$

and thus:

$$F_k = \sum_{n=1}^{3} N_n(r,z)F_{kn} \leqslant 0 \ ; \ k = 1,2...,p \quad (3.89)$$

where

$$F_{kn} = A_k\sigma_{rr}^n + B_k\sigma_{zz}^n + C_k\sigma_{rz}^n + D_k\sigma_{\theta\theta}^n - E_n \ ; \ k = 1,2...,p \ ; \ n = 1,2,3 \quad (3.90)$$

3.2.7 Required Yield Constraints for the 3-Noded Triangular Element

We have the shape functions $N_n \in [0;1]$ inside the element. Hence, in order to satisfy (3.89) throughout the element, it suffices to enforce the following constraint at each node n (and for $i = 1, 2, 3$):

$$F_{kn} \leqslant 0 \; ; \; k = 1, 2..., p \tag{3.91}$$

Thus at each node n, the linearized yield criterion gives rise to $3p + 3$ inequality constraints of the form:

$$[A_{yield}]\,[X] \;\leqslant\; [B_{yield}] \tag{3.92}$$

$$[R_{yield}]\,[X] \;\leqslant\; [\bar{R}_{yield}] \tag{3.93}$$

where

$$[A_{yield}] = \begin{bmatrix} A_1^i & B_1^i & C_1^i & D_1^i \\ .. & .. & .. & .. \\ A_p^i & B_p^i & C_p^i & D_p^i \end{bmatrix} \quad i = 1, 2, 3 \tag{3.94}$$

$$[R_{yield}] = \begin{bmatrix} \sin(\varphi) & \sin(\varphi) & 0 & 0 \\ 1 & 1 & 0 & -\frac{2(1-\sin(\varphi))}{1+\sin(\varphi)} \\ -1 & -1 & 0 & \frac{2(1+\sin(\varphi))}{1-\sin(\varphi)} \end{bmatrix} \tag{3.95}$$

$$[B_{yield}]^T = [E_1^i, .., E_p^i] \quad i = 1, 2, 3 \tag{3.96}$$

$$[\bar{R}_{yield}]^T = [2c\cos(\varphi), \frac{4c\cos(\varphi)}{1+\sin(\varphi)}, \frac{4c\cos(\varphi)}{1-\sin(\varphi)}] \tag{3.97}$$

$$[X]^T = [\sigma_{rr}^n, \sigma_{zz}^n, \sigma_{zr}^n, \sigma_{\theta\theta}^n] \tag{3.98}$$

3.2.8 Constraints From a Frictional Interface

Since the lower bound method considers only the stress field, one additional constraint is required to enforce the yield criterion at the cone-material interface. Considering the Mohr-Coulomb yield criterion, with the parameters c_i for the cohesion and φ_i for the friction angle

at the interface, the additional constraint reads:

$$|\tau| \leqslant c_i + \sigma_n \tan(\varphi_i) \tag{3.99}$$

where τ and σ_n are the shear stress and normal stress along the interface. This constraint is required to guarantee that the shear stress does not exceed the mobilized shear resistance at the interface. For a perfectly rough cone, it is reasonable to assume that

$$c_i = c_{material} \text{ and } \varphi_i = \varphi_{material} \tag{3.100}$$

where $c_{material}$ and $\varphi_{material}$ are the cohesion and friction angle of the material beneath the cone.

3.3 Extension Elements

The focus of the extension elements is to ensure that the stress field remains statically and plastically admissible in the whole domain and not only in the discretized domain.

The constraint conditions are derived for two types of extension elements:

- a triangular extension element, as shown in Figure 3-8 (a),
- a rectangular extension element, as shown in Figure 3-8 (b), which is a triangular extension element with an additional fourth dummy node. This dummy node is necessary to permit semi infinite stress discontinuities between adjacent extension elements.

3.3.1 Equilibrium

There is no additional constraint to enforce for the equilibrium of the 3-noded triangular extension element.

For each rectangular extension element on the contrary, four additional equalities are necessary to extend the linear stress distribution to the fourth node (result proven in Appendix

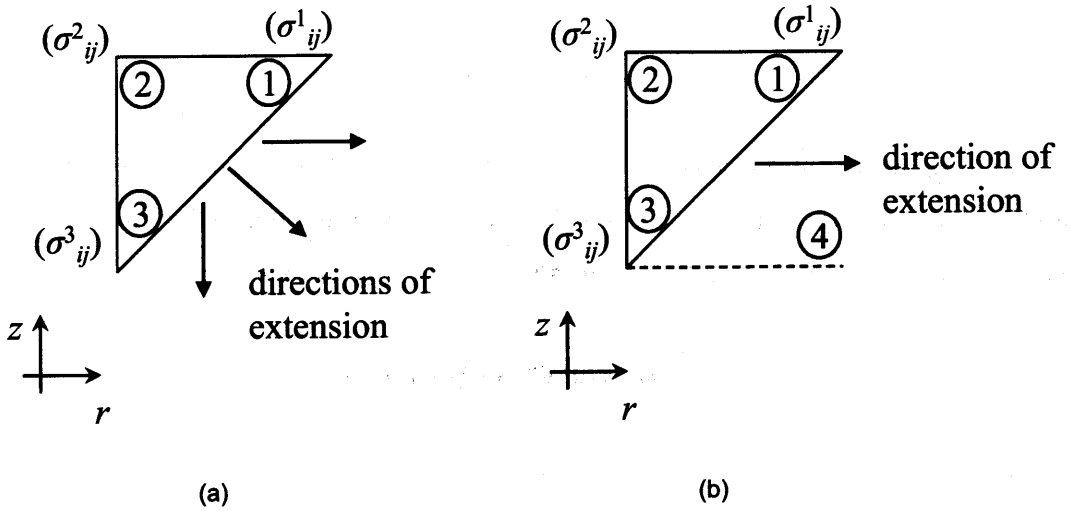

Figure 3-8: (a) 3-noded triangular extension element.(b) 4-noded rectangular extension element.

B). These equalities are:

$$\sigma^4_{rr} = \sigma^1_{rr} + \sigma^3_{rr} - \sigma^2_{rr} \tag{3.101}$$

$$\sigma^4_{zz} = \sigma^1_{zz} + \sigma^3_{zz} - \sigma^2_{zz} \tag{3.102}$$

$$\sigma^4_{rz} = \sigma^1_{rz} + \sigma^3_{rz} - \sigma^2_{rz} \tag{3.103}$$

$$\sigma^4_{\theta\theta} = \sigma^1_{\theta\theta} + \sigma^3_{\theta\theta} - \sigma^2_{\theta\theta} \tag{3.104}$$

and may be written as:

$$[A_{1'}]\,[X] = [B_{1'}] \tag{3.105}$$

where

$$[A_{1'}] = [I_4, -I_4, I_4, -I_4] \text{ , } I_4 \text{ being the 4 dimension identity matrix} \tag{3.106}$$

$$[X]^T = [\sigma^1_{rr}, \sigma^1_{zz}, \sigma^1_{zr}, \sigma^1_{\theta\theta}, ..., \sigma^4_{rr}, \sigma^4_{zz}, \sigma^4_{zr}, \sigma^4_{\theta\theta}] \tag{3.107}$$

$$[B_{1'}]^T = [0, 0, 0, 0] \tag{3.108}$$

3.3.2 Yield Constraints

Yield Constraints for the 3-noded Triangular Extension Element

The second set of constraint conditions for extension elements relates to yield constraint that ensure that the stress field is plastically admissible. In order to ensure that the stress field in both the non-extension and extension zone (Fig. 3-8 (a)) does not violate the linearized yield criterion, it can be proven (see Appendix A) that the stresses need to satisfy the following constraints:

$$F_{k2} \leqslant 0,\ F_{k1} \leqslant F_{k2} \text{ and } F_{k3} \leqslant F_{k2}\ ;\ k = 1, 2..., p \tag{3.109}$$

While the inequality constraints applied to the stresses at node 2 are identical to those described by relations (3.94) to (3.98), at node 1 and 3, the yield criterion gives rise to $3p + 3$ inequality constraints of the form:

$$\left[A_{yield\_triext}\right][X] \leqslant \left[B_{yield\_triext}\right] \tag{3.110}$$

$$[R_{yield}]\left[\tilde{X}\right] \leqslant \left[\bar{R}_{yield}\right] \tag{3.111}$$

where

$$\left[A_{yield\_triext}\right] = \begin{bmatrix} A_1^i & B_1^i & C_1^i & D_1^i & -A_1^i & -B_1^i & -C_1^i & -D_1^i \\ .. & .. & .. & .. & .. & .. & .. & .. \\ A_p^i & B_p^i & C_p^i & D_p^i & -A_p^i & -B_p^i & -C_p^i & -D_p^i \end{bmatrix} \quad i = 1, 2, 3 \tag{3.112}$$

$$\left[B_{yield\_triext}\right]^T = [0, .., 0] \quad i = 1, 2, 3 \tag{3.113}$$

$$[X]^T = [\sigma_{rr}^n, \sigma_{zz}^n, \sigma_{zr}^n, \sigma_{\theta\theta}^n, \sigma_{rr}^2, \sigma_{zz}^2, \sigma_{zr}^2, \sigma_{\theta\theta}^2] \quad n = 1 \text{ and } 3 \tag{3.114}$$

$$\left[\tilde{X}\right]^T = [\sigma_{rr}^n, \sigma_{zz}^n, \sigma_{zr}^n, \sigma_{\theta\theta}^n] \quad n = 1 \text{ and } 3 \tag{3.115}$$

where $[R_{yield}]$ and $\left[\bar{R}_{yield}\right]$ are defined as in (3.95) and (3.97).

Yield Constraints for the 4-noded Rectangular Extension Element

It can be proven (see Appendix B) that the stresses satisfy the yield criterion throughout the extension and non-extension zone (Fig. 3-8 (b)) by enforcing the following constraints:

$$F_{k2} \leqslant 0,\ F_{k1} \leqslant F_{k2} \text{ and } F_{k3} \leqslant 0\ ;\ k = 1, 2..., p \tag{3.116}$$

The inequality constraints that are applied to the stresses at node 2 and 3 are identical to those described by (3.94) to (3.98). In turn, at node 1 the yield criterion gives rise to $3p+3$ inequality constraints of the form:

$$\left[A_{yield\_rectext}\right][X] \leqslant \left[B_{yield\_rectext}\right] \tag{3.117}$$

$$[R_{yield}]\left[\tilde{X}\right] \leqslant \left[\bar{R}_{yield}\right] \tag{3.118}$$

where

$$\left[A_{yield\_rectext}\right] = \begin{bmatrix} A_1^i & B_1^i & C_1^i & D_1^i & -A_1^i & -B_1^i & -C_1^i & -D_1^i \\ .. & .. & .. & .. & .. & .. & .. & .. \\ A_p^i & B_p^i & C_p^i & D_p^i & -A_p^i & -B_p^i & -C_p^i & -D_p^i \end{bmatrix} \quad i = 1, 2, 3 \tag{3.119}$$

$$\left[B_{yield\_rectext}\right]^T = [0, .., 0]\ i = 1, 2, 3 \tag{3.120}$$

$$[X]^T = [\sigma_{rr}^1, \sigma_{zz}^1, \sigma_{zr}^1, \sigma_{\theta\theta}^1, \sigma_{rr}^2, \sigma_{zz}^2, \sigma_{zr}^2, \sigma_{\theta\theta}^2] \tag{3.121}$$

$$\left[\tilde{X}\right]^T = [\sigma_{rr}^1, \sigma_{zz}^1, \sigma_{zr}^1, \sigma_{\theta\theta}^1] \tag{3.122}$$

where $[R_{yield}]$ and $\left[\bar{R}_{yield}\right]$ are again defined as in (3.95) and (3.97).

3.4 Lower Bound Optimization Problem

3.4.1 Constraints

All previous equality and inequality constraints can be summarized in the following compact form:

$$[A'_1][\sigma] = [b_1] \tag{3.123}$$

$$[A'_2][\sigma] \leqslant [b_2] \tag{3.124}$$

where:

- $[A'_1]$ assembles the constraint matrices related to the equilibrium and stress boundary conditions, i.e. (3.43), (3.50), (3.55) and (3.106),
- $[A'_2]$ assembles the constraint matrices related to the linearized yield criterion, i.e. (3.94), (3.112) and (3.119),
- $[\sigma]$ is the nodal stresses vector.

3.4.2 Objective Function

The lower bound theorem provides a lower bound Q' of the nominal value of the actual limit load $Q^{\lim}$:

$$Q' \leqslant Q^{\lim} \tag{3.125}$$

The lower bound formulation therefore appears as a maximization problem: maximize the load value Q' subjected to the constraints (3.123) and (3.124) of the statically and plastically admissible stress field σ'_{ij}. It therefore suffices to employ appropriate optimization algorithms to solve the problem. Since optimization algorithms comes rather as minimization than maximization algorithms we recast the lower bound maximization problem as a minimization problem in the

form:

$$\left\{ \begin{array}{c} -\min_{\{\sigma\}}(-Q'(\{\sigma\})) \\ \textit{Subject to}: \\ [A_1'][\sigma] = [b_1] \\ [A_2'][\sigma] \leqslant [b_2] \end{array} \right\} \tag{3.126}$$

3.4.3 Objective Function of the Indentation Test

We are left with specifying the objective function of the indentation test. Figure 3-9 illustrates the indenter and the driving force to optimize. We have:

$$-P = \int_A \mathbf{e}_z \cdot \boldsymbol{\sigma} \cdot \mathbf{n} \, dA \tag{3.127}$$

where A is the cone area and $\mathbf{n}$ the outward normal vector to the material surface. Eq. (3.127)

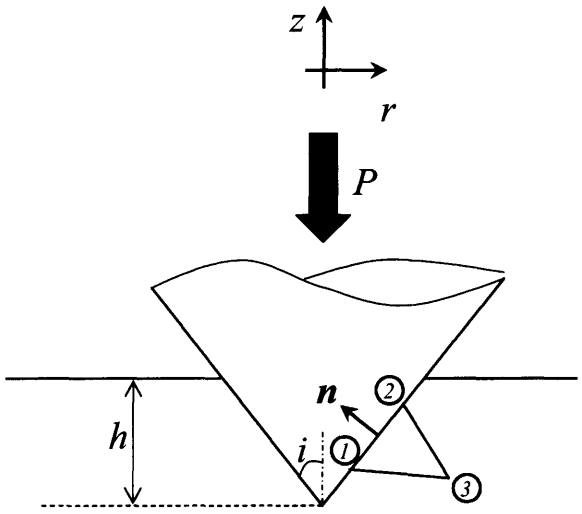

Figure 3-9: Penetrating cone and material interface.

yields:

$$-P = \int_A [\sin(i)\sigma_{zz} - \cos(i)\sigma_{rz}] \, dA \tag{3.128}$$

where i is the semi-apex angle (see Fig. 3-9).

Let us consider an edge of a triangular element defined by nodes 1 and 2 on the cone surface (Fig. 3-9). Since the stresses vary linearly throughout each element, Eq. (3.128) becomes:

$$-P_{edge} = \int_A \left(\tilde{\sigma}^1 (1 - \frac{s}{L_{12}}) + \tilde{\sigma}^2 (\frac{s}{L_{12}}) \right) r d\theta ds \tag{3.129}$$

where s is the curvilinear abscissa, L_{12} is the edge length and

$$\tilde{\sigma}^n = \sin(i)\sigma_{zz}^n - \cos(i)\sigma_{rz}^n \ , \ n = 1, 2 \tag{3.130}$$

Since $\tilde{\sigma}^n$ is θ-invariant, and $r = r_1 + s\sin(i)$, we have:

$$-P_{edge} = 2\pi \left[\int_0^{L_{12}} \left(\tilde{\sigma}^1 + \frac{s}{L_{12}} (\tilde{\sigma}^2 - \tilde{\sigma}^1) \right) r_1 ds + \left(\int_0^{L_{12}} \tilde{\sigma}^1 + \frac{s}{L_{12}} (\tilde{\sigma}^2 - \tilde{\sigma}^1) \right) s \sin(i) ds \right] \tag{3.131}$$

i.e.

$$-P_{edge} = 2\pi \left[\tilde{\sigma}^1 \left(r_1 L_{12} + \frac{L_{12}^2 \sin(i)}{2} \right) + (\tilde{\sigma}^2 - \tilde{\sigma}^1) \left(\frac{r_1 L_{12}}{2} + \frac{L_{12}^2 \sin(i)}{3} \right) \right] \tag{3.132}$$

Finally, expressing $-P_{edge}$ in terms of σ_{zz}^n and σ_{rz}^n, we obtain:

$$-P_{edge} = [c]_{edge}^T [\sigma] \tag{3.133}$$

where $[c]_{edge}$ is the vector of the objective function coefficients,

$$[c]_{edge} = \begin{bmatrix} 0 \\ 2\pi \sin(i)(\frac{r_1 L_{12}}{2} + \frac{L_{12}^2 \sin(i)}{6}) \\ -2\pi \cos(i)(\frac{r_1 L_{12}}{2} + \frac{L_{12}^2 \sin(i)}{6}) \\ 0 \\ 0 \\ 2\pi \sin(i)(\frac{r_1 L_{12}}{2} + \frac{L_{12}^2 \sin(i)}{3}) \\ -2\pi \cos(i)(\frac{r_1 L_{12}}{2} + \frac{L_{12}^2 \sin(i)}{3}) \\ 0 \end{bmatrix} \tag{3.134}$$

$$[\sigma]^T = [\sigma_{rr}^1, \sigma_{zz}^1, \sigma_{zr}^1, \sigma_{\theta\theta}^1, \sigma_{rr}^2, \sigma_{zz}^2, \sigma_{zr}^2, \sigma_{\theta\theta}^2] \tag{3.135}$$

Last, the contribution of the different elements sum up to the driving force:

$$-P = \sum_{edges} -P_{edge} \tag{3.136}$$

Then the optimization problem for the indentation test can be stated as follows:

$$\left\{ \begin{array}{c} -\min_{\{\sigma\}}([c]^T[\sigma]) \\ Subject\ to: \\ [A_1][\sigma] = [b_1] \\ [A_2][\sigma] \leqslant [b_2] \end{array} \right\} \tag{3.137}$$

where $[c]$ assembles the objective function matrices (3.134) for the nodes along the cone surface.

3.5 Chapter Summary

The lower bound computational formulation for axisymmetric problems derived in this Chapter constitutes (to our knowledge) the first complete adaptation of the plane stress/plane strain method.

The key ingredients of the lower bound discretization are:

- The constraint conditions to ensure statically and plastically admissible stress fields ex-

pressed by the equilibrium equation and the yield criterion,

- The discretization and linearization of the yield criterion.

We now have a tool in hand for analyzing the indentation tests from a lower bound perspective, which is the focus of the next Chapter.

Chapter 4

Lower Bound Solutions For Indentation Analysis

This Chapter presents lower bound solutions for the collapse load of different indenters, using the computational approach developed in Chapter 3. This computational lower bound method was implemented in a FORTRAN based environment that employs the BPMPD algorithm (see [62]) or the steep edge algorithm by Sloan [75]. The meshes are generated using the pre-processor of a commercially available finite element package, CESAR-LCPC^{TM}. Details on the meshing and boundary conditions are given first, before results are presented for different indenter geometries: sharp and spherical indenters. The effect of the apex-angle for sharp indenters and the effect of different indenter-material contact conditions are also discussed. The Chapter closes with a critical review of strength and limitations of the lower bound approach for the extraction of strength properties from hardness measurements.

4.1 Modeling the Indentation Test

4.1.1 Boundary Conditions. Zero Stress Locking Phenomena

The indenter is modeled as a cone. The stress-boundary condition for the lower bound are presented in Figure 4-1.

It is instructive to investigate the linearized equilibrium equations derived in Section 3.2.3

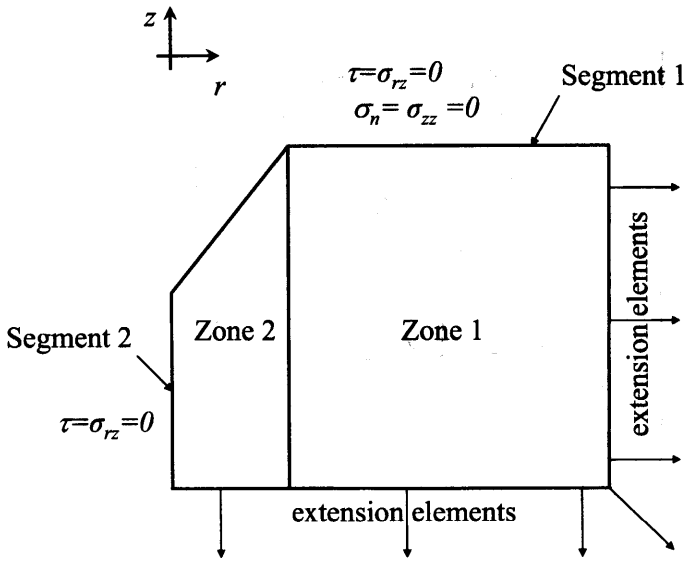

Figure 4-1: Stress boundary conditions.

(equations (3.36) to (3.41)). We first note that (3.40) and (3.41) yield:

$$\sigma_{zr} = ar \text{ inside each element} \tag{4.1}$$

where a is a constant. Since $\sigma_{zr} = 0$ on the free surface of the material (i.e. Segment 1 in Fig. 4-1), it follows that $\sigma_{zr} = 0$ in all triangle elements that have an edge on this surface. The same applies to the vertical stress on this surface. Indeed, since $\sigma_{zz} = 0$ on this surface, it follows from (3.39) that $\sigma_{zz} = 0$ in all triangle elements that have an edge on Segment 1. It is intuitively understood that this stress boundary condition, in a pure stress approach, has an influence on the stress field in Zone 1. To derive this effect, let us consider a set of 2 elements as displayed in Figure 4-2. Let us assume that $\sigma_{zr} = \sigma_{zz} = 0$ in the triangle T1 (see Fig. 4-2). We are interested in the stresses in the triangle 'below', which has a common interface with T1 inclined by an angle $\alpha \in [0, \frac{\pi}{2}[$. The continuity condition (3.3) at this interface read:

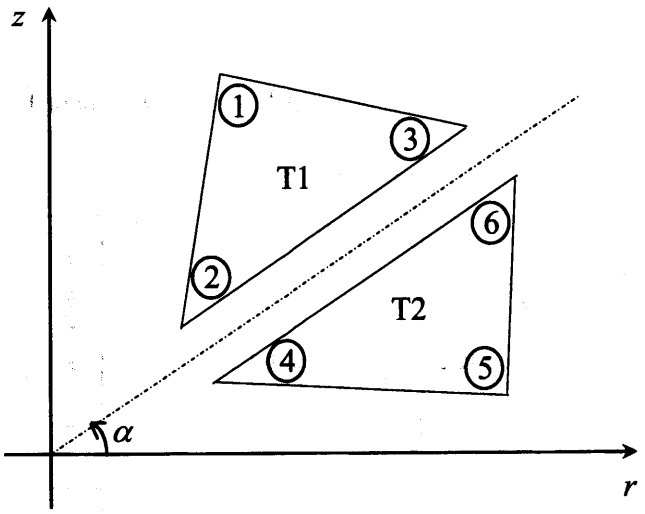

Figure 4-2: Stress propagation between triangles.

$$[[-\sin(\alpha)\sigma_{rr} + \cos(\alpha)\sigma_{rz}]] = 0 \tag{4.2}$$

$$[[-\sin(\alpha)\sigma_{rz} + \cos(\alpha)\sigma_{zz}]] = 0 \tag{4.3}$$

If $\alpha = 0$, Eq. (4.2) yields $\sigma_{zr}^4 = \sigma_{zr}^6 = 0$. Thus from (4.1)

$$\sigma_{zr} = 0 \text{ in T2} \tag{4.4}$$

From relation (4.3) we derive $\sigma_{zz}^4 = \sigma_{zz}^6 = 0$, meaning that σ_{zz} is independent of r. Furthermore, (3.39) implies:

$$\sigma_{zz} = 0 \text{ in T2} \tag{4.5}$$

Let us consider next that $\alpha \in]0, \frac{\pi}{2}[$. Eq. (4.3) and (4.1) yield:

$$\sigma_{zz}^4 - \sigma_{zz}^6 = \tan(\alpha)a(r_4 - r_6) \tag{4.6}$$

This relation indicates that σ_{zz} is independent of z in T2. Furthermore, relation (3.39) yields

$a = 0$. Hence:

$$\sigma_{zr} = 0 \text{ in T2} \tag{4.7}$$

Finally, relation (4.3) yields $\sigma^4_{zz} = \sigma^6_{zz} = 0$; and since $r_4 \neq r_6$, σ_{zz} is also found to be independent of r. Consequently:

$$\sigma_{zz} = 0 \text{ in T2} \tag{4.8}$$

In summary, since σ_{rz} and σ_{zz} are null below every triangle having an edge on Segment 1, it follows:

$$\left\{ \begin{array}{l} \sigma_{rz} = 0 \\ \sigma_{zz} = 0 \end{array} \right\} \text{ in Zone 1} \tag{4.9}$$

While running simulation with "random meshes" we sometimes encountered a locking problem: the optimized stress field turned out to be null, leading to a zero driving force. It is instructive to investigate this locking phenomena. To this end we consider an overlapping triangle T between Zone 1 and Zone 2 (Fig. 4-3) and 3 non aligned points (A, B, C in Fig. 4-3) inside the part of T in Zone 1.

Since the stresses are linear inside every triangle, we have:

$$\left\{ \begin{array}{l} \sigma_{rz} = 0 \\ \sigma_{zz} = 0 \end{array} \right\} \text{ in T} \tag{4.10}$$

Then, with a similar argument as developed above, it is readily shown that:

$$\left\{ \begin{array}{l} \sigma_{rz} = 0 \\ \sigma_{zz} = 0 \end{array} \right\} \text{ in Zone 1bis} \tag{4.11}$$

This effect propagates also from Zone 1bis to Zone 2bis for any overlapping element, and eventually $\sigma_{zz} = 0$ in the whole half-space, thus leading to a zero driving force.

The conclusion of this analysis is that a vertical boundary delimiting the indentation zone (Zone 2) from the free surface zone (Zone 1) is required to avoid any overlapping triangle (see Fig. 4-1).

It is worth noting that this requirement is relevant only for the axisymmetric case, as it is a direct consequence of the equilibrium equation. Indeed, contrary to the (cartesian) 2D or

full 3D equations, the axisymmetric equations mix stresses and stress derivatives (see Section 3.2.3).

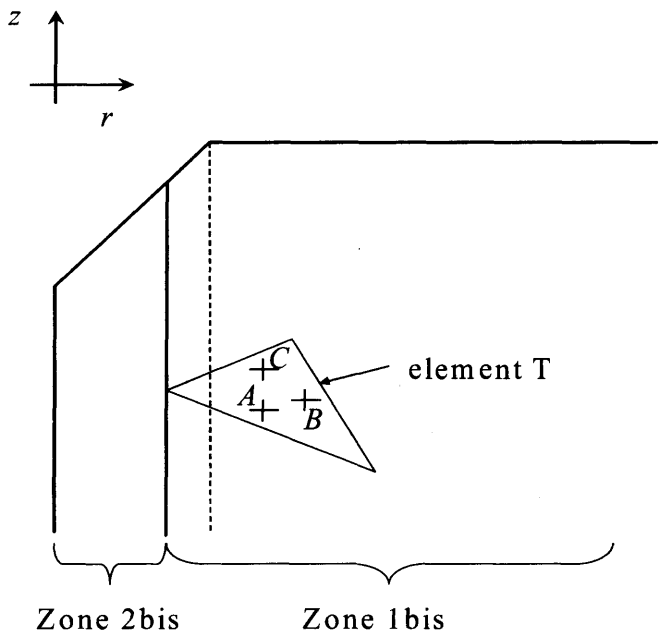

Figure 4-3: Overlapping triangle.

4.1.2 Simplification of the Stress Field

We already found that $\sigma_{zr} = 0$ in Zone 1. Let us now analyze a triangle in Zone 2 having an edge along the boundary delimiting Zone 1 and Zone 2 (Fig. 4-4).

Since the shear stress must be continuous between the elements, it follows that the shear stresses at the interface are zero:

$$\left\{ \begin{array}{l} \sigma_{rz}^1 = 0 \\ \sigma_{rz}^2 = 0 \end{array} \right\} \tag{4.12}$$

since σ_{zr} is linear with respect to r, cf. Eq. (4.1), $\sigma_{zr} = 0$ in this boundary triangle. Using the same development as in the previous section, we have

$$\sigma_{zr} = 0 \text{ in Zone 1ter} \tag{4.13}$$

And thus using the same arguments as in Section 4.1.1:

$$\sigma_{zr} = 0 \text{ in the entire half-space} \tag{4.14}$$

The conclusion of this analysis is that the stress field permitted by our computational approach is necessarily diagonal (meaning that the principal stresses are σ_{rr}, σ_{zz}, and $\sigma_{\theta\theta}$). The equilibrium equations (3.36) to (3.41) thus reduce to:

$$\sum_{k=1}^{3} \frac{\partial N_k(r,z)}{\partial r}(2\sigma_{rr}^k - \sigma_{\theta\theta}^k) = 0 \tag{4.15}$$

$$\sum_{k=1}^{3} \frac{\partial N_k(r,z)}{\partial z}(\sigma_{rr}^k - \sigma_{\theta\theta}^k) = 0 \tag{4.16}$$

$$\sum_{k=1}^{3} N_k(0,0) \times (\sigma_{rr}^k - \sigma_{\theta\theta}^k) = 0 \tag{4.17}$$

$$\sum_{k=1}^{3} \frac{\partial N_k(r,z)}{\partial z}\sigma_{zz}^k = 0 \tag{4.18}$$

This diagonal stress field also simplifies the Mohr-Coulomb criterion. Indeed, for $\sigma_{zr} = 0$, the Mohr-Coulomb criterion (3.58) is linear in stresses, which reduces greatly the computational time arising from the linearization. We only need to consider (3.61) instead of (3.92) and (3.93).

4.2 Lower Bound Solution for Perfectly Rough Cones

4.2.1 Independence of the Cone Geometry

The perfectly rough cone interface properties are defined by (3.100) and no additional interface constraint is required. All the constraints (equalities and inequalities), are therefore independent of the semi-apex angle i.

In addition, the stress field can be extended along the cone in the z direction to establish a "virtual" stress field in the whole half space (Fig. 4-5). The stress continuities equations imply

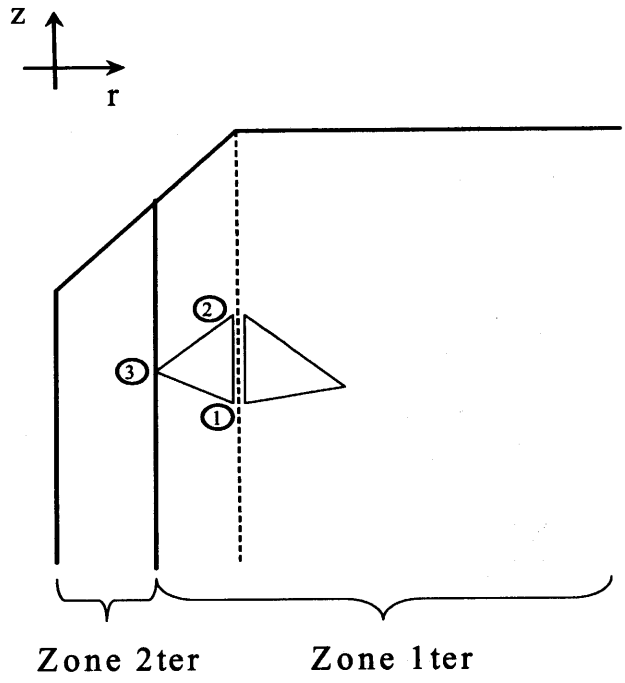

Figure 4-4: Triangle with edge along boundary Zone1-2.

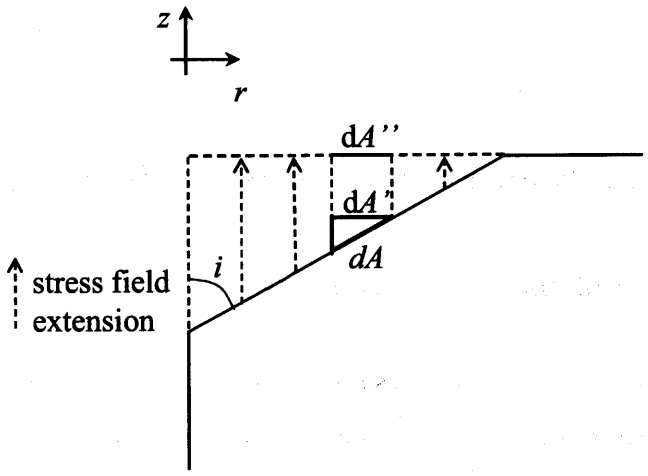

Figure 4-5: Surface element dA.

that σ_{zz} and σ_{rr} are continuous between all elements. We also have (see Fig. 4-5):

$$dA' = dA'' = dA\sin(i) \tag{4.19}$$

Since σ_{zz} is independent of z (see Eq. (4.18)) we can write:

$$-P = \int_{A''} \sigma_{zz} dA'' \tag{4.20}$$

This shows that the cone semi-apex angle i does not have any influence on the lower bound solution of the perfectly rough cone. All the solutions (i.e. the optimized stress fields) reduce to the flat punch solution.

It is important to note that this flat punch solution ($i = 90°$) does not depend on the roughness (of the flat punch), since the shear stress at the cone-material interface, σ_{rz}, is zero (meaning that no additional constraint due to the interface is taken into account).

4.2.2 Results

Figures 4-6 (a) to 4-7 (d) show the different meshes used for the lower bound analysis. The use of the rectangular and triangular extension elements enables the stress field to be extended indefinitely in the half plane without violating neither the statically nor plastically admissible stress field requirements. As expected, the optimized stress fields are found to be independent of the cone apex angle (three different apex angles are presented here). The optimized stress field in Zone 2 is constant with $\sigma_{rr} = \sigma_{\theta\theta}$. This result is found for all the meshes presented here. Figure 4-8 displays the results in the dimensionless form (2.11), i.e.

$$\frac{H'}{c} = \frac{P'}{c\pi R^2} = \mathcal{F}'(\varphi) \tag{4.21}$$

The obtained results are somewhat disappointing as far as the derived numerical function $\mathcal{F}'(\varphi)$ strictly coincides with the analytical lower bound solution of Section 3.1.2. For the reader's convenience the analytical lower bound results are reproduced below:

$$\text{in Zone 2 } (\Omega_1)\text{: } \sigma_{rr} = \sigma_{\theta\theta} = -\frac{2c\cos\varphi}{1-\sin\varphi} \text{ and } \sigma_{zz} = \frac{4c\cos\varphi}{(1-\sin\varphi)^2} \tag{4.22}$$

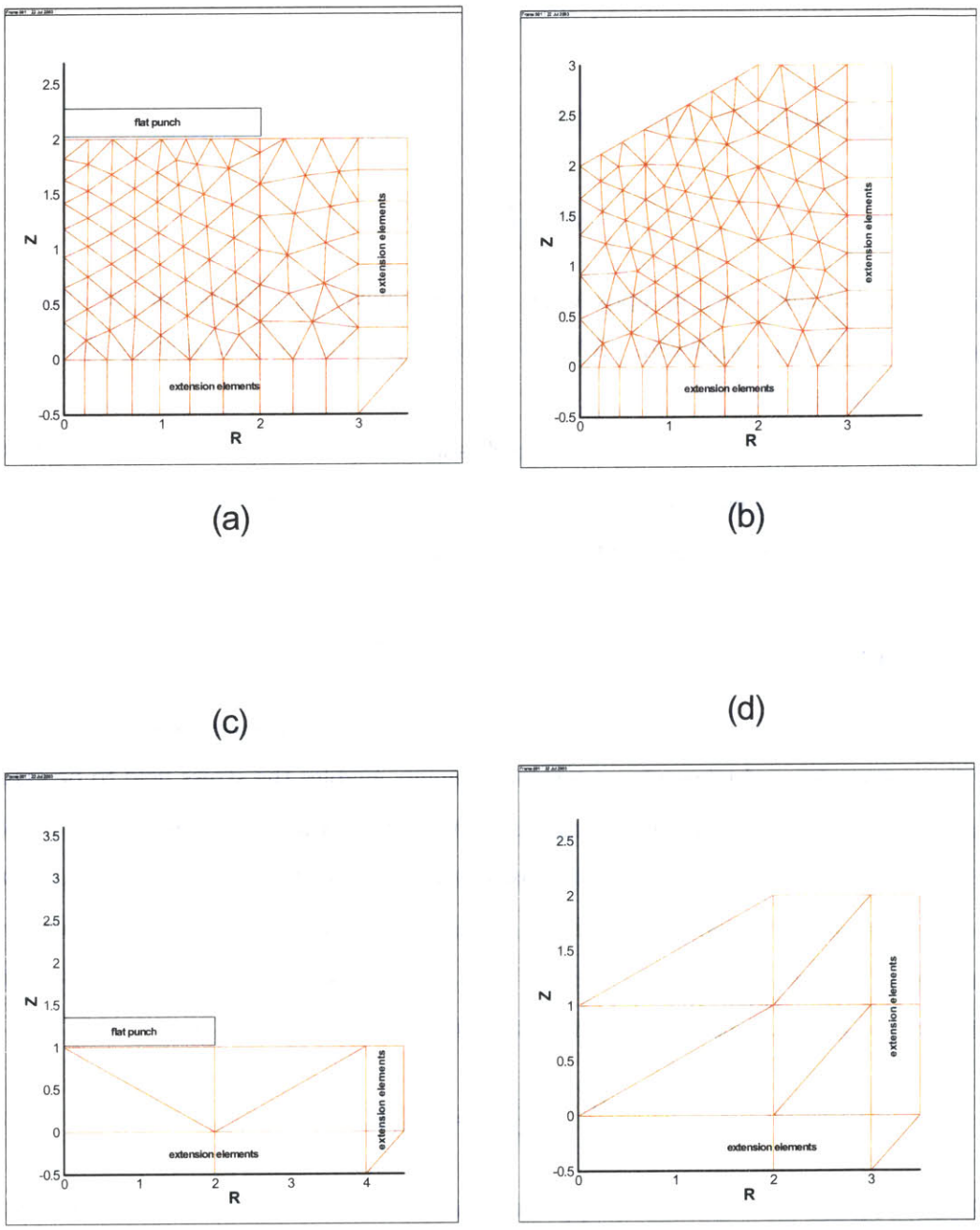

Figure 4-6: (a) Flat punch, 'random mesh'. (b) Cone indenter, 'random mesh'. $i = 63°$. (c) Flat punch, 'coarse mesh'. (d) Cone indenter, 'coarse mesh'. $i = 63°$.

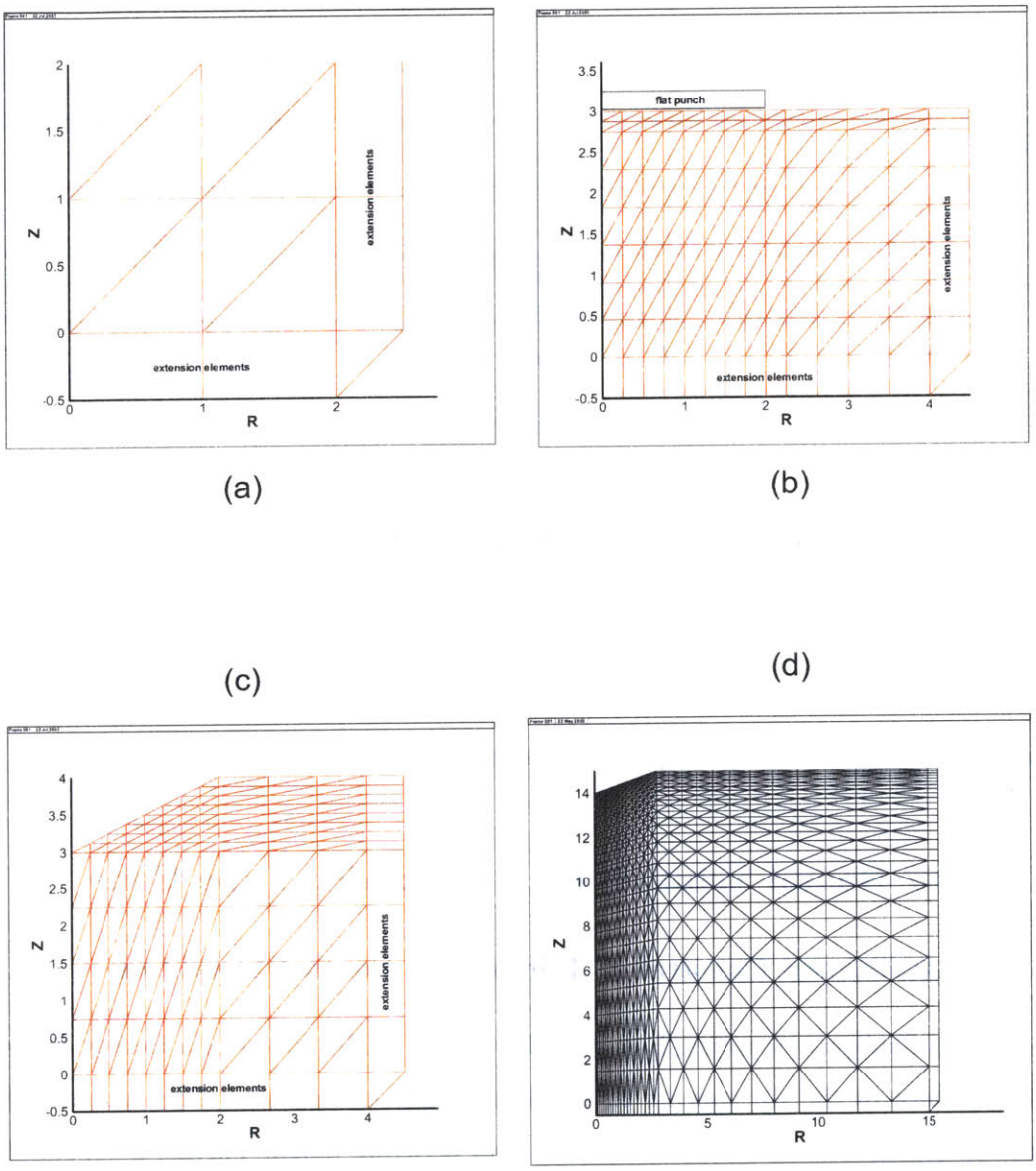

Figure 4-7: (a) Cone indenter, 'coarse mesh'. $i = 45°$. (b) Flat punch, 'regular mesh'. (c) Cone indenter, 'regular mesh'. $i = 63°$. (d) Cone indenter, 'fine mesh'. $i = 70.32°$.

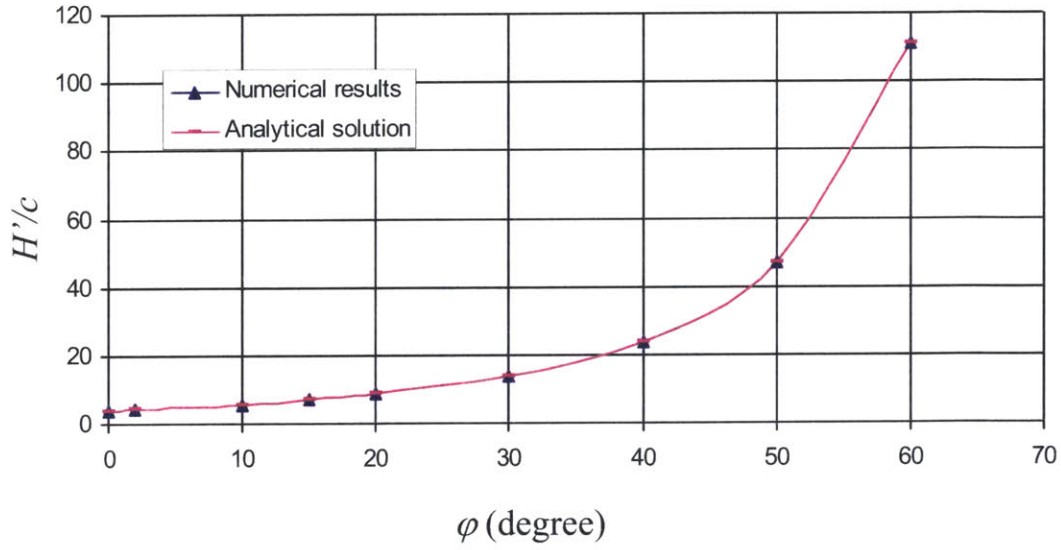

Figure 4-8: Numerical and analytical lower bound solutions for the dimensionless parameter $\frac{H'}{c}$ as a function of φ. Perfectly rough cone.

$$\text{in Zone 1 } (\Omega_2)\text{: } \sigma_{rr} = \sigma_{\theta\theta} = -\frac{2c\cos\varphi}{1-\sin\varphi} \text{ and } \sigma_{zz} = 0 \tag{4.23}$$

The numerical solution does not improve this already known lower bound.

4.3 Lower Bound Solution for a Berkovich Type Cone

4.3.1 An Additional Constraint: Frictionless Contact Condition

Figure 4-9 (a) displays a Scanning Electron Microscope (SEM) image of a Berkovich indenter tip. The surface of the tip appears to be almost perfectly smooth. The contact area can therefore be assumed to be rather frictionless than perfectly rough. Furthermore, simulations have shown that the effect of friction in the case of Berkovich indenter can be neglected (see [20], [19], [12]). This allows us to introduce an additional boundary condition along the cone (smooth interface condition):

$$\tau = 0 \tag{4.24}$$

that is, from Eq. (3.47) $\sigma_{rr} = \sigma_{zz}$ for any conical indenter along the indenter surface.

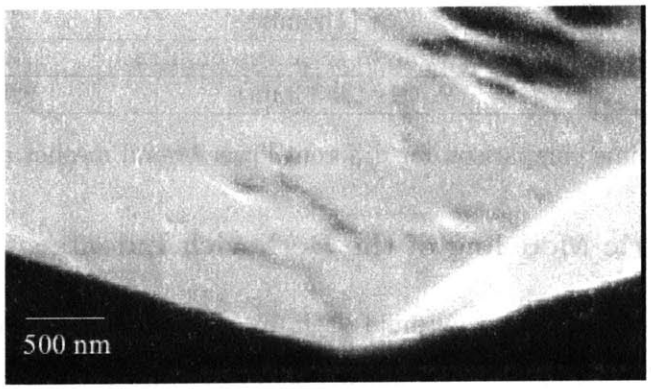

(a)

(b)

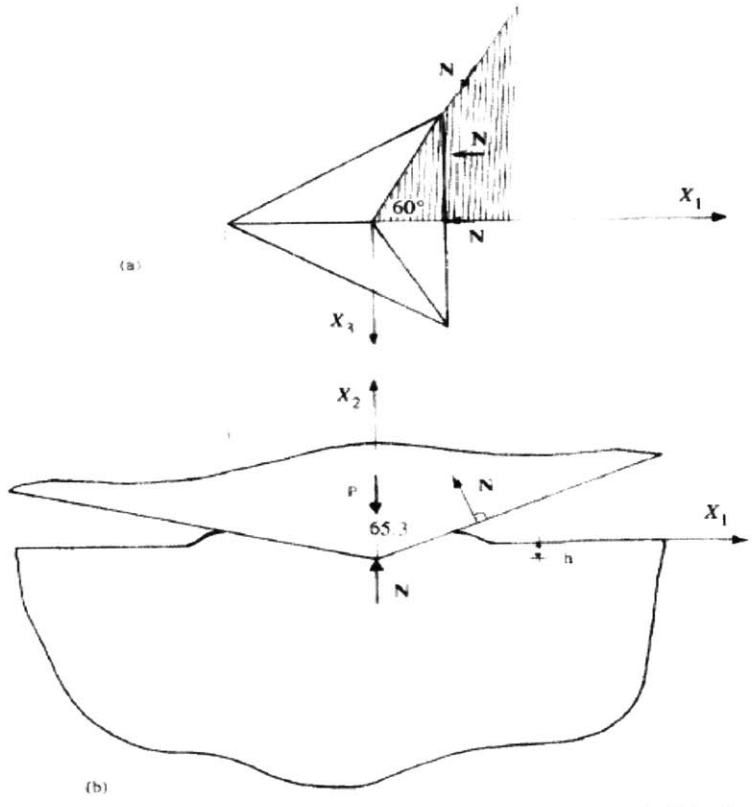

Fig. 1. Schematic of the geometry of the Berkovich test. (a) Top view. (b) Side view.

Figure 4-9: (a) Indenter tip (from [89]). (b) Berkovich indenter (from [52]).

	Steep edge algorithm [75]	BPMPD algorithm [62]
mesh in Fig. 4-10 (a)	3,973s (1h6min)	215s (3min35)
mesh in Fig. 4-10 (b)	breaks (unable to scale the problem)	1,699s (28min19s)
intermediate mesh	9,021s (2h30min)	980s (16min20s)

Table 4.1: CPU time comparison for different lower bound meshes and algorithms.

4.3.2 Axisymmetric Modeling of the Berkovich Indenter

The Berkovich indenter is a 3-sided pyramid with an apex angle of 130.6° (see Fig. 4-9 (b)). In this study, the Berkovich indenter is modeled as a cone with a 70.32° semi-apex angle (see Fig. 1-4), such that the projected contact area with respect to penetration depth of the cone is the same as that for the real indenter [20]:

$$A(h) = 24.56h^2 = \pi \tan^2(70.32)h^2 \tag{4.25}$$

The first mesh used (Fig. 4-10 (a)) has a high concentration of elements below the indenter. It is composed of 5,791 nodes: 1,848 triangles, 1 triangular extension element, 61 rectangular extension elements and 2,711 discontinuity elements. A convergence study was performed by subdividing the mesh (see Fig. 4-11). One of the finest meshes used is presented Figure 4-10 (b). It is composed of 16,023 nodes: 5,200 triangles, 1 triangular extension element, 105 rectangular extension elements and 7,905 discontinuity elements. The convergence was almost achieved with the first mesh, since the asymptotic result lies within the range of 1.7 % from the initial result. Table 4.1 presents a comparison of the CPU times for the two aforementioned meshes and one intermediate mesh, for two different optimization algorithms. The simulations were run on a Pentium3, 1.13GHz, 256Mb RAM.

4.3.3 Results

Figure 4-12 shows the evolution of $\frac{H'}{c}$ with respect to φ for the analytical solution (3.13) and the numerical one. The analytical lower bound reads (same method as in Section 3.1.2 with a triaxial stress state in Zone 2 due to (4.24)):

$$\text{in Zone 2: } \sigma_{rr} = \sigma_{\theta\theta} = \sigma_{zz} = -\frac{2c\cos\varphi}{1-\sin\varphi} \tag{4.26}$$

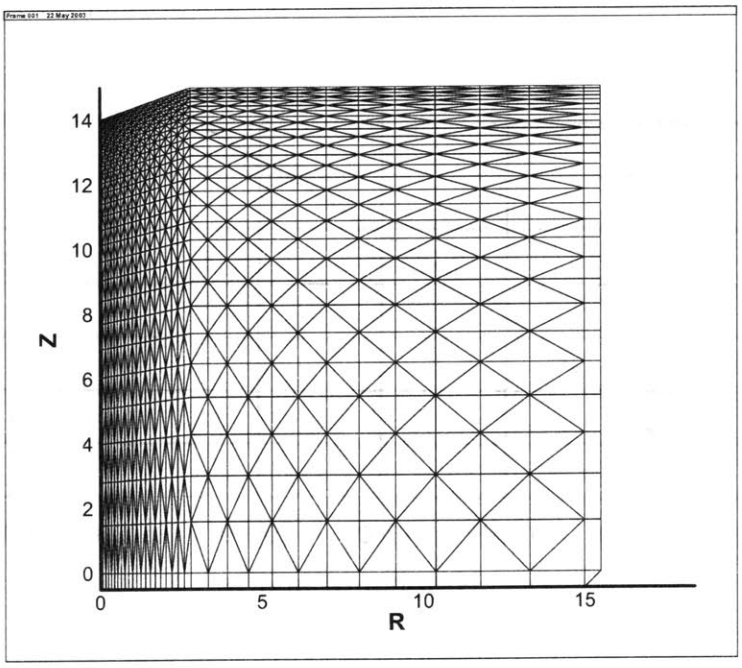

(a)

(b)

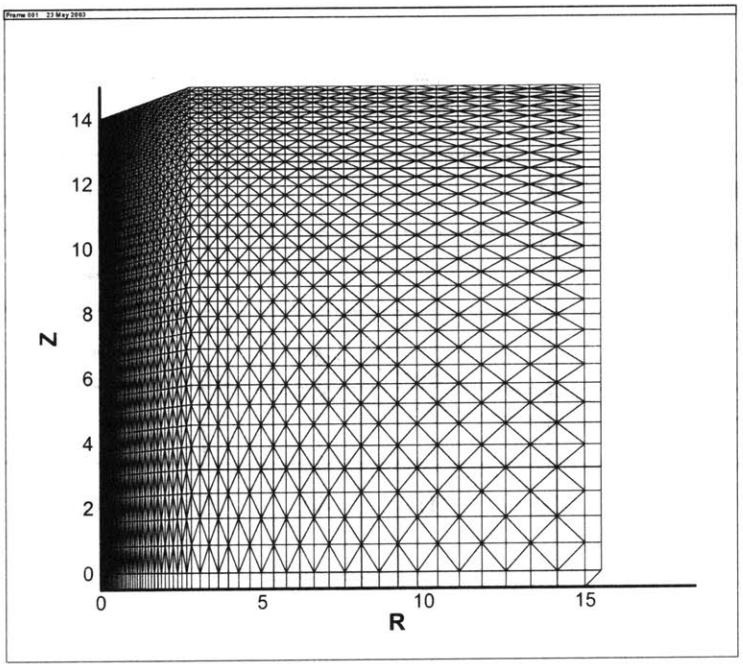

Figure 4-10: Lower bound meshes for a Berkovitch type indenter: (a) relatively fine mesh. (b) very fine mesh.

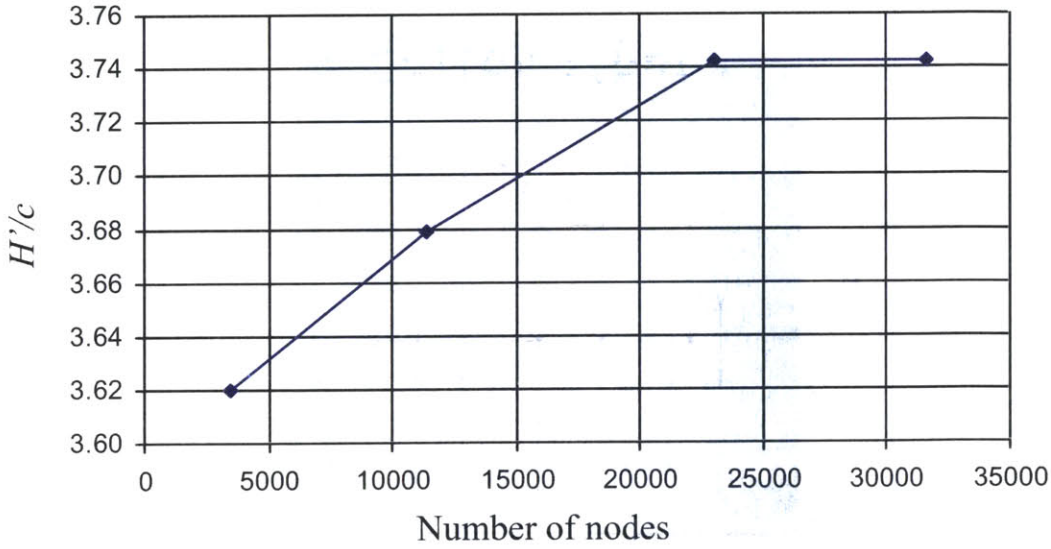

Figure 4-11: Mesh convergence study.

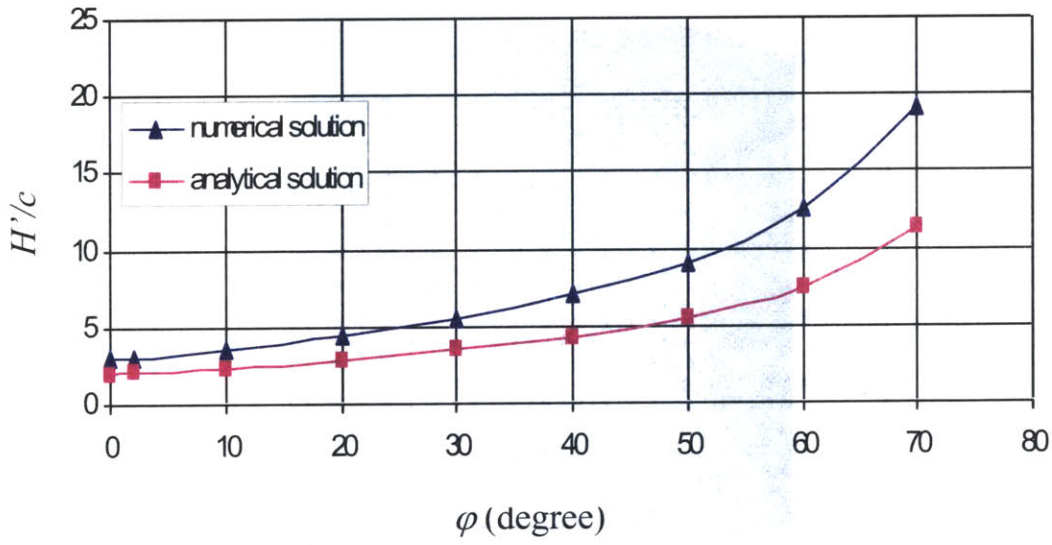

Figure 4-12: Lower bound for the dimensionless parameter $\frac{H'}{c}$ as a function of φ for a Berkovich type conical indenter.

$$\text{in Zone 1: } \sigma_{rr} = \sigma_{\theta\theta} = -\frac{2c\cos\varphi}{1-\sin\varphi} \text{ and } \sigma_{zz} = 0 \tag{4.27}$$

Figure 4-12 clearly shows that the numerical approach improves the (only) available analytical solution (to our knowledge) by more than 40 %.

It is instructive to investigate the optimized stress field:

From (4.18) and the stress jump equations (3.46) and (3.47) we see that σ_{zz} is a function of r. Indeed, the simulations show that σ_{zz} decreases from the tip of the indenter to zero in Zone 1 (see Fig. 4-13 (a)). It is also interesting to note that the values of σ_{zz} strongly depend on the friction angle (see Fig. 4-14 (a)); σ_{zz} is an increasing function of φ. This result is readily understood from the yield criterion which we recall:

$$\sigma_I(1+\sin(\varphi)) - \sigma_{III}(1-\sin(\varphi)) \leqslant 2c\cos(\varphi) \tag{4.28}$$

Since σ_{zz} is the minor principal stress, as φ increases, the right hand side of the inequality increases, permitting σ_I and σ_{III} to reach respectively higher and lower values. The plots shown in Figure 4-14 (a) cannot be fitted with conventional functions (exponential, power, polynomial...), they are the result of the optimization process and do not seem to have any obvious analytical approximation.

Below the indenter, σ_{rr} is the major principal stress (i.e. $\sigma_{rr} = \sigma_I$) and decreases away from the tip (Fig. 4-13 (b)). The radial jumps are related to the dependence of σ_{zz} on r only. As φ decreases, we also find that the bulk of the material which is highly stressed by the indenter decreases (Fig. 4-15 (a) and (b)). There seems to be an oblique plane distinguishing two zones as far as $\sigma_{\theta\theta}$ is concerned (Fig. 4-14 (b), Fig. 4-16 (a) and (b)). It could be appealing to relate such a pattern to a shear plane, but we should keep in mind that the obtained stress fields are the product of a lower bound optimization procedure, that does not necessary deliver mechanically meaningful stress fields.

4.3.4 Effect of Different Apex Angles

Finally, it is instructive to study the influence of the semi-apex angle i on the dimensionless parameter $\frac{H'}{c}$ (cf. Eq. (2.11)). The results indicate that as soon as i is different from 90° (flat punch), $\frac{H'}{c}$ is not affected by the variation of i. That means that the hardness derived from

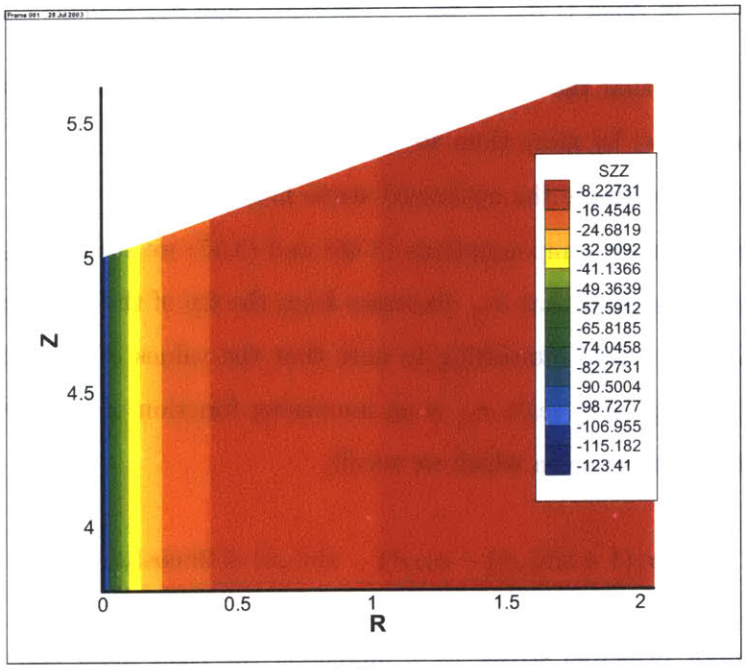

(a)

(b)

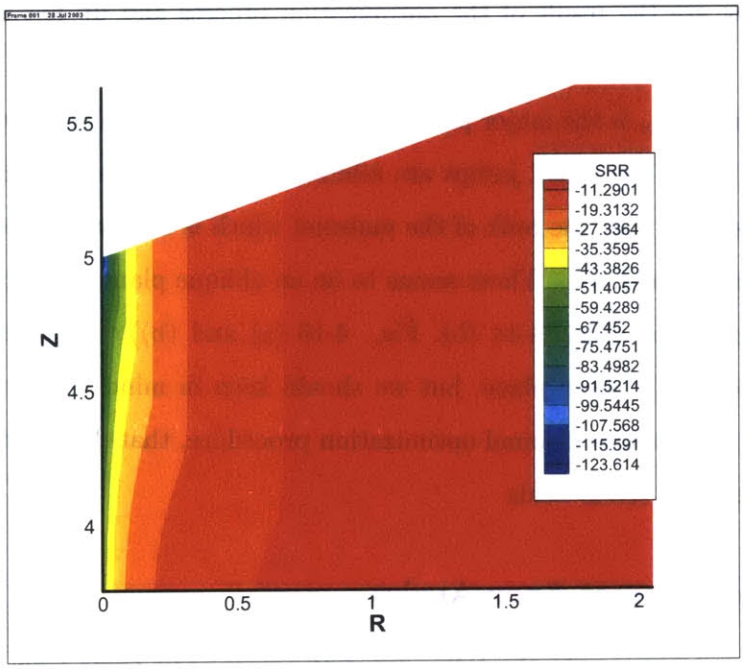

Figure 4-13: (a) Evolution of σ'_{zz}/c below the Berkovich indenter. $\varphi = 30°$. (b) Evolution of σ'_{rr}/c below the Berkovich indenter. $\varphi = 30°$. [stresses normalized by the cohesion].

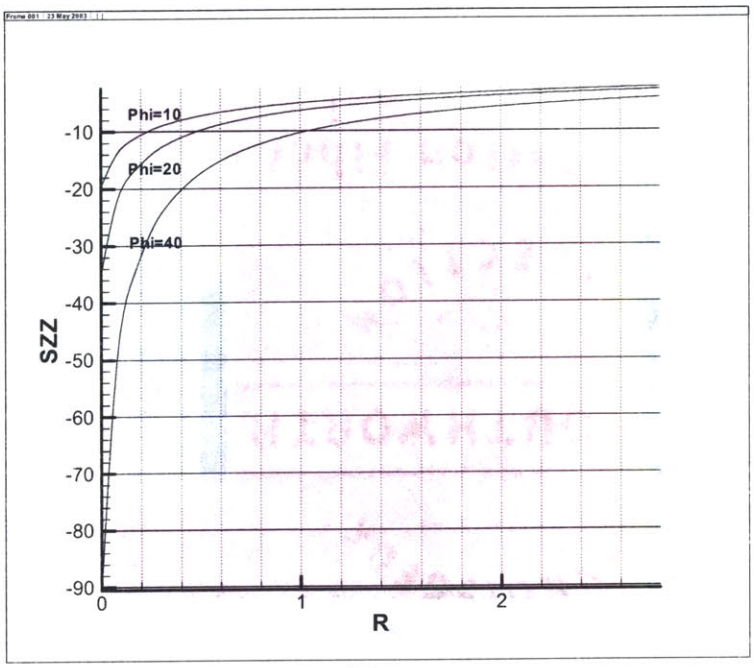

(a)

(b)

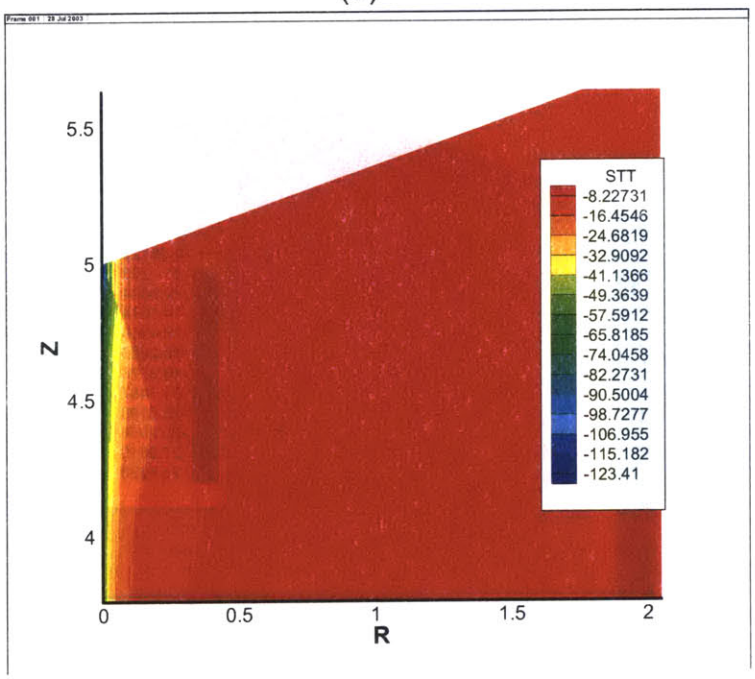

Figure 4-14: (a) Evolution of σ'_{zz}/c for different friction angles. (b) Evolution of $\sigma'_{\theta\theta}/c$ below the Berkovich indenter. $\varphi = 30°$. [stresses normalized by the cohesion].

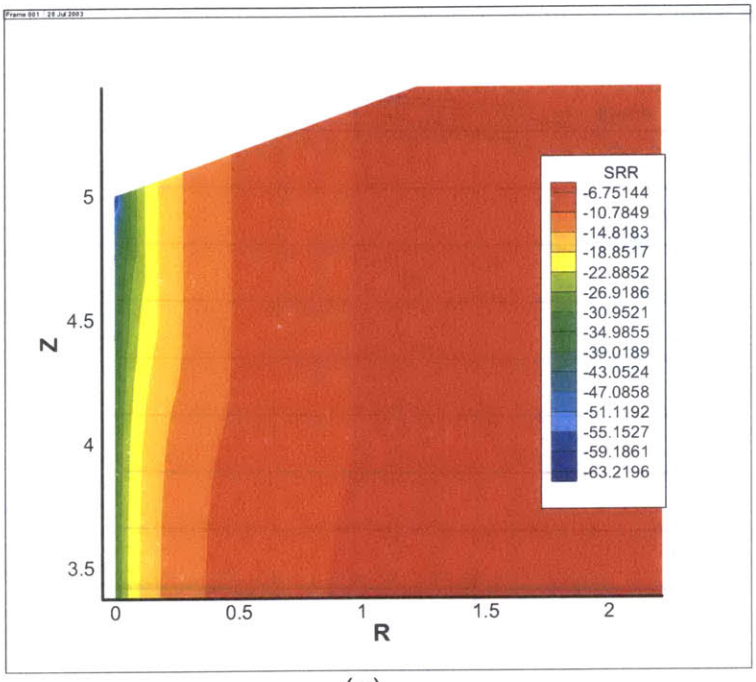

(a)

(b)

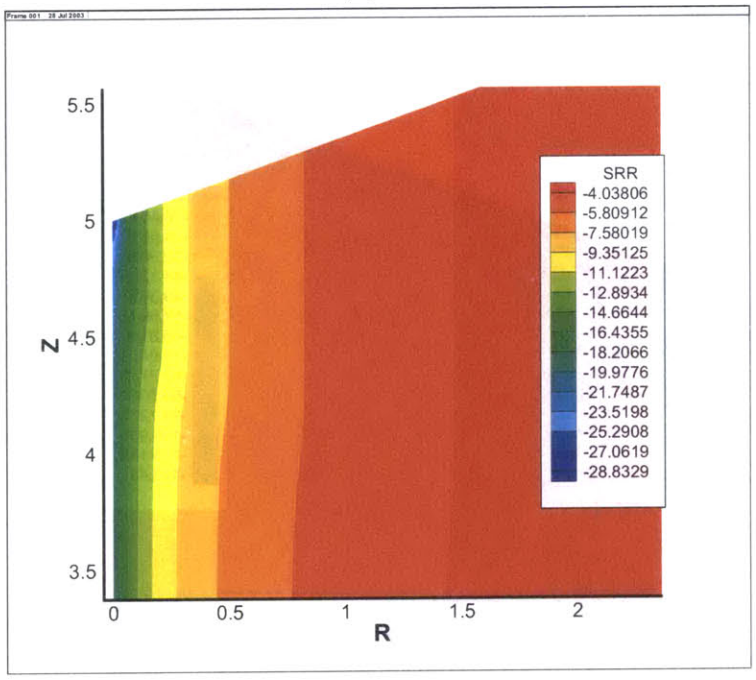

Figure 4-15: (a) Evolution of σ'_{rr}/c below the Berkovich indenter. $\varphi = 20°$. (b) Evolution of σ'_{rr}/c below the Berkovich indenter. $\varphi = 10°$. [stresses normalized by the cohesion].

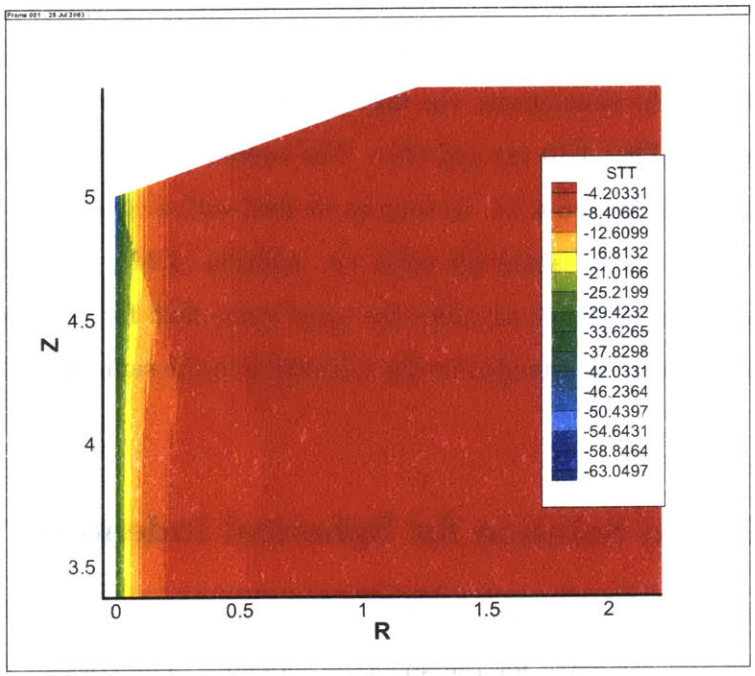

(a)

(b)

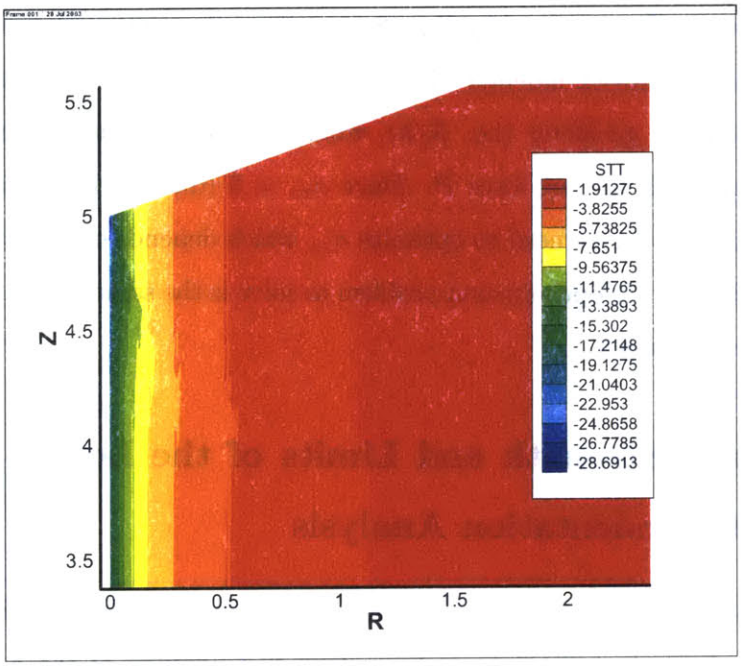

Figure 4-16: (a) Evolution of $\sigma'_{\theta\theta}/c$ below the Berkovich indenter. $\varphi = 20°$. (b) Evolution of $\sigma'_{\theta\theta}/c$ below the Berkovich indenter. $\varphi = 10°$. [stresses normalized by the cohesion].

this lower bound approach is independent of the apex angle.

Figure 4-17 (a) to 4-18 (b) show the optimized stress field for cones of semi-apex angle 15° and 45° for $\varphi = 30°$. In the simulations, the fineness of the meshes is comparable to the one previously employed (see Fig. 4-10 (a) and (b)). The results can be understood if we follow the reasoning developed in Section 4.2.1: as soon as we deal with a cone (i.e. not a flat punch), there is an additional constraint along the cone, i.e. relation (4.24). Once this constraint is satisfied, the optimization procedure provides the same stress field for any apex angle smaller than 90°, this stress field can be extended in the z direction in the same way irrespective of the apex angle.

4.4 Lower Bound Solution for Spherical Indenters

The last indenter geometry we consider is the spherical indenter. Figure 4-19 presents the boundary conditions and geometry for the spherical indenter. The contact is assumed to be frictionless as defined by (4.24). The optimized stress field turns out to be very similar to the one of the conical indenter (compare Fig. 4-20 (a) and (b) with Fig. 4-13). Furthermore, the dimensionless parameter $\frac{H'}{c}$ as defined by Eq. (2.11) follows the same evolution with respect to φ as in the case of the Berkovich indenter. The lower bound approach, therefore, appears to be insensitive to the indenter geometry (i.e. R/h), which can be explained in the following way: the goal is to optimize the driving force P. Since $\sigma_{rz} = 0$ (due to the frictionless boundary conditions, cf. Section 4.1.2), we need to optimize σ_{zz} which depends only on r. From a purely mathematical standpoint, the optimization problem to solve is the same for all shape geometries that differ from the flat punch.

4.5 Summary: Strength and Limits of the Lower Bound Approach for Indentation Analysis

The computational mechanics approach developed in the last two Chapters provides a rational means to construct lower bound solutions for indentation analysis of the hardness-cohesion-friction angle relation (2.11). The main characteristics of all lower bound solutions relate to the contact conditions between indenter and material:

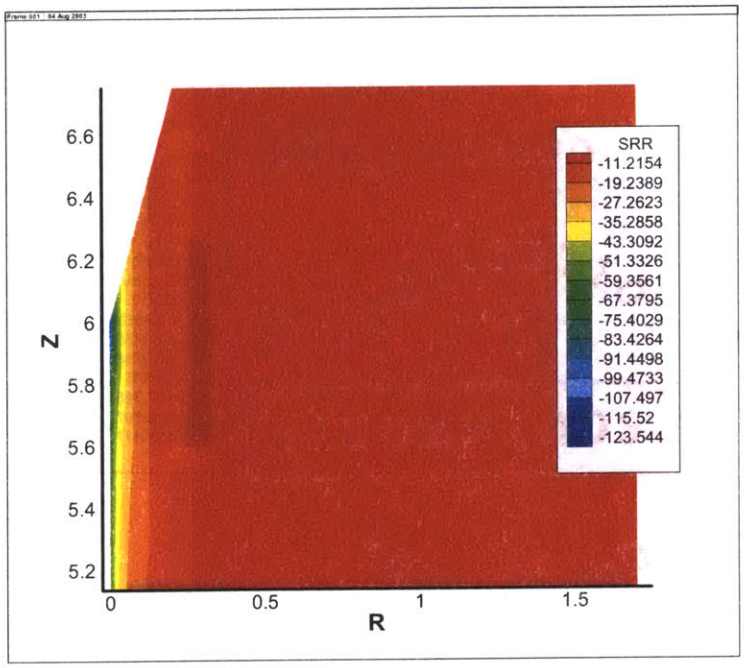

(a)

(b)

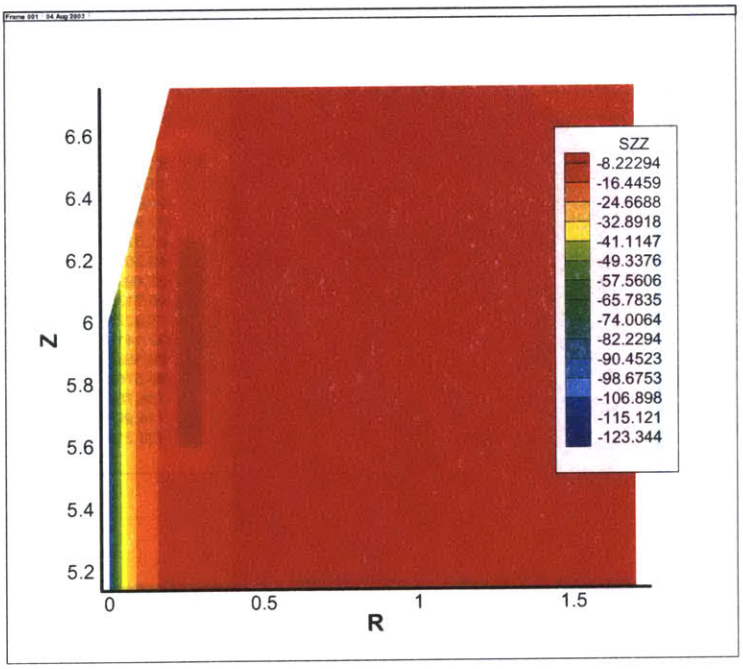

Figure 4-17: (a) Evolution of σ'_{rr}/c below a sharp indenter. ($i = 15°$, $\varphi = 30°$). (b) Evolution of σ'_{zz}/c below a sharp indenter. ($i = 15°$, $\varphi = 30°$). [stresses normalized by the cohesion].

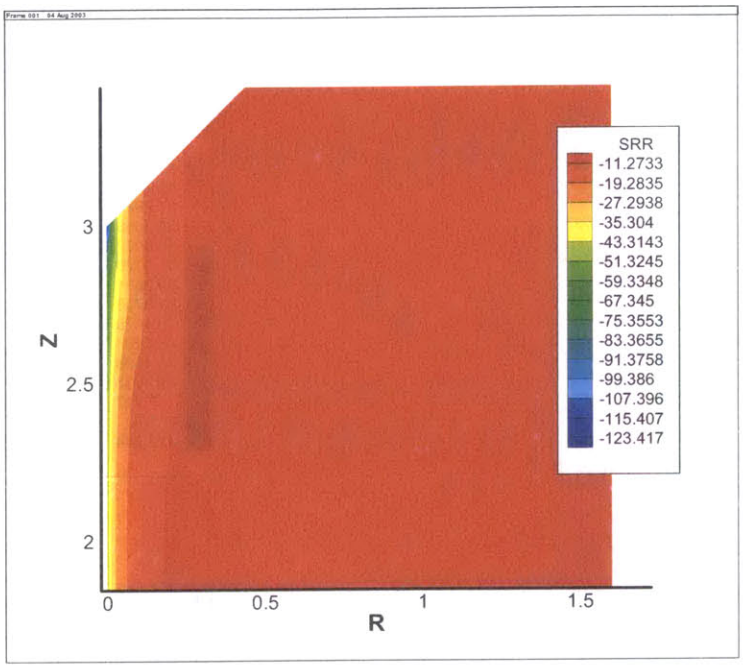

(a)

(b)

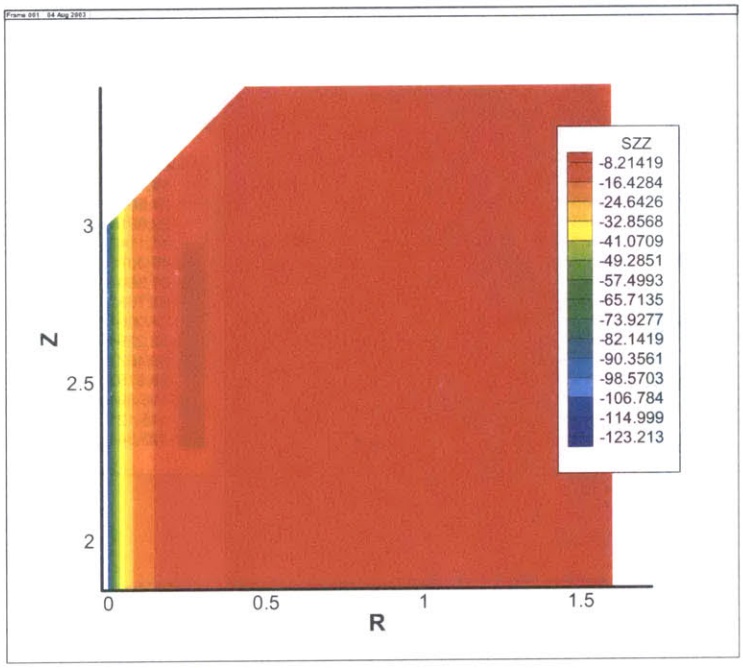

Figure 4-18: (a) Evolution of σ'_{rr}/c ($i = 45°$, $\varphi = 30°$). (b) Evolution of σ'_{zz}/c ($i = 45°$, $\varphi = 30°$). [stresses normalized by the cohesion].

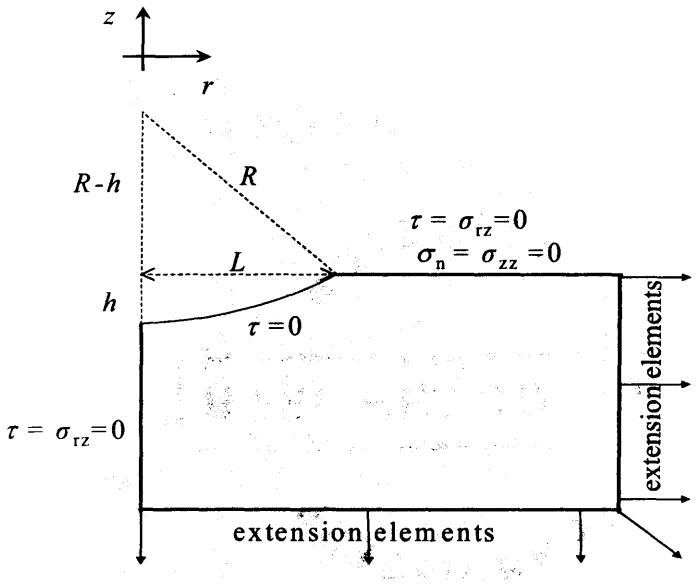

Figure 4-19: Boundary condition for a spherical indenter. L is related to R (indenter radius) and h through: $L = (2Rh - h^2)^{1/2}$.

- A smooth indenter yields higher hardness values than a rough indenter.
- A perfectly frictionless contact condition makes the lower bound solution insensitive to the indenter geometry (apex angle, conical or spherical indenter).
- For a perfectly rough cone, all lower bound solutions reduce to the flat punch solution, and are therefore insensitive to the indenter geometry.

These results are quite restrictive and highlight the limitations of the lower bound approach: the stress fields are mathematically obtained optimization results; and while mathematically correct, they may well lack physical significance. One example is the independence of σ_{zz} of z in the lower bound solution. This independence is clearly a consequence of the (linear) discretization and the boundary conditions, but is far from the "real" stress field expected below an indenter (see Fig. 2-1). Wether the found characteristics of the lower bound solutions are relevant or not will be confirmed by the upper bound solutions, which is the focus of the following Chapters.

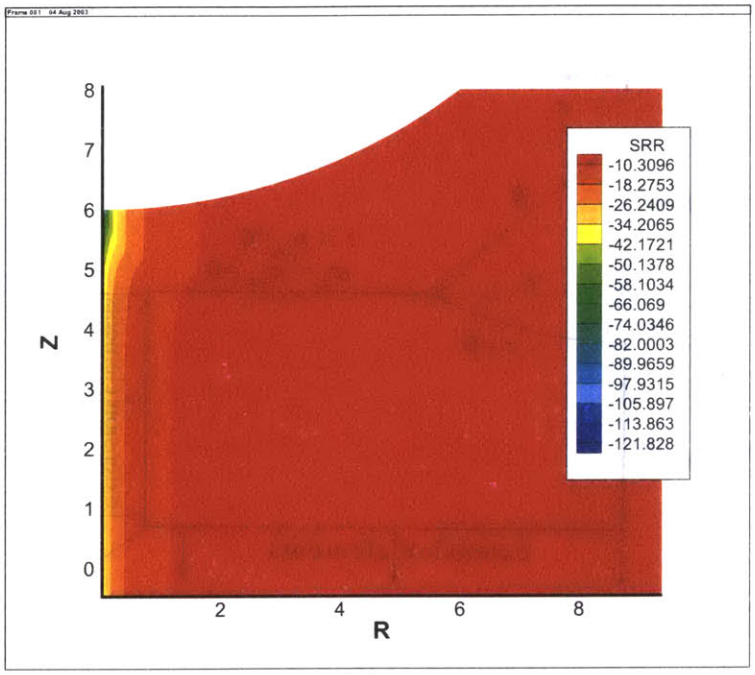

(a)

(b)

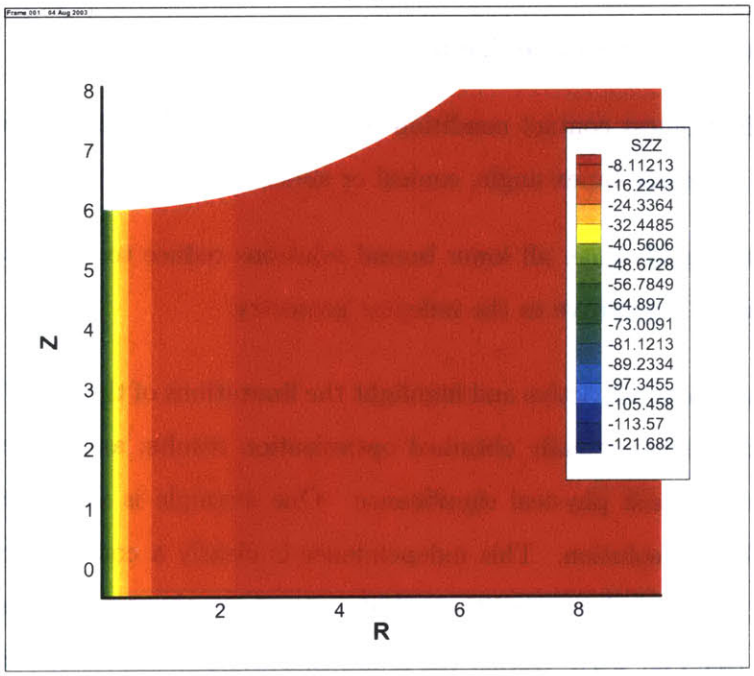

Figure 4-20: (a) Evolution of σ_{rr}/c below a spherical indenter (φ=30°). (b) Evolution of σ_{zz}/c below a spherical indenter (φ=30°). [stresses normalized by the cohesion].

Chapter 5

Formulation of Upper Bound Limit Analysis Using Finite Elements and Linear Programming: Axisymmetric Case

This and the next Chapter deal with the formulation and implementation of the upper bound theorem of yield design for indentation analysis on cohesive-frictional materials in axisymmetric conditions. The formulation presented in this Chapter is analogous to the lower bound formulation developed in Chapter 3. It uses finite element interpolation, evaluation of the dissipation functions and linearization of the "finite dissipation condition". The material is discretized into 3-noded triangular elements, with two nodal velocities at each node, and surfaces of discontinuity along the edges between two adjacent elements. The upper bound formulation leads to a linear programming problem whose objective function is the externally applied load (to be minimized) subject to the constraint of kinematic admissibility.

5.1 Theoretical Background

5.1.1 Upper Bound Limit Theorem

In contrast to the lower bound theorem (see Section 3.1.1), the upper bound theorem approaches the actual dissipation capacity at plastic collapse (3.1) through kinematically and plastically admissible velocity fields. These are velocity fields which:

- respect the velocity boundary conditions[1]:

$$\text{on } \partial\Omega_{\mathbf{V}^d} : \mathbf{V}^d = \mathbf{0} \tag{5.1}$$

- are compatible with the plastic flow rule of the material at plastic collapse.

In this case, it can be shown, through application of the principle of maximum plastic work (see [87] Chapter 9 for a more detailed presentation), that any kinematically and plastically admissible velocity field provides an upper bound for the actual dissipation capacity (3.1), that is:

$$\mathbf{Q}^{\lim} \cdot \mathbf{q} \leq \int_{\Omega} \boldsymbol{\sigma} : \mathbf{d}' \, d\Omega \; + \; \int_{\Gamma} \mathbf{T} : [[\mathbf{V}']] \, d\Gamma \tag{5.2}$$

where $\mathbf{d}'$ is the plastic strain rate tensor,

$$\mathbf{d}'(\mathbf{x}) = \frac{1}{2} \left(\operatorname{grad} \mathbf{V}'(\mathbf{x}) + {}^{t} \operatorname{grad} \mathbf{V}'(\mathbf{x}) \right) \tag{5.3}$$

which -at plastic failure- is defined by the flow rule

$$\mathbf{d}'(\mathbf{x}) = \dot{\lambda} \frac{\partial f}{\partial \boldsymbol{\sigma}'(\mathbf{x})}; \; \dot{\lambda} \geq 0; \; f \leq 0; \; \dot{\lambda} f = 0 \tag{5.4}$$

where $\dot{\lambda}$ is the plastic multiplier, and f the yield function. Analogously, the velocity jump $[[\mathbf{V}']]$ in (5.2) is defined by a flow rule

$$[[\mathbf{V}']] = \dot{\lambda} \frac{\partial f}{\partial \mathbf{T}}; \; \dot{\lambda} \geq 0; \; f \leq 0; \; \dot{\lambda} f = 0 \tag{5.5}$$

[1] It is useful to recall that the only meaningful velocity boundary condition at plastic failure are nullity conditions. In fact, any other non-zero velocity boundary condition would be in contradiction with the very notion of plastic collapse, that is an uncontrolled (i.e. spontaneous) indefinite yield.

where $\mathbf{T}$ is the stress vector.

For a given yield surface, the flow rule (5.4) (respectively (5.5)) establishes a unique relation between the stress tensor $\boldsymbol{\sigma}$ (respectively stress vector $\mathbf{T}$) and the strain rate tensor $\mathbf{d}'$ (respectively velocity jump $[[\mathbf{V}']]$), so that the dissipation rate can be expressed as a function of $\mathbf{d}'$ (respectively $[[\mathbf{V}']]$) only. The upper bound estimate of the dissipation capacity (right hand side of (5.2)) therefore is a function of $\mathbf{V}'$ only. These functions are referred to as dissipation functions, denoted by Φ_Ω and Φ_Γ respectively:

$$\Phi_\Omega(\mathbf{d}') = \boldsymbol{\sigma} : \mathbf{d}' \; ; \; \Phi_\Gamma([[\mathbf{V}']]) = \mathbf{T} : [[\mathbf{V}']] \tag{5.6}$$

The dissipation functions express the maximum capacity of the material to dissipate the externally supplied energy at plastic collapse into the form of heat. Since the stress tensor $\boldsymbol{\sigma}$ (resp. the stress vector $\mathbf{T}$) is not bound to satisfy the equilibrium condition, it is associated with a limit load that surely leads to failure.

The results can be summarized in form of the Upper Limit Theorem.

Theorem 2 *Any kinematically velocity field $\mathbf{V}'$ delivers an upper bound $\frac{d\mathcal{D}}{dt}(\mathbf{V}')$ to the actual dissipation rate the limit load $\mathbf{Q}^{\lim}$ realizes along the actual velocity field $\mathbf{q}$:*

$$\mathbf{Q}^{\lim} \cdot \mathbf{q} = \min_{on\ \partial\Omega_{\mathbf{V}^d}:\mathbf{V}'=\mathbf{V}^d\equiv 0} \left[\frac{d\mathcal{D}}{dt}(\mathbf{V}')\right] \tag{5.7a}$$

The dissipation rate $\frac{d\mathcal{D}}{dt}(\mathbf{V}')$ is the maximum dissipation the material can afford, dissipating energy in the material bulk and along surfaces of discontinuity into heat form:

$$\frac{d\mathcal{D}}{dt}(\mathbf{V}') = \int_\Omega \max\left[\Phi_\Omega(\mathbf{d}')\right] d\Omega \; + \; \int_\Gamma \max\left[\Phi_\Gamma([[\mathbf{V}']])\right] d\Gamma \tag{5.8}$$

where Φ_Ω and Φ_Γ are the dissipation functions.

5.1.2 Dissipation Functions and Finite Dissipation Conditions for the Mohr-Coulomb Material

The Mohr-Coulomb yield criterion reads:

$$F = \sigma_I(1+\sin(\varphi)) - \sigma_{III}(1-\sin(\varphi)) - 2c\cos(\varphi) \leqslant 0 \tag{5.9}$$

where $\sigma_I \geq \sigma_{II} \geq \sigma_{III}$ are the principal stresses.

Differentiating with respect to $\boldsymbol{\sigma}'(\mathbf{x})$ and using the flow rule (5.4) (see [72] Chapter 1 for details) yields (after some calculations) the sought dissipation functions. The volume dissipation function reads:

$$\Phi_\Omega(\mathbf{d}') = \left\{ \begin{array}{ll} \rho tr(\mathbf{d}') & \text{if } tr(\mathbf{d}') \geq [|d'_I| + |d'_{II}| + |d'_{III}|]\sin(\varphi) \\ +\infty & \text{if } tr(\mathbf{d}') < [|d'_I| + |d'_{II}| + |d'_{III}|]\sin(\varphi) \end{array} \right\} \tag{5.10}$$

where $\mathbf{d}'$ is the strain rate tensor, $d'_I \geq d'_{II} \geq d'_{III}$ the principal strain rates, $\rho = c\cot(\varphi)$; and the discontinuity dissipation function reads:

$$\Phi_\Gamma([[\mathbf{V}']]) = \left\{ \begin{array}{ll} c|[[V_t]]| & \text{if } [[V_n]] \geqslant |[[V_t]]|\tan(\varphi) \\ +\infty & \text{if } [[V_n]] < |[[V_t]]|\tan(\varphi) \end{array} \right\} \tag{5.11}$$

where $[[V_n]]$ and $[[V_t]]$ are respectively the normal and tangential velocity jump.

5.1.3 Limits and Shortcomings

An accurate estimation of the upper bound is very difficult to obtain in cases where the material dilates at failure (which is the case of many frictional materials like shales). Conventional analyses, which assume rigid block mechanisms, do not represent correctly the volume change of these dilating materials and hence do not fully satisfy the requirements of the upper bound theorem. Considering the difficulty of finding a correct velocity field, the need of an efficient numerical method becomes apparent, which motivates the forthcoming development of a robust numerical approach for computing the upper bound.

5.2 Upper Bound Theorem Discretization

5.2.1 Historical Background

General formulations of the upper bound theorem, which use finite elements and linear programming techniques emerged in the early 70s and 80s. We cite the work of Anderheggen and Knöpfel [3], Fremond and Salençon [27], Turgeman [84], Bottero et al. [8]. Anderheggen and Knöpfel [3] proposed a mixed formulation for bounded continua based on the linearization of the plasticity criterion. Fremond and Salençon [27] solved geotechnical problems using a non-linear optimization method. Following this work, Turgeman [84] proposed a kinematical method based on the linearization of the criterion, which was independently obtained by Capurso [13]. Bottero et al. [8] generalized the method of Anderheggen and Knöpfel to include velocity discontinuities in plane strain limit analysis. Although it constituted an important extension, Bottero et al.'s formulation has the disadvantage that the directions of shear must be *a priori* specified for each discontinuity. This precludes the use of a large number of discontinuities in an arbitrary arrangement, since it is generally not possible to determine these directions so that the mode of failure is kinematically admissible. More recently, in 1995, a new formulation that permits large number of velocity discontinuities has been derived by Sloan and Kleeman [77]. This method employs linear three-noded triangular elements, and velocity discontinuities may occur at any edge that is shared by a pair of adjacent triangles. The orientation of the shear is chosen automatically during the optimization process so to minimize the rate of dissipated energy, that is (5.7a). In addition, we should again mention that Sloan and Abbo are currently (November 2003) developing a 3-D software for the lower and upper bound based on non-linear programming and a different yield criterion [56] [57] (cf. Section 3.2.1).

Our implementation uses the same concept as the lower bound formulation; the material is discretized into 3-noded triangular elements whose nodal variables are the unknown nodal velocities. In contrast to Sloan and Kleeman's approach [77], the kinematically admissible velocity field is defined by the boundary condition constraints (5.1) and the "finite dissipation-function" conditions derived in Section 5.1.2. Furthermore, the implementation considers the axisymmetric case which, to our knowledge, has not been developed in details in previous works.

5.2.2 Finite Elements Discretization

In the (r, z) plane the material is discretized in 3-noded triangular elements, with radial and axial velocity as nodal unknowns (see Fig. 5-1). The velocities are assumed to vary linearly

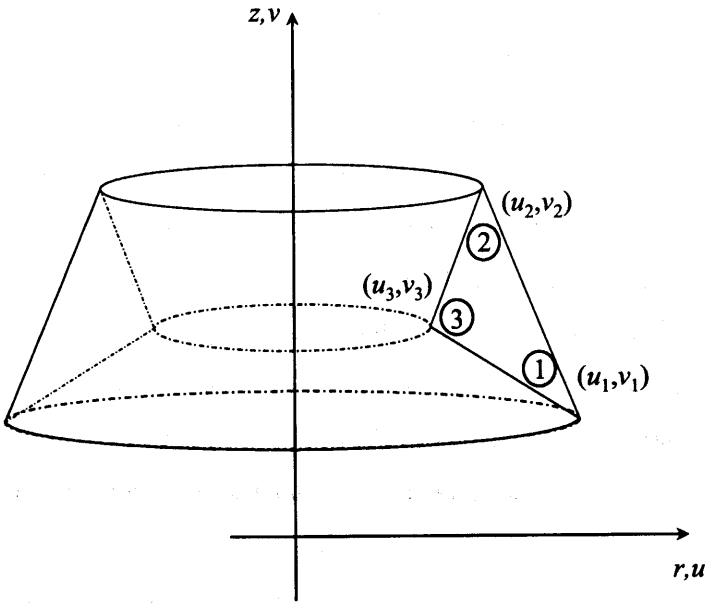

Figure 5-1: 3-noded triangular element (upper bound).

within each element according to:

$$u = \sum_{k=1}^{3} N_k(r,z)u_i \tag{5.12}$$

$$v = \sum_{k=1}^{3} N_k(r,z)v_i \tag{5.13}$$

where u is the radial velocity and v the vertical one. Indeed the problem (loading and geometry) being θ-invariant $v_\theta = 0$. The shape function are still given by (3.16) to (3.18).

Plastic deformation may occur not only within triangles, but also in the velocity discontinuities along edges between elements. Kinematically admissible velocity discontinuities are permitted along all edges shared by adjacent triangles, and are modeled by assuming that each node is unique to its element. We have employed the same discretization strategy as in the

lower bound approach (see Section 3.2.2).

5.2.3 Constraints From Velocity Boundary Conditions

To enforce prescribed boundary conditions, it is necessary to impose equality constraints on the nodal velocities. Consider a node i on the boundary where the radial and axial velocities are (u_p, v_p), then it is sufficient to enforce

$$u_i = u_p \tag{5.14}$$

$$u_i = u_p \tag{5.15}$$

This can be written as:

$$[A_1]\,[X] = [B_1] \tag{5.16}$$

where

$$[A_1] = \begin{bmatrix} 1 & 0 \\ 0 & 1 \end{bmatrix} \tag{5.17}$$

$$[B_1]^T = [u_p, v_p] \tag{5.18}$$

$$[X]^T = [u_i, v_i] \tag{5.19}$$

Following the yield design theorem (see Section 5.1.1), the only velocity boundary condition that can be prescribed is the zero velocity boundary on $\partial\Omega_{\mathbf{V}^d}$. Hence $[B_1]^T = [0, 0]$

5.2.4 Constraints Due to the Finite Surface Dissipation Condition Along Velocity Discontinuities

A typical stress discontinuity between adjacent elements is shown in Figure 5-2. It is defined by the nodal pairs (1,2) and (3,4), for which the nodes in each pair share the same coordinates.

A velocity discontinuity is plastically admissible for a Mohr-Coulomb yield criterion if the normal and tangential velocity jumps $[[V_n]]$ and $[[V_t]]$ satisfy (5.11) (cf. Section 5.1.2):

$$[[V_n]] \geqslant |[[V_t]]| \tan(\varphi) \tag{5.20}$$

Considering the nodal pair (i, j), the velocity jump in any direction defined with respect to

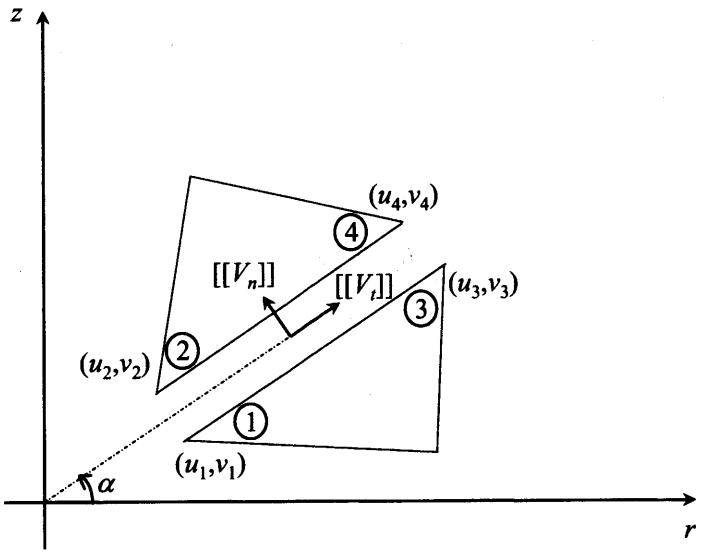

Figure 5-2: Velocity discontinuity.

node i is equal to the velocity of node j minus the velocity of node i for the same direction. Therefore, the normal and tangential velocity jump of the nodal pair (i, j) read:

$$[[V_n^{(i,j)}]] = -\sin(\alpha)(u_j - u_i) + \cos(\alpha)(v_j - v_i) \tag{5.21}$$

$$[[V_t^{(i,j)}]] = \cos(\alpha)(u_j - u_i) + \sin(\alpha)(v_j - v_i) \tag{5.22}$$

Relation (5.22) shows that the tangential jump $[[V_t^{(i,j)}]]$ can be either positive or negative. From a linear programming point of view this is referred to as an unrestricted in sign variable. Since any unrestricted variable can be decomposed into the difference of two non-negative variables, $[[V_t^{(i,j)}]]$ can be written as:

$$[[V_t^{(i,j)}]] = V_{t+}^{(i,j)} - V_{t-}^{(i,j)} \tag{5.23}$$

with the constraints

$$V_{t+}^{(i,j)} \geq 0 \tag{5.24}$$

$$V_{t-}^{(i,j)} \geq 0 \tag{5.25}$$

Since relations (5.23) to (5.25) are applied to the tangential velocity jump at both ends of the discontinuity, they also hold for the jump occurring at all points along the discontinuity:

$$[[V_t]] = V_{t+} - V_{t-} \tag{5.26}$$

with the constraints

$$V_{t+} \geq 0 \tag{5.27}$$

$$V_{t-} \geq 0 \tag{5.28}$$

Each decomposition of the tangential velocity jump generates two additional unknowns (Fig. 5-3). Therefore for each discontinuity there are four unknowns, namely $V_{t+}^{(1,2)}$, $V_{t-}^{(1,2)}$, $V_{t+}^{(3,4)}$, $V_{t-}^{(3,4)}$. Substituting (5.23) in (5.22) gives:

$$V_{t+}^{(i,j)} - V_{t-}^{(i,j)} = \cos(\alpha)(u_j - u_i) + \sin(\alpha)(v_j - v_i) \tag{5.29}$$

$$V_{t+}^{(i,j)} \geq 0 \tag{5.30}$$

$$V_{t-}^{(i,j)} \geq 0 \tag{5.31}$$

On the other hand, the absolute sign in relation (5.20) prevents the upper bound method to be implemented as a linear programming problem. Therefore, in order to preserve the structure of the linear programming problem, the absolute sign has to be eliminated. This can be achieved by substituting for $|[[V_t]]|$

$$|[[V_t]]| = V_{t+} + V_{t-} \tag{5.32}$$

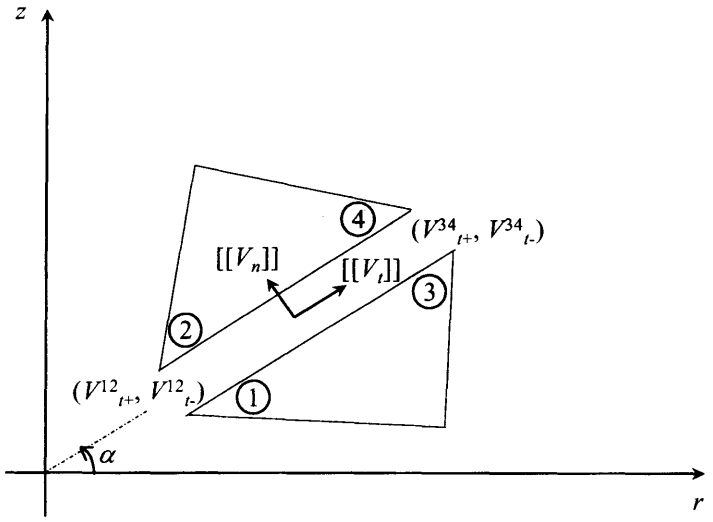

Figure 5-3: Variables for velocity discontinuity.

It is readily understood that (5.32) would be inexact if V_{t+} and V_{t-} were positive simultaneously. Thus the correct equality is satisfied only if either $V_{t+} = 0$ or $V_{t-} = 0$ at both end nodes of the discontinuity. Fortunately, it turns out that by replacing $|[[V_t]]|$ by $V_{t+} + V_{t-}$ and decomposing $[[V_t]]$ in $V_{t+} - V_{t-}$, where V_{t+} and V_{t-} are positive, the upper bound solution always gives either $V_{t+} = 0$ or $V_{t-} = 0$, thus the correct sign rule is always satisfied. This key result from [85] is proven in Appendix C.

Using (5.32), the finite dissipation condition (5.20) becomes:

$$[[V_n]] \geqslant (V_{t+} + V_{t-}) \tan(\varphi) \tag{5.33}$$

which must be enforced at both nodal pairs of the discontinuity element. For a surface of discontinuity along the edges of two triangular elements, the velocity jump constraints can be

rewritten in matrix form as:

$$[A_{21}]\,[X] - [A_{22}]\left[\tilde{X}\right] = [0] \tag{5.34}$$

$$\left[A'_{21}\right]\,[X] - \left[A'_{22}\right]\left[\tilde{X}\right] \geq [0] \tag{5.35}$$

$$\left[\tilde{X}\right] \geq [0] \tag{5.36}$$

where

$$[A_{21}] = \begin{bmatrix} [R] & 0 \\ 0 & [R] \end{bmatrix} \tag{5.37}$$

$$[R] = \begin{bmatrix} -\cos(\alpha) & -\sin(\alpha) & \cos(\alpha) & \sin(\alpha) \end{bmatrix} \tag{5.38}$$

$$\left[A'_{21}\right] = \begin{bmatrix} [R'] & 0 \\ 0 & [R'] \end{bmatrix} \tag{5.39}$$

$$\left[R'\right] = \begin{bmatrix} \sin(\alpha) & -\cos(\alpha) & -\sin(\alpha) & \cos(\alpha) \end{bmatrix} \tag{5.40}$$

$$[X]^T = [u_1, v_1, u_2, v_2, u_3, v_3, u_4, v_4] \tag{5.41}$$

and

$$[A_{22}] = \begin{bmatrix} 1 & -1 & 0 & 0 \\ 0 & 0 & 1 & -1 \end{bmatrix} \tag{5.42}$$

$$\left[A'_{22}\right] = \begin{bmatrix} \tan(\varphi) & \tan(\varphi) & 0 & 0 \\ 0 & 0 & \tan(\varphi) & \tan(\varphi) \end{bmatrix} \tag{5.43}$$

$$\left[\tilde{X}\right]^T = [V^{12}_{t+}, V^{12}_{t-}, V^{34}_{t+}, V^{34}_{t-}] \tag{5.44}$$

Each discontinuity thus gives rise to a total of 2 inequality and 6 equality constraints.

5.2.5 Constraints Due to the "Finite Volume Dissipation Function" in Solid Elements

The energy rate dissipated within an element is finite provided that relation (5.10) is satisfied (see Section 5.1.2), that is:

$$tr(\mathbf{d}') \geq [|d'_I| + |d'_{II}| + |d'_{III}|] \sin(\varphi) \tag{5.45}$$

where $\mathbf{d}'$ is the strain rate tensor and $d'_I \geq d'_{II} \geq d'_{III}$ are the principal strain rates. In cylindrical coordinates,the components of $\mathbf{d}'$ read (application of (5.3)):

$$\mathbf{d}' = \begin{bmatrix} \frac{\partial u}{\partial r} & 0 & \frac{1}{2}\left(\frac{\partial u}{\partial z} + \frac{\partial v}{\partial r}\right) \\ 0 & \frac{u}{r} & 0 \\ \frac{1}{2}\left(\frac{\partial u}{\partial z} + \frac{\partial v}{\partial r}\right) & 0 & \frac{\partial v}{\partial z} \end{bmatrix} \tag{5.46}$$

The principal strain rates of (5.46) read:

$$d'_{\theta\theta} = \frac{u}{r},\ d'_{+} = \frac{1}{2}\left(\frac{\partial u}{\partial r} + \frac{\partial v}{\partial z}\right) + \frac{1}{2}Rad \text{ and } d'_{-} = \frac{1}{2}\left(\frac{\partial u}{\partial r} + \frac{\partial v}{\partial z}\right) - \frac{1}{2}Rad \tag{5.47}$$

where

$$Rad = \sqrt{\left(\frac{\partial u}{\partial r} - \frac{\partial v}{\partial z}\right)^2 + \left(\frac{\partial u}{\partial z} + \frac{\partial v}{\partial r}\right)^2} \tag{5.48}$$

Furthermore, we have:

$$tr(\mathbf{d}') = \frac{u}{r} + \frac{\partial u}{\partial r} + \frac{\partial v}{\partial z} \tag{5.49}$$

The absolute sign in relation (5.45) prevents the upper bound method to be implemented as a linear programming problem. In order to preserve the linear programming problem structure we must get rid of the absolute values in (5.45).

Since $d'_+ \geqslant d'_-$, inequality (5.45) is equivalent to the combination of:

$$tr(\mathbf{d}') \geq [d'_+ + d'_- + \frac{u}{r}]\sin(\varphi) \quad \text{(i.e. } d'_+,\ d'_-,\ u \geq 0) \tag{5.50}$$

$$tr(\mathbf{d}') \geq [-d'_+ - d'_- + \frac{u}{r}]\sin(\varphi) \quad \text{(i.e. } d'_+,\ d'_- \leq 0,\ u \geq 0) \tag{5.51}$$

$$tr(\mathbf{d}') \geq [-d'_+ - d'_- - \frac{u}{r}]\sin(\varphi) \quad \text{(i.e. } d'_+,\ d'_- \leq 0,\ u \leq 0) \tag{5.52}$$

$$tr(\mathbf{d}') \geq [d'_+ + d'_- - \frac{u}{r}]\sin(\varphi) \quad \text{(i.e. } d'_+,\ d'_-,\ u \leq 0) \tag{5.53}$$

$$tr(\mathbf{d}') \geq [d'_+ - d'_- + \frac{u}{r}]\sin(\varphi) \quad \text{(i.e. } d'_+,\ u \geq 0,\ d'_- \leq 0) \tag{5.54}$$

$$tr(\mathbf{d}') \geq [d'_+ - d'_- - \frac{u}{r}]\sin(\varphi) \quad \text{(i.e. } d'_+,\ u \geq 0,\ d'_- \leq 0) \tag{5.55}$$

Substituting (5.47), (5.48) and (5.49) in (5.50) yields:

$$\frac{u}{r} + \frac{\partial u}{\partial r} + \frac{\partial v}{\partial z} \geq 0 \text{ within every triangle} \tag{5.56}$$

This inequality is satisfied in a triangle provided that the following conditions are satisfied at each node i (this original result is proven in Appendix D):

$$\text{if } r_i > 0: \ \frac{u_i}{r_i} + \sum_{k=1}^{3} \frac{\partial N_k(r,z)}{\partial r} u_k + \sum_{k=1}^{3} \frac{\partial N_k(r,z)}{\partial z} v_k \geq 0 \tag{5.57}$$

$$\text{if } r_i = 0: \ \sum_{k=1}^{3} \frac{\partial N_k(r,z)}{\partial r} u_k + \sum_{k=1}^{3} \frac{\partial N_k(r,z)}{\partial z} v_k \geq 0 \tag{5.58}$$

Similarly, (5.51) yields:

$$\text{if } r_i > 0: \ \frac{u_i}{r_i}\frac{1-\sin(\varphi)}{1+\sin(\varphi)} + \sum_{k=1}^{3} \frac{\partial N_k(r,z)}{\partial r} u_k + \sum_{k=1}^{3} \frac{\partial N_k(r,z)}{\partial z} v_k \geq 0 \tag{5.59}$$

$$\text{if } r_i = 0: \ \sum_{k=1}^{3} \frac{\partial N_k(r,z)}{\partial r} u_k + \sum_{k=1}^{3} \frac{\partial N_k(r,z)}{\partial z} v_k \geq 0 \tag{5.60}$$

Similar conditions can be derived for (5.52), which is equivalent to (5.50) since $sin(\varphi) \in [0, 1[$.

Following the same pattern, (5.53) becomes:

$$\text{if } r_i > 0: \frac{u_i}{r_i}\frac{1+\sin(\varphi)}{1-\sin(\varphi)} + \sum_{k=1}^{3}\frac{\partial N_k(r,z)}{\partial r}u_k + \sum_{k=1}^{3}\frac{\partial N_k(r,z)}{\partial z}v_k \geq 0 \tag{5.61}$$

$$\text{if } r_i = 0: \sum_{k=1}^{3}\frac{\partial N_k(r,z)}{\partial r}u_k + \sum_{k=1}^{3}\frac{\partial N_k(r,z)}{\partial z}v_k \geq 0 \tag{5.62}$$

The last two inequations are somehow more complicated to deal with since $d'_+ - d'_- = Rad$ given by (5.48), which is a non linear term. In order to linearize this term we employ the same method as presented in Section 3.2.6. Relation (5.54) yields:

$$Rad \leq R_5 \tag{5.63}$$

with

$$\text{if } r_i > 0: R_5 = \frac{u_i}{r_i}\left(\frac{1}{\sin(\varphi)} - 1\right) + \left(\sum_{k=1}^{3}\frac{\partial N_k(r,z)}{\partial r}u_k + \sum_{k=1}^{3}\frac{\partial N_k(r,z)}{\partial z}v_k\right)\frac{1}{\sin(\varphi)} \tag{5.64}$$

$$\text{if } r_i = 0: R_5 = \left(\sum_{k=1}^{3}\frac{\partial N_k(r,z)}{\partial r}u_k + \sum_{k=1}^{3}\frac{\partial N_k(r,z)}{\partial z}v_k\right)\frac{1}{\sin(\varphi)} \tag{5.65}$$

Analogously, relation (5.55) yields:

$$Rad \leq R_6 \tag{5.66}$$

with

$$\text{if } r_i > 0: R_6 = \frac{u_i}{r_i}\left(\frac{1}{\sin(\varphi)} + 1\right) + \left(\sum_{k=1}^{3}\frac{\partial N_k(r,z)}{\partial r}u_k + \sum_{k=1}^{3}\frac{\partial N_k(r,z)}{\partial z}v_k\right)\frac{1}{\sin(\varphi)} \tag{5.67}$$

$$\text{if } r_i = 0: R_6 = \left(\sum_{k=1}^{3}\frac{\partial N_k(r,z)}{\partial r}u_k + \sum_{k=1}^{3}\frac{\partial N_k(r,z)}{\partial z}v_k\right)\frac{1}{\sin(\varphi)} \tag{5.68}$$

The inequalities (5.54) and (5.55) can be rewritten as:

$$\left\{\begin{array}{c} X^2 + Y^2 \leqslant R_i^2 \\ R_i \geqslant 0 \end{array}\right\} \tag{5.69}$$

where

$$X = \frac{\partial u}{\partial r} - \frac{\partial v}{\partial z} \text{ and } Y = \frac{\partial u}{\partial z} + \frac{\partial v}{\partial r} \tag{5.70}$$

In the (X, Y) plane, the inequalities (5.69) represent two circles of radius R_i.

To rigorously satisfy these inequalities, each point must lie inside the circle. Following the development in Section 3.2.6 we replace the circle by an inscribed polygon with p sides. This allows us to express the finite dissipation function inequations (5.54) and (5.55) as a series of linear inequalities. The coordinates for the k^{th} and $k^{th}+1$ points (see Fig. 5-4 which shows a six-sided approximation) are given by:

$$X_k = R\cos(\pi(2k-1)/p) \; ; \; Y_k = R\sin(\pi(2k-1)/p) \tag{5.71}$$

$$X_{k+1} = R\cos(\pi(2k+1)/p) \; ; \; Y_{k+1} = R\sin(\pi(2k+1)/p) \tag{5.72}$$

Consider a velocity state with coordinates X and Y, the inequality (5.69) is satisfied if:

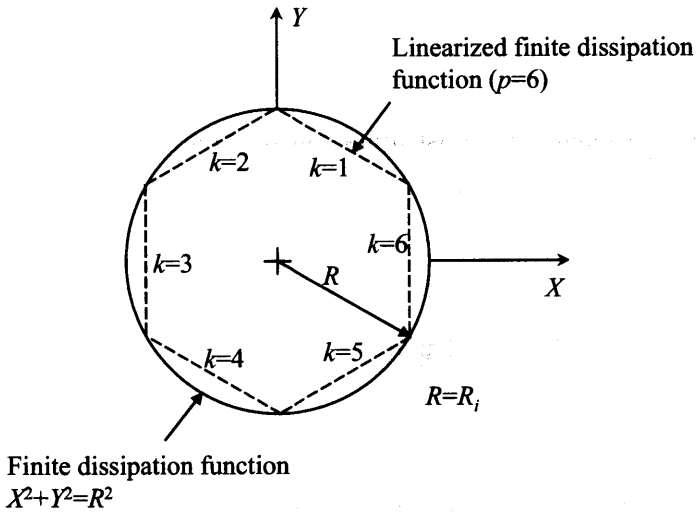

Figure 5-4: Internal linearization of the finite dissipation function.

$$(X_{k+1} - X)(Y_k - Y) - (X_k - X)(Y_{k+1} - Y) \leqslant 0 \; ; \; k = 1, 2..., p \tag{5.73}$$

Substituting (5.71) and (5.72) into (5.73) generates a set of inequality constraints:

$$F_{kl} = \sum_{j=1}^{3} A_{kj} u_j + \sum_{j=1}^{3} B_{kj} v_j \leqslant 0 \ ; \ k = 1, 2..., p; \ l = 1, 2, 3 \text{ (3 nodes)} \tag{5.74}$$

The expressions of A_{kj} and B_{kj} are somewhat lengthy, and are presented in Appendix E.

In summary, for the dissipation function to be finite we need to enforce the four inequations (5.50) to (5.53), and the linearized version of (5.54) and (5.55).

Finally, given the dilatancy behaviour of the Mohr-Coulomb material, it seems meaningful to assume u to be positive for an indentation test; which we confirmed after running a lot of simulations. Thus we only need to enforce inequations (5.50), (5.51) and the linearized version of (5.54), and the constraint $u_i \geqslant 0$ for each node, resulting in a substantial gain in CPU time (almost twice as fast).

5.3 Implementation of the Upper Bound Method as a Linear Optimization Problem

5.3.1 Constraints

All previous equality and inequality constraints can be summarized in the following compact form:

$$[A_1'][u] = [b_1] \tag{5.75}$$

$$[A_2'][u] \leqslant [b_2] \tag{5.76}$$

where

$[A_1']$ assembles the constraint matrices related to the velocity boundary conditions and the velocity jump equalities, i.e. (5.17), (5.37), (5.42),

$[A_2']$ assembles the constraint matrices related to the velocity jump inequalities and the finite dissipation function conditions, i.e., (5.39), (5.44), (5.50), (5.51), the linearized version of (5.54), and the constraint $u_i \geqslant 0$.

$[u]$ is the nodal velocity vector.

5.3.2 Objective Function

The upper bound theorem (5.2) provides an upper bound $\mathbf{Q}^{\lim} \cdot \mathbf{q}'$ of the actual dissipation $\mathbf{Q}^{\lim} \cdot \mathbf{q}$ at failure, by means of a kinematically and plastically admissible velocity field (see Section 5.1.1). Furthermore, this upper bound dissipation rate, that the "real" collapse load $\mathbf{Q}^{\lim}$ realizes along the kinematically admissible velocity $\mathbf{q}'$, is less or equal than the maximum dissipation capacity the material can develop for $\mathbf{V}'$, that is:

$$\mathbf{Q}^{\lim} \cdot \mathbf{q} \leq \mathbf{Q}^{\lim} \cdot \mathbf{q}' \leq \mathbf{Q}' \cdot \mathbf{q}' = \frac{d\mathcal{D}}{dt}(\mathbf{V}') \tag{5.77}$$

where $\mathbf{Q}'$ is the load vector associated with the dissipation capacity $\frac{d\mathcal{D}}{dt}(\mathbf{V}')$ of the material. The nominal value of $\mathbf{Q}'$ is greater than or equal to the actual limit load. Relation (5.77) defines a minimization problem: find the minimum value of $\mathbf{Q}' \cdot \mathbf{q}'$ subjected to the constraints of the kinematically and plastically admissible velocity field; that is:

$$\left\{ \begin{array}{c} \min_{\{\mathbf{u}\}} \left(\mathbf{Q}' \cdot \mathbf{q}' = \frac{d\mathcal{D}}{dt}(\mathbf{u}) \right) \\ \textit{Subject to :} \\ [A_1][u] = [b_1] \\ [A_2][u] \leqslant [b_2] \end{array} \right\} \tag{5.78}$$

The dissipation capacity $\frac{d\mathcal{D}}{dt}(\mathbf{u})$ is defined by the dissipation functions (5.10) and (5.11) (cf. Section 5.1.2). We are left with specifying the implementation of these functions within the context of the linear programming problem.

5.3.3 Discretization of the Dissipation Functions

Within each element, provided that (5.50) to (5.55) are satisfied, the energy rate dissipated reads:

$$\frac{d\mathcal{D}}{dt}(\mathbf{u})_{V_{element}} = \int_{V_{element}} \rho tr(\mathbf{d}') dV \tag{5.79}$$

where $\rho = c/\tan(\varphi)$. Substituting (5.49) in (5.79) yields:

$$\frac{d\mathcal{D}}{dt}(\mathbf{u})_{V_{element}} = \rho \int_{V_{element}} \frac{u}{r} d + \rho \int_{V_{element}} \left(\frac{\partial u}{\partial r} + \frac{\partial v}{\partial z} \right) dV \tag{5.80}$$

Since we use a linear interpolation for the velocity, the second term directly gives $\rho\left(\frac{\partial u}{\partial r}+\frac{\partial v}{\partial z}\right)V_{element}$, $V_{element}$ being the volume of the element. The first term can be rewritten $2\pi\rho\int udrdz$, that is $2\pi\rho u_G A$ with $u_G=\frac{1}{3}[u_1+u_2+u_3]$ and A the triangle area. In matrix form, we have:

$$\frac{d\mathcal{D}}{dt}(\mathbf{u})_{V_{element}}=[c_1]^T[u] \tag{5.81}$$

where

$$[c_1] = \rho\begin{bmatrix} 2\pi A/3+\frac{\partial N_1(r,z)}{\partial r}V_{element} \\ \frac{\partial N_1(r,z)}{\partial z}V_{element} \\ 2\pi A/3+\frac{\partial N_2(r,z)}{\partial r}V_{element} \\ \frac{\partial N_2(r,z)}{\partial z}V_{element} \\ 2\pi A/3+\frac{\partial N_3(r,z)}{\partial r}V_{element} \\ \frac{\partial N_3(r,z)}{\partial z}V_{element} \end{bmatrix} \tag{5.82}$$

$$\text{and } [u]^T = [u_1,v_1,u_2,v_2,u_3,v_3] \tag{5.83}$$

Analogously, the dissipation rate along a discontinuity of length L, as shown in Figure 5-2, is:

$$\frac{d\mathcal{D}}{dt}(\mathbf{u})_\Gamma=\int c|[[V_t]]|dL \tag{5.84}$$

That is

$$\frac{d\mathcal{D}}{dt}(\mathbf{u})_\Gamma=\int c(V_{t+}+V_{t-})dL \tag{5.85}$$

Since the velocity field varies linearly along the discontinuity, we have (cf. Section 3.4.2):

$$V_{t+} = V_{t+}^{12}+\frac{s}{L}(V_{t+}^{34}-V_{t+}^{12}) \tag{5.86}$$

$$V_{t-} = V_{t-}^{12}+\frac{s}{L}(V_{t-}^{34}-V_{t-}^{12}) \tag{5.87}$$

where s is the curvilinear abscissa ($s\in[0,L]$).

Substituting (5.86) and (5.87) into (5.85) yields:

$$\frac{d\mathcal{D}}{dt}(\mathbf{u})_\Gamma=[c_2]^T[u] \tag{5.88}$$

where

$$[c_2] = 2\pi Lc \begin{bmatrix} \frac{r_1}{2} + \frac{r_3 - r_1}{6} \\ \frac{r_1}{2} + \frac{r_3 - r_1}{6} \\ \frac{r_1}{2} + \frac{r_3 - r_1}{3} \\ \frac{r_1}{2} + \frac{r_3 - r_1}{3} \end{bmatrix} \tag{5.89}$$

$$\text{and } [u]^T = [V_{t+}^{12},\ V_{t-}^{12},\ V_{t+}^{34},\ V_{t-}^{34}] \tag{5.90}$$

Assembling all the dissipation rate contributions of the triangular elements and the surfaces of discontinuity yields the total dissipation capacity the material can afford:

$$\mathbf{Q}' \cdot \mathbf{q}' = \sum_{tri\ el=1}^{N} \frac{d\mathcal{D}}{dt}(\mathbf{u})_\Omega + \sum_{dis\ el=1}^{M} \frac{d\mathcal{D}}{dt}(\mathbf{u})_\Gamma = [c]^T[u] \tag{5.91}$$

where $[c]$ assembles the objective vectors.

Finally applied to the indentation test, $\mathbf{Q}' \cdot \mathbf{q}' = PV$, where P is the driving force and V the driving velocity. In this case the optimization problem (5.78) can be stated in a discretized form as follows:

$$\left\{ \begin{array}{c} \min_{\{\mathbf{u}\}}([c]^T[u]/V) \\ Subject\ to: \\ [A_1'][u] = [b_1] \\ [A_2'][u] \leqslant [b_2] \end{array} \right\} \tag{5.92}$$

5.4 Chapter Summary

In this Chapter we presented an upper bound computational formulation for axisymmetric problems. It constitutes (to our knowledge) the first complete work of this type, combining the following key ingredients:

- The discretization and linearization of the dissipation functions,
- The constraint conditions to ensure kinematically and plastically admissible velocity fields expressed by the finiteness of the dissipation within the triangles and along edges of adjacent elements representing potential surfaces of discontinuities.

We now have a powerful tool in hand to develop upper bound solutions for indentation tests, which is the focus of the next Chapter.

Chapter 6

Upper Bound Solutions for Indentation Analysis

This Chapter presents upper bound solutions for the hardness-cohesion-friction relation for indentation tests. The computational mechanics model developed in Chapter 5 was implemented in a FORTRAN based computational environment using the BPMPD algorithm [61]. The meshes are generated using the pre-processor of a commercially available finite element package, CESAR-LCPC^{TM}. The Chapter is structured as follows: we start with the flat punch solution, for which tow benchmark solutions are available. Following these verifications, upper bound solutions for conical and spherical indenters are presented, and the effect of the apex angle is discussed. Finally, by way of conclusion, we summarize the characteristics of the upper bound solutions, and conclude on the relevance of both upper and lower bound solutions for the extraction of strength properties of cohesive-frictional materials from indentation tests.

6.1 Mesh and Boundary Conditions

6.1.1 Mesh and Element Size

The indented material is discretized into 3-noded finite elements that are interfaced by discontinuity elements. The meshing procedure is very similar to the one employed for the lower bound: the meshes are generated using the pre-processor of a commercially available finite

element package, CESAR-LCPC^{TM} which allows one to discretize in a step-by-step fashion a material domain by triangular solid elements and to generate the interface elements along edges of adjacent triangular elements. However, not surprisingly, the main differences with respect to meshes employed in the lower bound approach relate to mesh density and size of meshed domain, which becomes critical for the upper bound solution. First, in contrast to the lower bound approach, in which extension elements are employed along the boundaries (see Section 3.3), the "natural" boundary condition in the upper bound solution are zero velocities at the limit of the discretized material domain (see Section 5.2.3). These zero velocity conditions must be sufficiently far away from the indenter in order not to interfere with the failure mechanism. The necessary size of the meshed domain depends on the friction angle: the greater the friction angle, the larger the domain of plastic dissipation (i.e. non zero velocities), and thus the required size of the meshed material domain. Second and equally important, the individual size of each element must be much smaller than the characteristic size of the indenter in order to capture localized dissipation phenomena that characterize all upper bound solutions. In a dimensionless form, the use of the upper bound computational method needs to consider the following set of dimensionless quantities for the hardness-cohesion-friction relation:

$$\frac{H}{c} = \frac{P}{cA} = \mathcal{F}(\varphi, \frac{l}{\sqrt{A/\pi}}, \frac{\sqrt{A/\pi}}{L}, ...) \tag{6.1}$$

where $\sqrt{A/\pi}$ is the characteristic size of the indenter (A is the projected contact area), l is the characteristic element size of the mesh and L is the size of the meshed domain. The dimensionless parameter $\frac{l}{\sqrt{A/\pi}}$ (which is a measure of the mesh density) and $\frac{\sqrt{A/\pi}}{L}$ (which is a measure of the meshed domain) should ideally be much smaller than unity, so that the discretization does not affect the result, i.e. the hardness-to-cohesion ratio. In our study, with friction angles up to 30°, a value of $\frac{l}{\sqrt{A/\pi}} \leq 0.05$ below the indenter has been found to deliver satisfactory results, while the ratio $\frac{\sqrt{A/\pi}}{L}$ decreased with the friction angle so that it does not interfere with the failure mechanism (typically $\frac{\sqrt{A/\pi}}{L} = 0.2$ for $\varphi = 10°$). We should also mention that a convergence study was carried out for all results presented below, and the linearization parameter p (see Section 5.2.5) was set to 24 (simulations with $p = 36$ showed a relative difference of less than 0.3 % and took much longer to run).

The mesh sensitivity of the upper bound solution gives rise to a large number of nodes and elements (typically 60,000 nodes), and thus gives rise to a large number of constraint conditions, requiring an effective optimization algorithm. As an indication, using the BPMPD algorithm [61], the CPU time was about 3h30min on a Pentium3, 1.13GHz, 768Mb RAM (as the number of inequalities dramatically increased from the linearization, more RAM was needed for an optimal use of the CPU).

6.1.2 Boundary Conditions and Velocity Conditions at the Indenter-Material Interface

The velocity-boundary condition for the upper bound are displayed in Figure 6-1. We have already mentioned the zero velocity boundary condition along the limit of the modeled domain. Furthermore, along the indenter, for the frictionless contact problem (Fig. 6-1 (a)) the normal velocity is the one of the indenter (see [71]):

$$V_n = -\cos(i)u + \sin(i)v = -V_{indenter}\sin(i) \tag{6.2}$$

In contrast, for the perfectly rough contact condition (Fig. 6-1 (b)) there is no tangential jump in velocity (see [71]):

$$[[V_t]] = 0 \tag{6.3}$$

6.1.3 Numerical Errors

In contrast to the lower bound algorithm, we could not explore the whole range of values for the friction angle in the upper bound algorithm. For values of φ below $2-3°$ the program often did not converge.

Theoretically, for $\varphi = 0°$, the Mohr-Coulomb yield criterion reduces to the Tresca criterion. Even though the Tresca criterion appears simpler in its formulation, we could not implement it in a linear programming fashion. The volumic dissipation function for the Tresca criterion reads:

$$\frac{1}{2}\sigma_0\left(|d'_I| + |d'_{II}| + |d'_{III}|\right) \text{ if } tr(\mathbf{d}') = 0 \tag{6.4}$$

and we cannot *a priori* derive the sum of the absolute value of the principal strain rates. This

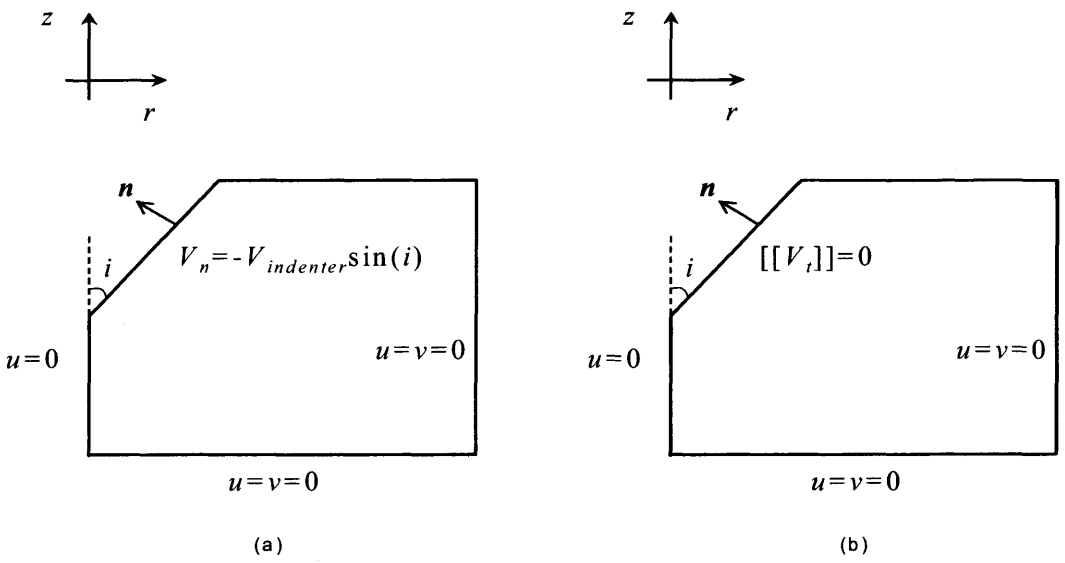

Figure 6-1: (a) Boundary conditions for a frictionless interface. (b) Perfectly rough interface.

is indeed different from prescribing an inequality involving absolute value (see the volumic dissipation function for the Mohr-Coulomb criterion, Section 5.1.2) for which one can enforce the several inequalities corresponding to the different expression of the absolute value terms (see Section 5.2.5).

In conclusion, the result presented below for the upper bound solutions are valid for friction angles greater than $2 - 3°$.

6.2 Verification 1: Smooth Flat Punch Solution

The first application of our upper bound method deals with the flat punch problem, for which a reference solution is available. This solution is due to Cox et al. [1]; it is based on the slip-line theory. Cox et al.'s solution is presented first and is then compared with the solution we obtain with our computational model.

6.2.1 Cox et al.'s Flat Punch Solution

The problem considered in [1] is the bearing capacity of a smooth[1], rigid circular footing resting on a cohesive-frictional soil (Mohr-Coulomb yield criterion). The solution is developed within the framework of limit equilibrium theory in axisymmetric conditions, assuming the Haar-Karman hypothesis[2] which is a posteriori verified. Cox et al. derived a slip-line solution which is an upper bound of the collapse load, as a kinematically admissible velocity field can be associated with the partial stress field in a bounded region below the footing. Cox et al. also showed that their partial stress field can be extended throughout the rest of the half space without violating the yield criterion nor the equilibrium conditions. This means that their slip-line solution is also a lower bound for the collapse load; and it is, therefore, the exact solution. Finally, the bearing capacity is derived by integrating the normal stress acting on the

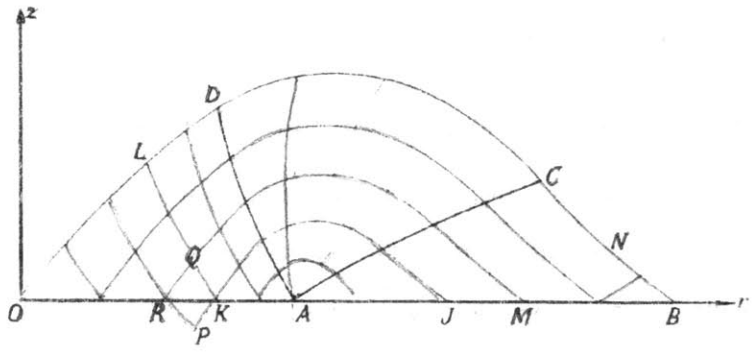

Figure 6-2: Cox et al.'s flat punch solution: Characteristic net in the meridian plane (from [1]).

foundation. Figure 6-3 displays, in a dimensionless form, the Cox et al.'s flat punch solution.

[1] That is there is no tangential stress at the interface (see the definition of the frictionless contact problem in Section 6.1.2).

[2] The Haar-Karman hypothesis assumes that the middle principal stress is equal either to the major principal stress or the minor principal stress:

$$\sigma_{II} = \frac{1}{2}\left[(\sigma_I + \sigma_{III}) - \epsilon\,(\sigma_I - \sigma_{III})\right] \tag{6.5}$$

$$\epsilon = \pm 1 \tag{6.6}$$

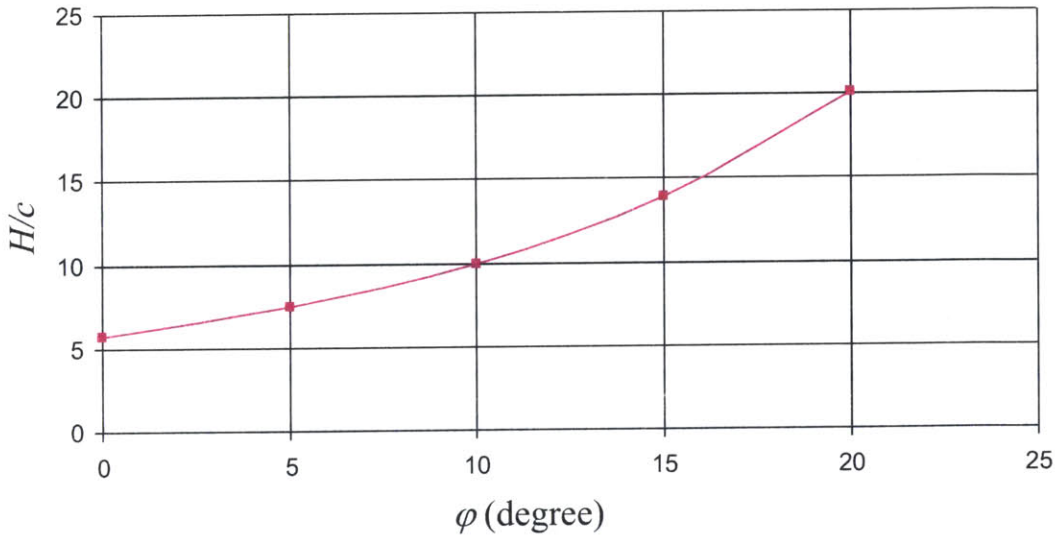

Figure 6-3: Cox et al.'s flat punch solution [1] for the dimensionless parameter $\frac{H}{c}$ as a function of φ. Frictionless interface condition.

6.2.2 Our Upper Bound Solution for the Smooth Flat Punch

Typical meshes employed in our analysis are displayed in Figure 6-4 (a), Figure 6-5 (a) and Figure 6-6 (a). The meshed domain in Figure 6-5 (a) has the following characteristics: 58,320 nodes, 24,129 elements, $\frac{l}{\sqrt{A/\pi}} = 0.05$ and $\frac{\sqrt{A/\pi}}{L} = 0.2$ (for $\varphi = 10°$). The meshes were chosen so that the zero velocity boundary at the limit of the domain does not interfere with the failure mechanism developing around the flat punch.

Following the solution proposed by Cox et al. [1], the interface between the punch (foundation) and the material (soil) is assumed to be frictionless; that is there is no shear stress at the interface and there is no normal jump in velocity (see relation (6.2) in Section 6.1.2). Figure 6-4 (b), Figure 6-5 (b) and Figure 6-6 (b) display the optimized velocity field for $\varphi = 2°$, $\varphi = 10°$ and $\varphi = 20°$ respectively. It is interesting to note that the main part of the failure mechanism develops in a broad band emerging below a vertical downward velocity zone and extending to the free surface (vertical upward velocity zone). As expected from a plastic dilating constitutive law, the velocity field at the surface can be associated with a pile-up mechanism that characterizes the Mohr-Coulomb material response: the area affected by plastic dilatation at

the surface is the larger the greater the friction angle.

6.2.3 Discussion

Figure 6-7 summarizes our results in form of a plot of the normalized hardness versus friction angle:

$$\frac{H}{c} = \mathcal{F}(\varphi) \tag{6.7}$$

The figure also displays the Cox et al.'s solution, as well as our lower bound solution (3.13). We note that our numerical upper bound solution comes remarkably close to the Cox et al.'s solution (the relative difference is about 7 %, a little better than Lyamin and Sloan's numerical lower bound solution [56]).

In contrast, there is a much larger error associated with lower bound results. In our interpretation, this is due to the fact that the lower bound method is unable to represent a broad range of stress fields[3], whereas the upper bound can virtually accommodate any failure mechanism.

In summary, the comparison of our "pure" upper bound solution with Cox et al.'s exact solution for the smooth flat punch problem verifies our computational mechanics upper bound model for the assessment of the hardness-cohesion-friction relation. It also provides strong evidence that the developed upper bound is much closer to the real solution than the lower bound approach; we keep this in mind for the application of the method to conical and spherical indentations.

6.3 Verification 2: Rough Flat Punch Solution

A second benchmark solution for the flat punch is due to Matar and Salençon [60]; and it is based on the method of characteristics. It is very similar to the solution by Cox et al. presented hereabove. The difference lies in the boundary conditions.

[3] We have shown in Section 4.1.2 that our method can only deal with diagonal stress fields.

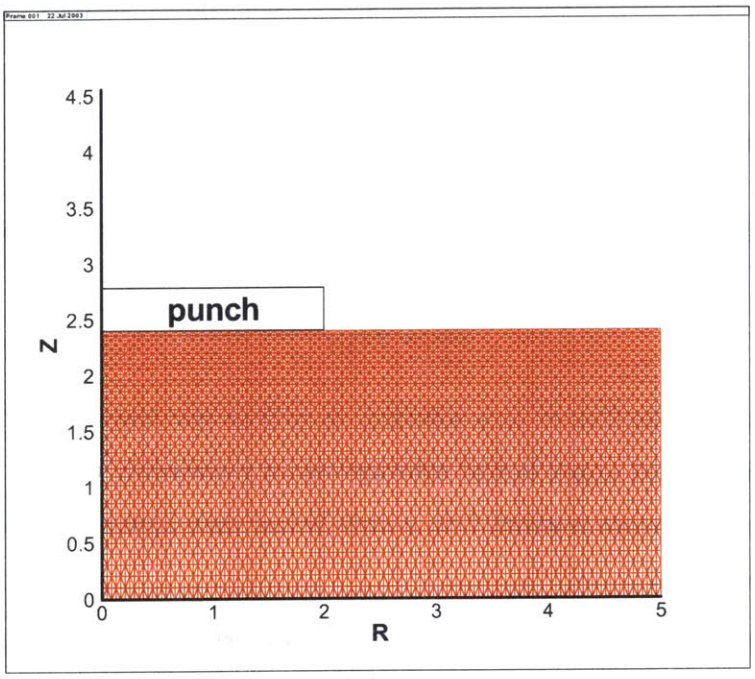

(a)

(b)

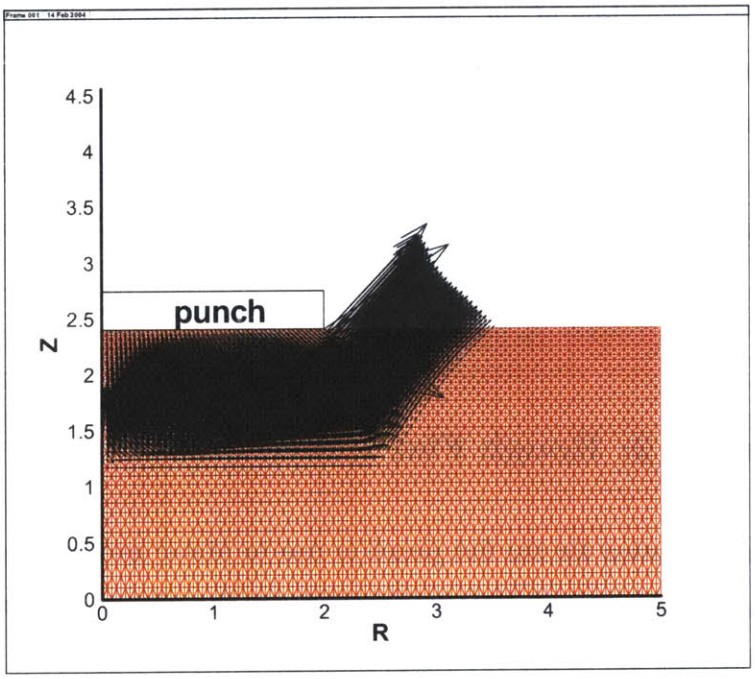

Figure 6-4: (a) Mesh for $\varphi = 2°$. (b) Failure mechanism for $\varphi = 2°$.

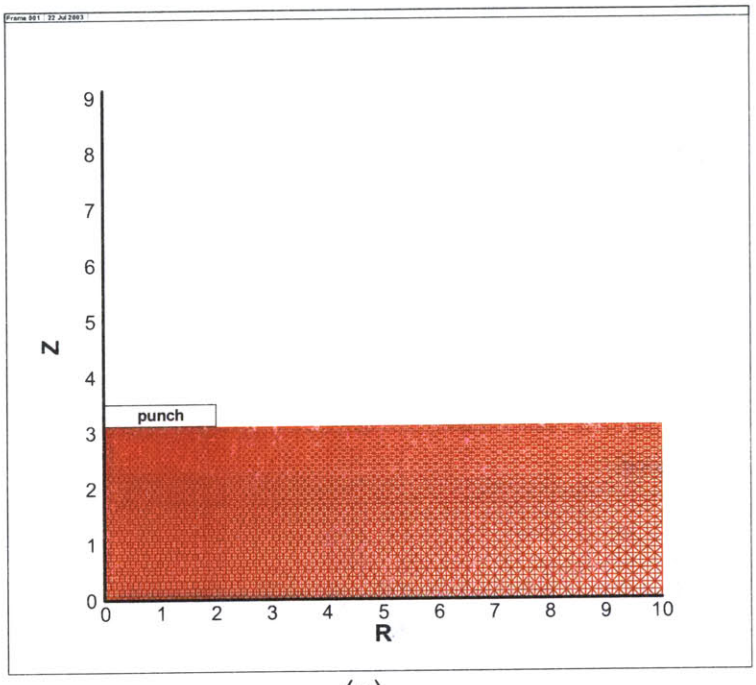

(a)

(b)

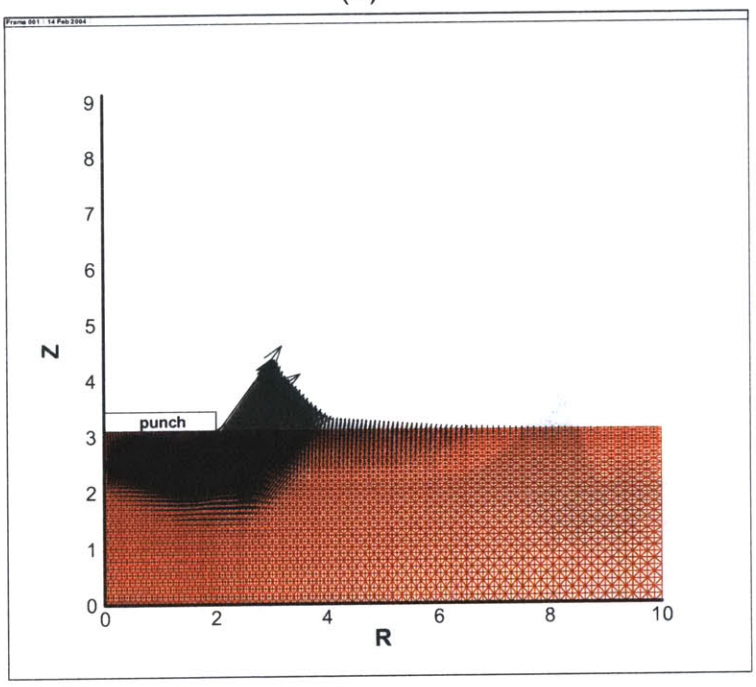

Figure 6-5: (a) Mesh for $\varphi = 10°$. (b) Failure mechanism for $\varphi = 10°$.

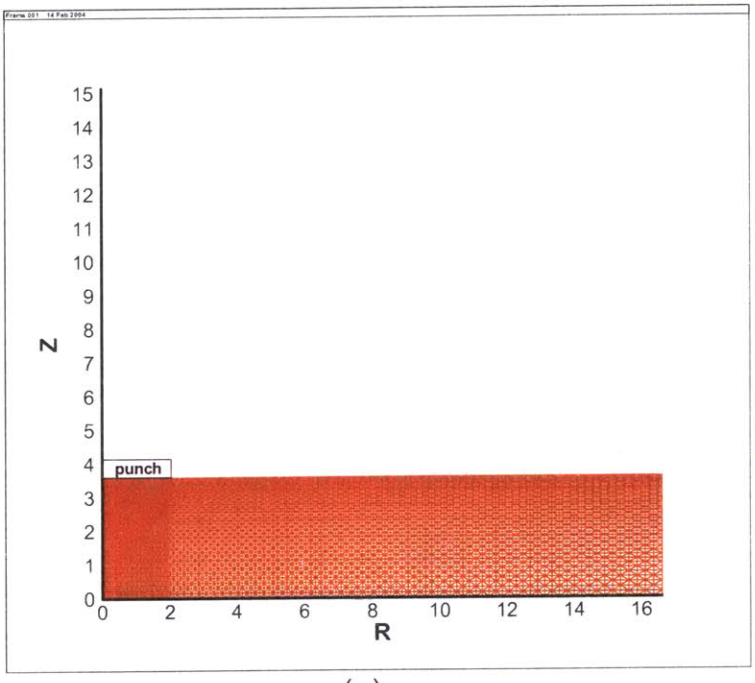

(a)

(b)

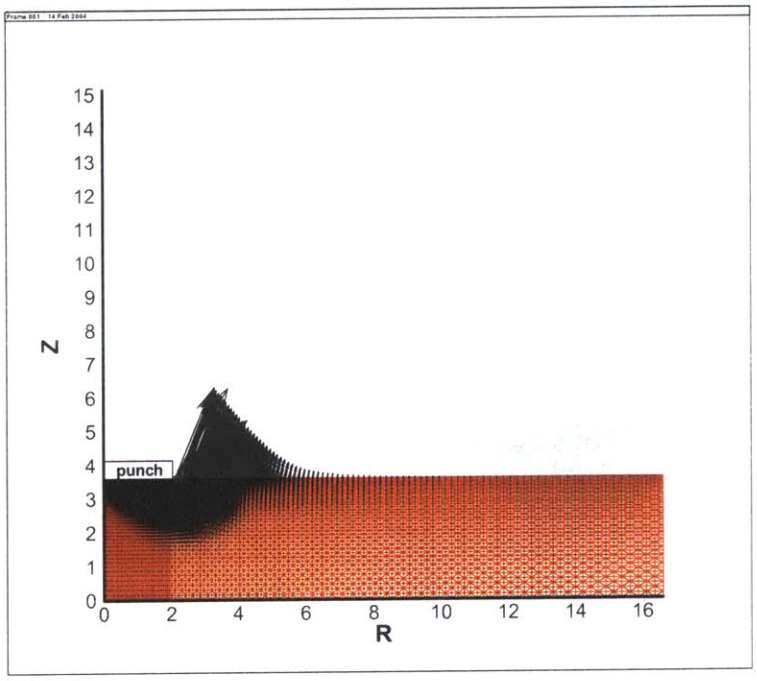

Figure 6-6: (a) Mesh for $\varphi = 20°$. (b) Failure mechanism for $\varphi = 20°$.

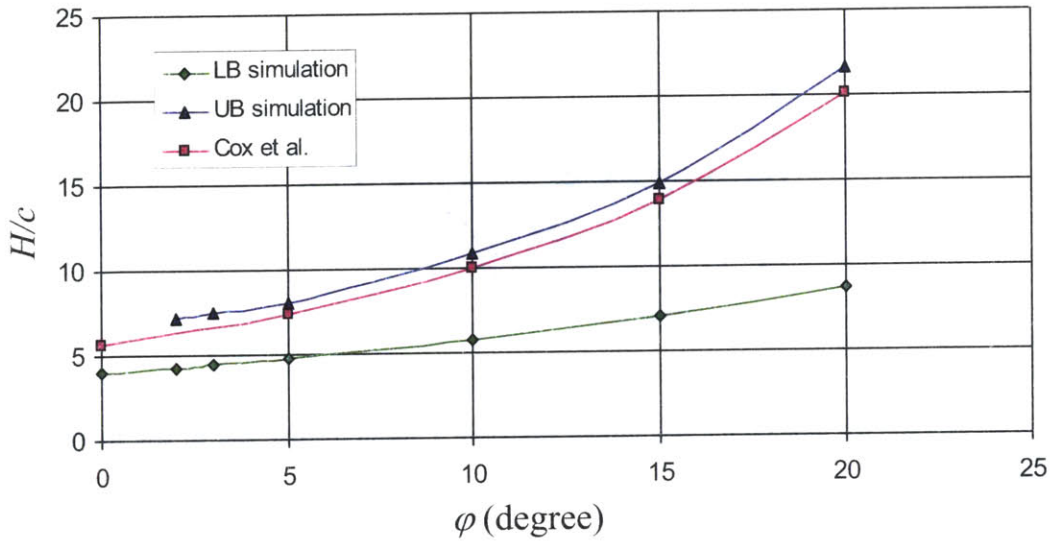

Figure 6-7: Bounds for the dimensionless parameter $\frac{H}{c}$. Comparison with Cox et al.'s solution.

6.3.1 Matar and Salençon's Flat Punch Solution

The problem considered in [60] is the bearing capacity of a perfectly rough[4] circular foundation on a cohesive-frictional soil (Mohr-Coulomb yield criterion). The solution is also developed within the framework of the limit equilibrium theory in axisymmetric conditions, assuming the Haar-Karman hypothesis which is verified afterwards. The stress field is obtained by the method of characteristics in a zone spreading under the foundation and emerging at the stress free surface (Fig. 6-8). The method of characteristics is based on a "lower bound" approach, or more precisely on a partial static approach, since the stress field derived along the characteristic lines (see Fig. 6-8) satisfies the equilibrium equations and the plasticity criterion. In addition to the pure lower bound approach, when a compatible velocity field can be constructed in the same zone where the stress field has been derived, an "incomplete solution", as introduced by Bishop [6], is obtained. Such a velocity field is obtained through the normality rule and must satisfy compatibility equations (see [60] for more details). Figure 6-9 displays, in a dimensionless form, the Matar and Salençon's flat punch solution. The Matar and Salençon's solution is said to

[4]That is there is no tangential velocity jump (see Section 6.1.2).

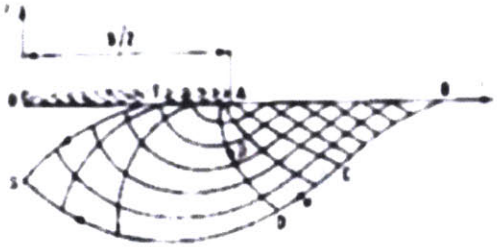

Figure 6-8: Matar and Salençon's flat punch solution: Characteristic net in the meridian plane (from [60]).

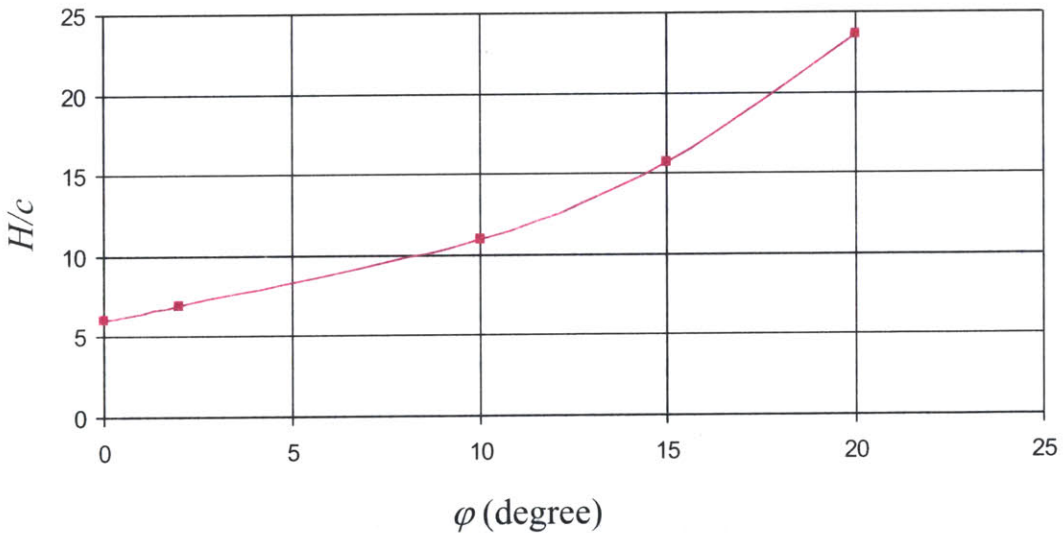

Figure 6-9: Matar and Salençon's flat punch solution for the dimensionless parameter $\frac{H}{c}$ as a function of φ. Perfectly rough interface condition.

be a "heuristic" solution in the sense that the stress field and the velocity field have not been extended throughout the whole domain. However, the extension possibility has been evidenced for similar planar problems.

6.3.2 Our Upper Bound Solution for the Rough Flat Punch

The meshes employed in this analysis are the same as in Section 6.2.2.

Following the solution proposed by Matar and Salençon [60], the interface between the punch (foundation) and the material (soil) is assumed to be perfectly rough; that is there is no constraint on the shear or normal stress at the interface and there is no tangential jump in velocity (i.e. relation (6.3) in Section 6.1.2). Figure 6-10 (b), Figure 6-11 (b) and Figure 6-12 (b) display the optimized velocity field for $\varphi = 20°$, $\varphi = 10°$ and $\varphi = 2°$ respectively. It is interesting to note that the zone below the indenter undergoes an almost rigid body motion (as one could expect from the boundary conditions), and that as previously, the main part of the failure mechanism develops in a broad band emerging below this vertical downward velocity zone and extending to the free surface (vertical upward velocity zone).

6.3.3 Discussion

Figure 6-13 summarizes our results in form of a plot of the normalized hardness versus friction angle:

$$\frac{H}{c} = \mathcal{F}(\varphi) \tag{6.8}$$

The Figure also displays the Matar and Salençon's solution as well as our lower bound solution (3.13). We note that our numerical upper bound solution comes remarkably close to the Matar and Salençon's solution (the maximum relative difference is about 10 % but consistently less than 6 %). This is even more remarkable since Matar and Salençon's "heuristic" solution is likely to be closer to a lower bound[5] thus explaining the small difference with our upper bound results, and the fact that our upper bound is indeed consistently above the reference solution.

In summary, the comparison of our "pure" upper bound solution with Matar and Salençon's "heuristic" one for the flat punch problem is another strong argument in favor of our compu-

[5] Recall that the method of characteristics is based on a stress field approach.

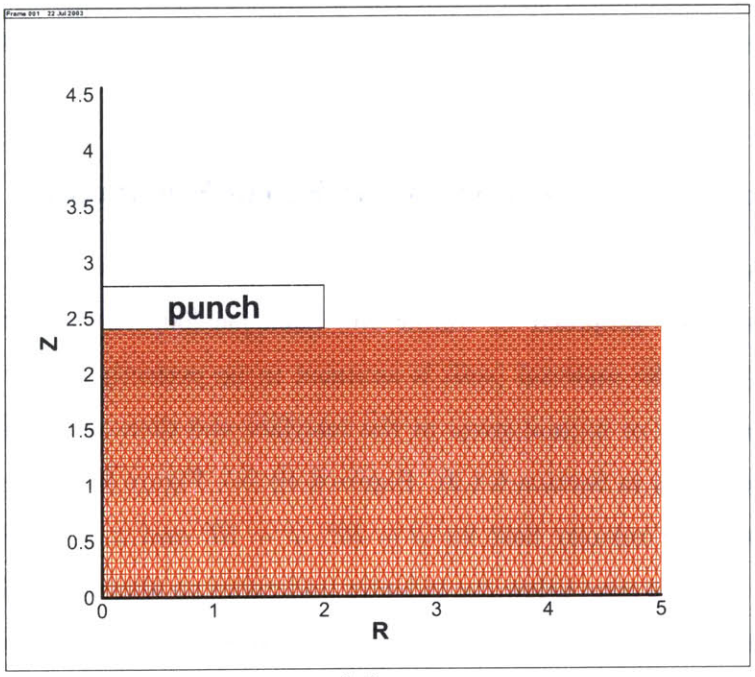

(a)

(b)

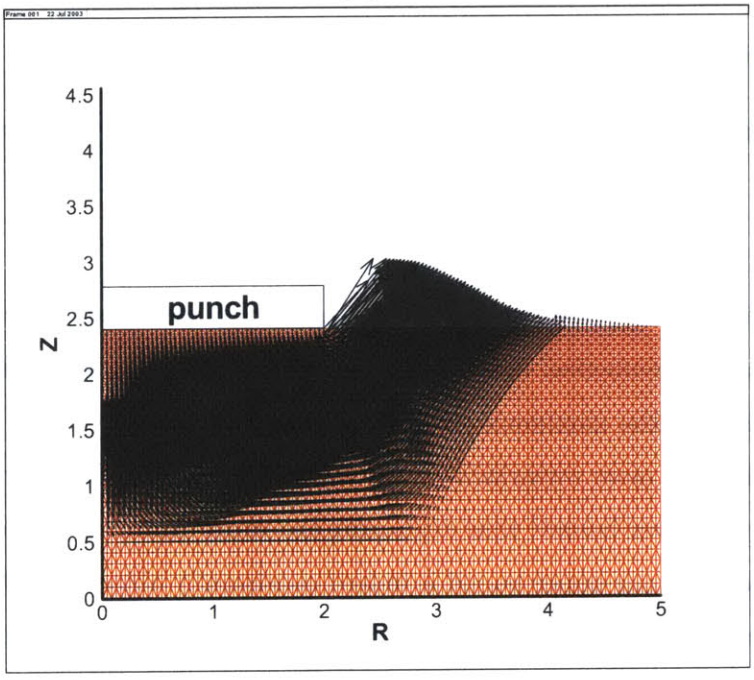

Figure 6-10: (a) Mesh for $\varphi = 2°$. (b) Failure mechanism for $\varphi = 2°$.

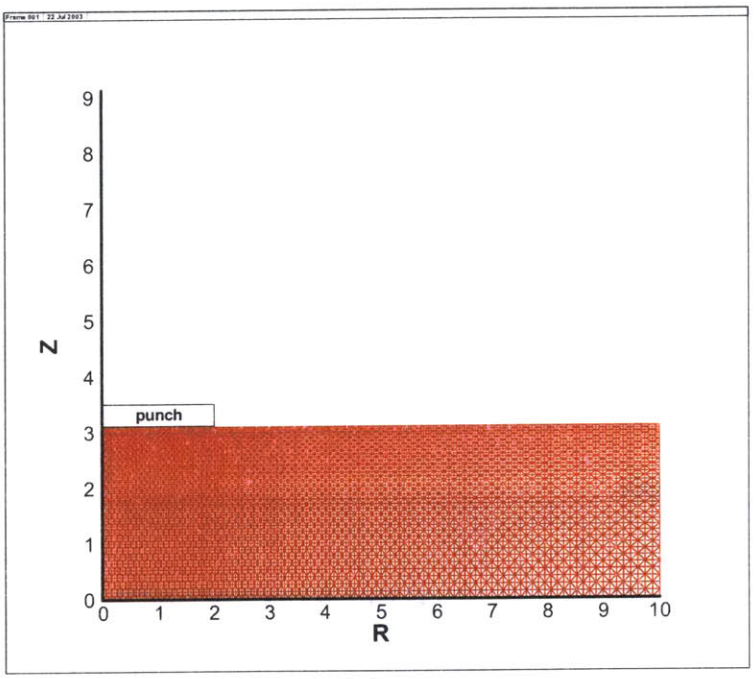

(a)

(b)

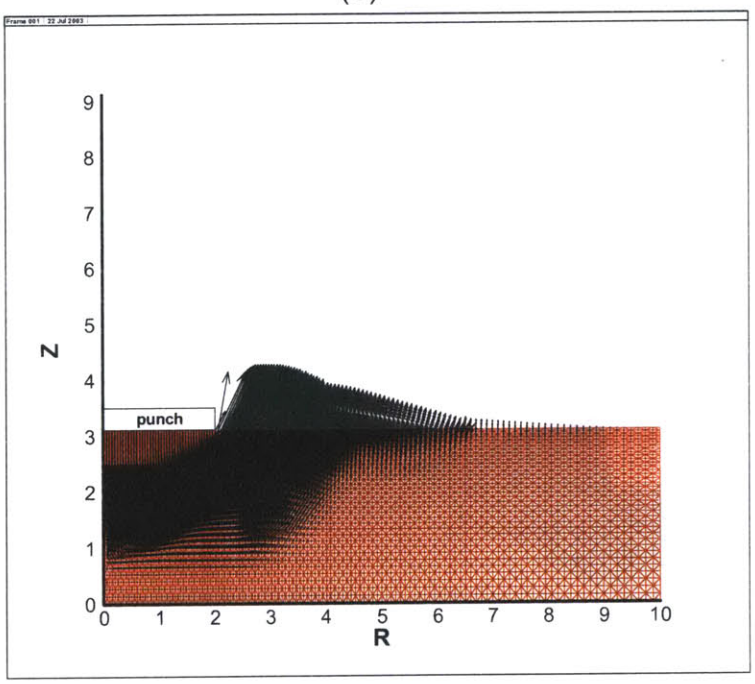

Figure 6-11: (a) Mesh for $\varphi = 10°$. (b) Failure mechanism for $\varphi = 10°$.

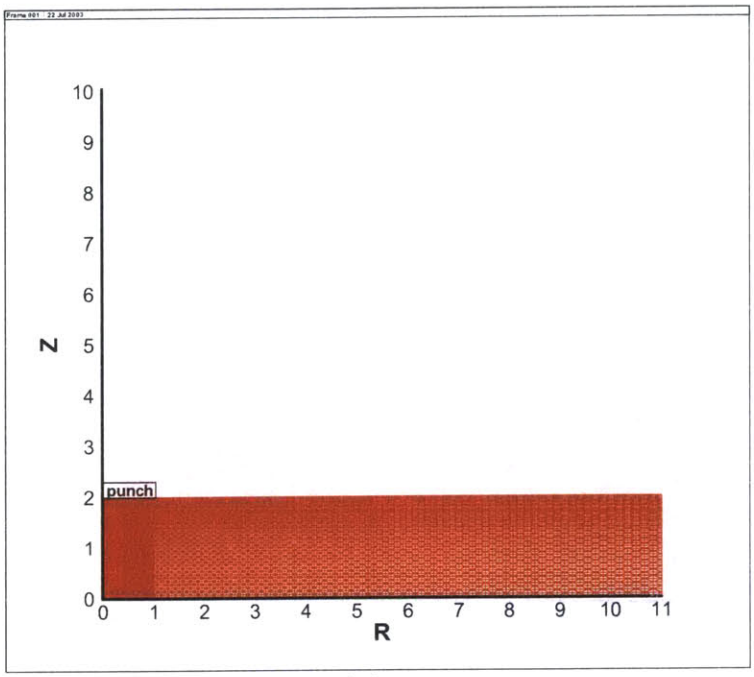

(a)

(b)

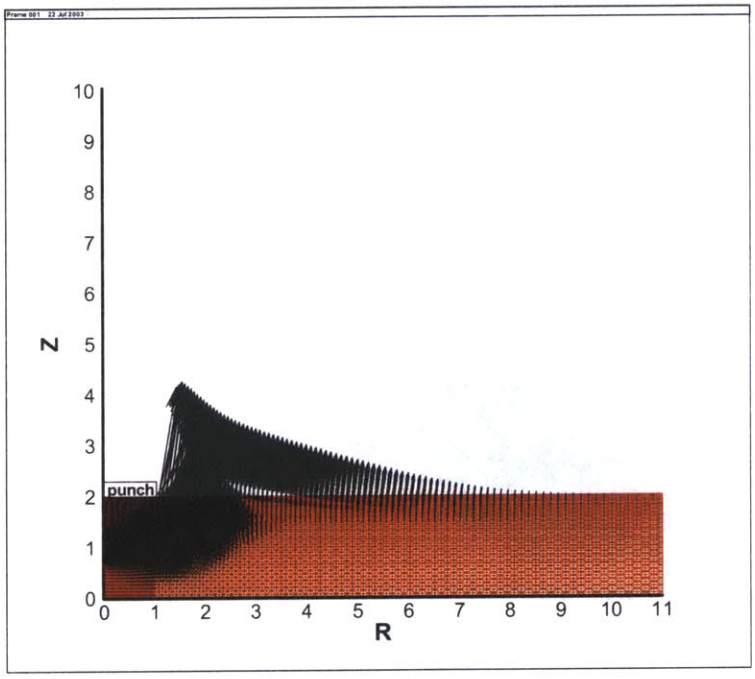

Figure 6-12: (a) Mesh for $\varphi = 20°$. (b) Failure mechanism for $\varphi = 20°$.

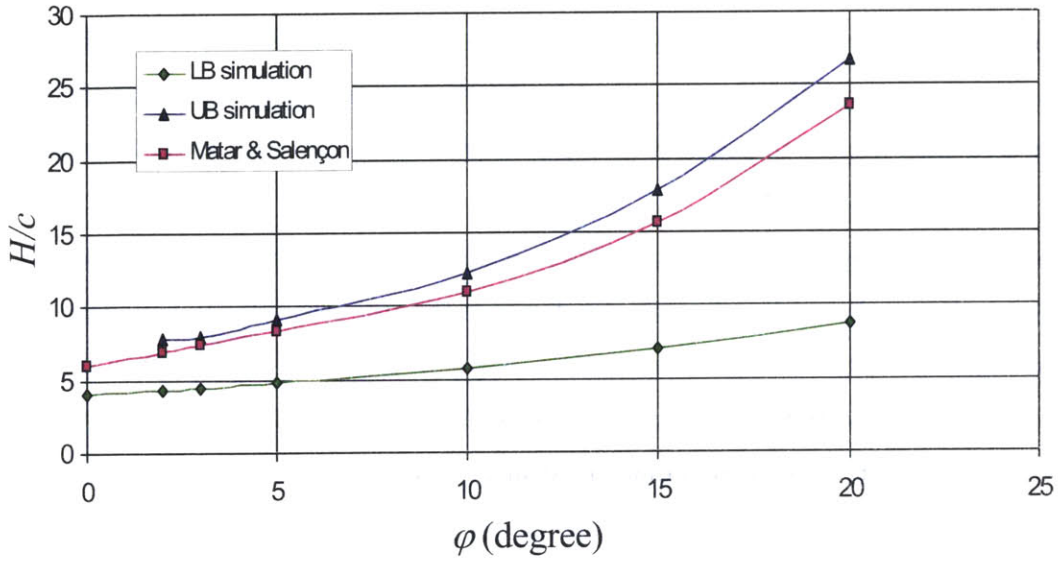

Figure 6-13: Bounds for the dimensionless parameter $\frac{H}{c}$. Comparison with Matar and Salençon's solution.

tational mechanics upper bound model for the assessment of the hardness-cohesion-friction relation.

6.4 Conical *Versus* Spherical Indenter Solutions

This Section presents original upper bound solutions for conical and spherical indenters for which (to our knowledge) no reference solution is available. The question we aim to answer is whether it is possible to extract from two hardness measurements, obtained with two different indenter geometries, the cohesion and friction angle of a Mohr-Coulomb material. The solution for the conical indenter is presented first and is then compared with the solution of the spherical indenter. Finally the effect of different apex angles is discussed. In all the simulations, the contact between the indenter and the material is frictionless, which is captured by the contact condition (6.2).

6.4.1 Upper Bound Solution for a Conical Indenter (Berkovich Indenter)

The conical indenter solution presented below is intended for a Berkovich-type indenter, modeled in axisymmetric conditions as a cone with a 70.32° semi apex angle, such that the projected contact area with respect to penetration depth of the cone is the same as that for the real indenter [20]; see Section 4.3.2.

Failure mechanisms and meshes for different friction angles are presented in Figures 6-14 (a) to 6-16 (b). Again, the meshed domain was chosen so that the zero velocity boundary condition does not interfere with the failure mechanism, $\frac{l}{\sqrt{A/\pi}} = 0.04$, and $\frac{\sqrt{A/\pi}}{L} = 0.15$ for $\varphi = 20°$. While the boundary conditions differ from the perfectly rough flat punch, it is interesting to note that the velocity field surrounding the conical indenter at the free surface appears more concentrated, producing a fair amount of pile-up related to the dilatancy behavior of the Mohr-Coulomb material.

Figure 6-17 presents the results for the evolution of $\frac{H}{c}$ with respect to φ. For purpose of comparison Figure 6-17 also displays the lower bound solution developed in Section 4.3.3. As for the flat punch solution, the lower bound is far off from the upper bound. Along a similar line of arguments as employed in Section 6.2.3, we suggest that the upper bound is much closer to the actual plastic collapse solution.

6.4.2 Upper Bound Solution for a Spherical Indenter

Figure 6-18 (a), Figure 6-19 (a) and Figure 6-20 (a) display typical meshes employed for the upper bound analysis of the spherical indentation test. The difference between the meshes is the indenter radius to penetration depth ratio R/h, which enters the dimensionless function as an additional invariant (see Section 2.5):

$$\frac{H}{c} = \mathcal{F}\left(\varphi, \frac{R}{h}\right) \tag{6.9}$$

Figure 6-18 (b), Figure 6-19 (b) and Figure 6-20 (b) display the optimized velocity fields for three R/h values: $R/h = 10$, 4 and 2, for the same friction angle $\varphi = 20°$. It is interesting to note that the velocity fields appear to be quite similar to the ones obtained for the conical indenter; particularly for $R/h = 10$, for which the geometry is very close to the conical indenter.

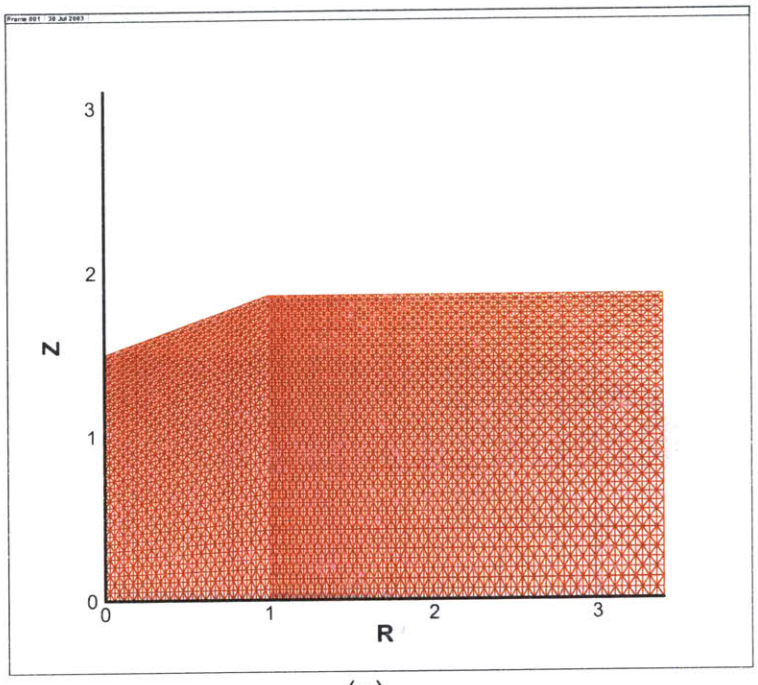

(a)

(b)

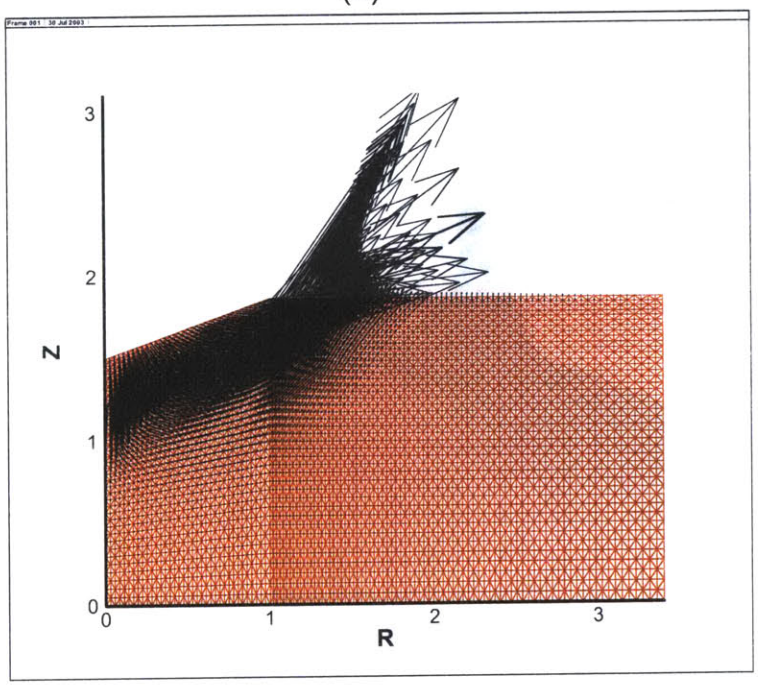

Figure 6-14: (a) Mesh for $\varphi = 5°$. (b) Failure mechanism for $\varphi = 5°$.

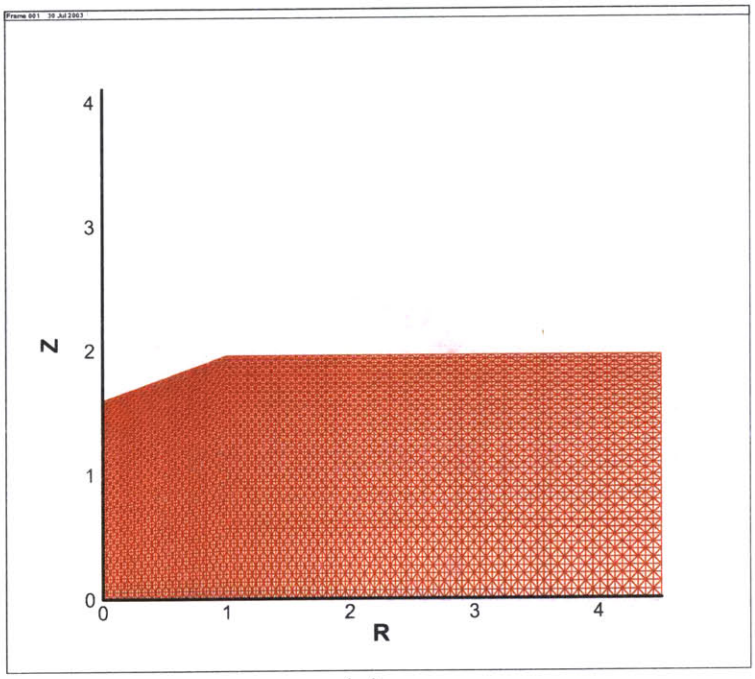

(a)

(b)

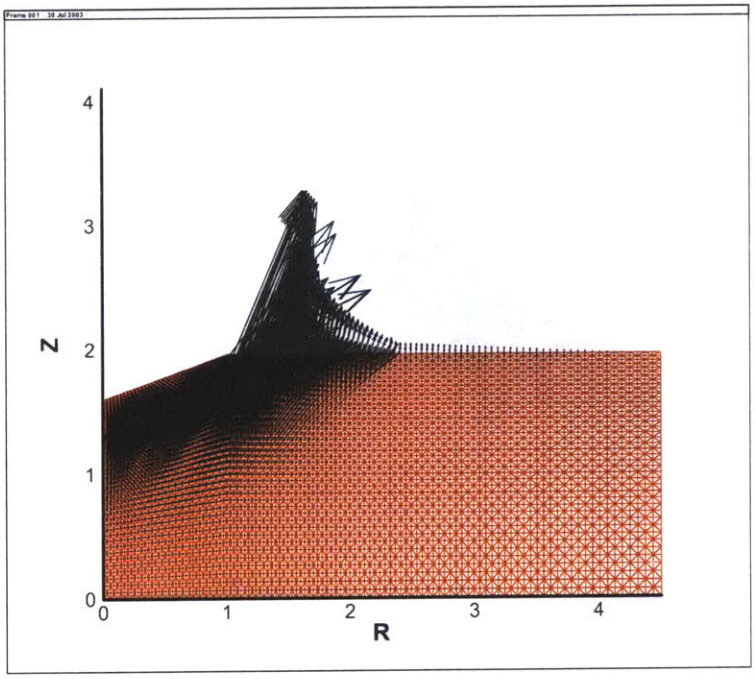

Figure 6-15: (a) Mesh for $\varphi = 10°$. (b) Failure mechanism for $\varphi = 10°$.

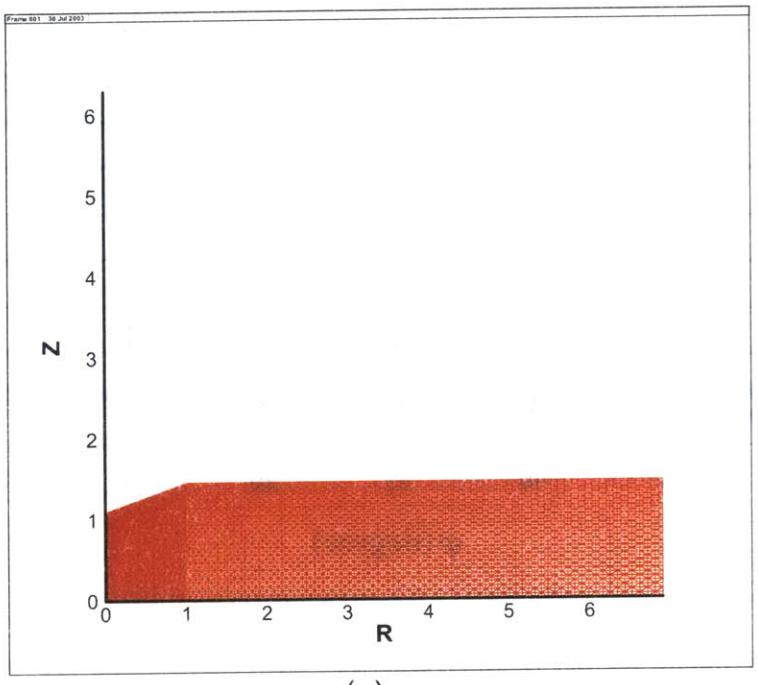

(a)

(b)

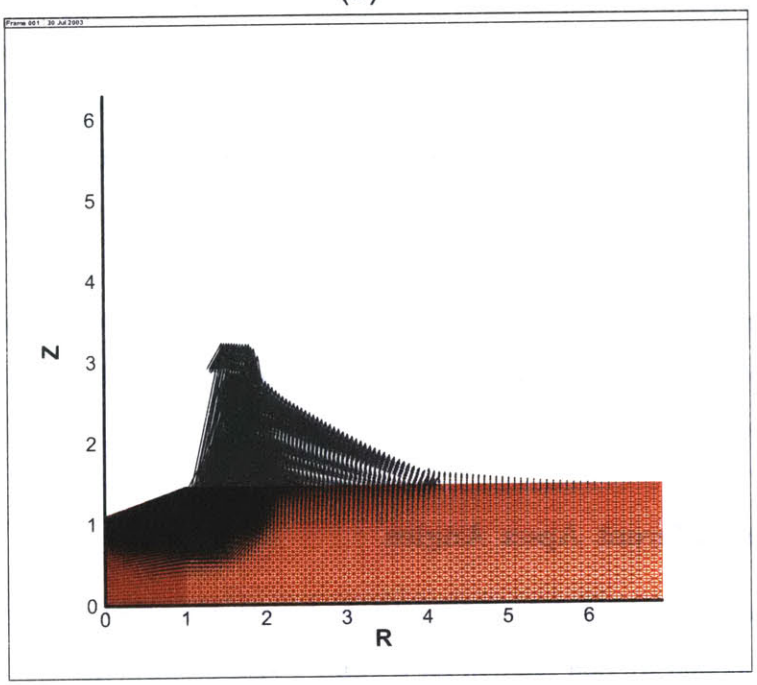

Figure 6-16: (a) Mesh for $\varphi = 20°$. (b) Failure mechanism for $\varphi = 20°$.

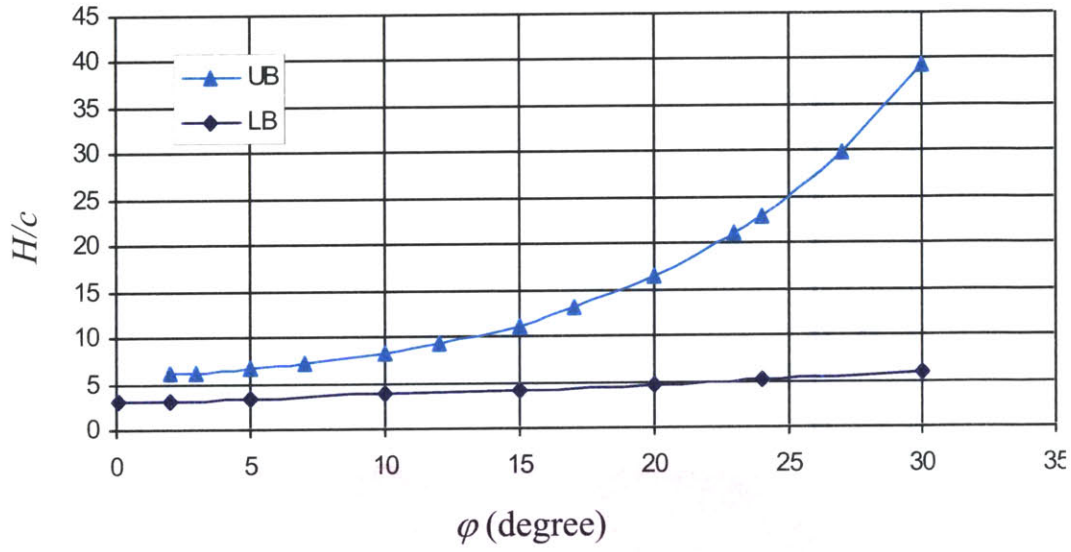

Figure 6-17: Upper bound for the dimensionless parameter $\frac{H}{c}$ as a function of φ. Berkovich type cone.

Failure mechanisms below the spherical and the Berkovich indenter are compared in Figure 6-21. Figure 6-22 displays the normalized hardness versus friction angle for the spherical indentation and three R/h values, as well as for the conical indenter. It can be seen that the H/c values are very similar, Figure 6-23 displays the ratios of H/c for the different values of R/h over H/c for the Berkovich indenter; i.e. the ratio of the hardness estimated by a spherical indenter over the one estimated by a conical (Berkovich) indenter.

The Figure shows that there seems to be no unique relation between the ratios and the friction angle. In other word it would be impossible to infer both c and φ from a Berkovich and a spherical indentation test.

6.4.3 Effect of Different Apex Angles

The last application of the upper bound model deals with the effect of the cone apex angle on the hardness-cohesion-friction relation for a Mohr-Coulomb material; that is in term of the dimensionless relation (2.11):

$$\frac{H}{c} = \mathcal{F}(\varphi, i) \tag{6.10}$$

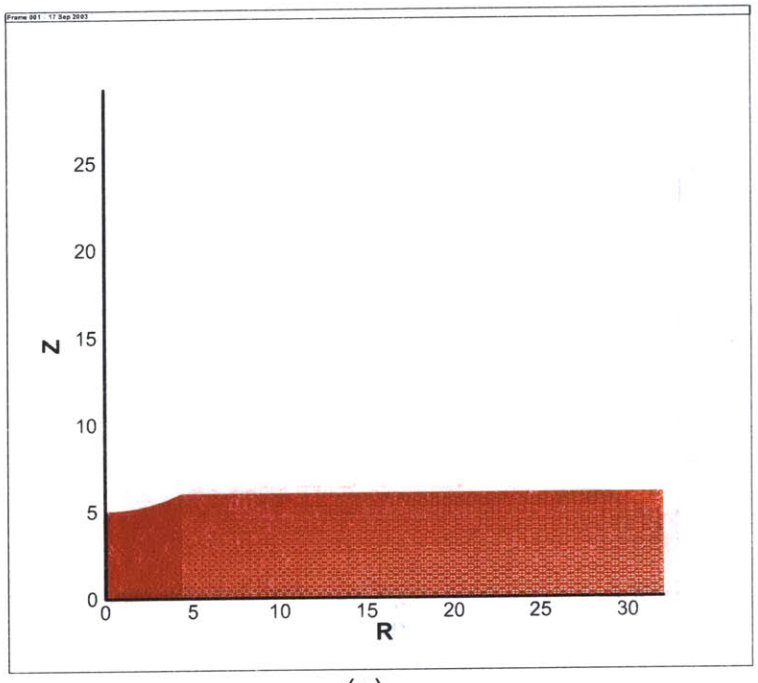

(a)

(b)

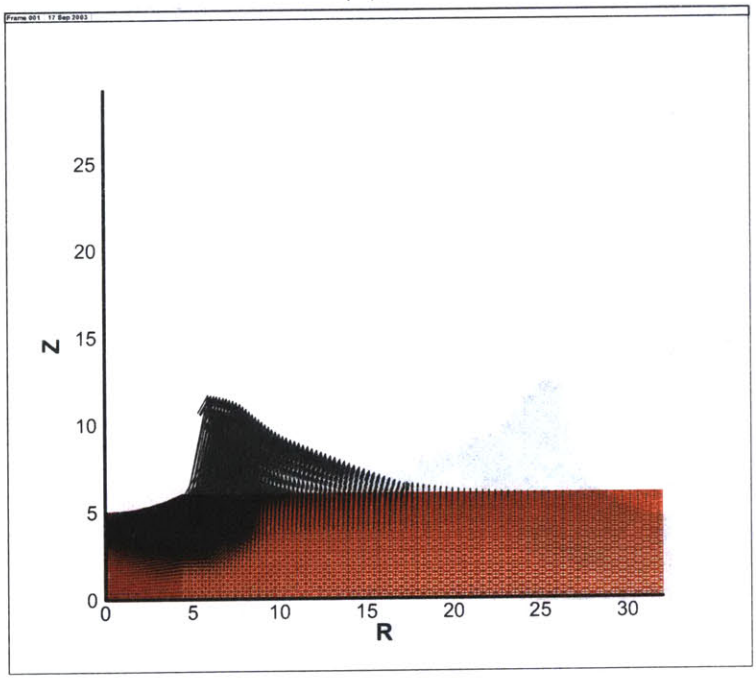

Figure 6-18: (a) Mesh for $\varphi = 20°$. (b) Failure mechanism for $\varphi = 20°$. $R/h = 10$.

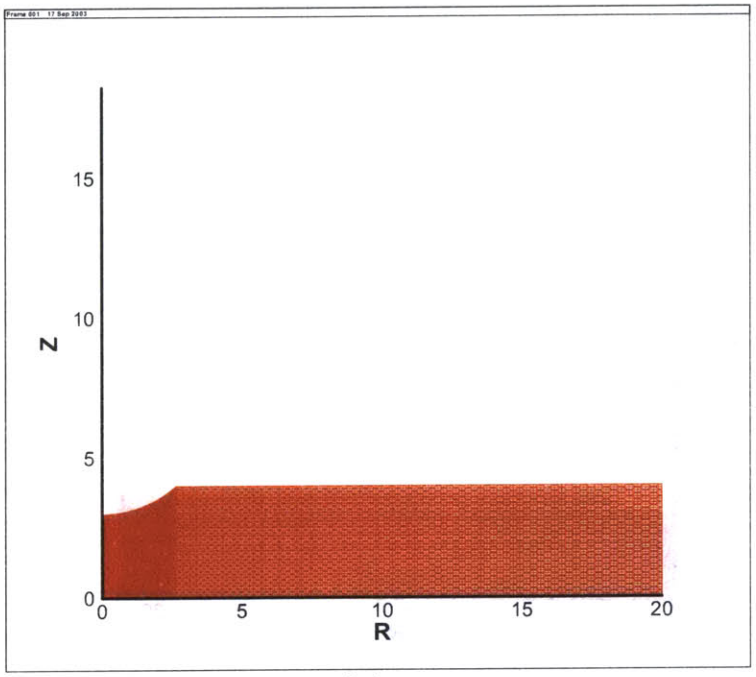

(a)

(b)

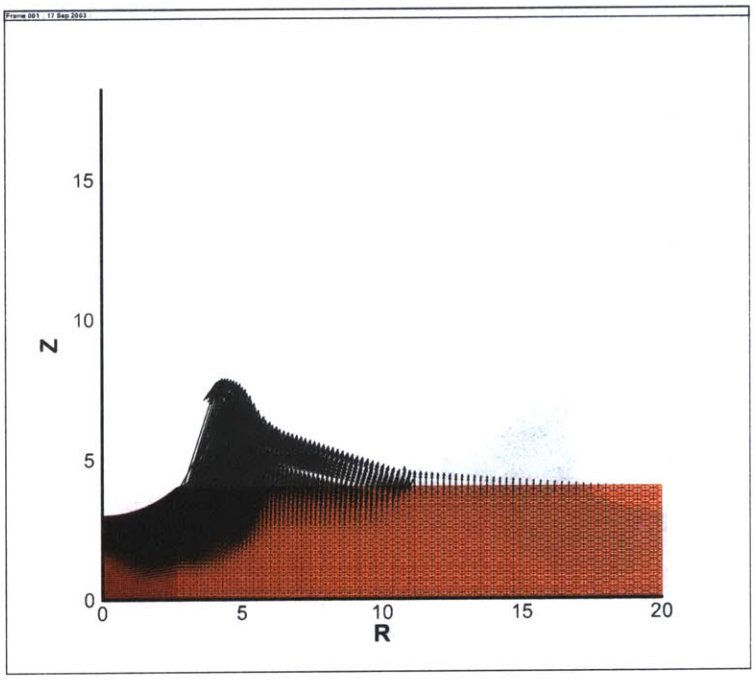

Figure 6-19: (a) Mesh for $\varphi = 20°$. (b) Failure mechanism for $\varphi = 20°$. $R/h = 4$.

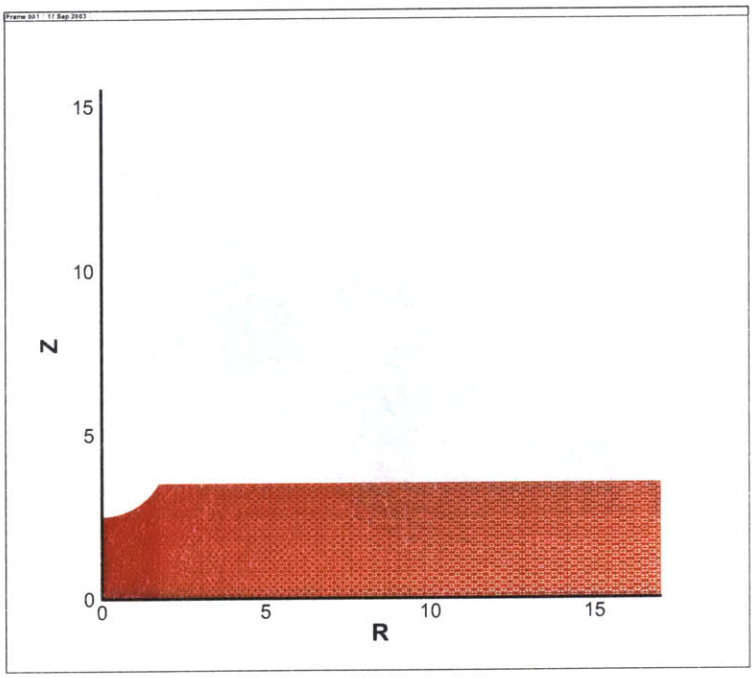

(a)

(b)

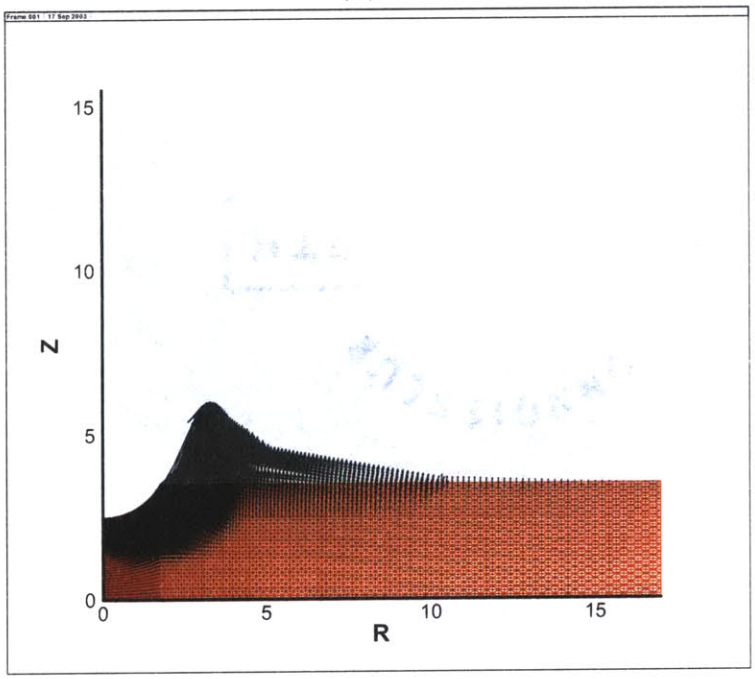

Figure 6-20: (a) Mesh for $\varphi = 20°$. (b) Failure mechanism for $\varphi = 20°$. $R/h = 2$.

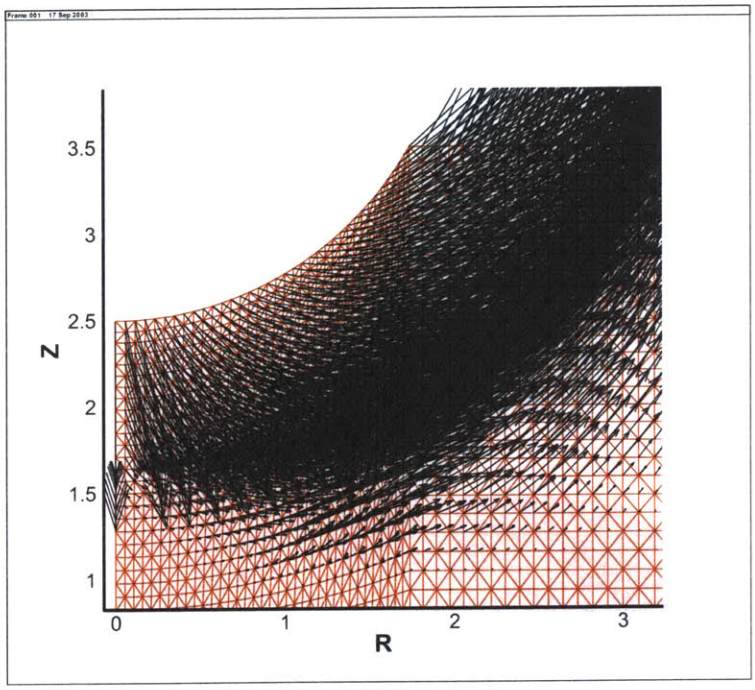

(a)

(b)

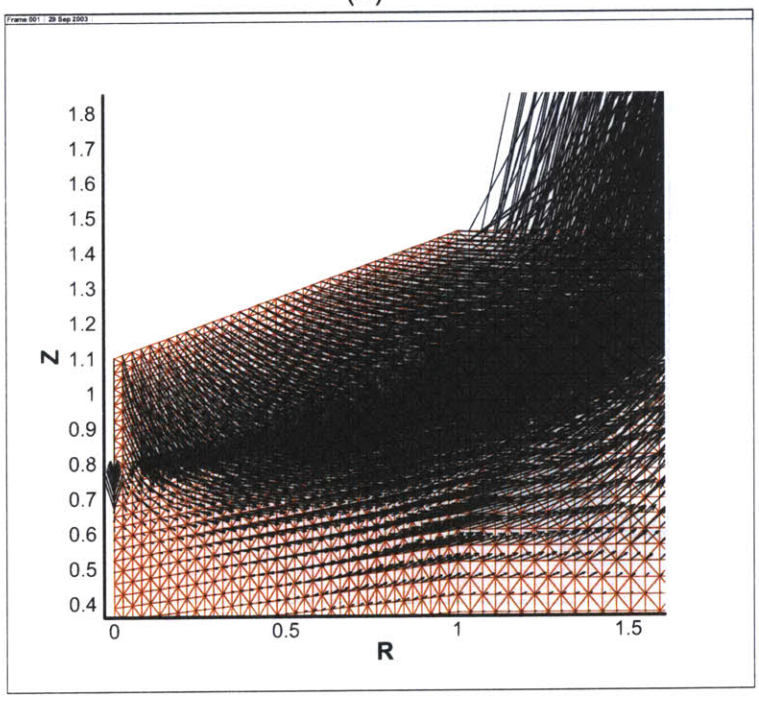

Figure 6-21: (a) Close up of the failure mechanism for $\varphi = 20°$. $R/h = 2$. (b) Close up of the failure mechanism for $\varphi = 20°$. Berkovich indenter.

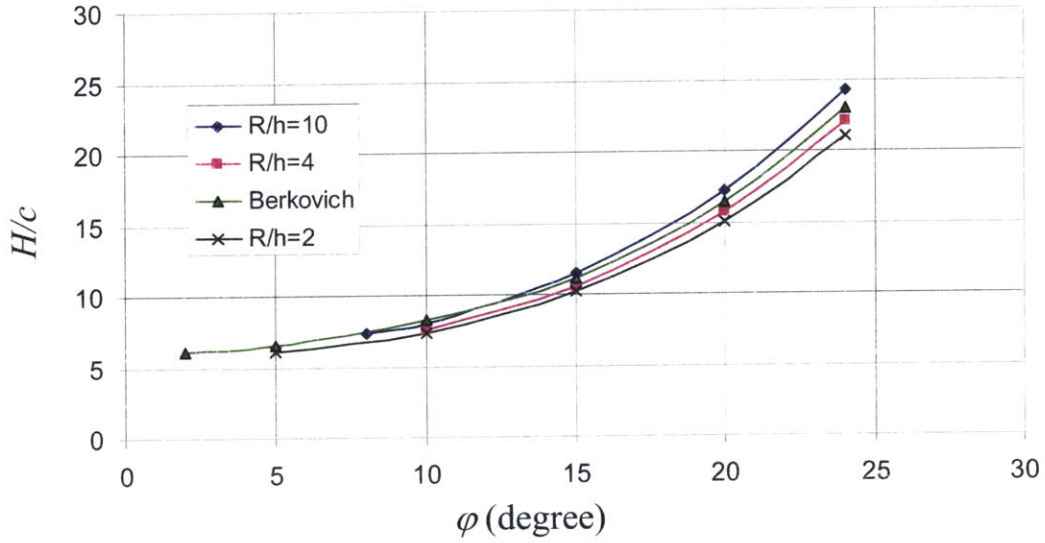

Figure 6-22: Comparison between spherical and Berkovich indenters.

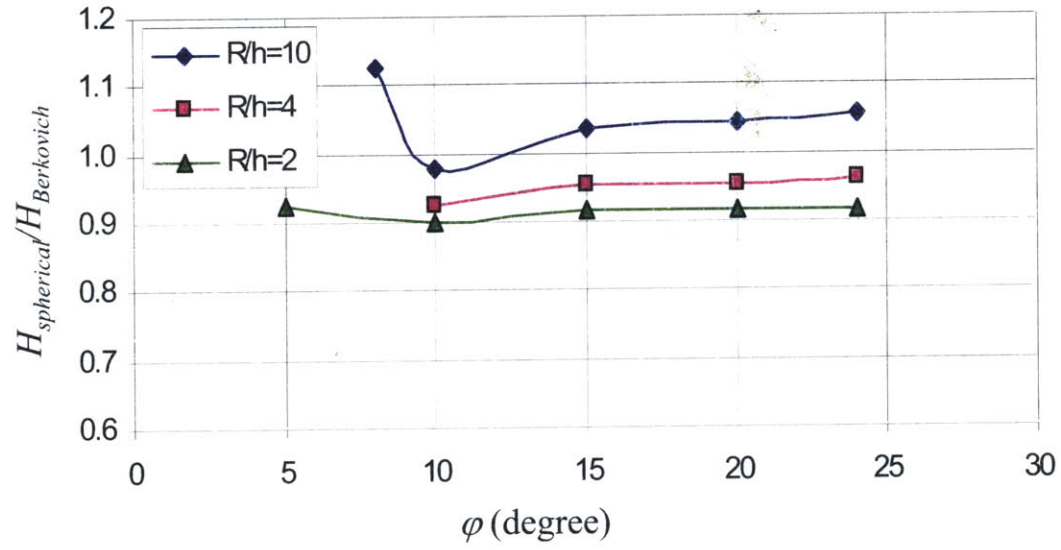

Figure 6-23: Evolution of the hardness ratios with respect to φ.

where i is the semi apex angle which enters as an additional invariant. The motivation for the analysis is two-fold: on the one side, it is motivated by the relative insensitivity of Berkovich versus spherical indentation hardness, which makes it difficult to envision the extraction of two strength properties (c and φ) from those two indentation tests. On the other hand, we have already seen in the previous Sections a considerable difference in failure mechanism between the flat punch and the Berkovich indenter. The flat punch can be seen as the limit of a cone with $i = 90°$, which was found to deliver significantly greater hardness values than the Berkovich type cone, for which $i = 70.32°$. The focus of this Section is therefore to explore the sensitivity of the upper bound solution with regard to the apex angle.

In addition to the already presented solutions for $i = 90°$ (Section 6.2.2) and $i = 70.32°$ (Section 6.4.1) we present solutions for smaller semi-apex angles: $i = 45°$, $42.28°$, $25°$ and $15°$. Figure 6-24 (a) and 6-25 (a) display typical meshes employed in this analysis, which have all similar characteristics as the one employed for the Berkovich indenter. Figure 6-24 (b) and 6-25 (b) display the optimized velocity fields for $i = 45°$, $25°$ and $\varphi = 10°$. It is interesting to note that the velocity field appears more concentrated for smaller apex angle, which suggest different overall dissipation rates, associated with different collapse loads. Figure 6-26 displays the normalized hardness H/c versus the semi-apex angle i for $\varphi = 10°$. The results confirm a sensitivity vis-à-vis apex angle for the hardness. The results also comforts the simple idea that a sharp cone is easier to drive into the material than a flat punch, but we could not come up with a satisfactory explanation for the apparent increase in harness for very sharp cones. There appears to be a minimum around $i = 45°$. It is noteworthy that a similar minimum phenomenon was reported by Houslby and Wroth [39]. They dealt with a lower bound approach for the cone penetration test and reported an optimum angle[6] about $50°$. We also present in Figure 6-27 the normalized hardness versus the friction angle for the Berkovich type conical indenter and the $45°$ semi apex angle cone.

In summary the result of our study provide strong evidence that it is indeed possible to extract the two strength properties of a Mohr-Coulomb material from two conical indentation tests that have a significantly different apex angle.

[6] We did not find such a minimum in our lower bound approach (see Section 4.3.4).

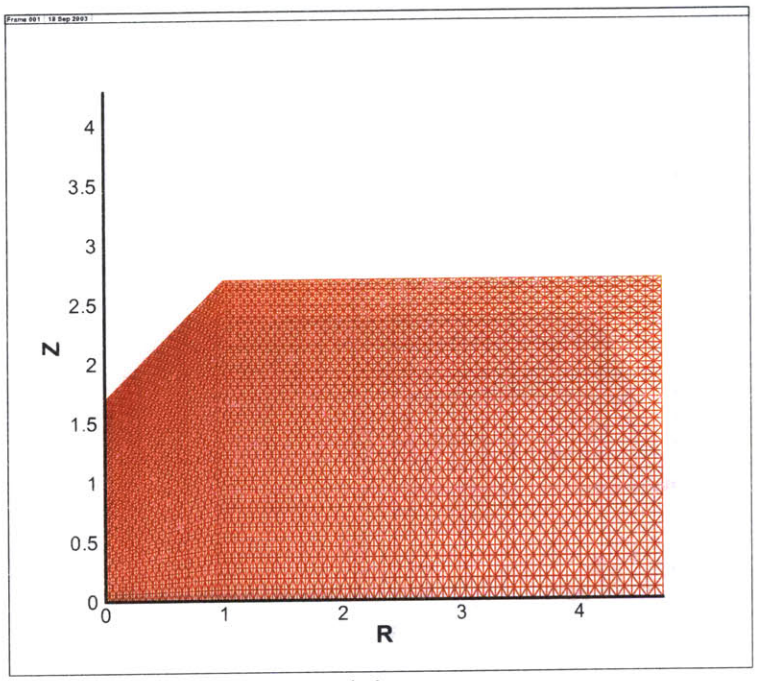

(a)

(b)

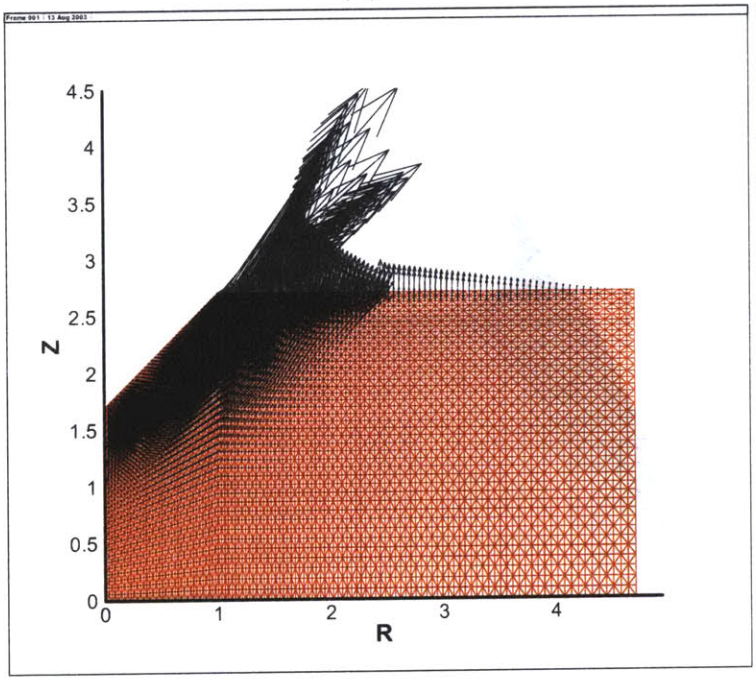

Figure 6-24: (a) Mesh for $\varphi = 10°$. (b) Failure mechanism for $\varphi = 10°$. $i = 45°$.

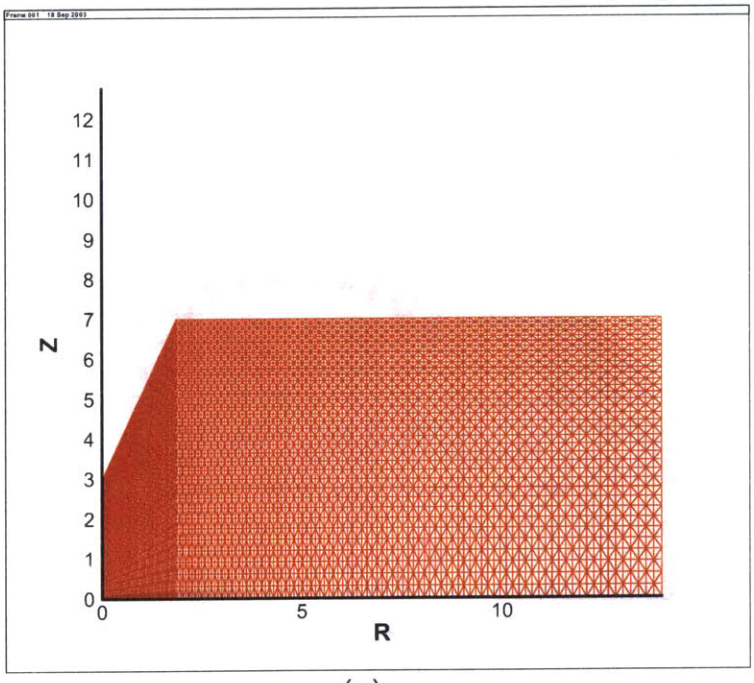

(a)

(b)

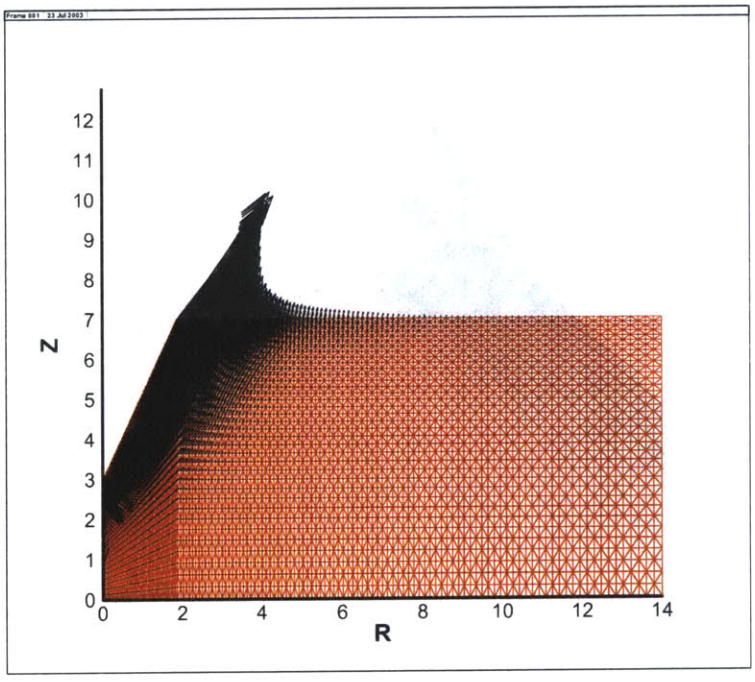

Figure 6-25: (a) Mesh for $\varphi = 10°$. (b) Failure mechanism for $\varphi = 10°$. $i = 25°$.

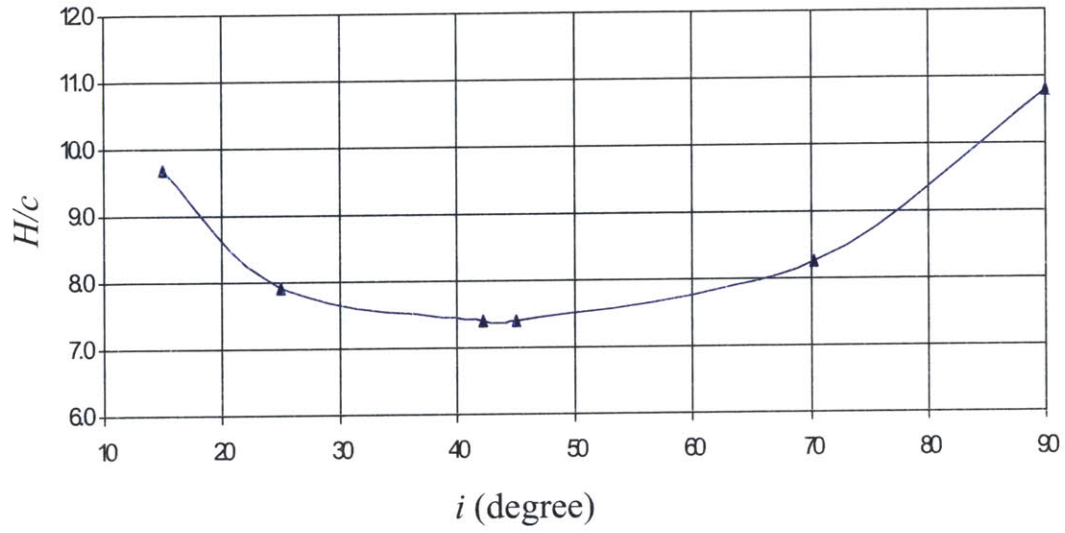

Figure 6-26: Influence of the semi-apex angle i on the hardness ($\varphi = 10°$).

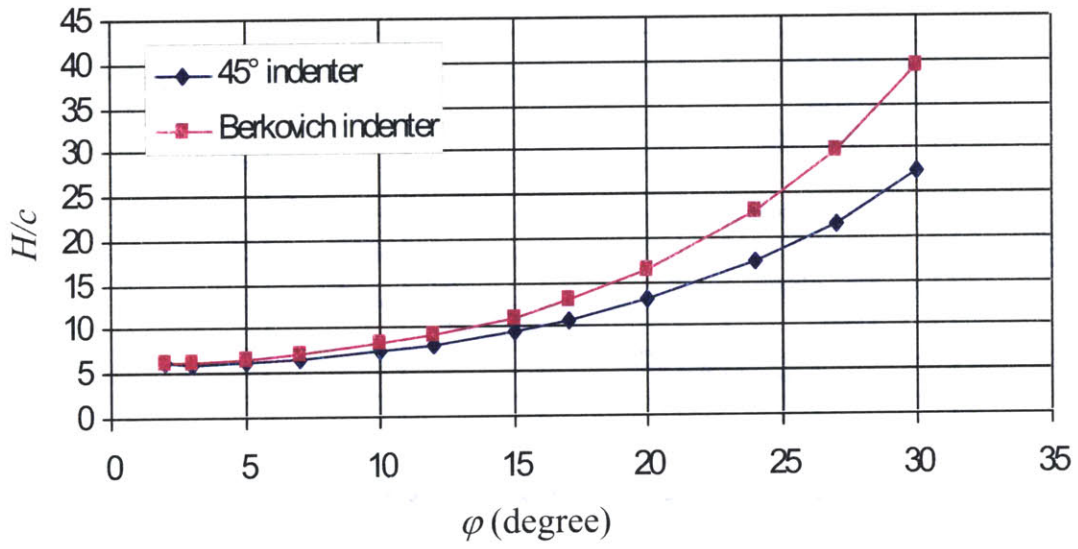

Figure 6-27: Upper bounds for the dimensionless parameter $\frac{H}{c}$. Berkovich type and 45° conical indenters.

6.5 Berkovich *Versus* Corner Cube Indentation

The Mohr-Coulomb criterion requires two different hardness tests in order to extract the cohesion c and the friction angle φ. An important finding of our study is that the Berkovich and spherical indenters deliver very similar hardness values. These two indentation tests therefore do not serve our purpose. In contrast, two conical indenters with significantly different apex angles yield relatively different hardness values, which meets our requirement.

From a practical point of view, it is convenient to employ standard indenters that are commercially available. We suggest a combined use of the Berkovich and the Corner Cube indenter which are both commonly employed for indentation tests. The Berkovich indenter can be assimilated to a cone of semi-apex angle $i = 70.32°$ (see Section 4.3.2). In turn, the three sided pyramidal Corner Cube, which has a total included angle of 90°, can be assimilated to a cone with a semi-apex angle $i = 42.28°$, which is very close to the minimum of the hardness versus apex angle relation (Fig. 6-26), and sufficiently different from the Berkovich type conical indenter. Figure 6-28 displays the normalized hardness-to-friction coefficient (i.e. $\tan(\varphi)$) for these two conical indentation tests. Figure 6-29 displays the hardness ratio of the

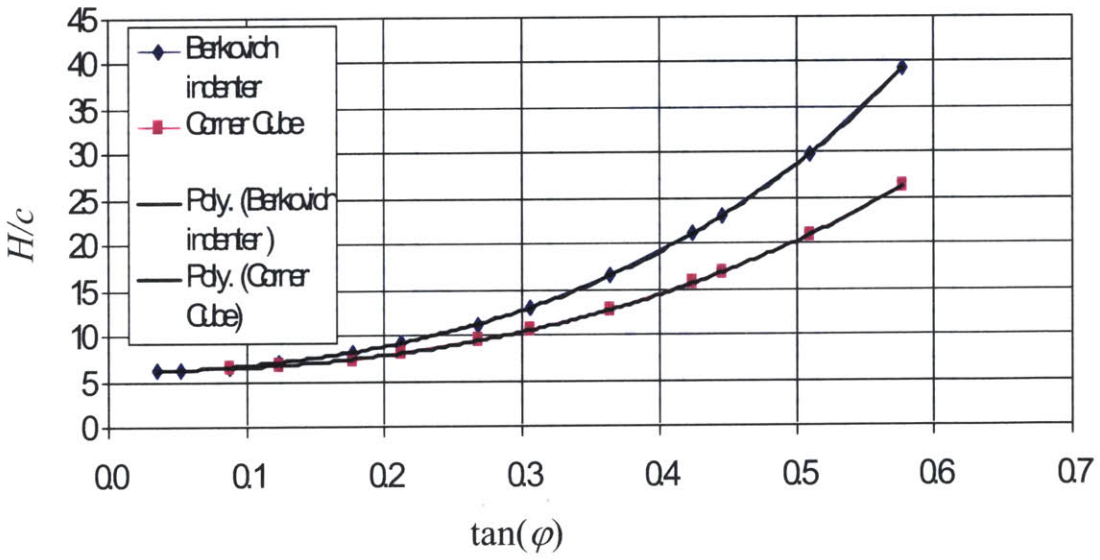

Figure 6-28: Fitting of the upper bound solutions by fifth order power functions. Berkovich and Corner Cube type conical indenters.

two indentation tests as a function of the friction angle. This result shows that there is a unique relation between the hardness ratio and the friction angle, which provides a means of assessing φ from the difference between a Berkovich indentation test and a Corner Cube indentation test. While relatively small for friction angles smaller than 10°, the ratio becomes significant for greater friction angles, for which the two indentation tests should provide a reliable means of extracting both the cohesion and the friction angle. We must mention here that the algorithm did converge for $\varphi = 2°$ and 3° for the Corner Cube, but the obtained dimensionless parameter values were both greater than for $\varphi = 5°$ and we therefore discarded the results. Finally, figure

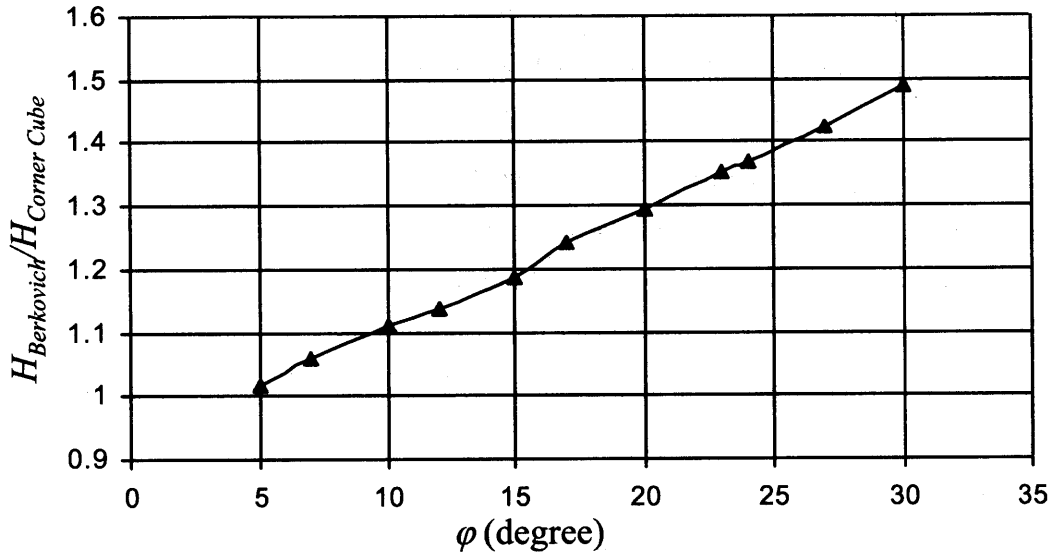

Figure 6-29: Evolution of the hardness ratio between a Berkovich indenter and a Corner Cube indenter with respect to φ.

6-28 also displays the fitting functions for the hardness-friction angle relations in form of fifth order power functions:

$$\frac{H}{c} = \sum_{k=0}^{5} a_k \tan^k(\varphi) \tag{6.11}$$

The coefficients a_k for the two indenters are given in Table 6.1.

The functions were determined using 13 values of the numerically determined $\frac{H}{c}$ relations, for which the fifth order power functions perfectly fit values of $\varphi \in [0, 30°]$. The functions may also serve for limited extrapolation to higher friction angles. We indeed ran simulations for

	a_0	a_1	a_2	a_3	a_4	a_5
Berkovich indenter	5.7946	8.6758	-18.21	338.82	-516.77	417.26
Corner Cube indenter	5.9455	5.8823	-20.974	259.91	-387.7	266.56

Table 6.1: Berkovich and Corner Cube indenters, fifth order power function fitting coefficients.

$\varphi = 35°$ and the result lay within the range of 1 % from the fitted values.

6.6 Conclusion and Appraisal of Method

The computational upper bound approach developed and employed in Chapter 5 and 6 provides a rational means to determine upper bound solutions for indentation tests. These upper bound solutions appear much more realistic than the lower bound solutions. This is strongly evidenced by the comparison of our upper bound solution with two reference solutions, the one of Cox et al. for a smooth flat punch (Section 6.2), and the one of Matar and Salençon for a rough flat punch (Section 6.3). In addition, the lower bound approach, because of its restriction to diagonal stress fields, is limited to a relative small range of possible solutions that appear too restrictive to come close to actual stress fields in indentation tests. In contrast, the upper bound approach is free of such restrictions and is able to accommodate any collapse mechanism. This and the excellent agreement of the flat punch solution with the reference solutions are very strong arguments in favor of the use of the upper bound solution for indentation analysis. This is why we suggest to consider only the upper bound solution to extract strength properties of cohesive-frictional materials from hardness measurements. In addition, as explained in Section 6.1.3, the upper bound solutions are available for friction angles greater than $2 - 3°$ (which should always be the case).

It was also shown that the ratio of the hardness estimated from a Berkovich indenter and a Corner Cube provides a unique correspondence with the friction angle (for $\varphi \geq 5°$). It should thus be possible to extract both c and φ from two simple indentation tests.

Finally, a fifth order power function appears suitable for fitting the upper bound curve (see Fig. 6-28). This function perfectly fits the curve for values of φ below 30° and in addition shows very good agreement for higher values.

Part III

Application to Nanoindentation

Chapter 7

Validation of the Indentation Solutions: Cohesion and Friction Angle of Metallic Glass

The third Part of this thesis is devoted to the validation of the yield design approach for indentation analysis, and to the application to shale materials. This Chapter deals with the validation of the upper bound solutions for a cohesive-frictional "model" material: the Vitreloy 1^{TM} metallic glass. The rational of validating our upper bound solution for this "model" material is twofold: (1) Vitreloy 1^{TM} is a fine-tuned man-made cohesive-frictional material which is much more homogeneous than highly heterogeneous "natural" composites (such as shales); (2) the cohesive-frictional nature of this metallic glass was recently identified by a comprehensive 3-D elastoplastic backanalysis of Berkovich indentation tests [88]. This study forms the background for the first part of this Chapter, in which we address the question whether the yield design approach is appropriate to capture the strength properties of an elastoplastic cohesive-frictional material. The second part of this Chapter aims at validating the proposed two-indentation test method, that is the extraction of cohesion and friction angle of metallic glass from a Berkovich and a Corner Cube indentation test.

7.1 Metal Glass Materials

7.1.1 General Presentation[1]

Most metals do crystallize as they cool, arranging their atoms into a highly regular spatial pattern called a lattice. But if crystallization does not occur, and the atoms settle into a nearly random arrangement, the final form is a metallic glass. The difficulty in making a metallic glass is to cool the metallic liquid (which has a disordered structure as well) down rapidly enough so that there is not enough time for the ordered, crystalline structure to develop. In the original metallic glasses (developed about forty years ago [74]), the required cooling rate was quite fast (as much as a million degrees Celsius per second). More recently, new alloys have been developed that form glasses at much lower cooling rates, around 1 to 100 degrees per second. While still fairly rapid, it is slow enough that bulk ingots of these metallic alloys can be cast, and they will solidify to form glasses. Metallic glasses are mostly prepared by casting methods[2] or by consolidation of glassy powders in the supercooled liquid region, through a process of warm-extrusion [49].

Metallic glasses owe their exceptional mechanical properties to their disordered atomic structure. Because of this disordered structure, amorphous metals (termed metallic glasses) exhibit different deformation mechanisms compared to polycrystalline metals. The vast majority of metallic glasses are homogeneous at all length scales greater than a few atomic diameters[3] (i.e. beyond the first few neighboring atomic shells). This assumes, however, that there are no fluctuations in composition. Some metallic glass-forming alloys phase separate by spinodal decomposition [42], introducing fluctuations from approximately 2 to 100 nm, and maybe larger. In this case one can consider that the material is homogeneous on length scales of more than one micrometer (10^{-6} m). Some recent work suggests that amorphous alloys do have structure on the 2 nm length scale, sometimes referred to as "medium-range order". Hufnagel et al. [43] have used fluctuation electron microscopy to examine this order in Zr-based alloys. The most

[1] This paragraph is strongly inspired and adapted from Pr. Hufnagel's presentation at http://www.jhu.edu/~matsci/people/faculty/hufnagel/hufnagel.html.

[2] An alloy ingot is prepared by arc melting pure metals in a purified argon atmosphere. Bulk amorphous alloys are then prepared in Pd or Zr based system by repeated melting of their molten alloys fluxed with B_2O_3 (from [64]).

[3] In the near-neighbor environment, of course, the atoms are not homogeneously distributed. Amorphous alloys can be considered to be homogeneous at length scales of more than about one nanometer.

recent models of structure of metallic glasses [63] postulates the existence of atomic clusters, with icosahedral[4] symmetry, of about this length scale.

7.1.2 Mechanical Properties

Bulk metallic glasses have been of great technological and scientific interest since their discovery in 1960 [74], and are considered today as emerging structural materials due to their high strength and large elastic deformation capacity prior to the onset of plastic deformation (see Fig. 7-1). Typical metallic glass has a Young's modulus on the order of $E = 100$ GPa, and uniaxial tensile strength of roughly 2 GPa for Zr-based glasses (between 1.3 and 1.5 GPa for Pd-based metallic glasses), thus allowing for a pure elastic deformation, in uniaxial tension of about 1/50 for Zr-based glasses (compared to 1/400 for steel). In addition, metallic glasses posses an excellent strength to weight ratio, usually around 300 kPa/kg/m^3 (compared to 63 kPa/kg/m^3 for steel). These exceptional mechanical performances make metallic glasses an extremely appealing material and have prompted intensive research.

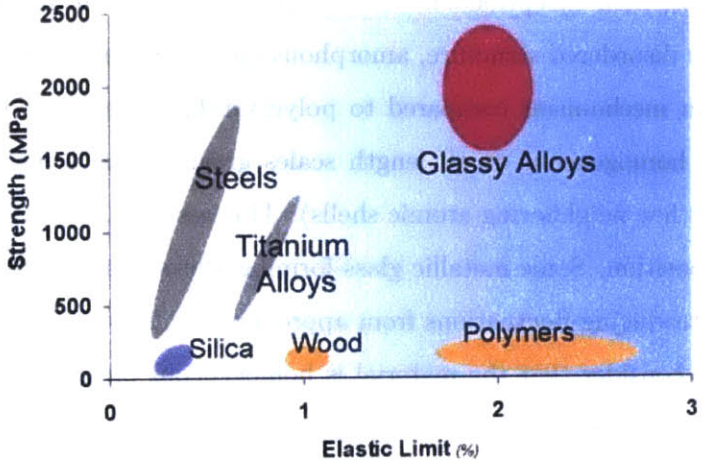

http://www.its.caltech.edu/~vitreloy/development.htm)

Figure 7-1: Typical strengths and elastic limits for various materials. Metallic glasses (Glassy Alloys) are unique.

[4] The isocahedral group is the point group of symmetries of the icosahedron and dodecahedron.

7.1.3 Cohesive-Frictional Behavior

There is a growing body of both experimental and theoretical evidence [22] [88] [73] [25] that metallic glasses are cohesive-frictional materials, that obey a Mohr-Coulomb criterion, and not purely cohesive materials of the Von Mises kind, as it was originally suggested.

Donovan [22] clearly evidenced the cohesive-frictional behavior of a Pd-based metallic glass at the macroscale, from uniaxial compression, plane-strain compression, plane-strain tension and pure shear tests. The macroscopic results proved that the $Pd_{40}Ni_{40}P_{20}$ metallic glass obeys a Mohr-Coulomb criterion with the following strength properties:

$$c = 0.795 \pm 0.025 \text{ GPa} \quad \text{and} \quad \tan(\varphi) = 0.113 \pm 0.03 \tag{7.1}$$

At the microscale, Vaidyanathan et al. [88] confirmed Donovan's finding for Zr-based Vitreloy 1^{TM} by means of a comprehensive 3-D elastoplastic backanalysis of microindentation tests. The results provide strong evidence that Vitreloy 1^{TM} metallic glass, at the microscale is not a Von Mises material but a Mohr-Coulomb material with the following strength properties:

$$c = 1.0816 \text{ GPa} \quad \text{and} \quad \tan(\varphi) = 0.13 \tag{7.2}$$

In addition, Schuh and Lund [73] provide theoretical atomistic arguments in favor of the cohesive-frictional behavior of metallic glasses. The key idea is that the relative motion of randomly packed atoms in a metallic glass is analogous to that of randomly packed particles in a granular solid [53]. This suggestion was confirmed by molecular statics simulations of Zr- and Cu-based metallic glasses, from which the authors derive the following friction angle:

$$\tan(\varphi) = 0.123 \pm 0.004 \tag{7.3}$$

It is remarkable to note from (7.1) to (7.3) that the friction angle of metallic glasses is scale transgressive: it is almost the same over at least eight orders of magnitude: from the scale of its atoms to the macroscale of laboratory test specimens. This scale independency is most likely related to the high homogeneity of the materials, a consequence of their amorphous structure. It is for these reasons that we have chosen metallic glass as a model material for validating our

yield design solutions.

7.2 Validation of Yield Design Approach

7.2.1 Focus of the Validation Set

The first validation case is performed by comparing semi-experimental data to our upper bound solution of a Berkovich indenter. The data were published by Vaidyanathan et al. [88]. With the study of this case we specifically want to validate the relevance and the quality of the yield design approach to establish a link between the nanohardness and the strength properties for cohesive-frictional materials. In fact, one may object that the very assumption of yield design approach, which only assesses the plastic dissipation at failure, is not appropriate for indentation analysis, which always includes an elastic and a plastic contribution (see Chapter 2, Section 2.3). The aim of this Section, therefore, is to show that the developed yield design approach applied to metallic glass allows one to extract strength properties from indentation tests.

The model material investigated in this Section is an as-cast fully amorphous, $Zr_{41.25}Ti_{13.75}Cu_{12.5}Ni_{10}Be_{22.5}$ (nominal composition at. %) alloy, manufactured by Howmet Corporation, Greenwich, CT (trade name Vitreloy 1^{TM}). It has a Young's modulus of $E = 96$ GPa [17] and a yield strength of $\sigma_y = 1.9$ GPa [88]. The density of Vitreloy 1^{TM} is 6.1 g/cc (strength to weight ratio of 328 kPa/kg/m^3). As mentioned in Section 7.1.1 the metallic glasses are extremely homogeneous materials and therefore very suitable for our validation sets.

7.2.2 Vaidyanathan et al.'s 3-D Elastoplastic Backanalysis

The background study of this validation is the comprehensive 3-D elastoplastic analysis of indentation test on Vitreloy 1^{TM} by Vaidyanathan et al. [88]. In this study, the authors analyzed two series of microindentation tests, carried out with a Berkovich indenter. The maximum indentation depths were 5 μm and 9 μm (see Fig. 7-3 (b)), the specimen dimensions were $2 \times 0.7 \times 0.3$ cm, and adjacent indents were separated by at least 10 μm.

3-D finite element simulations on ABAQUS modeling the six-fold geometry of the Berkovich

indenter[5] were performed assuming either a Von Mises or a Mohr-Coulomb criterion and finite deformation characteristics. A total of 11,040 eight noded, isoparametric elements were used to capture deformation modes. Figure 7-2 presents the overall mesh as well as the area directly in contact with the indenter.

The elastic properties used in the simulation are $E = 96$ GPa and $\nu = 0.36$ [17]. The predicted elastic response displayed in Figure 7-3 (a) is in excellent agreement with the loading portion of the two series of indentation experiments.

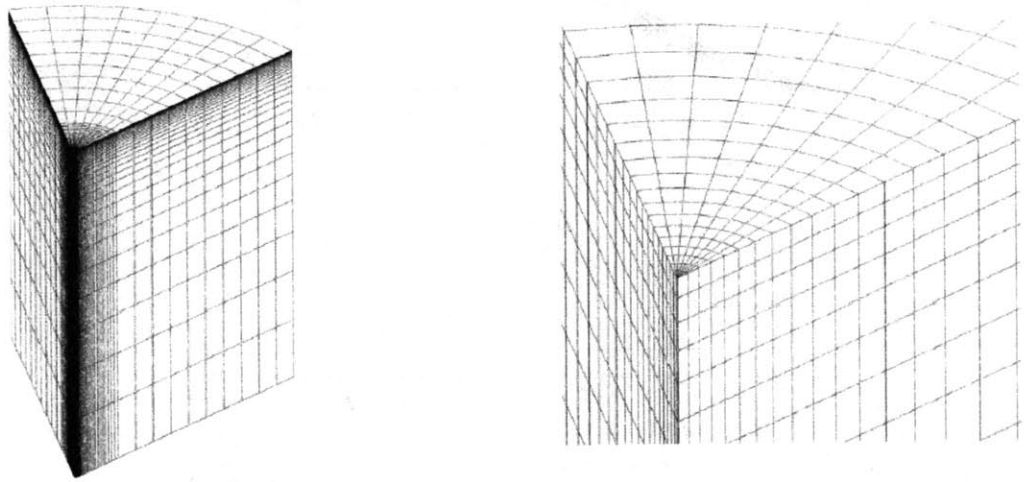

Figure 7-2: Overall mesh and detailed view of area in contact with the indenter tip (from [88]).

Using known elastic properties [17] and yield strength data (tensile yield strength of 1.9 GPa) Vaidyanathan et al. performed finite element simulations to investigate the yield criterion influence. For the Mohr-Coulomb criterion, the strength parameters were established so as to satisfy macroscopic tensile yielding and to fit the loading-unloading curve. Their main finding, which is summarized in Figure 7-3 (b), is that the metallic glass does not follow the Von Mises criterion but rather a Mohr-Coulomb criterion. The best fit was obtained with a friction coefficient $\alpha = \tan(\varphi) = 0.13$, that is a friction angle of $\varphi = 7.41°$, and a cohesion of $c = 1082.6$

[5] The model takes into account the real pyramidal geometry, not the associated cone ($i = 70.32°$).

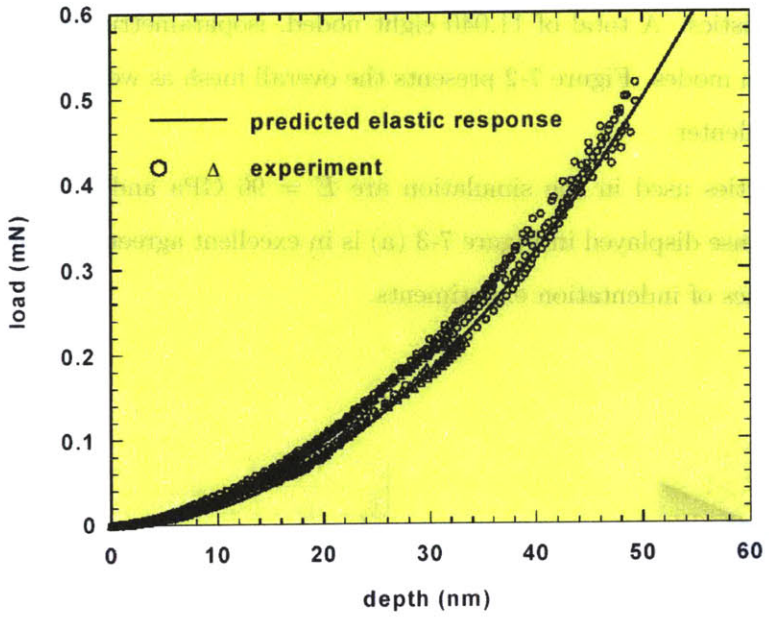

(a)

(b)

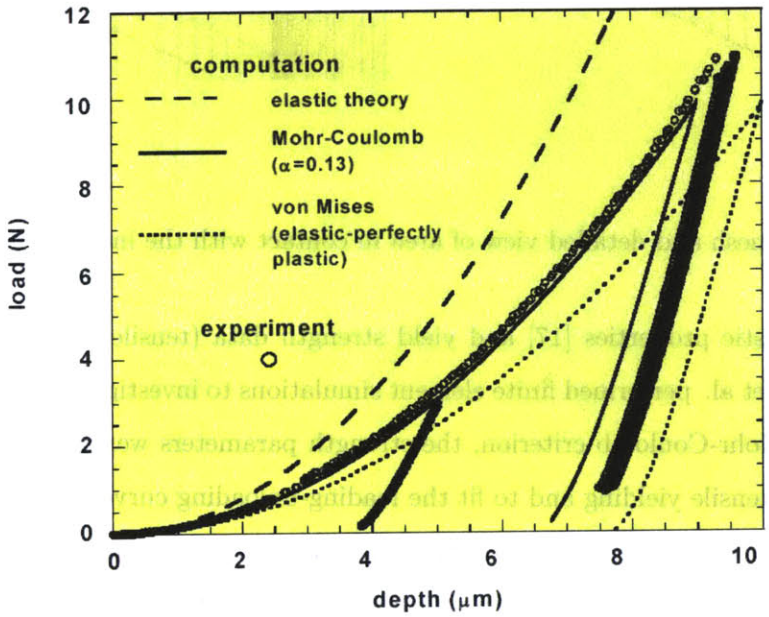

Figure 7-3: (a) Nanoindentation response of metallic glass during elastic loading (from [88]). (b) Microindentation response of metallic glass during loading and unloading (from [88]).

MPa. This friction angle compares well with the value of $\alpha = 0.11 \pm 0.05$ previously reported by Donovan [22] for $Pd_{40}Ni_{40}P_{20}$ metallic glass. To our knowledge, this work by Vaidyanathan et al. is the only comprehensive elastic-plastic analysis of indentation using a Mohr-Coulomb criterion for metallic glass.

7.2.3 Experimentally Determined Input Parameters

This Section presents the input parameters we need for our first validation set. Our upper bound solution for a Berkovich indenter (Section 6.4.1) established a link between the hardness H and the strength properties, c and φ, for a cohesive-frictional material. It is then easy to recast this relation as a link between the ratio of hardness to tensile yield strength and friction angle (Fig. 7-4):

$$\frac{H}{\sigma_y} = \mathcal{G}(\varphi) \tag{7.4}$$

where the tensile yield strength for a Mohr-Coulomb material is given by:

$$\sigma_y = \frac{2c\cos(\varphi)}{1+\sin(\varphi)} \tag{7.5}$$

Therefore, the only input parameters we need, are the tensile yield strength and the hardness.

- The tensile yield strength has been experimentally determined:

$$\sigma_y = 1.9 \text{ GPa} \tag{7.6}$$

- The hardness has also been experimentally determined:

$$H = 5.67 \pm 0.17 \text{ GPa} \tag{7.7}$$

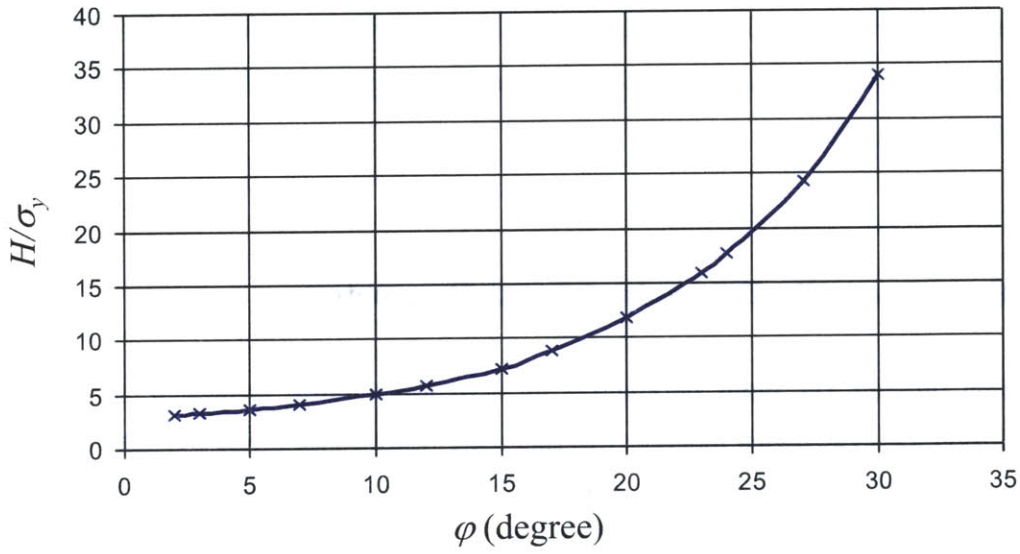

Figure 7-4: Evolution of H/σ_y as a function of φ.

7.2.4 Comparison With Yield Design Approach

We use our upper bound solution of the Berkovich indenter recast as a relation between H/σ_y and φ. Using (7.6) and (7.17) in (7.7), the computed ratio from the experimental data is

$$\frac{H}{\sigma_y} = 3.0 \tag{7.8}$$

yielding the following results for the metal glass (Vitreloy 1^{TM}):

$$\varphi = 3.0^\circ \quad \text{i.e.} \quad \tan(\varphi) = 0.052 \tag{7.9}$$

and from (7.5)

$$c = 1001 \text{ MPa} \tag{7.10}$$

These results, based on the yield design approach, are in good agreement with the results of [88], obtained by a 3-D elastoplastic backanalysis; especially for the cohesion (about 7 % of relative difference).

It is interesting to note that our approach does not need the elastic properties to obtain a

good estimate of the strength properties since we estimate the plastic dissipation which is not affected by the elastic properties.

A second way of validating our approach is to use our upper bound solution of the Berkovich indenter with the friction angle estimated from [88]: $\varphi = 7.41°$. This yields[6] $\mathcal{F}(\varphi) = \frac{H}{c} = 6.3$ and with the experimentally determined hardness H of 5.67 GPa (from (7.7))

$$c = 908 \text{ MPa} \tag{7.11}$$

This value compares well to the cohesion obtained by Vaidyanathan et al. through an elasto-plastic backanalysis (about 16 % of relative difference). Finally Figure 7-5 (a) presents the failure mechanism for $\varphi = 7.41°$ obtained with our upper bound approach. This failure mechanism appears to be consistent with the experimentally observed pile-up deformation around the indenter as displayed in Figure 7-5 (b).

This is the belief of the author that the classic definition of the hardness may be unsuited for cohesive frictional materials, and with respect to our yield design analysis. The following Section is an attempt to define a more meaningful value to only take into account the plastic dissipation.

7.2.5 Hardness Assessment

Yield design is based on the assumption that a material system, at plastic collapse, has exhausted its capacity to store any additional external work dW_{ext} into recoverable elastic energy. This is expressed by the Clausius-Duhem inequality, which at the structural level and for isothermal evolutions reads:

$$\frac{d\mathcal{D}}{dt} = \frac{\delta W_{ext}}{\delta t} - \frac{d}{dt}\int_\Omega \psi d\Omega \geq 0 \tag{7.12}$$

where

$$\frac{dW}{dt} = \frac{d}{dt}\int_\Omega \psi d\Omega \tag{7.13}$$

[6] We ran another simulation for $\varphi = 7.41°$.

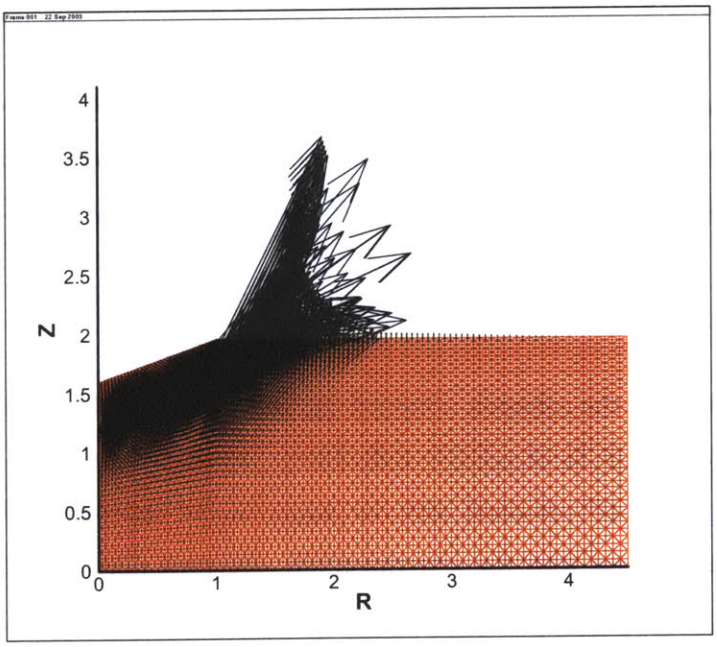

(a)

(b)

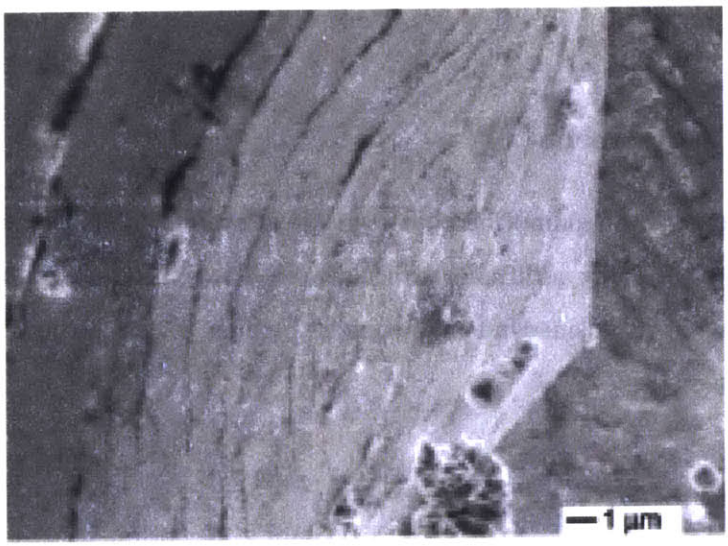

Figure 7-5: (a) Failure mechanism for $\varphi = 7.41°$. Berkovich indenter. (b) Shear bands on impression from Berkovich indenter face (from [88]).

is the variation of the recoverable free energy (see [87] Chapter 9 for a more detailed presentation). At plastic collapse, $\frac{dW}{dt} = 0$, which means that the yield design approach, or more specifically the upper bound approach, estimates the plastic dissipation at failure (cf. Section 5.1.1). At the same time, the unloading portion of the indentation test is purely elastic (see Fig. 7-6), and the elastic work W_e is not negligible with respect to the plastic work W_p. Therefore, to be consistent with the theory and the model we have developed, the hardness should relate to the dissipated plastic energy W_p which, in turn, should improve the quality of the prediction. We propose that the hardness be computed as the ratio of the driving force P by the contact area at "effective plastic depth" $A(h_{ep})$ (see Fig. 7-6):

$$H^* = \frac{P_{\max}}{A(h_{ep})} \tag{7.14}$$

We should mention here that the "effective plastic depth" is usually different from the residual depth h_r since the end of the unloading curve is often poorly defined because of contact problems (see Fig. 7-6). The "effective plastic depth" h_{ep} is conveniently extrapolated by fitting a polynome to match the first two thirds of the unloading curve, as to get rid of the contact problems at the end of the unloading curve. In our model h_{ep} is estimated by the "extrapolated residual depth" h'_f, the output of the fitting polynome:

$$P_{\max} = a\left(h - h'_f\right)^m \tag{7.15}$$

where a, m and h'_f are fitted parameters. This relates to several theoretical attempts to estimate the "corrected effective depth", in particular to the Oliver and Pharr method [69] (cf. Section 2.3). This new definition of the "hardness" H^* relates to our analysis of yield design and strength properties. This definition is valid as long as the "pile up height" is negligible compared to h_{ep}, which seems to be the case for the Berkovich indenter (see for example Fig. 7-7 (b)). But we have to account for the significant pile up occurring in a Corner Cube indentation test by estimating h_{ep} from the following relation:

$$h_{ep} = h'_f + h_{pile\ up} \tag{7.16}$$

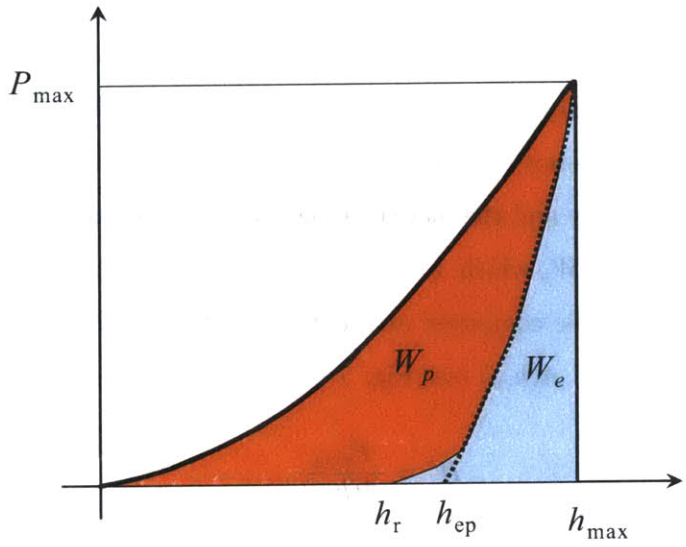

Figure 7-6: Definition of the "effective plastic depth" h_{ep}. W_p is the plastic energy, W_e the elastic energy and h_r the residual depth.

where $h_{pile\ up}$ is the "pile up height", that is the difference between the "top of the pile" and the initial contact point (initial $h = 0$). The value of $h_{pile\ up}$ could "theoretically" be estimated from a profilometer scan, but in practise this is a very time consuming and difficult task (see Section 7.3).

From Figure 7-3 (b) we can compute H^* for the two series of experiments. Table 7.1 contains details of this calculation. The two results are very consistent with each other[7] and the derived hardness is:

$$H^* = \frac{P_{\max}}{A(h'_f)} = 8.0 \text{ GPa} \tag{7.17}$$

7.2.6 Comparison With Yield Design Approach Revisited

This section reanalyses the results presented in Section 7.2.4, but using our new definition of the hardness H^*.

[7] This is readily understood since the indentation test is self-similar.

	5 μm experiment	9μm experiment
Maximum driving force $P_{\max}$ [N]	3	11
Extrapolated residual depth h'_f [μm]	3.9	7.5
Pile up Height [μm]	*negl*	*negl*
Hardness H^* [GPa]	8.03	7.96

Table 7.1: Details of parameters for the two microindentation series.

We use our upper bound solution of the Berkovich indenter recast as a relation between H^*/σ_y and φ. Using (7.6) and (7.17) in (7.4), the computed ratio from the experimental data is

$$\frac{H^*}{\sigma_y} = 4.2 \tag{7.18}$$

yielding the following results for the metal glass (Vitreloy 1$^{\text{TM}}$):

$$\varphi = 7.6^\circ \quad \text{i.e.} \quad \tan(\varphi) = 0.133 \tag{7.19}$$

and from (7.5)

$$c = 1085 \text{ MPa} \tag{7.20}$$

These results, based on the yield design approach and a modified expression of the hardness, are in excellent agreement with the results of [88], obtained by a 3-D elastoplastic backanalysis; namely about 2.6 % of relative difference for the friction angle and less than 1 % for the cohesion.

In the same vein as in Section 7.2.4, a second way of validating our approach is to use our upper bound solution of the Berkovich indenter with the friction angle estimated from [88]: $\varphi = 7.41^\circ$. This yields[8] $\mathcal{F}(\varphi) = \frac{H^*}{c} = 7.28$ and with the estimated hardness H^* of 8.0 GPa

$$c = 1099 \text{ MPa} \tag{7.21}$$

This value is very close to the cohesion obtained by Vaidyanathan et al. through an elasto-plastic backanalysis (about 1.5 % of relative difference). The new definition of hardness greatly improves the accuracy of the determination of the strength parameters from a Berkovich indentation test.

[8] We ran another simulation for $\varphi = 7.41^\circ$.

	Vaidyanathan et al. [88]	classic UB approach	UB approach & H^*
Cohesion c [MPa]	1082.6	1001	1085
Friction angle φ [°]	7.4	3.0	7.6

Table 7.2: Comparison of the strength properties.

7.2.7 Summary of the Validation Test

This validation set is based on the upper bound solution of the Berkovich indenter recast as a relation between the hardness over tensile yield strength ratio and the friction angle. From the experimentally determined ratio we derive an estimate of the friction angle, and then the cohesion from the formula linking the two strength parameters to the tensile yield strength (relation (7.5)). The validation based on the classic definition of the hardness shows that the yield design approach appears relatively sound to model the indentation tests and leads to good estimates of the plastic properties. The introduction of a new definition for hardness greatly improved the predictions, but needs further study to be confirmed as a valid approach. Table 7.2 summarizes the validation results.

7.3 Validation of the Two Indentation Test Method

7.3.1 Focus of the Validation Set

The second validation set focuses on the determination of both strength properties c and φ from a combination of Berkovich and Corner Cube indentation test. The validation compares experimental results on the Vitreloy 1^{TM} metal glass to our upper bound solutions. Specifically, we want to verify the relation between friction angle and hardness ratio for Berkovich and Corner Cube indenters (see Fig. 6-29).

7.3.2 Two Indentation Test Results

The tests were carried out by Georgios Constantinides in the nanolab facilities at MIT. Surfaces were polished with silicon carbide papers to obtain a very flat and smooth surface finish.

Following the experiments of Vaidyanathan et al. in [88], the Vitreloy 1^{TM} was indented to a penetration depth of about 10 μm. Series of a hundred tests were carried out using a

	E [GPa]	H [GPa]	$H_{corrected}$ [GPa]
Berkovich indenter	95.14 ± 1.82	5.67 ± 0.17	5.67 ± 0.17
Corner Cube indenter	124.25 ± 2.06	8.06 ± 0.26	5.02 ± 0.15

Table 7.3: Comparison of the strength properties. [Courtesy of G. Constantinides]

Berkovich and a Corner Cube indenter with a constant loading rate of 300mNs^{-1}. The specimen dimensions were $2\times1.5\times0.3$cm and adjacent indents were separated by at least 250μm to avoid any possible interference (same conditions as in Section 7.2.2); Figure 7-7 present SEM images of the indentation imprints.

A statistical analysis of the hundred indentation tests for each indenter yields the results summarized in Table 7.3. Two points deserve a particular attention: (1) the elasticity modulus of the two tests does not coincide, and (2) the Corner-Cube hardness value is greater than the Berkovich hardness value.

The elasticity equation used for extrapolating elastic properties of the indented material from the unloading portion of the indentation response has been proven to be a general characteristic of indentation. It is unaffected by the plastic properties of the materials and is a mere reflection of its elastic behavior. As a consequence the elastic properties measured by indentation are expected to be insensitive to the indenter geometry provided that the correct contact area is accounted for. We therefore think that the discrepancy observed between the elastic modulus obtained from Berkovich and Corner Cube indentation (cf. Table 7.3) is a consequence of the extensive pile-up taking place under the Corner Cube indenter. We recall that the method used for extrapolating the contact area from the unloading portion of the curve, known as the Oliver and Pharr method, has its basis on the elasticity solution and cannot account for any pile-up phenomena. As a consequence the error is significant for the case of Corner Cube indentation whereas its prediction are quite accurate for the Berkovich indentation. Determination of the projected contact area for Corner Cube is both time consuming and difficult (particularly given the 3-sided non-circular impression and pile-up). In order to circumvent the necessity to measure the contact area, one may use the known elasticity of metallic glass (e.g. from Berkovich indentation), and back analyze the projected contact area from the unloading slope

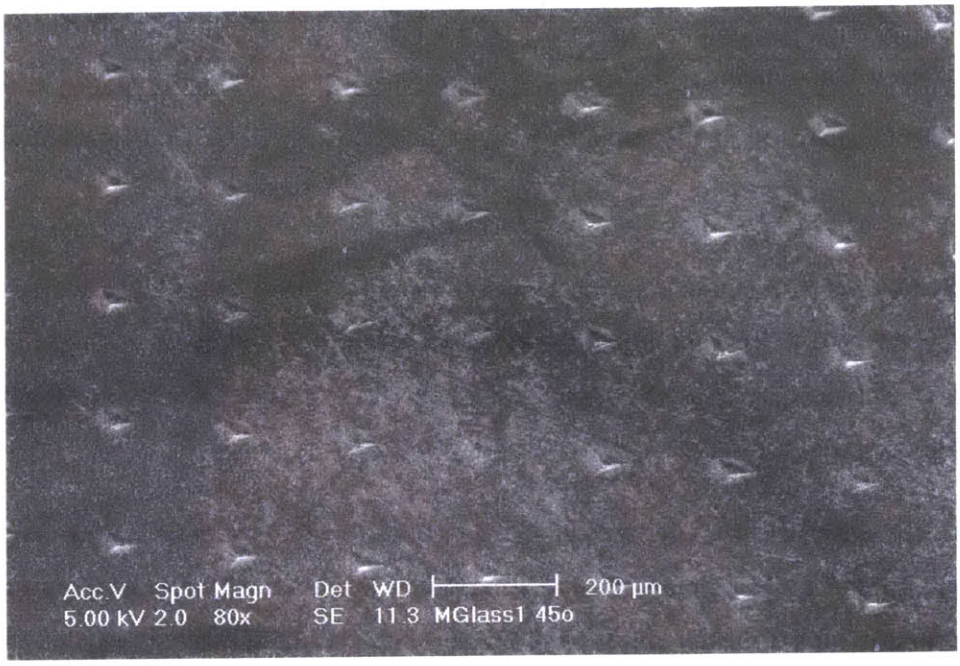

(a)

(b)

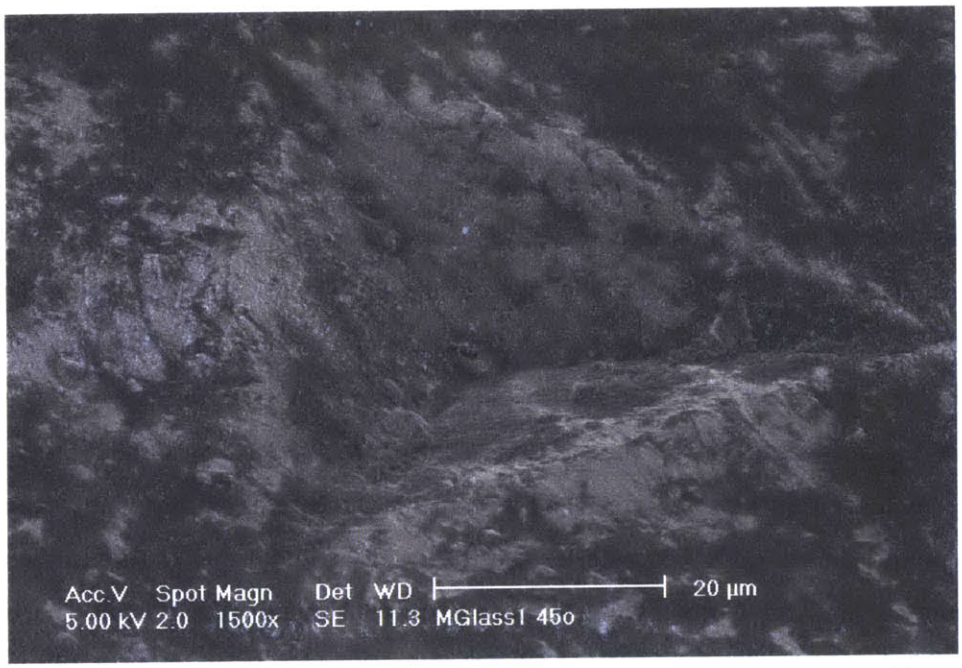

Figure 7-7: (a) SEM image of the indentation imprints. (b) SEM image of one indentation imprint. [Courtesy of Maria Paiva]

of the Corner Cube, based on relation (2.1) reproduced here:

$$\frac{dP}{dh} = c^* A^{1/2} E^* \tag{7.22}$$

This leads to a ratio between the corrected area and the experimentally determined area of

$$r_{el} = \frac{A_{corrected}}{A_{experimental}} = \left(\frac{E^*_{experimental}}{E^*_{corrected}} \right)^2 = 1.60 \tag{7.23}$$

and provides a first-order means to estimate the actual Corner Cube hardness within the limit of the accuracy of the unloading slope measurement, which is rather good for metallic glass since the experiments are easily reproducible and consistent with each other.

The values for the corrected hardness are given in the third column of Table 7.3. We note, as expected from our upper bound solutions (see Section 6.4.3) that the hardness evaluated from Corner Cube indentation is less than the hardness evaluated from Berkovich indentation.

7.3.3 Extraction of Strength Properties and Comparison with Published Results

Using the Classic Definition of Hardness

Based on the results of Section 6.5, the ratio between the Berkovich hardness and the Corner Cube hardness allows us to determine the friction angle. We start with the classic definition of the hardness. The computed ratio of 1.13 yields a friction angle of 11.2° (using the fitting function in Fig. 7-8); which in turn yields a cohesion of 655 MPa (using the fitting functions for the hardness-friction angle relation and the hardness value in (7.7)). With regards to the experimental results from Section 7.1.3, our results compare relatively well for the friction angle, and a little bit worse for the cohesion. This can be attributed to our simple evaluation of the projected contact area for the Corner Cube indentation tests.

Using Our New Definition of Hardness

The determination of H^* according to (7.14) requires determination of the projected contact area at "effective plastic depth". Using the extrapolation by means of power functions of the

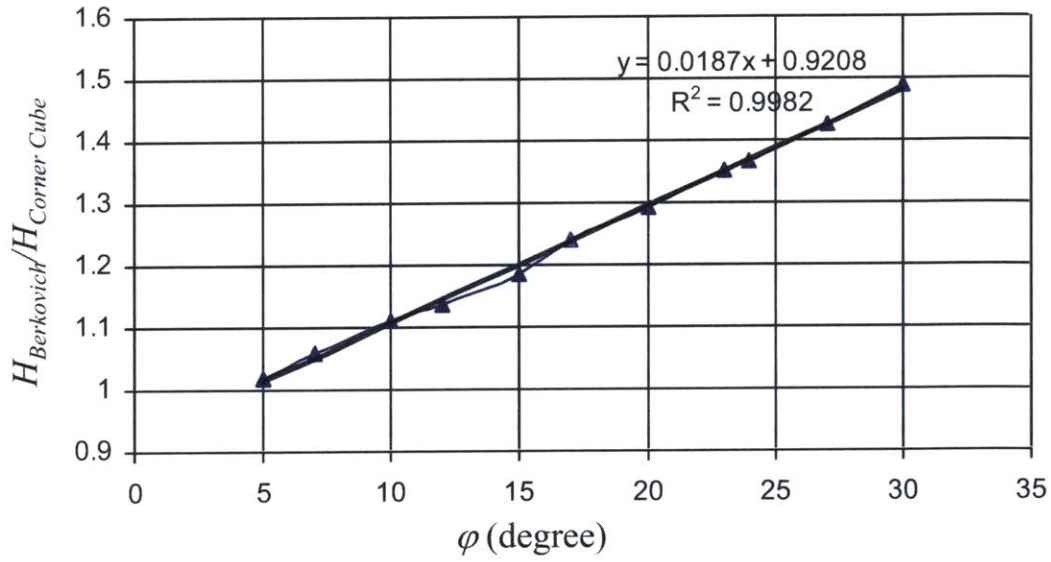

Figure 7-8: Evolution of the hardness ratios between a Berkovich indenter and a Corner Cube indener with respect to φ.

unloading branch is suitable for Berkovich indenter (which restrains because of its flatness excessive pile-up phenomena). It is more difficult for the Corner Cube due to the important pile-up phenomena that can freely develop because of the smaller apex angle; thus requiring a precise evaluation of the true projected contact area at "effective plastic depth", which takes into account the "pile up height" (recall that the effective plastic depth is meant to take only into account the plastic effects, see Section 7.2.5). Since the determination of the projected contact area for Corner Cube at "effective plastic depth" is both time consuming and difficult, the ratio $r_{el} = 1.60$ between the back analyzed "elastic" contact area and the "elastic" contact area given by the indenter (see Table 7.3 in Section 7.3.2) will be used to assess the contact area at effective plastic depth from the contact area estimated at the residual depth h'_f (accessible from the loading curves, see Section 7.2.5):

$$A(h_{ep}) = r_{el} A(h'_f) \tag{7.24}$$

This provides a first-order means to estimate the actual Corner Cube hardness within the limit of the accuracy of the unloading slope measurement. Figures 7-9 and 7-10 present typical

	Berkovich indenter	Corner Cube indenter
Max. load [mN]	11472 ± 172	1083 ± 32
Extrapolated residual depth h'_f [μm]	7700 ± 100	6800 ± 50
Pile up height [nm]	*negl*	N/A
Effective plastic depth, h_{ep} [nm]	7700 ± 100	N/A
Hardness H^* [GPa]	7.95 ± 0.2	5.7 ± 0.2[9]

Table 7.4: Comparison of the strength properties revisited. [Courtesy of G. Constantinides]

loading cycle for respectively a Berkovich and a Corner Cube indentation on Vitreloy 1^{TM}. Table 7.4 summarizes the needed parameters.

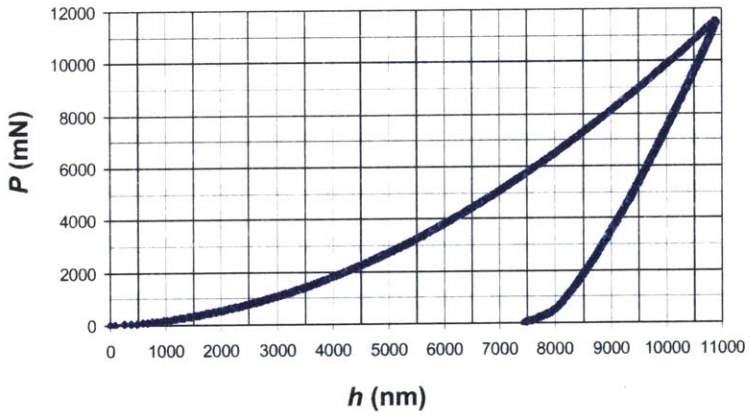

Figure 7-9: Loading cycle for a Berkovich indentation on Vitreloy 1^{TM}. [Courtesy of G. Constantinides]

The new ratio between the Berkovich hardness and the Corner Cube hardness allows us to determine the friction angle. The computed ratio of 1.39 yields a friction angle of 25° (see Fig. 7-8); which in turn yields a cohesion of 319MPa. Unfortunately, these results compare "relatively" poorly with the experimental results from Section 7.1.3. This can be attributed to our simple evaluation of the projected contact area at "effective plastic depth" for the Corner Cube indentation tests; and perhaps to our new definition of the hardness.

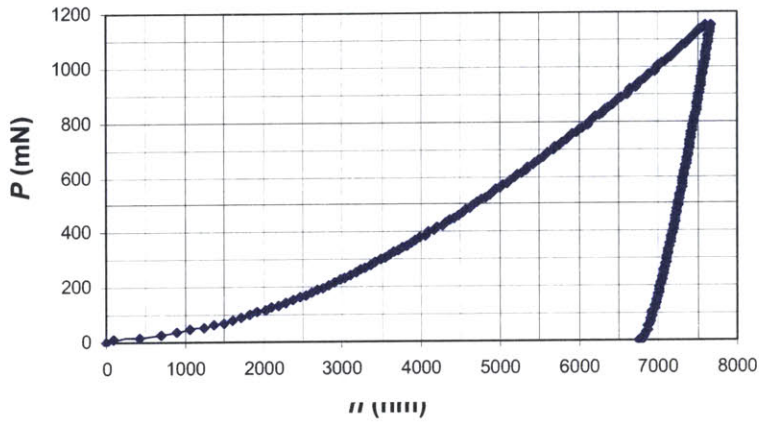

Figure 7-10: Loading cycle for a Corner Cube indentation on Vitreloy 1^{TM}. [Courtesy of G. Constantinides]

7.3.4 Summary of the Validation Test

The first important finding that should not be minimized is the actual difference in hardness values depending on the indenter; as well as the order of those values.

We encountered a problem in the determination of the correct contact area for the Corner Cube indenter. We tried to circumvent the necessity to measure the contact area by using the known elasticity of metallic glass, and back analyze the projected "elastic" contact area from the unloading slope of the Corner Cube. This is just a first-order means to estimate the actual Corner Cube hardness. However, as simple the method, it yields results on the same order as the experimental results. This is already satisfying in itself. On the other hand, the simplicity is at the expenses of the accuracy. In addition, using our definition of H^* did not improve the results; perhaps because of the simple contact area evaluation, or simply because our definition is unsuitable. But this has the merit of shedding some light on the difficulty of assessing the hardness based on a contact area definition, especially for cohesive-frictional materials.

7.4 Chapter Summary

The first validation set using the classic definition of the hardness led to relatively good results for the plastic properties of the Vitreloy 1^{TM} with regard to the experimental results found in the

literature. The introduction of a new definition for hardness greatly improved the predictions, but needs further study to be confirmed as a valid approach.

In turn, the second validation yielded satisfactory results for the friction angle and a reasonable estimate for the cohesion. This relative discrepancy with the experimental results can be attributed to the simple first order estimation of the contact area. Developing a method that can circumvent by design the need for measuring the contact area has been the hope for many experimentalists, and maybe we should focus on estimating the hardness, or a new property taking only the plastic effect into account, from an energy standpoint, or rather from a dissipated plastic energy W_p standpoint.

Finally we believe that the first validation using only the Berkovich indentation results as well as the verifications of our upper bound solutions give credibility and confidence in the global approach to derive good estimates on the strength properties of cohesive-frictional materials. This global approach will be applied in the next Chapter to shale materials.

Chapter 8

From Nano and Microhardness of Shale Materials to Macroscopic Cohesion Prediction

This Chapter serves as an application of our method to derive strength properties for cohesive-frictional materials from hardness measurements. The ultimate purpose is to show the usefulness of the model for such highly heterogeneous cohesive-frictional materials as shales. This application focuses on the cohesion and specifically the cohesion at different scales introduced by the heterogeneous nature of shale materials. In contrast to Chapter 7, in which we dealt with a extremely homogeneous material, we are here interested in shales, which exhibit heterogeneities at different scales. The first part of this Chapter is devoted to the presentation of shales and the hardness measurements; it is adapted form a research report to ChevronTexaco [86]. We shall identify the mechanically meaningful material scales for our analysis of the indentation tests. The second part focuses on assessing the cohesion at those different scales from nano and microindentation tests.

8.1 Introduction

Shales make up the majority of the geologic section in sedimentary basins, which is where most oil and gas exploration and production occurs. An understanding of shales is thus essential

for petroleum-related earth sciences. It is also well known that shale materials in oil and gas drilling applications are the major source of wellbore drilling instability, due to their highly heterogeneous and anisotropic composition. The strength properties, especially the cohesion c (cf. Section 1.1), of shales and other surrounding rocks play a critical role in the wellbore stability.

8.1.1 Context

This work contributes to a group project sponsored by ChevronTexaco which aims to assess, in a quantitative fashion and with high accuracy, the anisotropic elastic properties as well as the strength properties of shale materials at different scales: from the scale of the platy minerals of clays in the sub-micrometer range, to the scale of silt-size (quartz) grains in the micrometer range, to the scale of the deposition layers of shales in the sub-mm to cm range. The ultimate purpose of the project is to understand shale materials by breaking down such highly heterogeneous materials to the scale where physical chemistry meets continuum mechanics, that is where the intrinsic properties do not change from one material to another. Once this scale of invariant materials properties is identified, it will eventually be possible to upscale the intrinsic material behavior from the sub-microscale to the macroscale. Ultimately we could then reduce all mechanical field tests to some very elementary chemical tests to identify the phase volume fractions.

8.1.2 Challenge and Focus of the Application

The purpose of this third part is to estimate the macroscopic cohesion of the three shales from nano and microindentation tests with a Berkovich indenter[1]. What we specifically want to address is the possibility to extend the methodology developed in the previous Chapters to such highly heterogeneous materials like shales. We thus aim at contributing to the understanding of the strength properties evolution in shale materials at different scales.

Currently (November 2003), the Corner Cube test results on shales are not yet available, and we will therefore analyze the different scales in shale materials to relate the macroscopic friction angle, experimentally determined by triaxial stress tests [24], to the friction angle at

[1]Tests carried out by Georgios Constantinides at the Nanolab Facilities at MIT.

the nano and microscale. In regard to the validation in Chapter 7 for a Berkovich indenter, the hardness is estimated from:

$$H^* = \frac{P_{\max}}{A(h'_f)} \tag{8.1}$$

where h'_f is the extrapolated residual depth. All the tests presented here were carried out using a Berkovich indenter, so that the use of H^* makes sense.

Once we get an estimate of $\mathcal{F}(\varphi) = H^*/c$ (see relation (2.11)) at the nanoscale and combine this with the nanohardness values obtained experimentally, we have a means of assessing the cohesion c at the nanoscale. In turn, the two hardness measurements, at the nano and microscale, allow us to determine the Weibull modulus which we will use to extrapolate the cohesion from the nanoscale to the macroscale.

8.2 Presentation of Shales

The materials studied in this Chapter are three shale materials of different mineralogy provided by ChevronTexaco, labeled shale 1 to 3. The main difference in between the materials relates to the clay mineralogy and the porosity, as summarized in Table 8.1. The mineralogy was determined by quantitative X-ray diffraction by the mineralogy laboratory of ChevronTexaco. The porosity measurements were achieved by mercury injection (labeled 'M' in Table 8.1) and weight measurements (labeled 'W' in Table 8.1). In addition, the shale materials come from very different depths, ranging from 170m to over 3800m.

Shale 1 has the highest porosity of 26 %, measured by mercury injection; while shale 2 has a porosity of 13.25 %, and 7.48 % for shale 3. There appears to be a difference between the porosity measured by mercury injection, and by weight loss of a saturated versus a dry specimen ('W'). This difference may be attributed to structural (or non-evaporable) water that is extracted during oven-drying from a pore space that has a characteristic size still smaller than the characteristic pore throat radius in the tens of nanometer scale accessible by mercury intrusion. We also notice that the volume of the quartz inclusions for shale 1 is lower than for shales 2 and 3, for which it is very similar.

	Non Clay		Clay			Grain Density			Porosity [%]		V_I [%]
	Quartz	o	Si:Al=1:1	Si:Al=2:1	o	Min	Max	Mean	M	W	
Sl 1	17	8	35	33	6	2.6	2.8	2.7	26	26	25
Sl 2	23	9	19	36	13	2.6	2.9	2.8	13.25	17	32
Sl 3	21	9	9	54	7	2.6	2.9	2.8	7.48	12-14	30

Table 8.1: Mineralogy and Porosity of the shale materials: Si:Al=1:1 refers to Kaolinite, and Si:Al=2:1 refers to illite, illite-smectite, smectite, and possibly, muscovite. M=mercury injection porosimetry and W=wet-versus-dry weight measurements [all data from ChevronTexaco Mineral Analysis Laboratory]. Sl=Shale, o=others and V_I=Volume of the Inclusions.

8.2.1 A Multi-Scale Think Model of Shale Materials

Shale materials, like many other geomaterials, are highly heterogeneous materials, with heterogeneities that manifest themselves at multiple scales. For purpose of mechanical analysis, this complex microstructure can be broken down in four different scales, as sketched in Figure 8-1. These scales are discussed below[2].

Level '0': Scale of Elementary particles

The lowest level of shale materials is the one of the elementary particles of clay minerals. It is the scale of physical chemistry of clay materials and molecular models of the atomic structure of the different clay minerals. The characteristic length scale of the elementary particles is on the order of $1-2$ nm (10^{-9} m), and is governed by interatomic forces and potentials.

Level '1': Nanoscale of Mineral Aggregation

The minerals that form at lower scales aggregate to form platy mineral aggregates. Figures 8-2 through 8-7 display the typical appearance of these mineral aggregates as seen under a Scanning Electron Microscope (SEM) and an Environmental Scanning Electron Microscope (ESEM): Figures 8-2 to 8-4 display SEM images on a surface oriented normal to the bedding direction. From these figures it appears that the mineral aggregates, to which we refer as flakes, have a characteristic size of roughly 1000 nm (Fig. 8-2), and a thickness of roughly $100-250$ nm (Fig. 8-3), thus an aspect ratio greater than 4. While these flakes appear to have a privileged

[2]This multiscale characterization of the materials is still under investigation and has been briefly reviewed in [86].

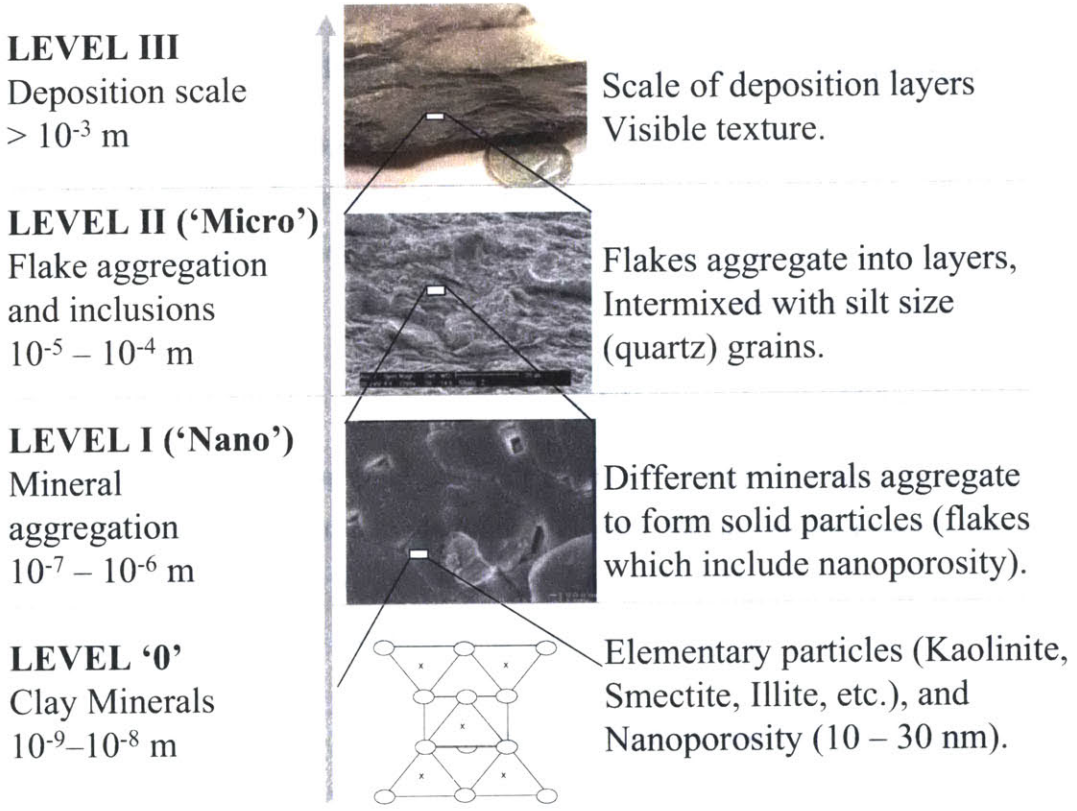

Figure 8-1: Multi-scale think model of shale materials: Four level microstructure.

orientation following the deposition direction, the SEM images also highlight that there is a fair amount of random orientation (see e.g. Fig. 8-4). This randomness (or rather weakly orientation) is confirmed by the ESEM images in Figures 8-5 to 8-6. Figure 8-5 which displays an image of the material in the bedding direction, confirms the elementary dimensions of the mineral aggregates, and Figure 8-6 highlights –at a larger scale– that the mineral aggregates are far from being perfectly aligned in the bedding direction.

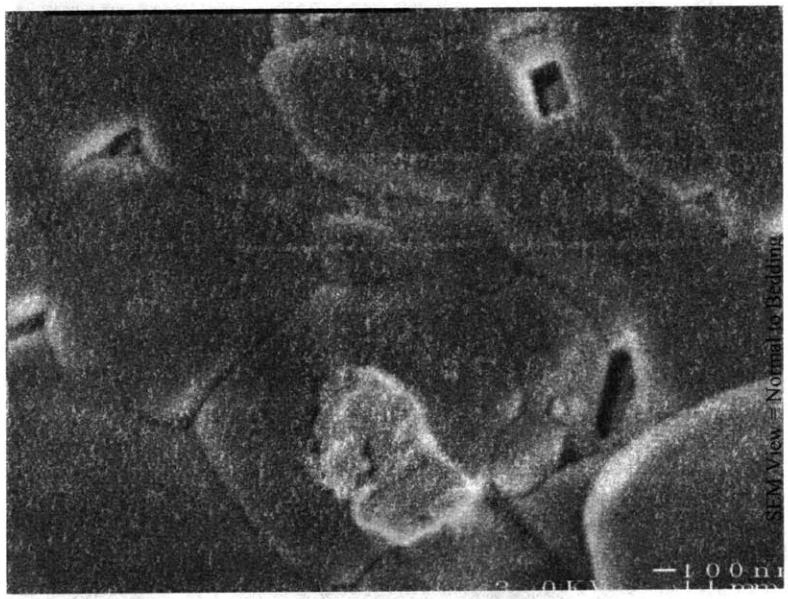

Figure 8-2: SEM-image of Shale 1-1 (View **normal** to bedding direction): The image shows the mineral aggregates of a characteristic dimension of 1000 nm.

Level 2: Microscale of Flake Aggregation

The flakes from level 1 aggregate into layers to form a visible layered texture of the shale materials. The ESEM images in Figures 8-7 and 8-8 display at two different magnifications this staggered scheme of flakes into flake aggregates of a characteristic length of several micrometers. The SEM images in Figures 8-9 and 8-10 show a similar feature at a slightly larger scale, displaying a layered structure of characteristic size in the tens of micrometer range, and an elementary thickness of roughly $1 - 5 \times 10^{-6}$ m. At the same scale, one can find traces of silt size quartz grains, intermixed in the flake aggregates (see Figs. 8-9 and 8-10).

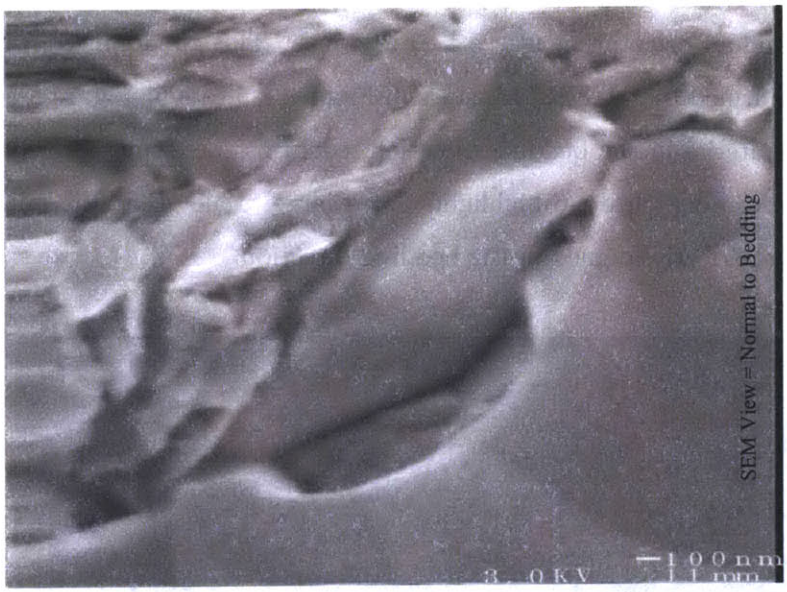

Figure 8-3: SEM-image Shale 1-1 (View **normal** to bedding direction): The image displays on the right bottom side a mineral flake of the similar form as in figure 8-2, adjacent to a zone where the flakes are oriented rather randomly.

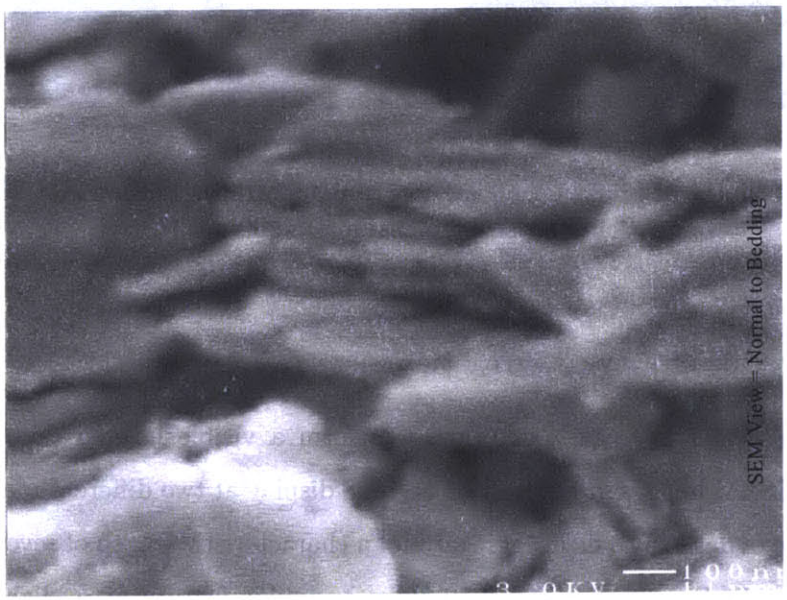

Figure 8-4: SEM image Shale 1-1 (View **normal** to bedding direction): The image shows some platelet structure of submicron dimension. Since this picture is taken normal to bedding, the image indicates that there is a fair amount of randomness in the mineral aggregate orientation.

Figure 8-5: ESEM image Shale 1-2 (View **in** bedding direction): The image shows the elementary dimension of the mineral aggregates: length = 1000 nm; thickness = 100 – 250 nm.

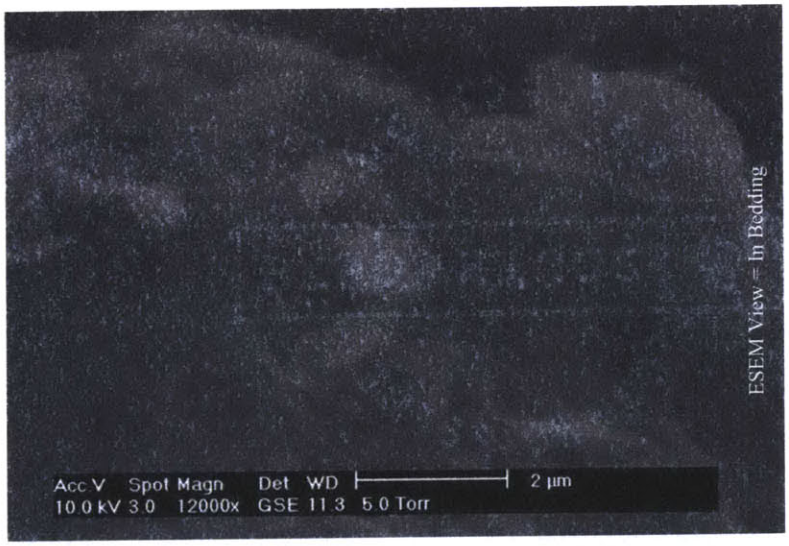

Figure 8-6: ESEM image Shale 2-2 (View **in** bedding direction): The image displays that there is a fair amount of randomness in the orientation of the mineral aggregates of submicron dimension.

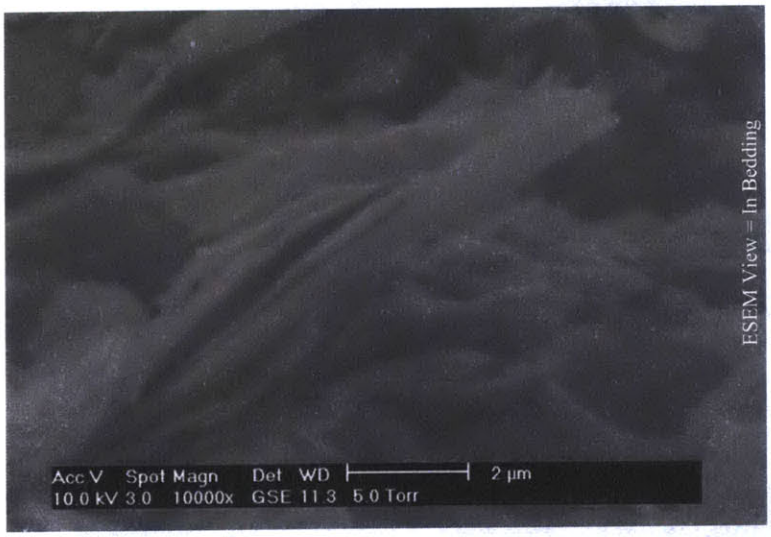

Figure 8-7: ESEM image Shale 2-2 (View **in** bedding direction): The image shows the aggregation of weakly oriented flakes into a layered structure.

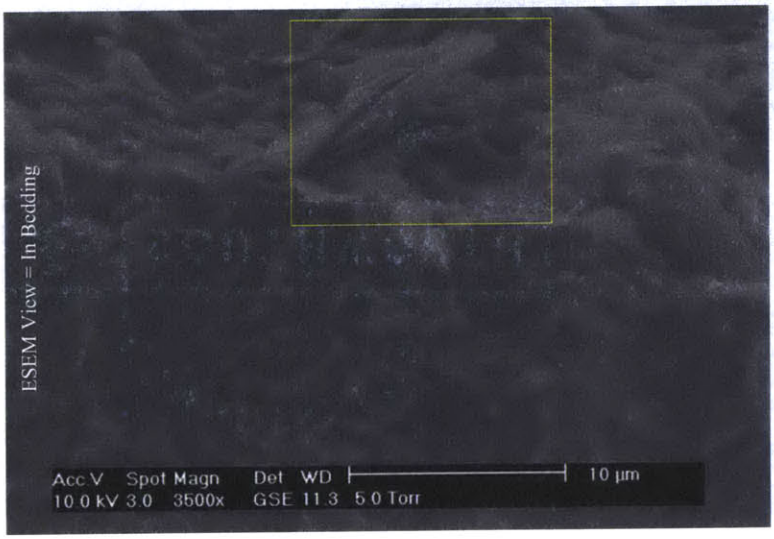

Figure 8-8: ESEM image Shale 2-2 (View **in** bedding direction): Same as Fig. 8-7 (size of frame) at a larger scale. Image highlights the flake aggregation.

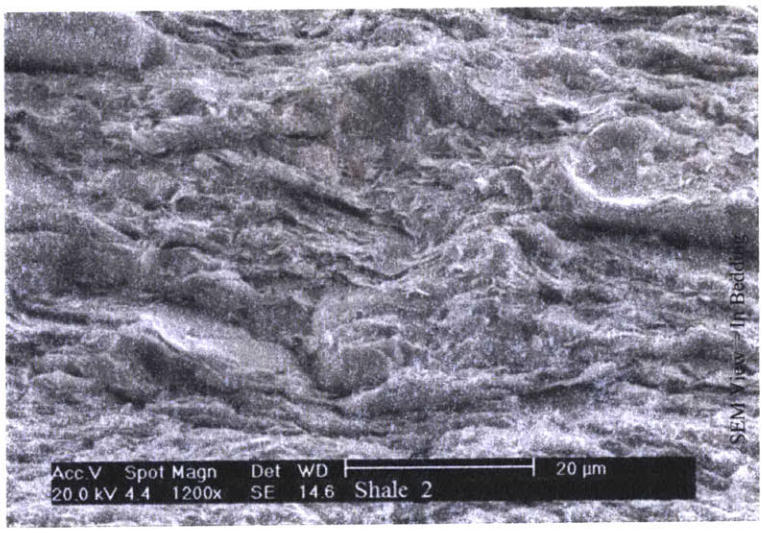

Figure 8-9: SEM image Shale 2 (View **in** bedding direction): The image shows the layered structure of shales in the tens of micrometer range. The image also shows some circular inclusion patterns that may well be attributed to silt-size grains [Image from ChevronTexaco].

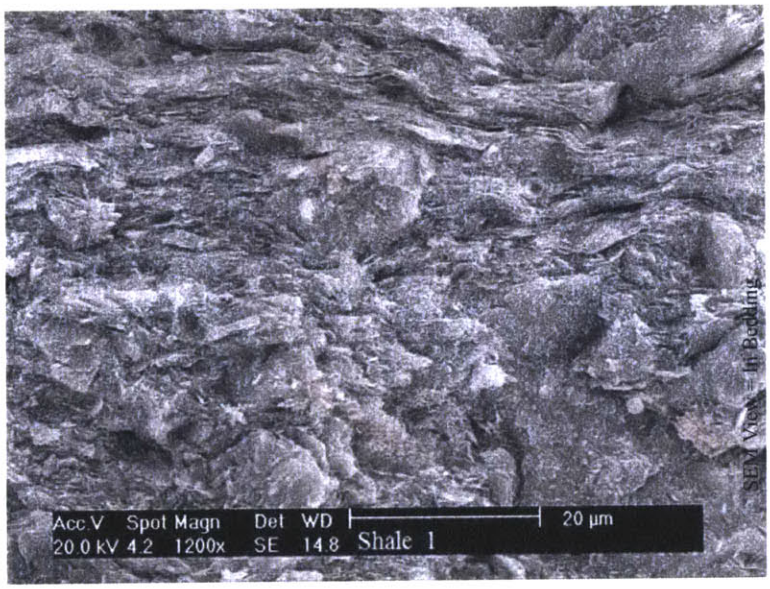

Figure 8-10: SEM image Shale 1 (View **in** bedding direction): The image shows the typical layered structure of shales in the tens of micrometer range. Some inclusion patterns can be attributed to silt-size grains [Image from ChevronTexaco].

Level 3: Scale of Deposition Layers

The macro scale of shale materials is the one of the deposition layers, having an elementary thickness in the millimeter range. This scale at which the materials are known to exhibit a transversal isotropic behavior, is the classical scale of macroscopic material testing of shale materials.

8.3 Nano and Microhardness of Shales

The focus of the nano and microindentation tests is on Level 1 ('nano') and Level 2 ('micro').

8.3.1 Test Presentation

Figures 8-11 and 8-12 show examples of typical nano and micro-indentation test. By 'nano'-indentation, we refer to tests in which the maximum indentation depth is smaller than one micrometer ($= 10^{-6}$ m), while 'micro'-indentation refers to tests with maximum indentation depths within $1 - 10$ μm. We should mention one more time that the hardness is estimated

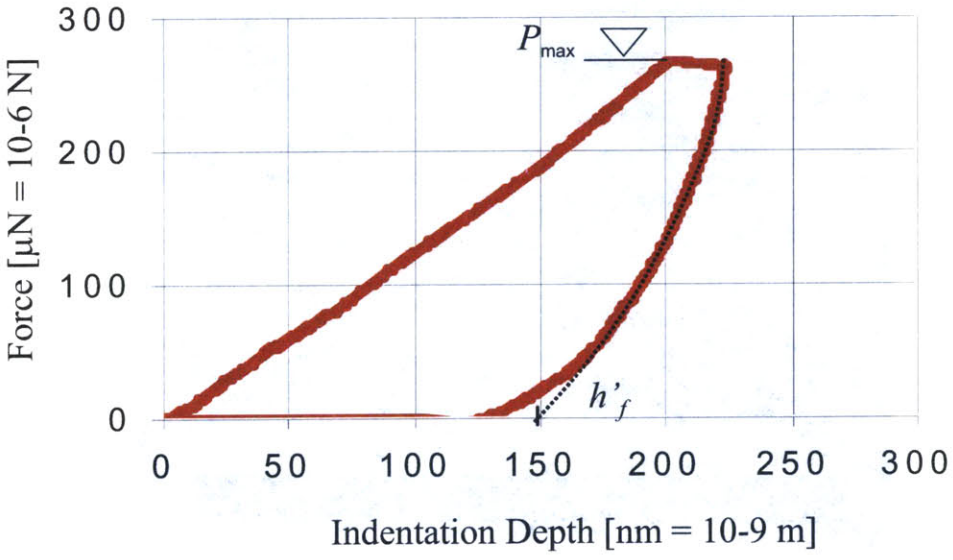

Figure 8-11: Typical result of **nano**-indentation test on shale materials (here Shale 1 normal to bedding). The figure displays the loading and the unloading response: $P_{\max} = 267$ μN; $h_{\max} = 224$ nm.

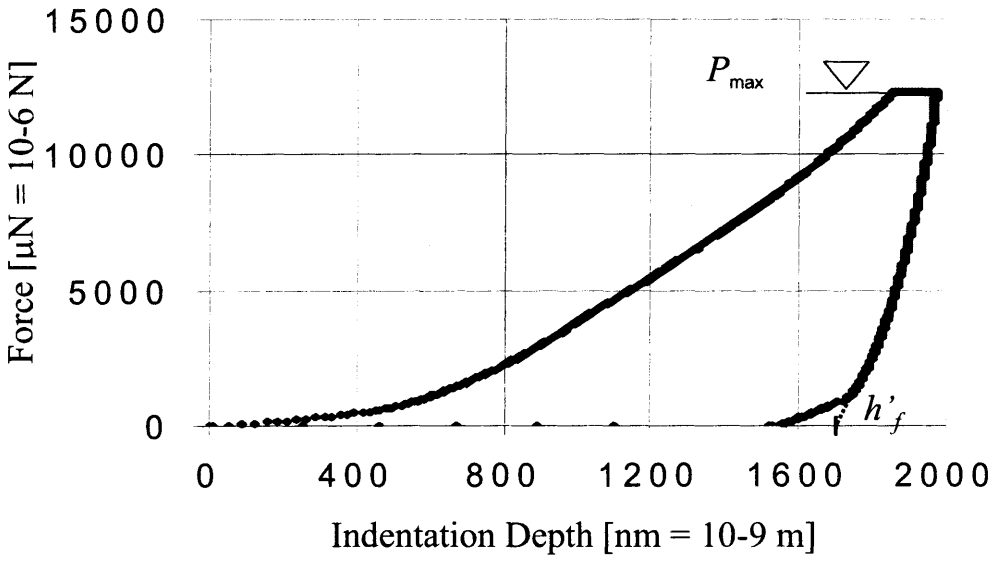

Figure 8-12: Typical result of **micro**-indentation test on shale materials (here Shale 1 normal to bedding). The figure displays the loading and the unloading response: $P_{\max} = 12,304\,\mu$N; $h_{\max} = 1,971$ nm.

from:

$$H^* = \frac{P_{\max}}{A(h'_f)} \tag{8.2}$$

where h'_f is the extrapolated residual depth.

Indentation gives access to bulk properties of the indented material at a length scale $\mathcal{L} \simeq 4 \times \max h$ (cf. Section 2.3), at which the material is considered homogeneous. The continuum assumption which is at the basis of the elasticity and strength–hardness formulas requires in addition that the characteristic length scale of the representative elementary material volume (r.e.v.) satisfies $\ell \ll \mathcal{L}$, where ℓ is the characteristic size of the heterogeneity. Given the highly heterogeneous nature of shale materials at different scales (see Fig. 8-1), it is unlikely that this condition is met in each indentation test. Hence, one needs to perform a sufficiently large number of indentation tests at different scales in order to extract mean values of the material properties and distributions.

	Nano level		Micro level	
	H^* [GPa]	h'_f [nm]	H^* [GPa]	h'_f [nm]
Shale 1-1	0.619 ± 0.101	134.5	0.258 ± 0.017	1397
Shale 1-2	0.557 ± 0.088	141.9	0.236 ± 0.017	1461
Shale 1-3	N/A	N/A	0.249 ± 0.020	1452
Shale 2-1	0.539 ± 0.043	134.4	0.374 ± 0.027	1182
Shale 2-2	N/A	N/A	0.336 ± 0.028	1245
Shale 2-3	0.494 ± 0.051	140.8	0.376 ± 0.028	1178
Shale 3-1	0.579 ± 0.050	130.3	0.444 ± 0.028	1091
Shale 3-3	0.653 ± 0.053	122.9	0.385 ± 0.023	1168

Table 8.2: Mean values $\pm$ Standard deviation of nano and microhardness, and the related extrapolated residual depth for the three shales in different testing directions. x-1 corresponds to the direction normal to bedding, x-2 and x-3 are in bedding.

8.3.2 Results

Nano and microindentation tests were carried out on the three different shales materials with a Berkovich indenter. The test is a force driven experiment. Figure 8-13 presents the typical evolution of the classic hardness value defined as $H = P/A(h)$, where h is the penetration depth recorded during a microindentation test. The Figure shows that following a decrease for small penetration depth, the hardness becomes a constant value. The first range can be associated with a plastic contraction phenomenon, while the constant hardness at larger penetration depths is an indication that the projected contact area continuously adapts so that the average pressure below the indenter is constant. Given the highly heterogeneous nature of the materials, the results of a large number of tests need to be analyzed as frequency plots. Since a material (or a dominant phase) will be indented to the same depth, a frequency pic relates to a single material. Figures 8-14 and 8-15 present the hardness distribution and frequency for shales 1 and 3. These Figures clearly show the dominating phase, that is the frequency pic.

The results merit some comments: First, the hardness-penetration depth relations appear to be independent of the testing direction; that is the strength behavior is isotropic. Second, from the distributions, shale 3 (Fig. 8-15) exhibits a higher degree of order than shale 1 (Fig. 8-14), which exhibits different distributions in different directions. From the Figures, one can extract the hardness values H^* of the dominating phases for each shale and testing direction. These results are summarized in Table 8.2.

	Nano level		Micro level	
	H^* [GPa]	h'_f [nm]	H^* [GPa]	h'_f [nm]
Shale 1	0.593 ± 0.095	137.5	0.247 ± 0.023	1439
Shale 2	0.511 ± 0.047	138.3	0.371 ± 0.039	1188
Shale 3	0.620 ± 0.051	126.1	0.417 ± 0.038	1124

Table 8.3: Mean values $\pm$ Standard deviation of nano and microhardness, and the related extrapolated residual depth. Averaged values for the three shales.

Similarly, Table 8.3 presents the average values (i.e. taking into account all the tests in the different testing directions). Figures 8-16 and 8-17 illustrate the distribution in form of frequency plots of the averaged hardness H^* for the three shales. These frequency plots represent the probability to encounter, in an indentation test on a surface, a specific hardness, associated with the heterogeneous distribution of the materials at a scale below.

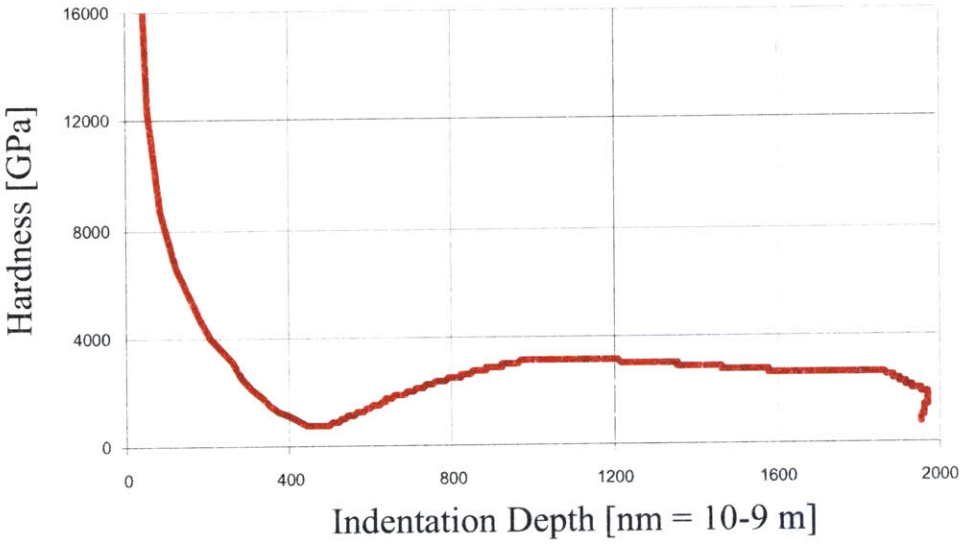

Figure 8-13: Evolution of the hardness with respect to the penetration depth.

8.3.3 Discussion

It is remarkable to note the perfect isotropy of the hardness values (see Fig. 8-14 and 8-15), which take the same value in the direction of bedding and normal to it, and this for both nanohardness and microhardness. This is remarkable in several regards: for one, a material

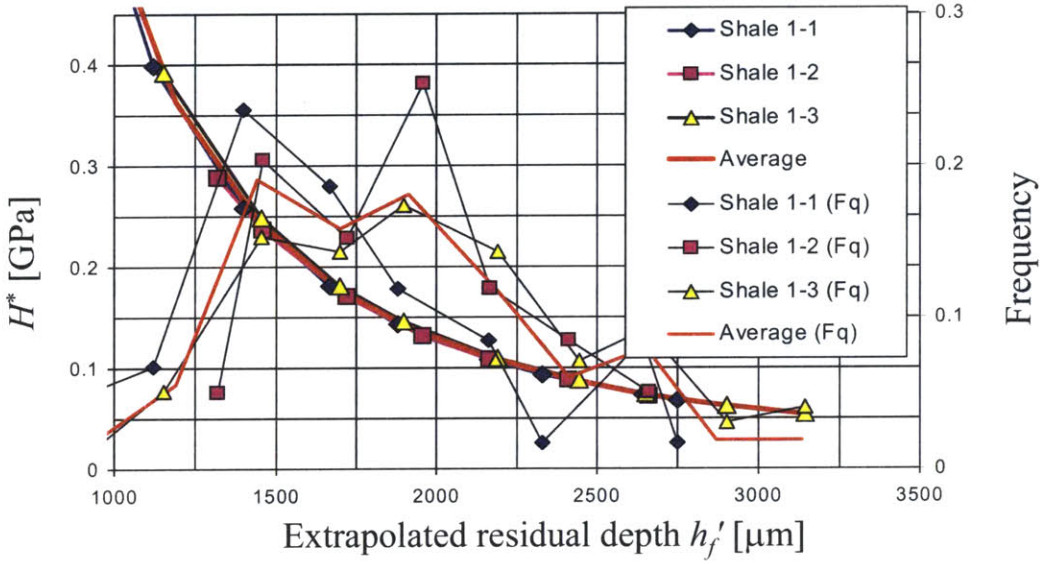

Figure 8-14: Hardness versus extrapolated residual depth and frequency plot of microhardness in the three directions for shale 1. Direction 1-1 is normal to bedding and 1-2 and 1-3 is in bedding.

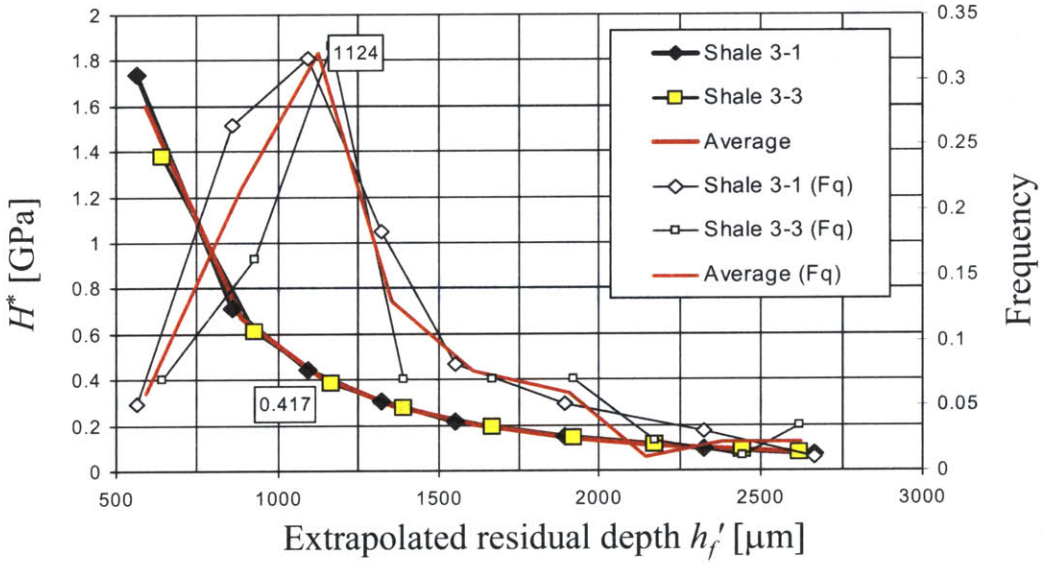

Figure 8-15: Hardness versus extrapolated residual depth and frequency plot of microhardness in two directions for shale 3. Direction 3-1 is normal to bedding and 3-3 is in bedding.

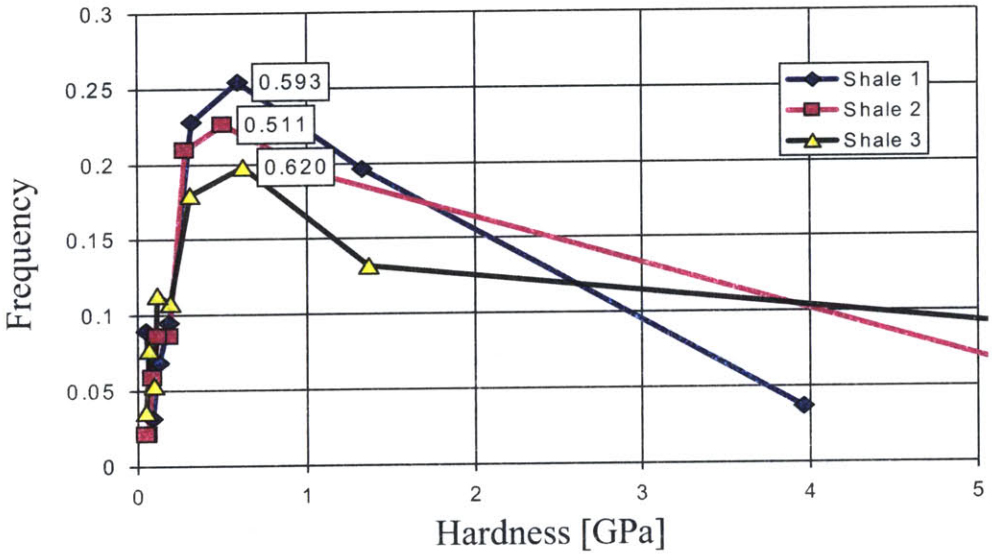

Figure 8-16: Frequency plot of nanohardness.

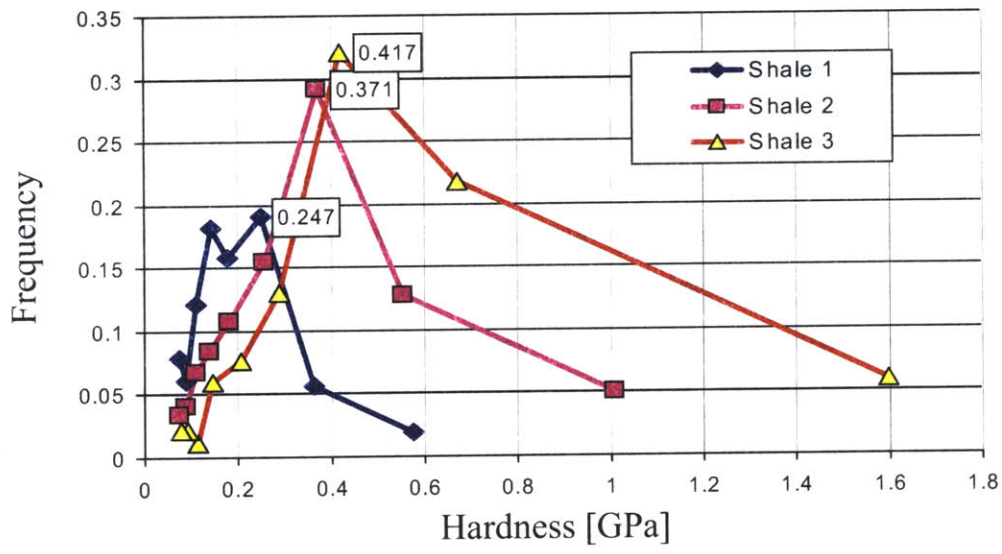

Figure 8-17: Frequency plot of microhardness.

which exhibits more or less pronounced anisotropic features in the elastic range, exhibits a pure isotropic hardness behavior, and this over almost two orders of length magnitudes. The result is, however, not surprising, as it confirms that the hardness values are related to strength properties only, after all elasticity reserves have been exhausted (see e.g. [87]). The isotropy of the hardness values, therefore, is a confirmation that the material is at free yield – in the sense of yield design theory.

The remarkable similarity of the nanohardness values[3] seems to suggest an independence regarding the mineralogy composition (cf. Table 8.1) that manifest itself at Level 0 (see Fig. 8-1). Indeed, the difference between nanohardness values is about 5 % of relative difference, whereas the mineralogy varies in much greater proportion.

In contrast, the microhardness values show some correlation with the porosity and the inclusion fraction of the materials. Indeed, Table 8.1 shows that shale 1 has the highest porosity (26 %), and thus a weaker structure, leading to a lower microhardness; while shale 3 that has the lowest porosity (7.5 %) has the highest microhardness. In terms of porosity, shale 2 is situated in between shales 1 and 3 (13.25 %). Furthermore, it has an inclusion fraction of roughly 30 %, which is very similar to shale 3 (in contrast to shale 1 that has 25 %, see Table 8.1). Concerning its microhardness, it may well be that the higher porosity of shale 2 (compared to shale 3) is somehow compensated by its inclusion fraction, so that the microhardness is on the same order as the one of shale 3 (and substantially higher than shale 1), and this despite its lower nanohardness value. Clearly here is an effect of the inclusions.

In summary, the microhardness values are a reflection of both the porosity and the inclusion fraction, while the nanohardness values appear to be neither sensitive to mineralogy nor to porosity. It could be hypothesized that the porosity in nanoindentation tests is de-activated because of the contracting behavior of the flakes during the indentation tests (as the hardness curves show so nicely, see Fig. 8-13). The nanohardness behavior seems to be an intrinsic *in situ* behavior of the compacted clayish matrix, that could be associated with the colloidal nature of these materials (e.g. electrostatic forces at interfaces). In contrast, the microhardness behavior is a consequence of the microstructure: the porosity manifests itself in the spaces between the mineral aggregates, which could be the locus of microscopic slippage planes. Thus,

[3] Particularly if one considers the standard deviations of $0.05 - 0.1$ GPa (see Table 8.3).

the higher the porosity, the more slippage planes in the material system. The inclusions in contrast become obstacles to this slippage, which could explain why shale 2 has a very similar microhardness as shale 3.

Also important is the scale effect between nano and microhardness. This scale effect is related to the highly heterogeneous nature of the shales (see Section 8.2.1); and very similar effects are usually seen in other composite materials, like concrete [90] [95] or bones [33]. We will have a closer look on these scaling properties of shales in the next Section.

8.4 Cohesion Assessment of Shales

8.4.1 Hypothesis

Since the Corner Cube results are currently not available, we will use our upper bound solution for a Berkovich indenter assuming that the friction angle at the nanoscale φ_n can be related to the macroscopic friction angle φ_M by [5]:

$$\tan(\varphi_n) = \tan(\varphi_M)\left(1+\frac{3}{2}V_I\left[1+\tan^2(\varphi_M)\right]\right)^{-\frac{1}{2}} \tag{8.3}$$

where V_I is the volume fraction of the inclusions. This formula has been derived for a Drucker-Prager yield criterion, which has the same dissipation functions as the Mohr-Coulomb yield criterion (see [87] or [72]), therefore making it suitable for our purpose. We should also mention that relation (8.3) excludes macroscopic failure planes and is based on a pure inclusion effect.

We will adopt a Weibull scaling law [91] to assess the macroscopic cohesion from the previously reported results. The Weibull model is a power relation between the properties and the length scale, based on the weakest link theory. The idea is that when considering a larger volume, the probability to encounter a weaker element increases [91] [26]. For our bulk nanoindentation test the Weibull scaling law reads:

$$c \propto [V_{eff}]^{-\frac{1}{m}} \tag{8.4}$$

where m is the Weibull modulus (a fitting parameter) and V_{eff} the effective volume, that is the bulk of the material affected by the test. From our indentation values in Table 8.3, m was

found to be around 20 for shales 2 and 3, and 8 for shale 1. Most ceramics are reported to have m values for the yield strength property in the range of 5–15, whereas metals, which produce ductile failures, have m values in the range of 30–100 [46]. Concrete, a highly heterogeneous frictional material, has a Weibull modulus of 12 for the yield strength [95]. Weibull moduli on Vickers hardness of sialon ceramics were reported to be between 23 (for a virgin sample) and 39 (for the samples crept at 1350 °C) [54], which is similar to what we have for shales 2 and 3. In general, a relatively high Weibull modulus ($m \geq 20$) indicates a smaller error range, and potentially, greater clinical reliability. Higher values of Weibull modulus correspond to a higher level of structural integrity of the material [7].

8.4.2 Methodology

The macroscopic friction angle is known for the three different shales as well as the volume fraction of the inclusions (results provided by ChevronTexaco, see Table 8.4). Using relation (8.3) yields the friction angle at the nanoscale φ_n. From the Berkovich nanohardness measurement we derive the corresponding nanohardness. Practically, we estimate the cohesion at the nanoscale c_n from (2.11):

$$c_n = H_n^*/\mathcal{F}(\varphi_n) \tag{8.5}$$

where H_n is the nanohardness given in Table 8.3. The macroscopic cohesion c_M is then assessed using (8.4):

$$c_M = c_n \left[\frac{(V_{eff})_M}{(V_{eff})_n}\right]^{-\frac{1}{m}} \tag{8.6}$$

The effective volume at the nanoscale $(V_{eff})_n$ is evaluated from our upper bound simulations; for a given friction angle we evaluate the volume affected by the failure mechanism (see Fig. 8-18). The effective volume at the macroscale is the volume of the shale tested in the triaxial test reported in [24].

Table 8.4 summarizes the relevant parameters for the extrapolation scheme.

8.4.3 Results and Discussion

Our Weibull model is based on the nano and microhardness results and is therefore fairly sensitive to those results. The difference in Weibull modulus for shale 1 is still under investigation,

	φ_M [°]	V_I [%]	m	$(V_{eff})_n$ [nm^3]	φ_n [°]	$\mathcal{F}(\varphi_n) = H^*_n/c_n$
Shale 1	11.8	22	8.0	$145\pi \left(\left(h'_f \right)_n \right)^3$	10.2	8.3
Shale 2	18.5	32	20.2	$420\pi \left(\left(h'_f \right)_n \right)^3$	15.1	11.1
Shale 3	10.9	30	16.5	$140\pi \left(\left(h'_f \right)_n \right)^3$	9.0	7.8

Table 8.4: Extrapolating parameters for Shales 1 to 3. The Weibull modulus is computed from the hardness values: $m = 3\ln[(h'_f)_{micro}/(h'_f)_{nano}]/\ln[H^*_{nano}/H^*_{micro}]$

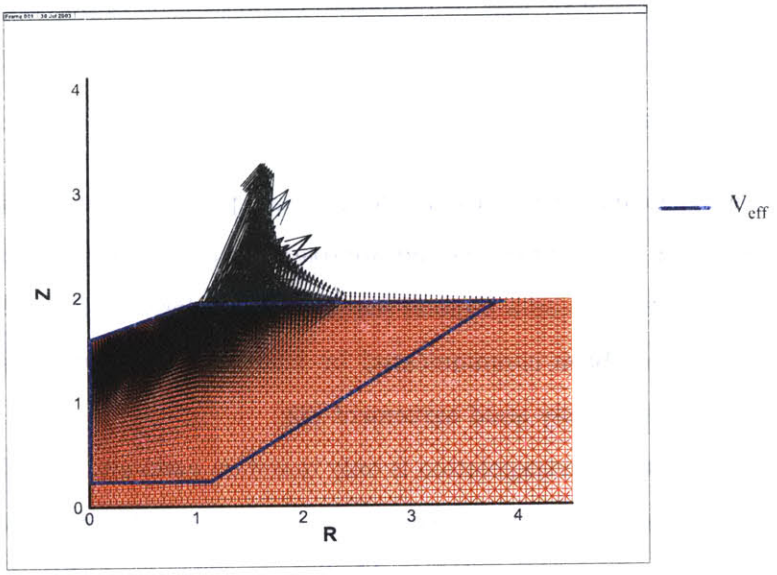

Figure 8-18: Example of determination of V_{eff}. $\varphi = 10.2°$.

but relates to the difference in hardness value between shale 1 and shales 2 and 3, and thus to the porosity. In fact, the lower Weibull modulus of shale 1 compared to shales 2 and 3 is an indication of the higher disorder of shale 1, compared to the highly compacted shales 2 and 3. This is consistent with the hardness distributions displayed in Figures 8-15 and 8-14.

The isotropy of the hardness is another strong argument in favor of the soundness of our yield design approach. The material at yield has exhausted the elasticity reserves and is therefore not influenced by the anisotropy of the elasticity.

The cohesion values at different scales are reported in Table 8.5. They might be on the higher range for shale materials because we did not take into account the friction planes, which manifest themselves at Level 3 (see Section 8.2.1), and which are likely to weaken the macrostructure.

	nanocohesion [MPa]	microcohesion [MPa]	macroscopic cohesion [MPa]
Shale 1	71.5	29.8	1.75
Shale 2	45.9	33.3	11.0
Shale 3	79.1	53.2	12.8

Table 8.5: Cohesion values of shale materials at different scales.

In addition, the difference between shale 1 and shales 2 and 3 seems to relate to the porosity and/or the volume of the inclusions; and requires more research. In the same way, the decrease in the cohesion with the length scale may be related to the activation of porosity at larger scale.

8.5 Chapter Summary

This case study shows the capability of the model to make predictions about the macroscopic cohesion. Estimates based on the upper bound approach developed in Chapter 6, on our new definition of the hardness H^* and on a Weibull scaling law are derived. Even though the exact macroscopic values have not been communicated by ChevronTexaco, we were told that our extrapolated values are in relatively good agreement [23].

It is useful to recall that our extrapolation is only based on nano and microhardness values; and one would need a third value at a penetration depth about $10,000$ nm to confirm the Weibull scaling law. Such a third test series would allow us either to confirm the scaling, or to refine it. In fact, the real macroscopic value is expected to be somehow smaller than the values predicted by the Weibull model as inclusions and interfacial properties may well add a higher degree of disorder to the system. In this case, our extrapolated values would help identifying the scale at which these mechanism enter the picture. Indeed, comparing the cohesion at different scales with the one estimated by the Weibull law one could easily determine at which scale inclusions and interfacial properties affect the strength properties.

Part IV

Conclusions & Perspectives

Chapter 9

Conclusions & Perspectives

This Chapter presents a summary of this study on the link between nanohardness and strength parameters for cohesive frictional materials. In addition conclusions are drawn underlining the main findings of this research. Some future research is finally proposed and perspectives on the strength properties assessment are given.

9.1 Summary of the Main Findings

Accessing material properties at or below the nanoscale represents a breakthrough for material science and this potential is far from being fully explored. From a material science perspective, the increased knowledge regarding indentation of cohesive-frictional materials is in itself helpful and opens a new era for probing material properties at such a small scale. Nanoindentation techniques makes it possible today to break down highly heterogeneous materials to the scale where physical chemistry meets continuum mechanics, that is when the intrinsic properties do not change from one material to another. Once this scale of invariant materials properties is identified it is possible to upscale the intrinsic material behavior from the sub-microscale to the macroscale. The research presented in this theses contributes to this goal through the development of a comprehensive method to reasonably assess the intrinsic strength properties for cohesive and frictional materials from two different sharp indentation tests.

The review of the existing informations in the open literature revealed some missing knowledge to link nanohardness to strength properties of cohesive-frictional materials. To address

this issue a yield design approach was implemented in a finite element code and the theoretical dimensionless function $H/c = \mathcal{F}(\varphi, i)$ (cf. relation (2.11)) was derived for a broad variety of indenter shape.

The theoretical study on the discretization of the limit analysis theorems, in axisymmetric conditions, revealed the following results:

- Our lower bound algorithm does not yield accurate results. It is readily understood since the only available stress fields are diagonal, thus dramatically reducing the range of possibilities (cf. Section 4.1.2).

- The upper bound approach, on the contrary, seems very accurate to assess the dimensionless function in (2.11), since it can accommodate virtually any failure mechanism. Indeed the verifications with the Cox et al.'s solution as well as with the Matar and Salençon's solution showed remarkable agreement (Section 6.2 and 6.3).

- The yield design approach was proven sound and yielded a reasonable link between hardness and strength properties (Section 7.2). This strength properties extraction was greatly improved using a new definition of hardness as the ratio between the maximum driving force over the area estimated at the "effective plastic depth".

- It is impossible, from our results, to derive the strength properties from the hardness estimated with a Berkovich and a spherical indenter. There seem to be no unique relation between c and φ and the ratio of the hardness for those two different indenters. Only two different sharp indenters, for example the commercially available Berkovich and Corner Cube indenters can yield the assessment of strength properties for cohesive-frictional materials (Section 6.5).

- The dual indenter method yielded very interesting results, but was relatively inaccurate because of the difficulty to assess the correct contact area needed for the evaluation of the hardness

In this study several new contributions were made, they include:

1. The implementation of a reliable limit analysis program for axisymmetric problems. We

developed a lower and an upper bound algorithm to bracket the collapse load on a cohesive-frictional system. To our knowledge, it is the first complete work of this type.

2. The explanation of the locking problem for the lower bound algorithm and the limitation of the available stress fields.

3. The validation of the relevance and great accuracy of the upper bound algorithm.

4. The first simple development of a method to extract strength properties for cohesive-frictional materials from two simple sharp indentation tests.

5. The extrapolation of macroscopic cohesion for several shale materials from nano and microindentation tests.

9.2 Industrial Benefits

The estimation of strength properties for cohesive-frictional materials is crucial for the oil and gas industry. Through easy to carry out and reasonably cheap tests we should be able to reasonably assess both the cohesions c and the friction angle φ. This still needs further development, but it will most certainly be very useful to the oil industry and can have a considerable economic impact.

The finite element based upper bound application is a powerful design tool. This axisymmetric procedure can be employed to study foundations and particularly the problem of driving a pile into the soil (cf. Section 2.6). The soil weight effect can easily be incorporated into the program (as an additional term in the equilibrium equations) as well as a linear variation of the cohesion with depth (see [85] for more details).

9.3 Current Limitations and Future Perspectives

From the analysis of the lower bound results it emerges that the algorithm can be improved. A higher order element could be investigated, but would yield difficulties to linearize the yield criterion. It may then be interesting to incorporate a non linear optimizer, as some are currently commercially available. Regarding the indentation solutions we derived, although the meshes

can accommodate any geometry we did not take into account any pile-up or sink-in effect. This effect could easily be investigated by running simulations with different mesh geometries around the indenter. In addition, some additional yield criterions (e.g. Cam clay, Tresca, ...) could be incorporated in the algorithm, which currently only features the Mohr-Coulomb yield criterion. It may also be interesting to carry out indentation tests with conical indenters to check that the Berkovich and the Corner Cube indenters yield the same results as their equivalent conical indenters. Even though there is strong evidence that Berkovich indentation is frictionless, this aspect has not been investigated to the same depth for the Corner Cube indenter.

It also appeared that the plastic properties extraction is very sensitive to the definition of the hardness, and that more research is needed to correctly evaluate this quantity, or develop a new definition only based on a plastic energy standpoint, thus circumventing the need to assess the contact area.

From the results presented in this research, it also appears that the method to extract both strength properties (provided this can be done) would be difficult to carry out for friction angles less than 8° since the ratio between the Berkovich and the Corner Cube hardness is then below 8 %. Future research should therefore focus on using different indenters than the ones proposed in this thesis. From Figure 6-26 is seems that a more pronounced difference could be obtained using real conical indenters (and not pyramidal ones) with semi apex angles of 45° and 80°. In addition, other validation sets on well characterized cohesive frictional materials should also be performed.

Finally, the cohesion assessment of shales is based on a Weibull scaling law, and the refinement of upscaling schemes taking into account the particularities of the different scales is of utmost importance and is the focus of on-going research.

Part V

Appendices

Appendix A

Yield Constraints for the 3-Noded Triangular Extension Element (Lower Bound Approach)

This appendix presents the derivation of the constraints arising from the discretized yield criterion for the triangular extension element used in the lower bound approach. It complements the presentation of Section 3.3. Figure A-1 shows the 3 noded triangular element and extension zone. Referring to Eq. (3.89), the value of the k^{th} side of the linearized Mohr-Coulomb yield criterion is given by:

$$F_k = \sum_{n=1}^{3} N_n(r,z) F_{kn} \leqslant 0 \ ; \ k = 1, 2..., p \tag{A.1}$$

where

$$F_{kn} = A_k \sigma_{rr}^n + B_k \sigma_{zz}^n + C_k \sigma_{rz}^n + D_k \sigma_{\theta\theta}^n - E_n \ ; \ k = 1, 2..., p \ ; \ n = 1, 2, 3 \tag{A.2}$$

From (A.1), F_k varies linearly within the element, and thus

$$F_{kE} = F_{k2} + \frac{x}{L_{12}}(F_{k1} - F_{k2}) \tag{A.3}$$

The yield criterion must be satisfied at point E, i.e. $F_{kE} \leqslant 0$. Since $\frac{x}{L_{12}}$ is positive, the

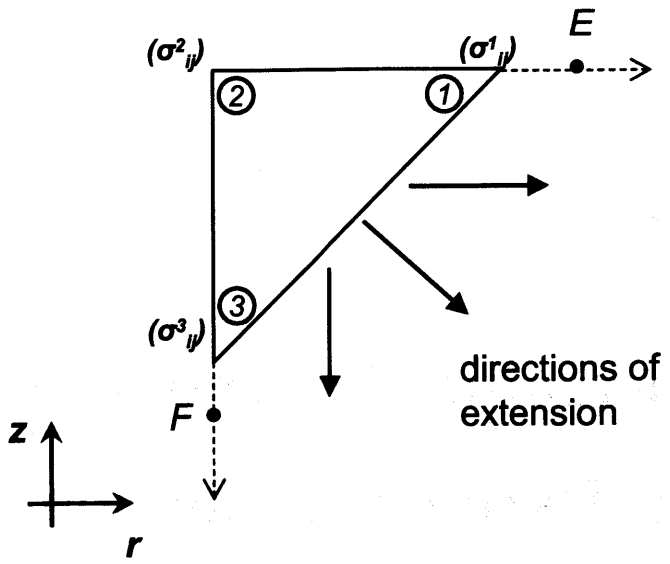

Figure A-1: 3-noded triangular extension zone.

condition is satisfied by enforcing the following constraints:

$$F_{k2} \leqslant 0 \text{ and } F_{k1} - F_{k2} \leqslant 0 \tag{A.4}$$

Similarly, for point F we derive:

$$F_{k2} \leqslant 0 \text{ and } F_{k3} - F_{k2} \leqslant 0 \tag{A.5}$$

Combining equations (A.4) and (A.5), the constraints for a 3-noded triangular element are:

$$F_{k2} \leqslant 0 \ , \ F_{k1} - F_{k2} \leqslant 0 \text{ and } F_{k3} - F_{k2} \leqslant 0 \tag{A.6}$$

Finally, it must then be proven that these conditions are valid for the stresses throughout the extension zone.

Using the shape function identity ($\sum_{n=1}^{3} N_n(r,z) = 1$), Eq. (A.1) can be rewritten as:

$$F_k = N_1(F_{k1} - F_{k2}) + F_{k2} + N_3(F_{k3} - F_{k2}) \tag{A.7}$$

Since the shape functions for the 3-noded triangular extension element satisfy:

$$N_1 \geqslant 0,\ N_2 \leqslant 1,\ N_3 \geqslant 0 \tag{A.8}$$

we conclude from (A.6) and (A.7) that $F_k \leq 0$ throughout the extension zone.

Appendix B

Yield Constraints for the 4-Noded Rectangular Extension Element (Lower Bound Approach)

This appendix presents the derivation of the constraints arising from the discretized yield criterion for the rectangular extension element, complementing the presentation of Section 3.3. Figure B-1 shows the 4-noded rectangular element and the extension zone. Compared to the constraint of the 3-noded triangular extension element (see Appendix A), an additional equality constraint needs to be enforced. It is obtained as follows. The stresses vary linearly within the element. Hence, the stresses at midpoint M are:

$$\sigma_{ij}^{M} = \sigma_{ij}^{1} + \sigma_{ij}^{3} \tag{B.1}$$

$$\sigma_{ij}^{M} = \sigma_{ij}^{2} + \sigma_{ij}^{4} \tag{B.2}$$

yielding:

$$\sigma_{ij}^{4} = \sigma_{ij}^{1} - \sigma_{ij}^{2} + \sigma_{ij}^{3} \tag{B.3}$$

- The derivation of the constraints arising from the yield criterion follows the one presented

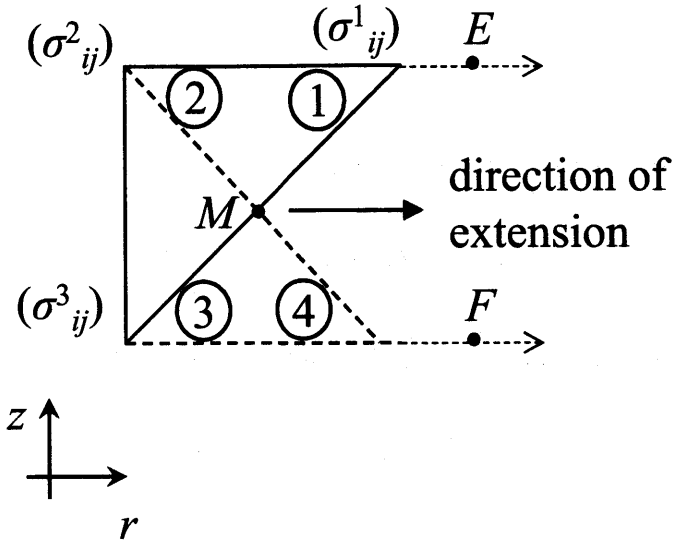

Figure B-1: 4-noded rectangular element.

in Appendix A. Since F_k is a linear function of the nodal stresses, we have:

$$F_k^4 = F_k^1 - F_k^2 + F_k^3 \tag{B.4}$$

Furthermore, Eq. (A.3) still holds:

$$F_{kE} = F_{k2} + \frac{x}{L_{12}}(F_{k1} - F_{k2}) \tag{B.5}$$

The yield criterion must be satisfied at point E, i.e. $F_{kE} \leqslant 0$. Since $\frac{x}{L_{12}}$ is positive, the condition is satisfied by enforcing the following constraints:

$$F_{k2} \leqslant 0 \text{ and } F_{k1} - F_{k2} \leqslant 0 \tag{B.6}$$

Similarly:

$$F_{kF} = F_{k3} + \frac{x}{L_{12}}(F_{k4} - F_{k3}) \tag{B.7}$$

Substituting (B.7) in (B.4) we get:

$$F_{kF} = F_{k3} + \frac{x}{L_{12}}(F_{k1} - F_{k2}) \tag{B.8}$$

Hence, the conditions to be enforced are:

$$F_{k2} \leqslant 0 \ , \ F_{k3} \leqslant 0 \text{ and } F_{k1} - F_{k2} \leqslant 0 \tag{B.9}$$

Finally, since the shape functions for the 4-noded rectangular extension element satisfy:

$$N_1 \geqslant 0, N_2 \leqslant 1, 0 \leqslant N_3 \leqslant 1 \tag{B.10}$$

and writing F_k as:

$$F_k = N_1(F_{k1} - F_{k2}) + F_{k2}(1 - N_3) + N_3 F_{k3} \tag{B.11}$$

the constraints defined by (B.9) enforce the non-positivity of the yield criterion throughout the extension zone.

Appendix C

Proof of Velocity Jump Decomposition

The goal of this appendix is to show that by assuming $|\Delta V_t| = V_{t+} + V_{t-}$ and $\Delta V_t = V_{t+} - V_{t-}$, subject to the constraints, V_{t+} and $V_{t-} \geq 0$, at least one of the two variables, V_{t+} or V_{t-} is zero. This Appendix complements the presentation in Section 5.2.4. We distinguish:

- Case 1; $\Delta V_t = 0$: in this case,

$$0 = V_{t+} + V_{t-} \tag{C.1}$$

$$0 = V_{t+} - V_{t-} \tag{C.2}$$

and

$$V_{t+} \geq 0 \tag{C.3}$$

$$V_{t-} \geq 0 \tag{C.4}$$

This proves that $V_{t+} = 0$ and $V_{t-} = 0$.

- Case 2; $\Delta V_t = a > 0$: in this case,

$$a = V_{t+} + V_{t-} \tag{C.5}$$

$$a = V_{t+} - V_{t-} \tag{C.6}$$

and

$$V_{t+} \geq 0 \tag{C.7}$$

$$V_{t-} \geq 0 \tag{C.8}$$

Thus $V_{t+} = a$ and $V_{t-} = 0$.

- Case 3; $\Delta V_t = -a$, $a > 0$: in this case,

$$a = V_{t+} + V_{t-} \tag{C.9}$$

$$-a = V_{t+} - V_{t-} \tag{C.10}$$

and

$$V_{t+} \geq 0 \tag{C.11}$$

$$V_{t-} \geq 0 \tag{C.12}$$

Thus $V_{t+} = 0$ and $V_{t-} = a$.

It can then be concluded that the correct normality rule is always satisfied.

Appendix D

Equivalence of the Constraints Within a Triangular Element

The purpose of this appendix is to prove that satisfying relations (5.50) to (5.55) within a triangular element is equivalent to satisfy the same relations at each node.

We first note that inequalities (5.50) to (5.55) have the same form:

$$\frac{u}{r} \geq \gamma \tag{D.1}$$

Thus if (D.1) holds within the element, it holds at its nodes as well.

Let us assume now that (D.1) holds at the three nodes of a triangular element. We then have:

$$\frac{u}{r} = \frac{\sum_{i=1}^{3} N_i(r,z)u_i}{\sum_{i=1}^{3} N_i(r,z)r_i} \geq \frac{\sum_{i=1}^{3} N_i(r,z)\gamma.r_i}{\sum_{i=1}^{3} N_i(r,z)r_i} = \gamma \tag{D.2}$$

Which concludes the proof.

Appendix E

Linearization of the Finite Dissipation-Function Inequations

This appendix presents the derivation of the constraints arising from the linearization of the finite dissipation conditions, and complements the presentation of Section 5.2.5.

Referring to Eq. (5.74) the set of inequations generated reads:

$$F_{kl} = \sum_{j=1}^{3} A_{kj} u_j + \sum_{j=1}^{3} B_{kj} v_j \leqslant 0 \ ; \ k = 1, 2..., p; \ l = 1, 2, 3 \text{ (3 nodes)} \tag{E.1}$$

where: if $r_l = 0$ (r_l is the radius of node l)

$$\begin{aligned} A^0_{kj} \ = \ & \Big(4 \frac{\partial N_j(r,z)}{\partial z} \sin(\pi k/p) \cos(\pi k/p) \sin(\pi/p) + \\ & \frac{\partial N_j(r,z)}{\partial r} \sin(\pi/p)[-2 + 4\cos^2(\pi k/p) \sin(\pi/p)] \Big) \sin(\varphi) \\ & -2 \frac{\partial N_j(r,z)}{\partial r} \sin(\pi/p) \cos(\pi/p) \end{aligned} \tag{E.2}$$

$$B^0_{kj} = \left(-4\frac{\partial N_j(r,z)}{\partial r}\sin(\pi k/p)\cos(\pi k/p)\sin(\pi/p)+ \right. \tag{E.3}$$
$$\left.\frac{\partial N_j(r,z)}{\partial z}\sin(\pi/p)[2-4\cos^2(\pi k/p)\sin(\pi/p)]\right)\sin(\varphi)$$
$$-2\frac{\partial N_j(r,z)}{\partial z}\sin(\pi/p)\cos(\pi/p)$$

The above formulas are valid for both inequations (5.54) and (5.55) since for $r_l = 0$ they reduce to

$$Rad \leq \left(\sum_{k=1}^{3}\frac{\partial N_k(r,z)}{\partial r}u_k + \sum_{k=1}^{3}\frac{\partial N_k(r,z)}{\partial z}v_k\right)\frac{1}{\sin(\varphi)} \tag{E.4}$$

From now on, we assume $r_l > 0$:

- For $i = 1$ and $l = 1$ (node 1):

$$A_{k1} = \left(4r_1\frac{\partial N_1(r,z)}{\partial z}\sin(\pi k/p)\cos(\pi k/p)\sin(\pi/p) + 2\sin(\pi/p)\cos(\pi/p)+ \right. \tag{E.5}$$
$$\left. r_1\frac{\partial N_1(r,z)}{\partial r}\sin(\pi/p)[-2+4\cos^2(\pi k/p)\sin(\pi/p)]\right)\sin(\varphi) -$$
$$2\sin(\pi/p)\cos(\pi/p) - 2r_1\frac{\partial N_1(r,z)}{\partial r}\sin(\pi/p)\cos(\pi/p)$$

$$A_{k2} = r_1 A^0_{k2} \tag{E.6}$$
$$A_{k3} = r_1 A^0_{k3} \tag{E.7}$$

$$B_{k1} = r_1 B^0_{k1} \tag{E.8}$$
$$B_{k2} = r_1 B^0_{k2} \tag{E.9}$$
$$B_{k3} = r_1 B^0_{k3} \tag{E.10}$$

$l = 2$ (node 2):

$$A_{k1} = r_2 A^0_{k1} \tag{E.11}$$

$$A_{k2} = \left(4r_2\frac{\partial N_2(r,z)}{\partial z}\sin(\pi k/p)\cos(\pi k/p)\sin(\pi/p) + 2\sin(\pi/p)\cos(\pi/p) + \right. \quad \text{(E.12)}$$
$$\left. r_2\frac{\partial N_2(r,z)}{\partial r}\sin(\pi/p)[-2+4\cos^2(\pi k/p)\sin(\pi/p)]\right)\sin(\varphi) -$$
$$2\sin(\pi/p)\cos(\pi/p) - 2r_2\frac{\partial N_2(r,z)}{\partial r}\sin(\pi/p)\cos(\pi/p)$$

$$A_{k3} = r_2 A^0_{k3} \quad \text{(E.13)}$$

$$B_{k1} = r_2 B^0_{k1} \quad \text{(E.14)}$$

$$B_{k2} = r_2 B^0_{k2} \quad \text{(E.15)}$$

$$B_{k3} = r_2 B^0_{k3} \quad \text{(E.16)}$$

- $l = 3$ (node 3):

$$A_{k1} = r_3 A^0_{k1} \quad \text{(E.17)}$$

$$A_{k2} = r_3 A^0_{k2} \quad \text{(E.18)}$$

$$A_{k3} = \left(4r_3\frac{\partial N_3(r,z)}{\partial z}\sin(\pi k/p)\cos(\pi k/p)\sin(\pi/p) + 2\sin(\pi/p)\cos(\pi/p) + \right. \quad \text{(E.19)}$$
$$\left. r_3\frac{\partial N_3(r,z)}{\partial r}\sin(\pi/p)[-2+4\cos^2(\pi k/p)\sin(\pi/p)]\right)\sin(\varphi) -$$
$$2\sin(\pi/p)\cos(\pi/p) - 2r_3\frac{\partial N_3(r,z)}{\partial r}\sin(\pi/p)\cos(\pi/p)$$

$$B_{k1} = r_3 B^0_{k1} \quad \text{(E.20)}$$

$$B_{k2} = r_3 B^0_{k2} \quad \text{(E.21)}$$

$$B_{k3} = r_3 B^0_{k3} \quad \text{(E.22)}$$

- For $i = 2$ and $l = 1$ (node 1):

$$A_{k1} = \left(4r_1\frac{\partial N_1(r,z)}{\partial z}\sin(\pi k/p)\cos(\pi k/p)\sin(\pi/p) - 2\sin(\pi/p)\cos(\pi/p) + \right. \quad \text{(E.23)}$$
$$\left. r_1\frac{\partial N_1(r,z)}{\partial r}\sin(\pi/p)[-2 + 4\cos^2(\pi k/p)\sin(\pi/p)]\right)\sin(\varphi) -$$
$$2\sin(\pi/p)\cos(\pi/p) - 2r_1\frac{\partial N_1(r,z)}{\partial r}\sin(\pi/p)\cos(\pi/p)$$

$$A_{k2} = r_1 A^0_{k2} \quad \text{(E.24)}$$

$$A_{k3} = r_1 A^0_{k3} \quad \text{(E.25)}$$

$$B_{k1} = r_1 B^0_{k1} \quad \text{(E.26)}$$

$$B_{k2} = r_1 B^0_{k2} \quad \text{(E.27)}$$

$$B_{k3} = r_1 B^0_{k3} \quad \text{(E.28)}$$

$l = 2$ (node 2):

$$A_{k1} = r_2 A^0_{k1} \quad \text{(E.29)}$$

$$A_{k2} = \left(4r_2\frac{\partial N_2(r,z)}{\partial z}\sin(\pi k/p)\cos(\pi k/p)\sin(\pi/p) - 2\sin(\pi/p)\cos(\pi/p) + \right. \quad \text{(E.30)}$$
$$\left. r_2\frac{\partial N_2(r,z)}{\partial r}\sin(\pi/p)[-2 + 4\cos^2(\pi k/p)\sin(\pi/p)]\right)\sin(\varphi) -$$
$$2\sin(\pi/p)\cos(\pi/p) - 2r_2\frac{\partial N_2(r,z)}{\partial r}\sin(\pi/p)\cos(\pi/p)$$

$$A_{k3} = r_2 A^0_{k3} \quad \text{(E.31)}$$

$$B_{k1} = r_2 B^0_{k1} \quad \text{(E.32)}$$

$$B_{k2} = r_2 B^0_{k2} \quad \text{(E.33)}$$

$$B_{k3} = r_2 B^0_{k3} \quad \text{(E.34)}$$

$l = 3$ (node 3):

$$A_{k1} = r_3 A^0_{k1} \tag{E.35}$$

$$A_{k2} = r_3 A^0_{k2} \tag{E.36}$$

$$\begin{aligned} A_{k3} = & \left(4r_3 \frac{\partial N_3(r,z)}{\partial z} \sin(\pi k/p)\cos(\pi k/p)\sin(\pi/p) - 2\sin(\pi/p)\cos(\pi/p) + \right. \\ & \left. r_3 \frac{\partial N_3(r,z)}{\partial r} \sin(\pi/p)[-2 + 4\cos^2(\pi k/p)\sin(\pi/p)]\right)\sin(\varphi) - \\ & 2\sin(\pi/p)\cos(\pi/p) - 2r_3 \frac{\partial N_3(r,z)}{\partial r} \sin(\pi/p)\cos(\pi/p) \end{aligned} \tag{E.37}$$

$$B_{k1} = r_3 B^0_{k1} \tag{E.38}$$

$$B_{k2} = r_3 B^0_{k2} \tag{E.39}$$

$$B_{k3} = r_3 B^0_{k3} \tag{E.40}$$

Bibliography

[1] H.G. Hopkins A.D. Cox, G. Eason. Axially symmetric plastic deformation in soils. *Philosophical Transactions of Royal Society of London, Series A*, 254(1036):1–45, 1961.

[2] J. Alcalá, F. Gaudette, S. Suresh, and S. Sampath. Instrumented spherical micro-indentation of plasma-sprayed coatings. *Materials Science and Engineering*, A316:1–10, 2001.

[3] E. Anderheggen and H. Knöpfel. Finite element limit analysis using linear programming. *International Journal of Solids and Structures*, 8:1413–1431, 1972.

[4] A. Assadi and S.W Sloan. Undrained stability of shallow square tunnel. *J. Geotech. Eng., ASCE*, 8(117):1152–1173, 1990.

[5] J.F. Barthélémy, L. Dormieux, and E. Lemarchand. Proceedings of the euro-c conference 2003, A micromechanical approach to the strength criterion of composite materials. In Bicanic de Borst Mang Meschke, editor, *Computational Modeling of Concrete Structures*, St. Johann im Pongau, Austria, March 2003. A.A. Balkema, Netherlands.

[6] J.F.W. Bishop. On the complete solution to problems of deformation of a plastic rigid material. *Jnl. Mech. Phy. Solids*, 2(1):43–53, 1953.

[7] A. D. Bona, K.J. Anusavice, and P.H. DeHoff. Weibull analysis and flexural strength of hot-pressed core veneered ceramic structures. *Dental Materials*, 19(7):662–669, 2003.

[8] A. Bottero, R. Negre, J. Pastor, and S. Turgeman. Finite element method and limit analysis theory for soil mechanics problems. *Computer Methods in Applied Mechanics and Engineering*, 22:131–149, 1980.

[9] J. Boussinesq. Applications des potentiels à l'étude de l'équilibre et du mouvement des solides élastiques. *Gauthier-Villars*, 1885.

[10] J.A Brinell. In *Congrès International des Méthodes d' Essai des Matériaux de Construction*, Paris, Tome 2, 83-94 1901.

[11] J.L. Bucaille, E. Felder, and G. Hochstetter. Identification of the viscoplastic behaviour of a polycarbonate based on experiments and numerical modeling of the nano-indentation test. *Journal of material science*, 37:3999–4011, 2002.

[12] J.L. Bucaille, S. Stauss, E. Felder, and J. Michler. Determination of plastic properties of metals by instrumented indentation using different sharp indenters. *Acta Materialia*, 51:1663–1678, 2003.

[13] M. Capurso. Limit analysis for continuous media with piecewise linear condition. *Mecanica*, 6:53–58, 1971.

[14] M.J. Cassidy and G.T. Houlsby. Vertical bearing capacity factors for conical footings on sand. *Géotechnique*, 52(9):687–692, 2002.

[15] M. M. Chaudhri. Subsurface strain distribution around Vickers hardness indentations in annealed polycrystalline copper. *Acta Materialia*, 46(9):3047–3056, May 1998.

[16] N. Chollacoop, M. Dao, and S. Suresh. Depth-sensing instrumented indentation with dual sharp indenters. *Acta Materialia*, 51:3713–3729, 2003.

[17] R.D. Conner, R.B. Dandliker, and W.L. Johnson. Mechanical properties of tungsten and steel fiber reinforced Zr41.25Ti13.75Cu12.5Ni10Be22.5 metallic glass matrix composites. *Acta Materialia*, 46:6089–6102, 1998.

[18] G. Constantinides. The elastic properties of calcium-leached cement pastes and mortars: A multi-scale investigation. M.Sc. dissertation, Massachusetts Institute of Technology, USA, 2002.

[19] M. Dao, N. Chollacoop, K.J. Van Vliet, T.A. Venkatesh, and S. Suresh. Computational modeling of the forward and reverse problems in instrumented sharp indentation. *Acta Materialia*, 49(19):3899–3918, 2001.

[20] M. Dao, N. Chollacoop, K.J. Van Vliet, T.A. Venkatesh, and S. Suresh. Computational modeling of the forward and reverse problems in instrumented sharp indentation. *Acta Materialia*, 49:3899–3918, 2001.

[21] M. F. Doerner and W. D. Nix. A method for interpreting the data from depth sensing indentation instruments. *J. Mater. Res.*, 1:601–609, 1986.

[22] P.E. Donovan. A yield criterion for Pd40Ni40P20 metallic glass. *Acta Metall.*, 37:445–456, 1989.

[23] R.T. Ewy. ChevronTexaco Rock Mechanics Analysis Team. Personal communication. 2003.

[24] R.T. Ewy, R.J. Stankovitch, and C.A. Bovberg. Mechanical behaviour of some clays and shales from 200m to 3800m depth. In *SARA Conference*, Cambridge,MA, 2003.

[25] K.M. Flores and R.H. Dauskardt. Mean stress effect on flow localization and failure in a bulk metallic glass. *Acta Materialia*, 49:2527–2537, 2001.

[26] D. François, A. Pineau, and A. Zaoui. *Comportement mécanique des matériaux.* Hermès, 1995.

[27] M. Fremond and J. Salençon. Limit analysis by finite element methods. In A. C. Palmen, editor, *Proc. Symp. on Role of Plasticity in Soil Mech.*, Cambridge, England, August 1973.

[28] H. Gao, Y. Huang, W.D. Nix, and J.W. Hutchinson. Mechanism-based strain gradient plasticity – I. theory. *Journal of the Mechanics and Physics of Solids*, 47:1239–1263, 1999.

[29] A. E. Giannakopoulos, P. L. Larsson, and R. Vestergaard. Analysis of Vickers indentation. *International Journal of Solids and Structures*, 31(19):2679–2708, 1994.

[30] A.E. Giannakopoulos. Indentation of graded substrates. *Thin Solid Films*, 332:172–179, 1998.

[31] A.E. Giannakopoulos and S. Suresh. Determination of elastoplastic properties by instrumented sharp indentation. *Scripta Materialia*, 40(10):1191–1198, 1999.

[32] G. Gottardi and R. Butterfield. On the bearing capacity of surface footing on sand under general planar loads. *Soils and Found.*, 33(1):68–79, 1993.

[33] Ch. Hellmich and F-J. Ulm. Are mineralized tissues open crystal foams reinforced by crosslinked collagen? - Some energy arguments. *Journal of Biomechanics*, 35(9):1199–1212, 2002.

[34] E.G. Herbert, G.M. Pharr, W.C. Oliver, B.N. Lucas, and J.L. Hay. On the measurement of stress-strain curves by spherical indentation. *Thin Solid Films*, 398-399:331–335, 2001.

[35] H. Hertz. On the contact of elastic solids (in German), Zeitschrift für die reine und angewandte Mathematik. *English translation in miscellaneous papers (translated by D.E. Jones and G.A. Schott):99.146-62. Macmillan, London, UK, 1986*, 92:156–71, 1881.

[36] F. Heukamp. *Chemomechanics of calcium leaching of cement-based materials at different scales: The role of C-S-H degradation on strength and durability performance of materials and structures.* Ph.D. dissertation (report R02-03), Massachusetts Institute of Technology, USA, 2002.

[37] G. Hochstetter, A. Jimenez, and J-L. Loubet. Strain-rate effects on hardness of glassy polymers in the nanoscale range. Comparison between quasi-static and continuous stiffness measurements. *Journal of Macromolecular Science-Physics*, 38 (B)(5):681–692, 1999.

[38] G.T. Houlsby. Theoretical analysis of the fall cone test. *Géotechnique*, 32, 1982.

[39] G.T. Houlsby and C.P. Wroth. Determination of undrained strengths by cone penetration tests. In *Proceedings of the Second European Symposium on Penetration Testing*, Amsterdam, 1982.

[40] Y. Huang, Z. Xue, H. Gao, W.D. Nix, and Z.C. Xia. A study of microindentation hardness tests by mechanism-based strain gradient plasticity. *J. Mate. Res.*, 15(8):1786–1796, 2000.

[41] N. Huber, W.D. Nix, and H. Gao. Identification of elastic-plastic material parameters from pyramidal indentation on thin films. *Proc. R. Soc. Lond. A*, 458:1593–1620, 2002.

[42] T. C. Hufnagel. Associate Professor, Department of Materials Science and Engineering, Johns Hopkins University. Personal communication. 2003.

[43] T. C. Hufnagel and S. Brennan. Short- and medium- range order in Zr70Cu20Ni10 bulk amorphous alloys. *Phys. Rev. B*, 67, 2003.

[44] K.C. Hwang, H. Jiang, Y. Huang, H. Gao, and N. Hu. A finite deformation theory of strain gradient plasticity. *Journal of the Mechanics and Physics of Solids*, 50:81–99, 2002.

[45] S. Igarashi, A. Bentur, and S. Mindess. Characterization of the microstructure and strength of cement paste by microhardness testing. *Advances in cement research*, 8(30):877–92, 1996.

[46] C.A. Johnson. Fracture statics of multiple flaw distribution. In D.P.H. Hasselman R.C. Bradt, A.G. Evans and F.F. Lange, editors, *Fracture mechanics of ceramics: surface flaws, statics, and microcracking vol. 5*, 365-386, New York , USA, 1983. Plenum Press.

[47] K.L. Johnson. *Contact Mechanics.* Cambridge University Press, Cambridge UK, 1985.

[48] O. Katz, Z. Reches, and J-C Roegiers. Evaluation of mechanical rock properties using a Schmidt hammer. *International Journal of Rock Mechanics and Mining Sciences*, 37:723–728, 2000.

[49] Y. Kawamura, H. Kato, A. Inoue, and T. Masumoto. Effects of extrusion conditions on mechanical properties in Zr-Al-Ni-Cu glassy powder compacts. *Mater. Sci. Eng.*, pages 39–43, 1996.

[50] R.B. King. Elastic analysis of some punch problems for a layered medium. *International Journal of Solids and Structures*, 23:1657–1664, 1987.

[51] C. Engin Koncagül and Paul M. Santi. Predicting the unconfined compressive strength of the breathitt shale using slake durability, shore hardness and rock structural properties. *International Journal of Rock Mechanics and Mining Sciences*, 36:139–153, 1999.

[52] P. L. Larsson, A. E. Giannakopoulos, E. Söderlund, D.J. Rowcliffe, and R. Vestergaard. Analysis of Berkovich indentation. *International Journal of Solids and Structures*, 33(2):221–248, February 1995.

[53] J.J Lewandowski and P. Lowhaphandu. Effects of hydrostatic pressure on the flow and fracture of a bulk amorphous metal. *Phil. Mag. A*, 82:3427–3441, 2002.

[54] M. T. Lin, D. Y. Jiang, L. Li, Z. L. Lu, T. R. Lai, and J. L. Shi. The effect of creep deformation of a beta sialon on vickers hardness, fracture toughness and Weibull modulus. *Materials Science and Engineering A*, 351(1-2):9–14, 2003.

[55] J-L. Loublet, M. Bauer, A. Tonck, S. Bec, and B. Gauthier-Manuel. *Mechanical properties and deformation behaviour of materials having ultra-fine microstructures.* Kluwer Academic Publishers, 1993.

[56] A. V. Lyamin and S. W. Sloan. Lower bound limit analysis using non-linear programming. *International Journal for Numerical Methods in Engineering*, 55:573–611, 2002.

[57] A. V. Lyamin and S. W. Sloan. Upper bound limit analysis using linear finite elements and non-linear programming. *International Journal for Numerical and Analytical Methods in Geomechanics*, 26:181–216, 2002.

[58] L. Lysmer. Limit analysis of plane problems in soil mechanics. *ASCE Journal of the Soil Mechanics and Foundations Division*, 96:1311–1334, 1970.

[59] Dejun Ma, Chung Wo Ong, Jian Lu, and Jianwen He. Methodology for the evaluation of yield strength and hardening behaviour of metallic materials by indentation with spherical tip. *Journal of Applied Physics*, 94(1):288–294, 2003.

[60] M. Matar and J. Salençon. Capacité portante des fondations superficielles circulaires. *Journal de Mechanique Théorique et Appliquée*, 1(2):237–267, 1982. Available in English in "Foundation Engineering, Volume 1, Soil properties-Foundation design and construction". Presse de l'Ecole Nationale des Ponts et Chaussées.

[61] Cs. Meszaros. *The Efficient Implementation of Interior Point Methods for Linear Programming and their Applications.* Ph.D. dissertation, Eötvös Loránd University of Sciences, Budapest (Hungary), 1996.

[62] Cs. Meszaros. Fast cholesky factorization for interior point methods of linear programming. *Computers And Mathematics with Applications*, 31(4/5):49–51, 1996.

[63] D.B. Miracle and O.N. Senkov. A geometric model for atomic configurations in amorphous Al alloys. *Journal of Non-Crystalline Solids*, 39(1-2):174–191, 2003.

[64] Toshiji Mukai, T.G. Nieh, Yoshihito Kawamura, Akihisa Inoue, and Kenji Higashi. Dynamic response of a Pd40Ni40P20 bulk metallic glass in tension. *Scripta Materialia*, 46(1):43–47, 2002.

[65] J.D. Murff. Limit analysis of multi-footing foundation systems. In *Proc of the 8th Int. Conf. on Comp. Methods and Advances in Geomechanics*, Tome 1, 233-244, 1994.

[66] J. Pastor. *Application de l'analyse limite à l'étude de la stabilité des pentes et des talus.* Ph.D. dissertation, USMG, Grenoble (France), 1976.

[67] J. Pastor and S. Turgeman. Mise en oeuvre numérique des méthodes de l'analyse limite pour les matériaux de Von Mises et de Coulomb standards en déformation plane. *Mech. Res. Comm.*, 3:469–476, 1976.

[68] G.M. Pharr and A. Bolshakov. Methodology understanding nanoindentation unloading curves. *J. Mater. Res.*, 17(10):2260–2271, 2002.

[69] G.M. Pharr, W.C. Oliver, and F.R. Brotzen. On the generality of the relationship among contact stiffness, contact area, and elastic modulus during indentation. *J. Mat. Res.*, 7(3):613–617, 1992.

[70] G. D. Quinn. Hardness testing of ceramics. *Advanced Materials and Processes*, 154(2):2260–2271, 1998.

[71] J. Salençon. *Calcul à la rupture et analyse limite.* Presse de l'école nationale des Ponts et Chaussées, Paris FR, 1983.

[72] J. Salençon. *Elasto-plasticité et calcul à la rupture.* Editions de l'Ecole Polytechnique, Palaiseau FR, 2001.

[73] C.A. Schuh and A.C. Lund. Atomistic basis for the plastic yield criterion of metallic glass. *Nature Materials*, 2:449–452, 2003.

[74] C.A. Schuh and T.G. Nieh. A survey of instrumented indentation studies on metallic glasses. *Submitted to Journal of Materials Research, June 2003.*

[75] S.W. Sloan. Lower bound limit analysis using finite elements and linear programming. *Int. J. Numer. Anal. Methods in Geomech*, 1(12):61–77, 1988.

[76] S.W. Sloan. A steepest edge active set algorithm for solving sparse linear programming problems. *Int. J. Numer. Anal. Methods in Geomech.*, 12(26):2671–2685, 1988.

[77] S.W. Sloan and P.W. Kleeman. Upper bound limit analysis with discontinuous velocity fields. *Comput. Meth. Appl. Mech. Engng.*, 127:293–314, 1995.

[78] Ian Sneddon. The relation between load and penetration in the axisymmetric Boussinesq problem for a punch of arbitrary profile. *International Journal of Engineering Science*, 3:47–57, 1965.

[79] S. Suresh, A. E. Giannakopoulos, and J. Alcala. Spherical indentation of compositionally graded materials: Theory and experiments. *Acta Materialia*, 45(4):1307–1321, 1997.

[80] S. Suresh and A.E. Giannakopoulos. Report Inst 2/98, Massachusetts Institute of Technology, 1998.

[81] S. Suresh, A.E. Giannakopoulos, and J. Alcalá. Spherical indentation of compositionally graded materials: Theory and experiments. *Acta Materialia*, 45(4):1307–1321, 1997.

[82] D. Tabor. *The Hardness of Metals.* Clarendon Press, Oxford, 1951.

[83] P. Trtik, C.M. Reeves, and P.J.M. Bartos. Use of focused ion beam (fib) for advanced interpretation of microindentation test results applied to cementetious composites. *Materials and Structures*, 33(227):189–193, 2000.

[84] S. Turgeman. *Etude des fondations sollicitées à l'arrachement par la théorie de l'analyse limite.* Ph.D. dissertation, USMG, Grenoble (France), 1976.

[85] Ph. Ukrichton. Evaluation of numerical limit analysis by finite elements and linear programming. M.Sc. dissertation, Massachusetts Institute of Technology, USA, 1996.

[86] F-J. Ulm, G. Constantinides, and Y. Abousleiman. Toward the mechanical 'blueprint' of shales materials. Preliminary report to ChevronTexaco, 2003.

[87] F-J. Ulm and O. Coussy. *Mechanics and Durability of Solids, Volume I: Solid Mechanics.* MIT and Prentice Hall series on Civil, Environmental and Systems Engineering, Prentice Hall, Upper Saddle River, New Jersey, 2003, 2002.

[88] R. Vaidyanathan, M. Dao, G. Ravichandran, and S. Suresh. Study of mechanical deformation in bulk metallic glass through instrumented indentation. *Acta Materialia*, 49:3781–3789, 2001.

[89] T. A. Venkatesh, K. J. van Vliet, A. E. Giannakopoulos, and S. Suresh. Determination of elasto-plastic properties by instrumented sharp indentation: Guidelines for property extraction. *Scripta Materialia*, 42(9):833–839, April 2000.

[90] Marcel R.A. Van Vliet and Jan G.M. Van Mier. Effect of strain gradients on the size effect of concrete in uniaxial tension. *International Journal of Fracture*, 95:195–219, 1999.

[91] W. Weibull. A statistical theory of the strength of materials. *Royal Swedish Academy of Eng. Sci. Proc.*, 151:1–45, 1939.

[92] B. Wolf and A. Richter. The concept of differential hardness in depth sensing indentation. *New Journal of Physics*, 5:15.1–15.17, 2003.

[93] E. Yasar and Y. Erdogan. Estimation of rock physicomechanical properties using hardness methods. *Engineering Geology, In Press, Corrected Proof, Available online 9 July 2003.*

[94] Isik Yilmaz and Hüsseyin Sendir. Correlation of Schmidt hardness with unconfined compressive strength and young's modulus in gypsum from sivas (Turkey). *Engineering Geology*, 66:211–219, 2002.

[95] B. Zech and F.H. Wittmann. A complex study on the reliability assessment of the containment of a PWR. Part II, Probabilistic approach to describe the behaviour of materials. *Nuclear Engineering and Design*, 48:563–593, 1978.

[96] K. Zeng and C. h Chiu. An analysis of load-penetration curves from instrumented indentation. *Acta Materialia*, 49:3539–3551, 2001.